DEFORMATION, WAVE PHENOMENA, AND BREAKUP OUTCOMES OF ROUND NONTURBULENT LIQUID JETS IN UNIFORM GASEOUS CROSSFLOW

By

CHEE-LOON NG

Bachelor of Science
Oklahoma State University
Stillwater, Oklahoma
1998

Master of Science
Oklahoma State University
Stillwater, Oklahoma
1999

Submitted to the Faculty of the
Graduate College of the
Oklahoma State University
in partial fulfillment of
the requirements for
the Degree of
DOCTOR OF PHILOSOPHY
July, 2006

DEFORMATION, WAVE PHENOMENA, AND

BREAKUP OUTCOMES OF ROUND

NONTURBULENT LIQUID JETS IN

UNIFORM GASEOUS CROSSFLOW

Dissertation Approved:

Khaled A. Sallam

Dissertation Advisor
Peter M. Moretti

Andrew S. Arena

Arland H. Johannes

A. Gordon Emslie

Dean of the Graduate College

To my parents.

ACKNOWLEDGMENTS

I wish to give my special appreciation to my parents for their precious love, support, and strong encouragement at times of difficulty. My appreciation extends to my advisor, Dr. Khaled A. Sallam for his supervision, guidance, support, and friendship. I also wish to express my sincere gratitude to my other committee members Dr. Peter M. Moretti, Dr. Andrew S. Arena Jr. and Dr. Arland H. Johannes, whose suggestions, assistance and friendship are also invaluable. Finally, I would like to thank Dr. Hossam M. Metwally (FLUENT Inc., Evanston, IL, United States) and Dr. Christian Aalburg (GE Global Research, Munich, Germany) for their suggestions and the staff of Microflow Laboratory for their assistance with apparatus development.

This research was sponsored by National Science Foundation under Grant No. EPS-0132534 (Oklahoma EPSCoR).

TABLE OF CONTENTS

Chapter **Page**

LIST OF TABLES

LIST OF FIGURES

NOMENCLATURE

Alphabetical

a	acceleration
A	Atwood number, $= (\rho_2 - \rho_1)/(\rho_2 + \rho_1)$
A_{sc}	cross-sectional area of liquid jet in x-z plane
C	constant that incorporates the drag coefficient
C_b	empirical parameter of Eqn. 4.16
C_d	orifice discharge coefficient
C_D	drag coefficient, $= \text{drag}/(0.5\rho_G U_G^2)$
C_L	empirical parameter of Eqn. 5.7
C_p	pressure coefficient, $= (P_{static} - P_G)/(0.5\rho_G U_G^2)$
C_λ	empirical parameter of Eqn. 4.11
Ca	capillary number, $= \mu U/\sigma$
d_{Bag}	diameter of droplets produced by the breakup of the bag-membrane
d_c	liquid span-wise diameter
$d_{Droplets}$	diameter of droplets
d_{eq}	equivalent injector diameter
d_f	orifice diameter
d_j	nozzle exit diameter
d_L	diameter of ligament at onset
d_{Node}	diameter of droplets produced by the breakup of the node

d_{Ring}	diameter of droplets produced by the breakup of the ring
d_s	liquid cross-stream diameter
$dx_{pixel,i}$	diameter of drop i in pixel dimensions
D	diameter of two-dimensional liquid column
$\overline{\overline{D}}$	second invariant of the rate of deformation tensor, $= \partial u_j / \partial x_i + \partial u_i / \partial x_j$
$\vec{F}$	force vector
F_{vol}	volume force
$\vec{g}$ (or g)	gravitational acceleration, = 9.81 m/s^2
k	wave number
κ	curvature
L	length of a cylindrical liquid column
L_s	length of the liquid column from the onset of bag formation to the end of liquid core
$\dot{m}$	mass flowrate
M	mach number
n	surface normal
$\hat{n}$	unit normal
N_B	bag count
Oh	liquid jet Ohnesorge number, $= \sqrt{We_L} / Re_L = \mu_L / \sqrt{\rho_L \sigma d_j}$
p	pressure
q	liquid jet momentum ratio, = $\rho_L v_j^2 / \rho_G U_G^2$
R	surface curvature
R_c	length scale/pixel conversion factor

Re_G	Reynolds number of the crossflow, $= \rho_G U_G d_j / \mu_G$
Re_L	Reynolds number of the liquid jet, $= \rho_L v_j d_j / \mu_L$
s	standard deviation of Eqn. A.1
S	source term
SMD	sauter mean diameter, $= \sum d^3 / \sum d^2$
t	time
t^*	Ranger and Nicholls (1969) aerodynamic characteristic time, $= d_j(\rho_L/\rho_G)^{0.5}/U_G$
t_v^*	characteristic viscous time, $= d_j^2/\upsilon_L$
u	velocity in the x-direction
u_c	x-velocity at (x, y, 0)
u_L	characteristic liquid velocity, $\sim U_G/[1+(\mu_L\rho_L/\mu_G\rho_G)^{0.5}]$
$u_{Lthreshold}$	liquid velocity threshold requires to form ligaments that produce droplets
u_{max}	maximum x-velocity in the wake region
U	uncertainty, if not otherwise specified, subscript represents variable
U_f	volume flux through the face of the cell
U_G	crossflow velocity
v	velocity in y-direction
$\|v\|$	velocity magnitude
v_j	nozzle exit velocity
v_s	jet surface velocity
$v_{s(mass\text{-}avg)}$	mass-weighted average liquid cross-sectional velocity
V	volume of the cell

w	z-velocity
We_G	crossflow weber number, $= \rho_G d_j U_G^2/\sigma$
x	cross-stream coordinate (i.e. direction of the gaseous crossflow)
x_0, y_0, z_0	location of the center of the jet at the nozzle exit, = (0, 0, 0)
y	streamwise coordinate (i.e. direction of the injection of the liquid jet)
y_{bf}	onset of bag formation
z	span-wise coordinate (i.e. direction normal to both the gaseous crossflow and liquid jet)
z_o	width of the outer wake region
$z_{1/2}$	wake half width

Greek

α	liquid phase volume fraction
$\dot{\gamma}$	shear rate
Δ	change in variable
η	growth rate of wavelength
λ	wavelength of Rayleigh instability
λ_c	column wavelength
λ_s	surface wavelength
μ	molecular viscosity
ν	kinematic viscosity
ξ	magnitude of vorticity vector, $= \nabla \times \vec{V}$
ρ	density
σ	surface tension

Ω	angular velocity of rotation

Subscripts

avg	mean value
b	location of the end of liquid core
Bag	bag-membrane property
f	fluid property
G	gas property
i	location of the onset of breakup
j	nozzle exit property
L	liquid property
local	local property
max	maximum value
Node	node property of the bag-like structure
Ring	ring property of the bag-like structure
∞	ambient gas property

Symbol

∇	gradient operator

CHAPTER I

INTRODUCTION

1.1 Background

The breakup of liquid jets in gaseous crossflow has applications in after-burners in jet engine, gas turbine combustors, liquid rocket engines, ramjet engines, scramjet engines, diesel engines, and agricultural sprays, among others. The spray formation occurs in two stages: (1) The disintegration of the liquid jet, termed the primary breakup of liquid jet, and (2) the disintegration of the liquid droplets, termed the secondary breakup of the liquid droplets. The primary breakup of liquid jet is significant because of its role in initiating the atomization process, in controlling the extent of liquid core, and in providing properties of the dispersed phase flow. The development of accurate predictions for spray formation requires a fully coupled analysis of the complex interactions among the various phases of the multiphase flow. Components of such an analysis must include knowledge of any cavitation flow, jet instabilities, drop-drop interactions, and turbulence. The current work presents an experimental and computational investigation of the deformation, wave phenomena, and droplet properties/transport dynamics of round nonturbulent liquid jets in uniform gaseous crossflow. The photograph of round nonturbulent liquid jets in still air is shown in Fig. 1.1. Those are similar to liquid cutting jets (typically operating at 60,000 psi) used to cut ceramics, glass, and steels, among others, as shown in Fig. 1.2.

In the absence of an advanced imaging technique capable of operating in the optically-challenging dense-spray near-injector region, experimental persuasion of the primary breakup mechanisms is often limited. Without sophisticated analysis tool and computational resources, computational modeling is restricted to two-dimensional symmetrical flowfield about the jet vertical axis or two-dimensional slices of the jet in the direction of the crossflow. Both do not directly account for the three-dimensional waves that dictate the onset of the primary breakup of liquid jets in crossflow. As such, a good understanding of liquid jets breakup lies in the basic knowledge of the full-field flow dynamics that involve interfaces between different fluids.

1.2 Problem Statement

The objectives of the present investigation were to complete the experimental observations of round nonturbulent liquid jets in uniform gaseous crossflow within the bag breakup regime, and to develop a validated, time-accurate, three-dimensional computational fluid dynamic (CFD) simulation to study the surface properties of round nonturbulent liquid jets in uniform gaseous crossflow within column, bag, and shear breakup regimes by considering the effects of crossflow Weber number at large liquid/gas density ratio (> 500) and small Ohnesorge number (Oh < 0.1). The present experiments utilized a pressure-fed supercavitating nozzle system to generate the round nonturbulent liquid jets and employed pulsed photography, single- and double-pulsed shadowgraphy, and high-speed imaging to investigate the wave phenomena and breakup mechanisms under various test conditions. The computational simulations employed the Volume of Fluid (VOF) formulation of FLUENT, with an Euler explicit surface-tracking scheme followed by a geometric reconstruction (piecewise-linear) interpolation treatment

to the cells that lie near the predicted liquid-gas interface. The solution-adaptive mesh refinement feature of FLUENT was employed to refine the grid based on the numerical evolution of the liquid volume fraction surrounding the liquid-gas interface in order to minimize grid dependency of the final solution. The computational simulations, in conjunction with the experimental persuasions, can provide detailed analysis of the deformation and surface properties along the liquid column and enhance the understanding of the conditions of breakup regime transitions, and the properties of the dispersed phase flow. These results are of interest due to direct applications in a variety of industrial atomizers.

1.3 Previous Related Studies

Mazallon et al. (1999) classified the primary breakup of nonturbulent liquid jet in gaseous crossflow into four breakup regimes: (1) Column breakup regime, (2) bag breakup regime, (3) multimode breakup regime, and (4) shear breakup regime. The visualization of primary breakup processes of round nonturbulent liquid jets in uniform gaseous crossflow for no breakup ($We_G = 0$), column breakup ($We_G = 3$), bag breakup ($We_G = 8$), multimode breakup ($We_G = 30$), and shear breakup ($We_G = 220$) are shown in Fig. 1.3. The column breakup involved the breakup of the entire liquid column as a whole into droplets of about the same size. In bag breakup, the liquid column was flattened and deflected in the direction with respect to the gas motion, forming the bag-like structure that subsequently breakup into droplets of different sizes. In multimode breakup, both the bag-like structures and liquid ligaments appeared at the same time. In shear breakup, liquid ligaments were formed due to the shearing of the liquid from the liquid column. At very high crossflow Weber number, the liquid jet is expected to shatter

into ligaments and droplets of various sizes, called the catastrophic breakup regime, which is somewhat similar to the catastrophic breakup of drops reported by Hwang et al. (1996) and Chryssakis and Assanis (2005). Vich (1997), Wu et al. (1997), Mazallon et al. (1999), Aalburg et al. (2003 and 2005), and Sallam et al. (2004) have reported striking similarities between the properties of the primary breakup of round nonturbulent liquid jets in uniform crossflow and the secondary breakup of drops subjected to shock wave disturbances. The bag breakup of a three-dimensional liquid drop subjected to a shock wave disturbance is shown in Fig. 1.4. The structure of the bag formed in the primary breakup of liquid jet is similar to the secondary breakup of drop. In the shear breakup regime, however, both Mazallon et al. (1999) and Sallam et al. (2004), reported that the time of onset of breakup of liquid jets in crossflow was significantly lower than those associated with the breakup of droplets within the shear breakup regime. Furthermore, Sallam et al. (2004) reported that the deformation of the liquid jets on the onset of breakup within the shear breakup regime was significantly lower than those associated with the breakup of drops at the same crossflow Weber number. The reasons of these behaviors were not understood though. More information about the secondary breakup of drops can be found at Faeth (1997), Leong et al. (2000), and references cited therein.

1.3.1 Basic Relevant Numbers

The tendency of the liquid jet to break up is characterized by several dimensionless numbers that quantify the relationship between the forces attempting to destabilize the liquid jets and those forces attempting to stabilize it. For liquid jet in crossflow, the surface tension and liquid viscosity stabilize the cross-sectional surface area of the liquid column by retarding the distortion to prevent aerodynamic breakup.

1.3.1.a Ohnesorge Number (Oh) The Ohnesorge number ($Oh = \sqrt{We_L}/Re_L = \mu_L/\sqrt{\rho_L \sigma d_j}$) represents the ratio of the viscous forces to surface tension forces. For primary breakup of liquid jets in gaseous crossflow, viscous effects become important when the Ohnesorge number exceeds 0.1.

1.3.1.b Crossflow Weber Number (We_G) The crossflow Weber number ($We_G = \rho_G d_j U_G^2/\sigma$) represents the ratio of the aerodynamic force ($\sim \rho_G U_G^2 dj^2$) of the crossflow to the surface tension force ($\sim \sigma d_j$) of the liquid jet. For primary breakup of liquid jets in gaseous crossflow, the breakup regime transitions are solely controlled by the crossflow Weber number when the viscous effects are small (Oh << 1).

1.3.2 Experimental Studies

This section reviews relevant experimental studies associated with the investigation of liquid jets in gaseous crossflow. The current status of experimental studies is discussed.

1.3.2.a Penetration Length and Jet Trajectory Earlier work of round nonturbulent liquid jets in uniform gaseous crossflow had emphasized penetration lengths and jet trajectories due to their practical importance (Geary and Margettes, 1969, Kitamura and Takahashi, 1976, Schetz and Padhye, 1977, Less and Schetz, 1986, and Nguyen and Karagozian, 1992). The liquid jet momentum ratio ($q = \rho_L v_j^2/\rho_G U_G^2$), was found to control the penetration length of the liquid jet. Schetz and Padhye (1977) determined that the maximum penetration length (y_b) normalized by the orifice diameter (d_f) has the form

$$\frac{y_b}{d_f} = C\sqrt{q}C_d\left(\frac{d_{eq}}{d_f}\right) \tag{1.1}$$

where C represents a constant that incorporates the drag coefficient, C_d is the discharge coefficient of the orifice, and d_{eq} denotes the equivalent injector diameter. For a circular orifice, d_{eq}/d_f is equal to unity. Wu et al. (1997) expressed the trajectory of the liquid jet as

$$\frac{y}{d_f} = \sqrt{\frac{\pi x q}{C_D d_f}} \tag{1.2}$$

where C_D is the average drag coefficient that incorporated the effects of column deformation and the stripping of droplets from the column surface. Sallam et al. (2004) argued that the drag coefficient of liquid jets in crossflow depends on the geometry of the liquid jet and hence on the breakup regimes. They presented separate trajectories correlations for bag, multimode and shear breakup regimes. Investigations of liquid jet trajectory included the studies performed by Heister et al. (1989) and Inamura (2000) that utilized an ellipsoidal-shaped liquid cross-section model to provide a better prediction of the liquid jet trajectory.

1.3.2.b Breakup Regimes Transitions Several experimental observations have led to the understanding of the conditions for the transitions of breakup regimes. Hinze (1955) found that the transitions between breakup regimes for liquid drop depend on the crossflow Weber number (We_G) and Ohnesorge number (Oh). The breakup regimes of round nonturbulent liquid jets in crossflow were correlated in terms of crossflow Weber number and Ohnesorge number based on the ideas of Hinze (1995) by Mazallon et al.

(1999). For Oh < 0.1, it was found that the viscous effects are small and the drag forces acting on the liquid jet was stabilized by the surface tension forces alone. As such, the breakup regime transitions occurred at a constant critical We_G. For Oh > 0.1, the breakup regime transitions of round nonturbulent liquid jet in crossflow were influenced by both the We_G and Oh number. Aalburg et al. (2005) suggested the breakup regime transitions were solely controlled by a new dimensionless number $We^{1/2}/Oh$ prior to the location of whole column breakup.

1.3.2.c Surface and Column Waves Surface waves were observed along the windward and leeward sides of the liquid jet. Column waves along the liquid column propagate along the liquid jet, magnified in amplitude, until liquid jet breakup occurs.

Wu et al. (1997) observed that surface waves appear on the windward and leeward sides of the liquid jet, where the latter (if developed) was observed to appear before the formal. As jet velocity increases, the amplitude of the leeward wave increases until surface breakup or droplets stripping occurred from the downwind side of the liquid jet. The crossflow bent the liquid column and produced the windward waves that increased in amplitude and led to the breakup of liquid jet into globules and ligaments. The transverse height to the point of column fracture was found to depend on the square root of the liquid jet momentum ratio. The downstream distance to the point of column fracture was independent of the liquid jet momentum ratio. The observation, performed at the plane of symmetry of the deflecting jet, prevented the observation of the waves occurring in direction parallel to the crossflow.

Mazallon et al. (1999) measured the column and upwind surface waves along the liquid jet. The observations were limited to the plane of symmetry of the deflecting jet.

1.3.2.d Breakup Outcomes Sallam et al. (2004) studies the primary breakup of round nonturbulent round liquid jet in gaseous crossflow employing pulsed shadowgraphy and pulsed holography. The breakup regime transitions of Mazallon et al. (1999) were revised by Sallam et al. (2004). Their experimental data focused on multimode and shear breakup regimes. They found conditions required for the onset of ligament and drop formation, ligament and drop sizes along the liquid surface, drop velocities after breakup, rates of liquid breakup between the onset of drop formation and breakup of liquid column as a whole, and conditions required for the breakup of liquid column as a whole.

1.3.2.e Summary of Experimental Studies The following summarizes the current status of the experimental studies related to liquid jets in gaseous crossflow:

- The penetration lengths and jet trajectories of liquid jets in crossflow have been studied extensively. The penetration length depends on the liquid jet momentum ratio.
- For small Ohnesorge number ($Oh < 0.1$), the breakup regime transitions of round nonturbulent liquid jet in gaseous crossflow were controlled by the crossflow Weber number.
- The previous experimental studies were limited to shadowgraphy observations at the plane of symmetry of the deflecting liquid jet. The phenomena occurring along the sides of the liquid jet were not observed.

- The previous experimental observations were not performed by high-speed imaging, which prevented studies related to the dynamics of the wave phenomena and the breakup mechanisms.
- In bag breakup, the observations and measurements were limited to the column wavelength, deformation at the onset of breakup, and time of onset of breakup. The breakup outcomes of the bags were not known.

1.3.3 Computational Studies

Kitamura and Takahashi (1976) performed an analytical study of liquid jet breakup in incompressible crossflow employing a disturbances growth rate characteristic equation derived based on two assumptions: (I) Disturbances were symmetric about the liquid jet axis (i.e., assuming that for low crossflow velocity, the effect of the flow inertial on the disturbances was small and can be neglected), and (II) disturbances in surrounding air were non-symmetric. The model assumed that the aerodynamic effect of the crossflow was not the major factor that caused the liquid jet to break up, and attributed liquid jet breakup to symmetric disturbances within the liquid jet. The analysis is limited to column breakup region ($U_G \leq 7.6$ m/s with $d_j = 0.124$ cm). At higher crossflow, the pronounced aerodynamic effect bent the jet and produced asymmetries along the surface wave disturbance rendered the main assumption in the model invalid. The numerical analysis predicted that the maximum growth rate (point where liquid jet broke into drops) would increase with the Weber number, similar to the observation of Schetz and Padhye (1997). The analytical model was validated based on its compliance in breakup length with experimental measurements using water, ethanol and aqueous

glycerol solution at air velocity less than 5 m/s, where disintegration by symmetric disturbance was observed.

Li (1990) studied the breakup of liquid fuels in hot air crossflow by employing two analytical/numerical two-dimensional models for sonic point calculations: (I) Elliptical jet cross-section analysis, and (II) transverse jet represented by a two-dimensional blunt body. The non-reacting liquid jet breakup location was determined by the local sonic point criterion (Schetz et al., 1980). An auxiliary criterion based on surface tension stability was used as an alternative means of determining the breakup location.

Nguyen and Karagozian (1992) solved the two-dimensional compressible flowfield about the elliptical liquid jet cross-section (represented by elliptical vortex pair re-circulation cell) at various locations along the jet trajectory via analytical means (for local Mach number, $M_{\infty,local} < 0.3$) and numerical means (second-order total variation diminishing (TVD) scheme of Harten (1983) for $0.3 < M_{\infty,local} < 0.7$ and first-order scheme of Godunov et al. (1961) for $0.7 < M_{\infty,local} < 1.0$) to predict the behavior of non-reacting and reacting liquid jet in subsonic crossflow. The mass loss due to boundary layer shedding, evaporation, and combustion were incorporated into trajectory calculation. However, the actual breakup of the liquid jet was not studied which made the proposed model inaccurate in the farfield region.

Yi and Reitz (2002 and 2004) tracked the growth of waves on the liquid-gas interface of liquid jets using a reduced one-dimensional continuity and momentum model to investigate the primary breakup of low-speed jets. In the absence of multi-dimensional effects, the wave growth on the liquid-gas interface was not physical.

1.3.3.a Deformation The deformation of the liquid cross-section is induced by the aerodynamic forces. Experimental observation shows that the liquid jet which initially exits the orifice has a round cylindrical cross-section (Mazallon et al., 1999 and Sallam et al., 2004). The jet then deforms into a kidney-shape (Aalburg et al., 2005). A possible cause of the kidney-like shaped cross-section may be attributed to the presence of a counter-rotating vortex pair within the liquid jet. Aalburg (2003 and 2005) developed a procedure to extend the parameter range of existing studies (Vich, 1997, Wu et al., 1997, and Mazallon et al., 1999) of nonturbulent round liquid jets in uniform crossflows to conditions representing practical high-pressure spray combustion processes that were difficult to address by experiments. The numerical scheme solved time-dependent two-dimensional incompressible Navier-Stokes equations by treating the flow as isothermal with constant physical properties on a uniform staggered grid, utilizing the projection method of Chorin (1968) and the Level Set method of Sussman et al. (1994). The simulations studied the independent effects of four dimensionless variables: (I) Weber numbers from 0.1 to 100,000, (II) Ohnesorge numbers from 0.001 to 100, (III) Reynolds numbers from 12.5 to 200, and (IV) liquid/gas density ratios from 2 to ∞ (using Richardson extrapolation), that utterly described the problem. The computation results were validated based on its good agreement with Mazallon et al. (1999) measurements at large liquid/gas density ratios and its compliance with wake and drag properties of spheres and cylinders in crossflows. However, the two-dimensional symmetrical computational model inherently could not capture waves properties that had been observed in the third dimension (parallel to the jet axis) along the liquid-gas interface of the jet reported by the experimental investigations of Mazallon et al. (1999) and Sallam et

al. (2004). Simulation results reflected the following conclusions: (I) Liquid/gas density ratio was found to have little effect on the jets deformation for values of $\rho_L/\rho_G > 30$, particularly when Oh is small. (II) Crossflow Reynolds number has only a small effect on the deformation for $Re_G > 50$, where the liquid jet drag coefficient is relatively independent of the Reynolds number.

1.3.3.b Summary of Computational Studies The following summarizes the current status of the computational studies related to liquid jets in gaseous crossflow:

- One-dimensional model was used to study the wave growth on the liquid-gas interface and the primary breakup of low-speed and high-speed jet.
- Two-dimensional model of symmetrical flowfield about the jet vertical axis was used to study the penetration lengths and trajectories of the liquid jets in gaseous crossflow.
- Two-dimensional slices of the jet in the direction of the crossflow were used to study the jet deformation but the interactions between the different cross-sections were neglected.
- The liquid/gas density ratio was found to have little effect on the jets deformation for $\rho_L/\rho_G > 30$, particularly when Ohnesorge number is small. For $Re_G > 50$, the crossflow Reynolds number has only a small effect on the jets deformation.
- Three-dimensional time-accurate full configuration model is needed to investigate the effects of the crossflow and the liquid properties on the jet deformation and the waves' properties.
- The ability to compute the breakup of three-dimensional time-accurate liquid jets within a reasonable time is considered to be decades away.

1.3.4 Effects of Supersonic Crossflow Velocities

In scram jet applications, liquid fuel jets are typically injected in supersonic crossflow. A liquid jet in a supersonic crossflow exhibits the same structure as a liquid jet in subsonic crossflow except for the formal posts a bow shock afore the liquid jet structure. Furthermore, the supersonic crossflow velocities can result in a more intense shearing of the liquid jet that yielded a more violent/turbulent breakup when compared to the subsonic crossflow (Schetz and Padhye, 1977).

1.4 Specific Objectives

In view of the current understanding of round nonturbulent liquid jets in gaseous crossflow, the objectives of the present study were to conduct an experimental and computational investigation, as follows:

1.4.1 Experimental Work

- Extend the recent studies of Mazallon et al. (1999) and Sallam et al. (2004) in the bag breakup regime by observing the upwind and downwind surfaces of the liquid jet using high speed photograph rather than shadowgraphy.
- Revisit the column wavelength correlation in the bag breakup regime developed by Mazallon et al. (1999). Observe the waves' convection using high-speed imaging.
- Observes and measure the bag breakup dynamics using high-speed imaging. Complete measurements including: velocity of jet surface, bag counts, liquid droplets sizes after breakup, velocities of liquid droplets after breakup, and

trajectories of liquid droplets using pulsed photography and double-pulsed shadowgraphy.

- Develop phenomenological theories to help interpret and correlate all the new measurements.

1.4.2 Computational Work

- Construct a validated, time-accurate, three-dimensional computational model using Volume of Fluid (VOF) to study the deformation and surface waves properties within the column, bag, and shear breakup regimes that could not be studied in previous two-dimensional models.
- Compute the surface properties of the liquid jet including: jet cross-stream and span-wise deformations, jet cross-sectional area, and column and surface wavelengths.
- Compute internal flowfield, i.e., the liquid phase provided liquid velocities along the trajectory of the liquid jet and the flowfield within the cross-sectional areas of the liquid jet and find the conditions at the onset of the various breakup regimes.
- Compute the external flowfield, i.e., the flow involving the gas phase around the liquid jet, and provide wake velocity defects and wake widths behind the liquid jet.
- Develop phenomenological theories to provide physical insight of the aerodynamic effects of the crossflow.

1.5 Organization of the Dissertation

This dissertation is organized into six chapters and two appendices. The problem statement, previous related studies, and specific objectives of the present study have been presented in the first chapter. The second chapter describes the experimental methods used in the present study. The third chapter details the computational methods used in the present study. The experimental results are presented and discussed in the fourth chapter. The fifth chapter provides computational results for liquid jet in uniform gaseous crossflow. Finally, the summary and main conclusions of the present investigation, including recommendations for future study, are presented in the sixth, and last, chapter. The two appendices deal with experimental uncertainty analysis, and provide tabulations of the experimental data.

Figure 1.1 Photograph of a fountain created using round nonturbulent liquid jets.

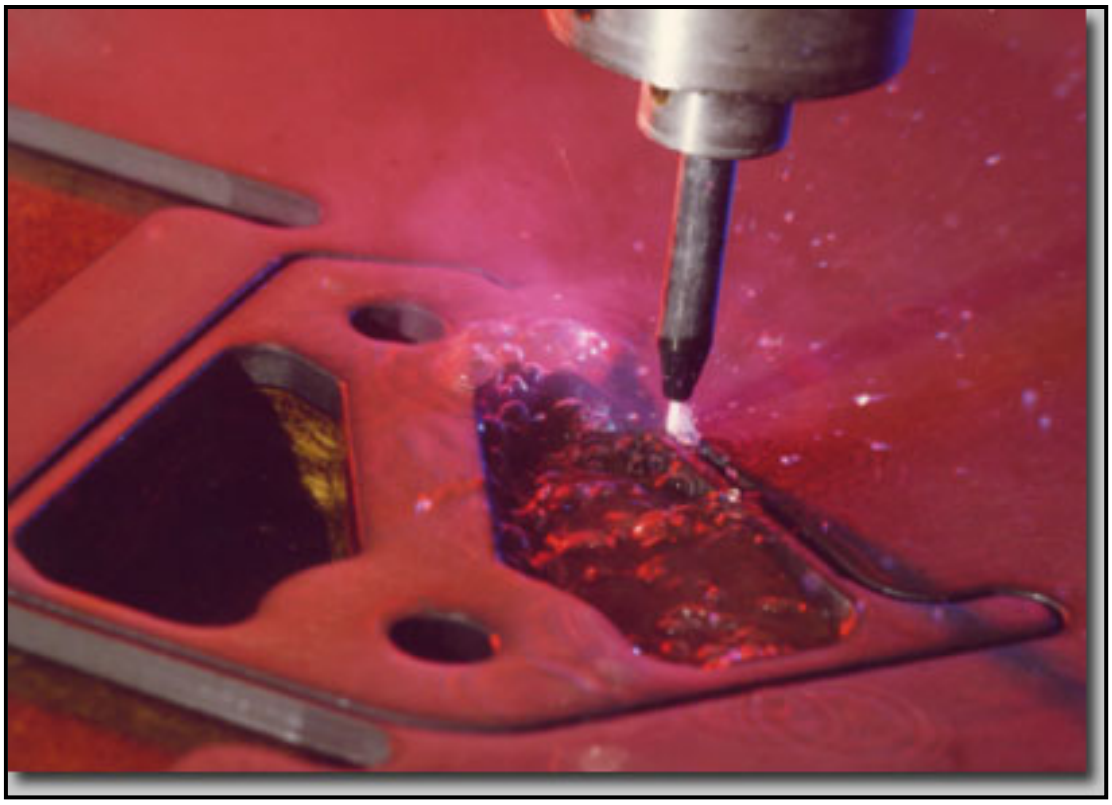

Figure 1.2 Liquid cutting jets (Responsive Engineering, 2005).

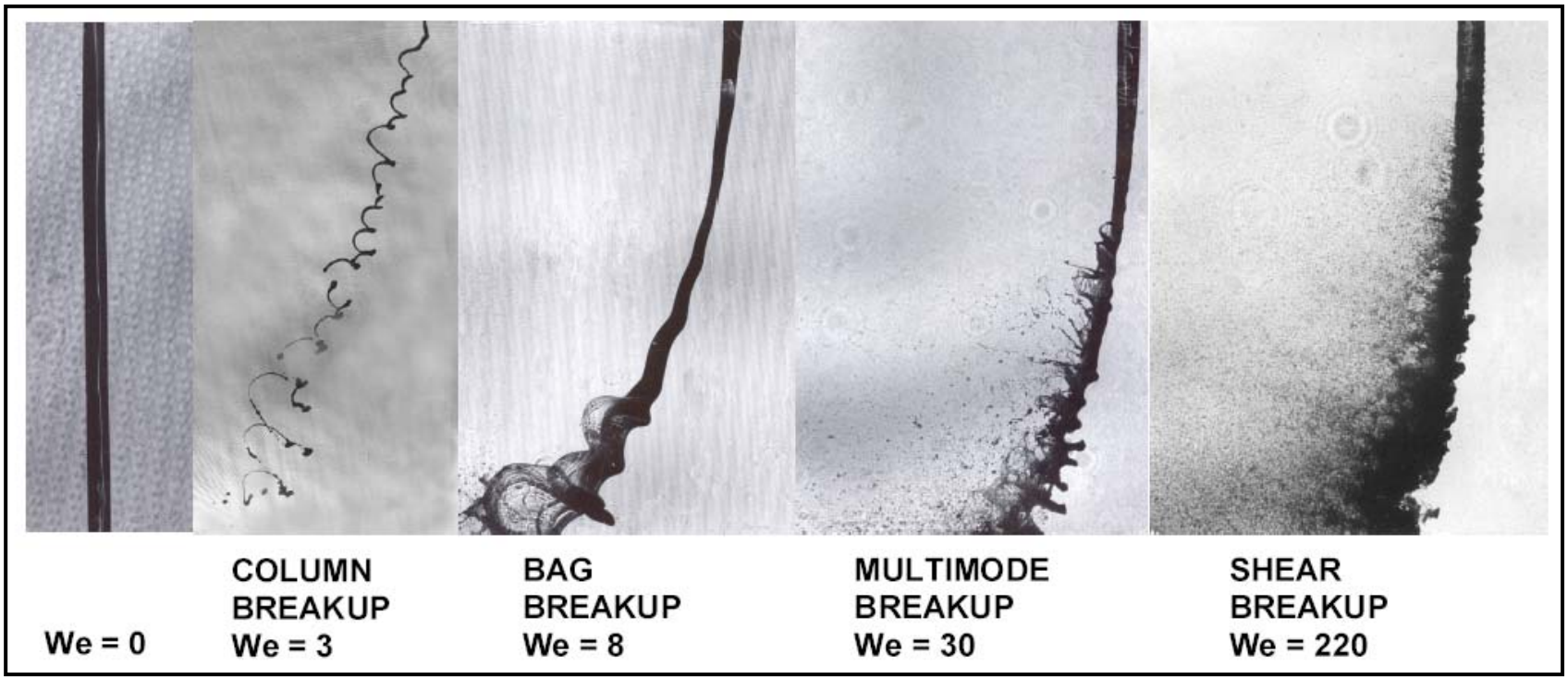

Figure 1.3 Visualization of primary breakup processes of round nonturbulent liquid jets in gaseous crossflow by Sallam et al. (2004): no breakup ($We_G = 0$), column breakup ($We_G = 3$), bag breakup ($We_G = 8$), multimode breakup ($We_G = 30$), and shear breakup ($We_G = 220$).

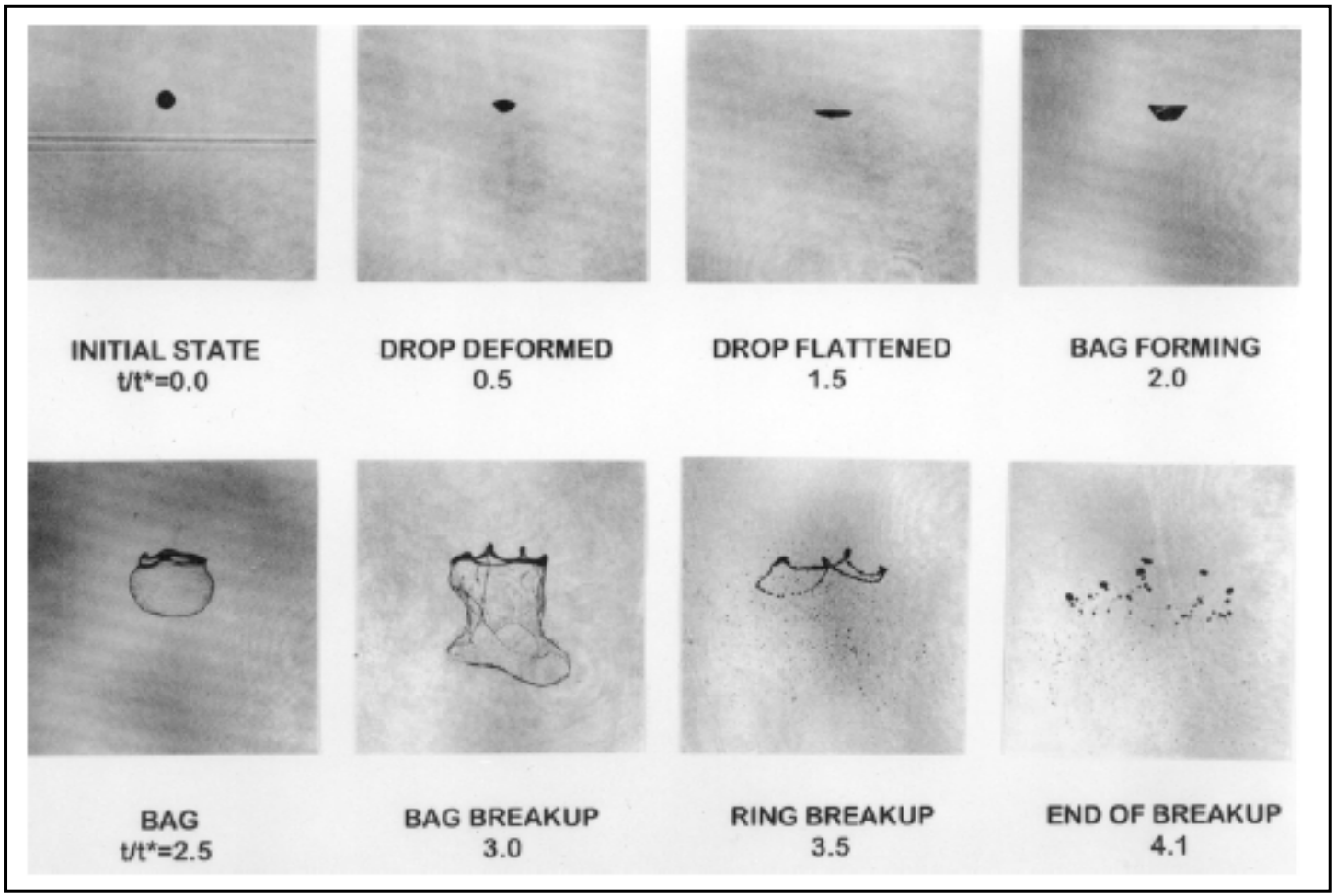

Figure 1.4 Bag breakup of a drop subjected to a shock wave disturbance by Dai and Faeth (2001) (test conditions: $We_G = 15$, $Oh = 0.0045$).

CHAPTER II

EXPERIMENTAL METHODS

2.1 Overview

This chapter describes the experimental setup employed for investigating the wave phenomena and droplets properties/transport dynamics of round nonturbulent liquid jets in uniform gaseous crossflow within the bag breakup regime. The apparatus, instrumentation, and test conditions are described in the following section.

2.2 Apparatus

The schematic of the injection system employed to generate round nonturbulent liquid jets in this study is shown in Fig. 2.1. Pressure injection was used to feed the test liquids stored in a type 304 stainless steel cylindrical storage chamber (diameter = 100 mm and height = 150 mm) through a supercavitating nozzle directed vertically downward into the test section of a subsonic wind tunnel (0.3 m x 0.3 m x 0.6 m) at room temperature and pressure. The supercavitating nozzle had a sharp-edged inlet and internal to exit diameter ratio of more than 20 (see Fig. 2.1) to generate a round nonturbulent liquid jet. Pressurized air was admitted to the top of the chamber through a solenoid valve to force the test liquid out of the supercavitating nozzle. A baffle at the air inlet prevented excessive aeration of the test liquid during injection. The pressurized air was stored on the upstream side of the solenoid valve in an accumulator tank (volume =

0.18 m^3). The injector was flush-mounted with the test section ceiling. Liquid injection times were greater than 33 s which was long compared to the 8-157 ms flow development times. The open circuit wind tunnel (Engineering Lab Design, Model: Aerovent 22-CBD-2616-15) had a contraction ratio greater than 16:1, as shown in Fig. 2.2. The wind tunnel test section has optical quality glass sidewalls and floor, and acrylic ceiling to provide optical access to the test section. The operating range of the air velocities in the test section was from 3 m/s to 60 m/s with a velocity variation of less than ± 1% of the mean free stream velocity. According to the manufacturer calibration data, the turbulence level inside the test section was less than 0.25%.

2.3 Instrumentation

The equipment list is outlined in Table 2.1. Pulsed photography, single- and double-pulsed shadowgraphy, and high-speed imaging were used to observe the wave phenomena, breakup mechanisms, and droplets properties/transport dynamics of round nonturbulent liquid jets in uniform gaseous crossflow under various test conditions. All measurements performed had experimental uncertainties of less than 10% (95% confidence).

2.3.1 Pulsed Photography

The pulsed photography setup employed to measure the column and surface waves, bag counts, node- and ring-droplet sizes after breakup, and the trajectories of the liquid droplets is shown in Fig. 2.3. The light source for pulsed photography (and pulsed shadowgraphy) came from a frequency-doubled Nd:YAG laser (Spectra Physics, Model: LAB-150) that generated a light pulse of 532 nm in wavelength and an optical energy of

up to 300 mJ per pulse. The beam energy of the Nd:YAG laser was controlled by an external half waveplate (Thorlabs, Model: WPMH05M-532). The laser beam was expanded by an objective lens (Newport, Model: M-20X) and redirected by a flat mirror (Newport, Model: 30D10ER.1) to illuminate the liquid jet through the glass floor of the wind tunnel test section. The images were recorded using a CCD camera (Cooke, Model: PCO 2000) that has 2048 x 2048 pixels CCD sensor equipped with a camera lens (Nikon, Model: D-AF Micro-Nikkor 105mm f/2.8). The camera was normal to the plane of symmetry of the wind tunnel for all of the aforementioned investigations except for the downwind surface waves measurements. To measure the downwind surface waves, the camera was tilted 40 degrees in the downwind direction from the normal position to the crossflow. A relay lens (Newport, Model: KPX232AP.14) was positioned between the wind tunnel and the CCD video camera to enlarge the resulting image. For all measurements, the camera was operated with an open shutter under dark room conditions and the exposure times were controlled by the duration of the light pulse (7 ns).

2.3.2 Pulsed Shadowgraphy

The pulsed shadowgraphy setup employed to measure the bag-droplet diameter after the breakup of the bag-membrane is shown in Fig. 2.4. Similar to the optical setup used in the pulsed photography, the beam energy of the Nd:YAG laser was controlled by an external half waveplate. The laser beam passed through an objective lens (Newport, Model: M-5X) and spatial filter and then collimated by a positive lens (Newport, Model: KPX226AR.14) to illuminate the liquid jet through the glass sidewall of the wind tunnel test section. A relay lens (Newport, Model: KPX232AP.14) was used on the opposite side of the glass sidewall to provide image magnification of 3.2X. The resulting image

was constructed at the CCD camera instrumented with a bellow expander (Nikon, Model: PB-6). This allowed the drops sizes as small as 43 μm to be measured within 10% uncertainties (95% confidence). This was adequate to measure the SMD of the bag-droplet, which was 140 um. The Sauter Mean Diameter (SMD) characterizes the atomization quality of sprays and is defined as the ratio of the summation of $d^3_{Droplets}$ to the summation of $d^2_{Droplets}$ of the drops population. It represents the diameter of a droplet having the same volume to surface area ratio as the entire spray. Similar to pulsed photography, the camera was set to operate with an open shutter under dark room conditions and the exposure times were controlled by the duration of the light pulses. The resulting image was analyzed using the SigmaScan Pro 5 software. The measurement was done by filling the image of the droplet (i.e., for a dark droplet on light background, any dark area was filled and the fill automatically stopped at the light areas) and compared the major and minor axes lengths of the filled image to create the theoretical diameter of the droplet with the same cross-sectional area.

2.3.3 Double-pulsed Shadowgraphy

Double-pulsed shadowgraphy was used to measure the surface velocity of the liquid jet and the velocities of the droplets after the breakup. Two laser pulses were used to record two images on the CCD camera operating in the double-exposure mode, as shown in Fig. 2.4. The time delay between the two pulses was controlled by a delay generator (Quantum Composers, Model: 9518, with a resolution of 100 ns) and was varied in the range of 40-120 μs based on the test conditions. By measuring the distance traveled by the liquid surface or liquid droplets between the two shots, the velocities were computed.

2.3.4 High-Speed Imaging

High-speed imaging was used to visualize the waves' convection, bag and nodes dynamics, and droplets transport dynamics after the breakup. To observe the node dynamics, the camera was tilted 13 degrees in the upwind direction from the normal position to the crossflow. Two Sylvania 500 watt double-ended halogen bulbs (Model: 58865) provided continuous light sources required for the high-speed imaging. The two halogen lights were positioned at different locations (i.e., the acrylic ceiling, the sidewall, and/or the glass floor of the wind tunnel test section) to illuminate the liquid jet for high-speed imaging under various test conditions. A high-speed camera (IDT, Model: X-Stream VISION XS-4) with a 512 x 512 CMOS sensor was used to record the images at 5145 frames per second at full resolution. The movies were slowed down using Avifrate (Version 1.10) software to observe various bag breakup phenomena.

2.4 Test Conditions

The liquid properties and test conditions employed in the present investigation are summarized in Table 2.2. Tap water (referred herein as water), distilled water, and ethyl alcohol were used as test liquids in the present investigation. The test liquid was discarded after each run to maintain liquid properties integrity. For water jet, 0.5, 1.0, and 2.0 mm nozzle exit diameters were employed to study a crossflow Weber number variation from 4 to 30 and a liquid jet momentum ratio variation from 9 to 1199. For ethyl alcohol jet, 0.5 mm and 1.0 mm nozzle exit diameters were used to study a liquid jet Weber number variation from 8 to 28 and a liquid jet momentum ratio variation from 52

to 902. For all cases, the Ohnesorge number was small (< 0.1), implying that the viscous effects were negligible.

The daily averaged temperature and pressure (NOAA Satellite and Information Service, July-September 2005) were used to investigate the variations of the density and viscosity of the test liquids based on the measurements of the Handbook of Thermodynamics Tables and Charts (Kuzman, 1976), as shown in Table B.14 and Table B.15, respectively. The properties variations were computed based on the analysis of Crow et al. (1955). The variations of the density and viscosity with respect to the temperature and pressure were less than 1%. A tensiometer (Fisher, Model: 20) is used to measure the surface tension of the tap water (Stillwater and Tulsa) and distilled water (Wal-mart), as shown in Table B.16. The variation of the averaged surface tension between the tap water (Stillwater) and the distilled water (Wal-mart) was less than 0.2%. As such, it can be concluded that the variation of the fluid properties will have little effect on the experimental uncertainties dominated by sampling limitations.

Table 2.1 Equipment list.

Component	Manufacturer	Model	Description
CCD Camera	PCO. Imaging The Cooke Corp.	PCO. 2000	2048 x 2048 pixels CCD sensor
Focusing Lens	Nikon	D-AF Micro-Nikkor	105 mm f/2.8
High-speed Camera	IDT	X-Stream VISION XS-4	512 x 512 pixels CMOS sensor
Camera Bellow Expander	Nikon	PB-6	50 mm diameter
Nd:YAG laser	Spectra Physics	Quanta-Ray LAB-150	532 nm wavelength
Halogen Lamp	Regent Lighting Corp.	PQS45	4.2 amps, 60 Hz. Type T-3 bulb (max. 500 watts)
Optical Table	Newport Corp.	LabLegs RL-2000	
Flat Mirror	Unaxis	BD 103 079 05 VIS	1" dia.
Flat Mirror, Pyrex	Newport Corp.	30D10ER.1	76.2 mm dia., 1/5 wave. R>93% avg. 450-700 nm
POL Cube Beamsplitter	Newport Corp.	10BC16PC.3	532 nm, Tp/Ts>1000:1, 25.4 mm
IRIS Diaphragm	Newport Corp.	ID-1.0	1"
Objective Lens	Newport Corp.	M-5X, 0.10	Microscope, 5x
Objective Lens	Newport Corp.	M-20X, 0.40	Microscpoe, 20x
Object Beam Collimating Lens	Newport Corp.	KPX226AR.14	76.2 mm dia. x 150 fl. (focal length) 380 - 2100 nm uncoated
Relay Lens	Newport Corp.	KPX232AP.14	76.2 mm dia. x 300 fl. (focal length) BBAR coat 430 - 700 nm
Half Waveplate	ThorLabs, Inc.	WPMH05M-532	AR Coated $\lambda/2$ = 532 nm
Pulse Generator	Quantum Composers	9518	
12" Open Circuit Wind Tunnel	Engineering Lab. Design, Inc.	Aerovent 22-CBD-2616-15	15 horsepower, 60 Hz. 16:1 Contraction
Compressor	RIX		2.2SCFM
Accumulator Tank	Niles Steel Tank Co.		MAWP: 1500 psi @ 250 deg. F MAMT: 1500 psi @ -20 deg. F
Pressure Scale	Heise		300 psig/0.5 subdivisions
Computer	Dell	Dimension 8400	P4 HT 3.6 Ghz.
Imaging Processing Software	SigmaScan PRO	Version 5	
Surface Tensiometer	Fisher	20	Du Nuoy's ring method, specified by ASTM methods D-971 and D-1331

Table 2.2 Liquid properties and test conditions[*].

Liquid	Water	Ethyl Alcohol
Density, kg/m^3	997	809
Liquid/gas density ratio, ρ_L/ρ_G	821	665
Liquid viscosity, kg/m.s x 10^{-4}	8.94	12.3
Liquid/gas viscosity ratio, μ_L/μ_G	48	66
Surface tension, N/m x 10^{-3}	70.8	27
Nozzle exit diameter, mm	0.5, 1.0, and 2.0	0.5 and 1.0
Crossflow Weber number, We_G	4 – 30	8 – 28
Crossflow Reynolds number, Re_G	709 – 3818	876 – 1638
Liquid jet momentum ratio, q	9 – 1199	52 – 902
Liquid jet Ohnesorge number, Oh x 10^{-3}	< 4.8	< 11.8

[*] Air Crossflow at room temperature and pressure.

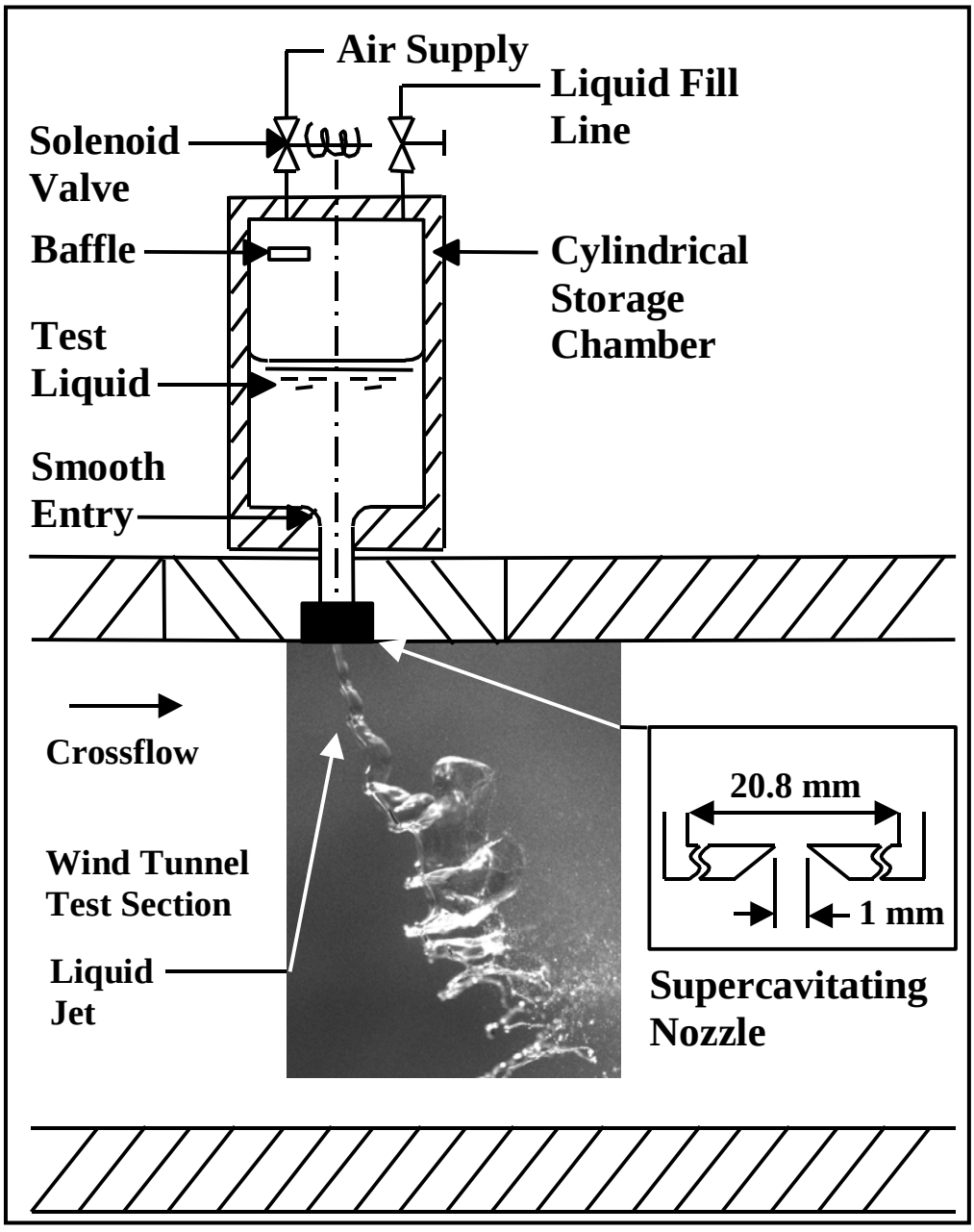

Figure 2.1 Pressure-fed supercavitating nozzle system.

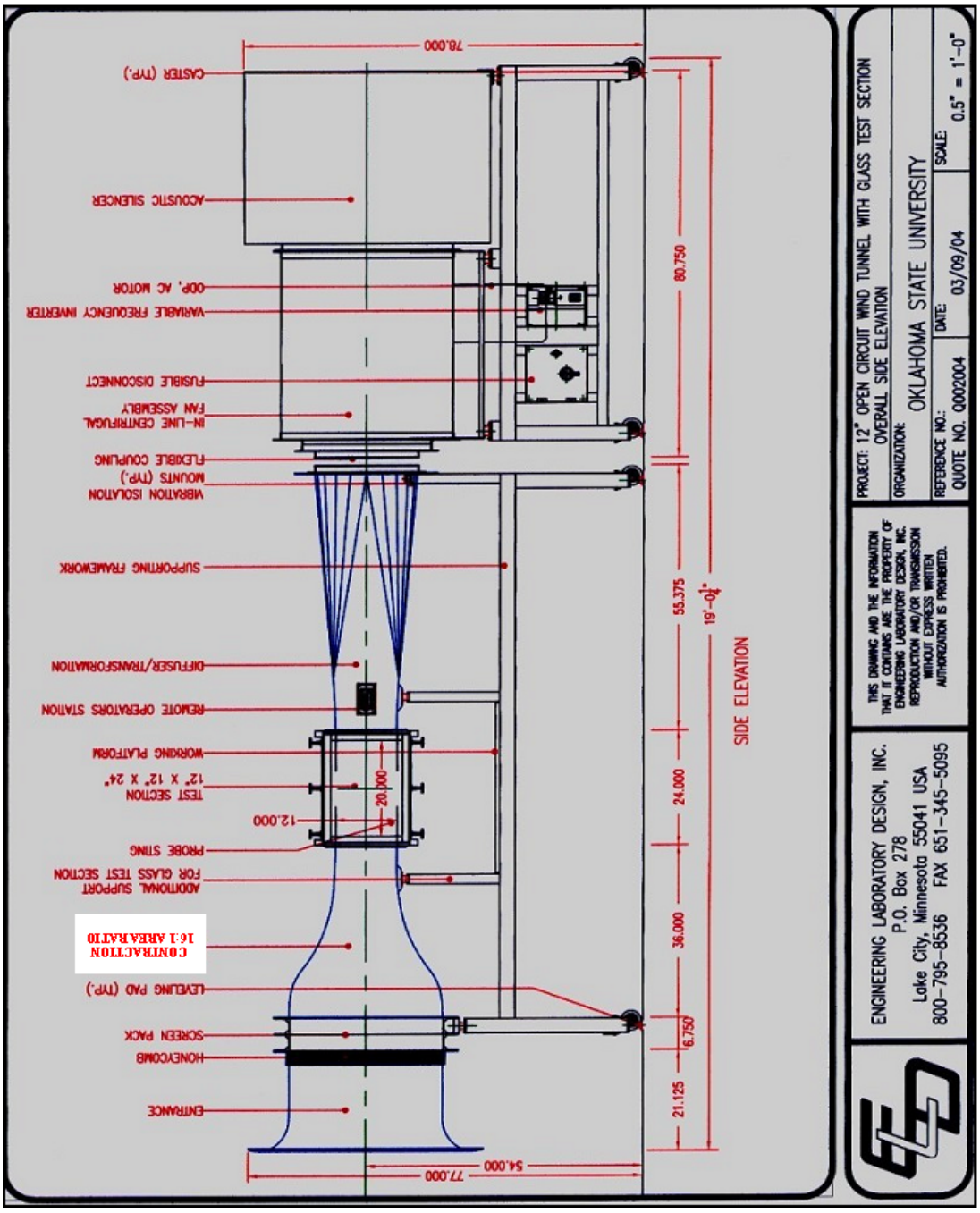

Figure 2.2 12'' open circuit wind tunnel.

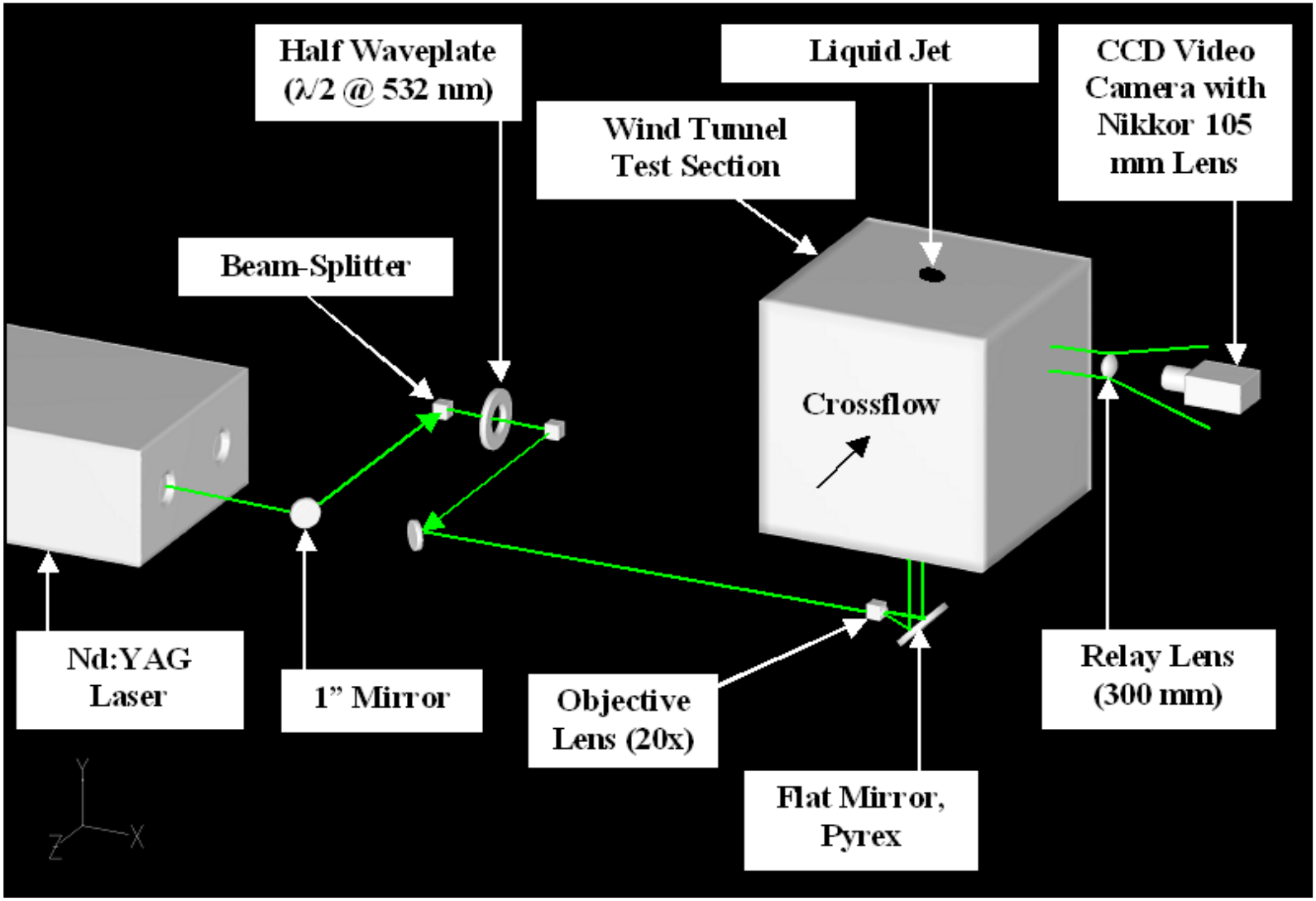

Figure 2.3 Pulsed photography test setup.

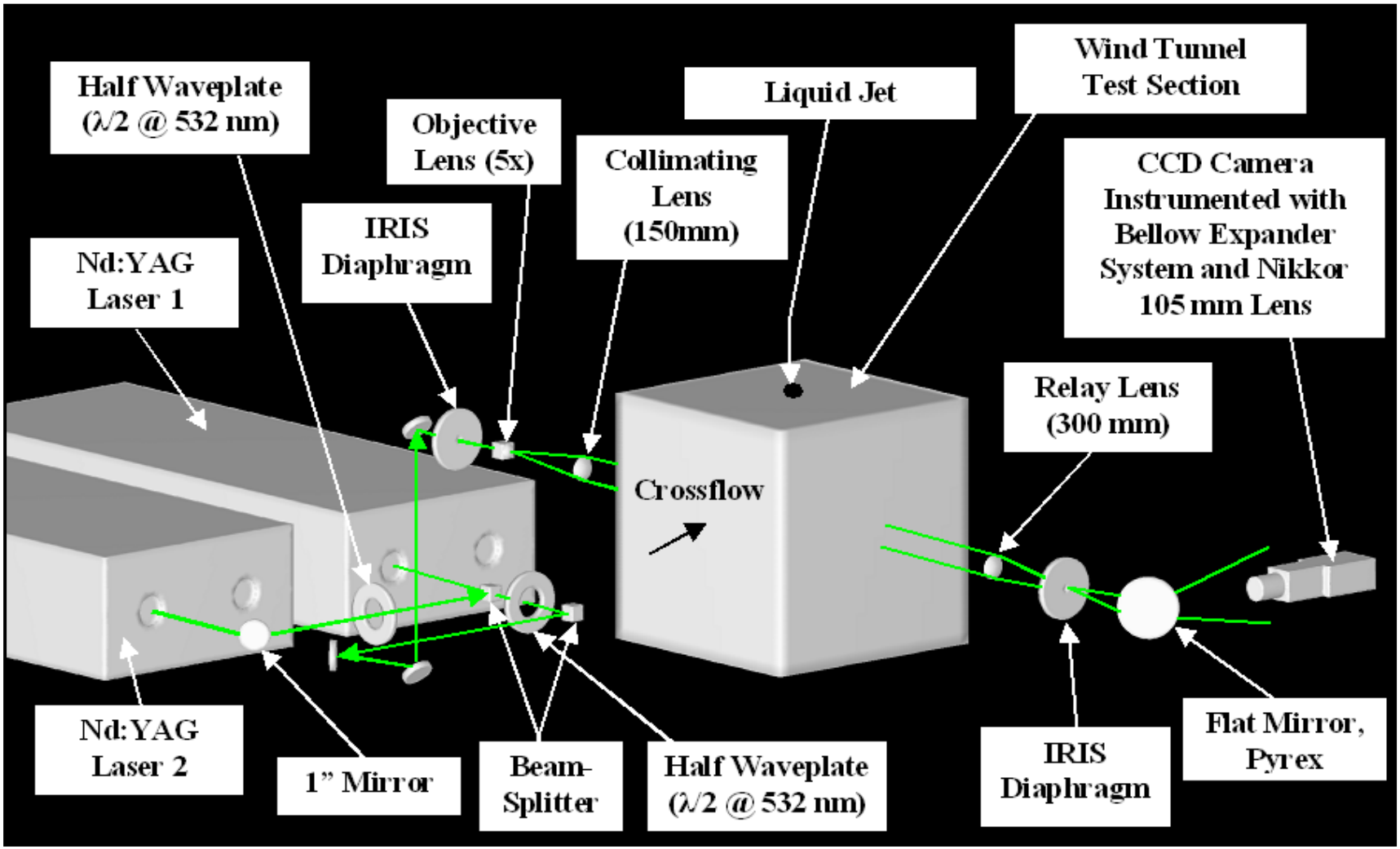

Figure 2.4 Double-pulsed shadowgraphy test setup.

CHAPTER III

COMPUTATIONAL METHODS

3.1 Overview

This chapter describes the methodology employed for conducting time-accurate multiphase modeling of round nonturbulent liquid jets in uniform gaseous crossflow. Numerical model attempts to analyze the primary breakup of liquid jets in gaseous crossflow must be three-dimensional in space based on the complex interaction between the gaseous crossflow and the liquid surface as shown by experimental measurements of Mazallon et al. (1999) and Sallam et al. (2004). In this chapter, the concept and algorithm employed to conduct parallel processed, time-accurate, three-dimensional multiphase flow modeling using Volume of Fluid (VOF) formulation are discussed. The effect of the presence of surface tension at the liquid-gas interface is evaluated on a two-dimensional cylindrical element. In order to verify the numerical predictions, the diameter of a liquid jet in still air, cross-stream deformation of a liquid jet in uniform crossflow, jet velocities, and column and surface wavelengths were compared with existing experimental measurements from the literature.

3.2 Governing Equations

An Euler-Euler approach with a Volume of Fluid (VOF) formulation was used in FLUENT to predict the evolution of the liquid-gas interface of time-accurate three-

dimensional liquid jets in uniform gaseous crossflow in space and time. In the Euler-Euler approach, different phases are treated mathematically as interpenetrating continua, and the concept of phasic volume is applied by assuming the volume fractions are continuous functions of space and time that summed to one. The VOF algorithm models two or more immiscible fluids by tracking the volume fraction of each fluid in each cell throughout the computational domain. The face fluxes of each cell were calculated using an Euler explicit surface tracking scheme which was followed by a geometric reconstruction (piecewise-linear) interpolation treatment to the cells that lie near the predicted liquid-gas interface in order to capture surface waves. The solution-adaptive mesh refinement feature of FLUENT was employed to refine the grid based on the numerical evolution of the liquid volume fraction surrounding the liquid-gas interface in order to minimize grid dependency of the final solution.

3.2.1 Volume of Fluid (VOF) Model

The VOF formulation models two or more immiscible fluids by solving a single set of momentum equations and tracking the volume fraction of each fluids in each cell throughout the computational domain. The number of variables introduced corresponds to the number of phases in the model. The fields for all variables and properties in each cell are shared by the phases and represents volume-averaged values. The properties and variables are assigned to each control volume within the domain based on the local fluid's volume fraction (i.e., α_q - the q^{th} fluid's volume fraction) in the cell. There are three possible conditions, as outlined below:

- $\alpha_q = 1$: The cell is filled with q^{th} fluid.
- $\alpha_q = 0$: The cell is empty.

- $0 < \alpha_q < 1$: The cell encompasses the interface of q^{th} fluid and other fluids.

  The VOF model is appropriate for stratified or free surface flows.

3.2.1.a The Volume Fraction Equation The solution to the continuity equation for the volume fraction of one (or more) phases is used to track the interface between the phases. For q^{th} phase:

$$\frac{1}{\rho_q}\left[\frac{\partial}{\partial t}(\alpha_q \rho_q) + \nabla \cdot (\alpha_q \rho_q \vec{v}_q) = S_{\alpha_q} + \sum_{p=1}^{n} (\dot{m}_{pq} - \dot{m}_{qp})\right] \tag{3.1}$$

By default, the source term, S_{α_q}, is zero. The $\dot{m}_{pq}$ and $\dot{m}_{qp}$ represent the mass transfers from phase p to phase q and from phase q to phase p, respectively. For time-dependent computations, Eqn. 3.1 is solved using an explicit time-marching scheme. The time step for the integration of the volume fraction equation is automatically refined by FLUENT. Should desired, modification to the time step calculation can be accomplished by changing the Courant number in the VOF parameters. The Courant number relates to the time for a fluid particle to move a fraction of the grid spacing in a single time step. During this research, a Courant number of 0.25 was used to maintain solution stability. The volume fraction can be updated every time step or every iteration at the expenses of the computational time (Fluent User Services Center, 2004).

3.2.1.b Properties The component phases in each control volume determine the properties in the transport equations. For example, the density of a two-phase system in each cell is given by:

$$\rho = \alpha_2 \rho_2 + (1 - \alpha_2)\rho_1 \tag{3.2}$$

The subscripts 1 and 2 denote the volume fraction of primary and secondary phase, respectively. The volume fraction equation for the primary phase is computed based on the constraint:

$$\sum_{q=1}^{n} \alpha_q = 1 \tag{3.3}$$

(Fluent User Services Center, 2004).

3.2.1.c The Momentum Equation A single momentum equation (Eqn. 3.4) that depends on the volume fraction of all phases through density and viscosity is solved throughout the computational domain. The resulting velocity field is shared among the phases.

$$\frac{\partial}{\partial t}(\rho \vec{v}) + \nabla \cdot (\rho \vec{v}\vec{v}) = -\nabla p + \nabla \cdot [\mu \nabla \vec{v} + \nabla \vec{v}^{T})] + \rho \vec{g} + \vec{F} \tag{3.4}$$

(Fluent User Services Center, 2004).

3.2.1.d Surface Tension FLUENT models surface tension using the continuum surface force (CFS) model proposed by Brackbill et al. (1992). The surface tension coefficient can be specified as a constant, as a function of temperature, or through a user-defined function (UDF). In this research, the surface tension is specified as a constant because variable surface tension coefficients effects are usually important only in zero or near-zero gravity conditions.

To model surface tension in the VOF calculation, a source term is being added to the momentum equation (Eqn. 3.4). When a constant surface tension is applied, the

forces normal to the interface is the only forces needs to be considered. The pressure drop across the surface depends on the surface tension coefficient.

$$p_2 - p_1 = \sigma(\frac{1}{R_1} + \frac{1}{R_2}) \tag{3.5}$$

p_1 and p_2 represent the pressure in the two fluids on either side of the interface. R_1 and R_2 denote the surface curvature as measured by two radii in the orthogonal direction. For CFS, these curvatures were computed from the local gradients in the surface normal (n) to the interface.

$$n = \nabla \alpha_q \tag{3.6}$$

Based on Brackbill (1992), the curvature (κ) is defined in terms of the divergence of the unit normal ($\hat{n}$).

$$\kappa = \nabla \cdot \hat{n} = \nabla \cdot \frac{n}{|n|} \tag{3.7}$$

Applying the divergence theorem, the surface force can be expressed as a volume force (F_{vol}) that is added as a source term to the momentum equation.

$$F_{vol} = \sum_{\text{pairs ij, i<j}} \sigma_{ij} \frac{\alpha_i \rho_i \kappa_j \nabla \alpha_j + \alpha_j \rho_j \kappa_i \nabla \alpha_i}{\frac{1}{2}(\rho_i + \rho_j)} \tag{3.8}$$

If only two phases are present, which is the case of the present investigation, $\kappa_i = -\kappa_j$ and $\nabla \alpha_i = -\nabla \alpha_j$, and the equation reduces to

$$F_{vol} = \sigma_{ij} \frac{\rho \kappa_i \nabla \alpha_i}{\frac{1}{2}(\rho_i + \rho_j)} \tag{3.9}$$

where ρ is computed from Eqn. 3.2. Quadrilateral face cells and hexagonal volume cells should be used to compute the surface tension effects for best accuracy. Surface tension should be applied based on two dimensionless parameters, Re_L and We_G. When $Re_L << 1$, the capillary number ($Ca = \mu_L U_G/\sigma$) is of interest. When $Re_L >> 1$, the Weber number (We_G) is important. Surface tension can only be neglected when $Ca >> 1$ or $We_G >> 1$. As such, surface tension effects must be considered in this research.

3.2.1.e Interpolation Near the Interface FLUENT requires the convection and diffusion fluxes through the control volume faces to be computed and balanced with the source terms within the control volume. As mentioned earlier, quadrilateral face cells and hexagonal volume cells should be used to mesh the computational domain in order to maintain a good computational accuracy for surface tension calculations discussed in section 3.2.1.d. Furthermore, the mesh density must be concentrated near the liquid jet and additional mesh nodes must be placed near the liquid jet trajectory to provide greater solution resolution in the regions of high flow gradients and liquid-gas interface. Although the donor-acceptor scheme, as shown in Fig. 3.1(b), identifies one cell as the donor of an amount of fluid from one phase and another neighboring cell as the acceptor of that same amount of fluid that can prevent numerical diffusion at the interface (Hirt and Nichols, 1981), it cannot be used for hybrid mesh containing twisted hexagonal cells. A test run employing the donor-acceptor scheme corroborated with the speculations, as it did not yield results that can be compared favorably with the experimental data for

wavelengths and liquid cross-stream deformations. The implicit scheme is suitable mainly for steady-state simulation and for situation where the intermediate transient flow behavior is not important. Therefore, the Euler explicit scheme which was followed by a geometric reconstruction (piecewise-linear) interpolation treatment to the cells that lie near the predicted liquid-gas interface were used in the present study. In this approach, the solution to the continuity equation for the volume fraction of one (or more) phases were used to track the liquid-gas interface. Then, the convection and diffusion fluxes through the control volume faces were computed and balanced with the source terms within the control volume using an Euler explicit scheme. Finally, the geometric reconstruction (piecewise-linear) scheme applied a special interpolation treatment to refine the predicted liquid-gas interface to capture the downwind surface waves.

The Euler explicit scheme computes the face fluxes by applying a standard finite-difference interpolation schemes to the volume fraction that were computed in the previous time step.

$$\frac{\alpha_q^{n+1}\rho_q^{n+1} - \alpha_q^n\rho_q^n}{\Delta t} V + \sum_f (\rho_q^n U_f^n \alpha_{q,f}^n) = [\sum_{p=1}^{n} (\dot{m}_{pq} - \dot{m}_{qp}) + S_{\alpha_q}]V \qquad (3.10)$$

where n and n+1 are the index of the previous and current time step, V is the volume of the cell, $\alpha_{q,f}$ represents the face value of the qth volume fraction computed from the discretization (i.e., first- or second- order, and QUICK) scheme, and U_f denotes the volume flux through the face based on the normal velocity. During each time step, the Euler explicit scheme does not require an iterative solution of the transport equation because it does not require the volume fraction values at the current time step (i.e,

$\sum_f (\rho_q^n U_f^n \alpha_{q,f}^n)$). For Euler explicit scheme, a time-dependent solution must be computed (Fluent User Services Center, 2004).

The geometric reconstruction scheme applies the standard interpolation schemes to obtain the face fluxes when a cell is filled with one phase or another. Near the interface, a piecewise-linear approach is employed to represent the interface by assuming that the interface between two fluids has a linear slope within each cell, and the linear shape is employed to compute the advection of fluid through the cell faces, as shown in Fig. 3.1(c). This scheme is generalized for unstructured meshes in the work of Youngs (1982) and represents the most accurate scheme in FLUENT. For geometric reconstruction scheme, a time-dependent solution must be computed (Fluent User Services Center, 2004).

3.3 Numerical Scheme

3.3.1 Solver

The Volume of Fluid (VOF) model in FLUENT was computed using the segregated implicit solver employing the first-order implicit time-stepping. A segregated solver solves the continuity, momentum, energy, species, and additional scalar equations (i.e., turbulence equations) sequentially. The manner in which the governing equations are linearized to facilitate their solution may take an "implicit" or "explicit" form with respect to the dependent variable (or set of variables) of interest. In short, the segregated implicit approach solves for a single variable field (i.e., pressure) by considering all cells simultaneously, before computing other dependent variables (i.e., velocity, etc.) in the same manner. The segregated implicit solver uses under-relaxation to control the update

of computed variables at each iteration. Under-relaxation factors employed in this investigation are provided in Table 3.1.

3.3.2 Discretization

The flows surrounding the liquid-gas interface involved a curved domain. As such, the PRESTO! discretization for pressure interpolation in FLUENT software applicable for solving flows within strongly curved domains was employed in this study. The Pressure Implicit with Splitting of Operator (PISO) discretization for pressure-velocity coupling employing neighbor and skewness correction was used in this study due to its ability to handle transient calculations. The second-order upwind discretization for the volume fraction equations was applied to minimize diffusivity. For the discretization of momentum, second-order upwind method is used mainly because the accuracy of the converged solution is rated over the computational expenses.

3.4 Computational Grid

3.4.1 Mesh Generation

Grids were based on a vertex-defined geometry, representing a velocity inlet for crossflowing air, a velocity inlet for the liquid jet, a no-slip wall at the top, and two pressure outlets at the bottom and rear surfaces. Vertex location information of the three-dimensional liquid-gas interface was first computed based on the experimental data (Sallam et al. 2004) of the trajectories of liquid jets in gaseous crossflow. The drawback of the aforementioned computational grid was that the Eulerian mesh was not dynamically modified in time. To overcome this shortcoming, the experimental predicted jet trajectory was replaced by a vertical jet trajectory. The solution-adaptive

mesh refinement feature in FLUENT was then used to modify the grid based on the location of the gas-liquid interface. To resolve the waves along the liquid jet, the computational grid were constructed such that 10 grid points were employed per wavelength. The wavelengths of column and surface waves were obtained from the experimental data of Mazallon et al. (1999) and Sallam et al. (2004).

GAMBIT was employed to generate hexagonal computational mesh. A trapezoidal-shaped computational domain, as shown in Fig. 3.2, allowed the saving of the computational time. Three-dimensional half configuration employing experimental predicted trajectory was first attempted but soon was replaced by a full configuration in order to resolve the unsymmetrical jet wake. The geometries of the computational domains that are associated with the dimensions shown in Figs. 3.2 and 3.3 are listed in Table 3.2. To maintain stability of the simulation in FLUENT, the jet was first simulated in still air. Then, the crossflow was introduced and gradually increased in each successive simulation, until the desired crossflow Weber number was reached. The solution-adaptive mesh refinement feature of FLUENT was employed to refine the grid based on the numerical evolution of the liquid volume fraction surrounding the liquid-gas interface in order to minimize grid dependency of the final solution.

The method employed to dynamically modify the Eulerian mesh in time involved five steps, as given below:

1. Create a data file from the converged solution (i.e., $We_G = 2$) for all cell zones and all fields (i.e., pressure, volume fraction, etc.).
2. Interpolate the data file into the original mesh with vertical jet trajectory. (i.e., $We_G = 0$).

3. Increase the crossflow velocity (i.e., $We_G = 3$). Run the simulation, for instance, 1000 time-step; allowing the solutions to acclimatize to the original mesh and new crossflow velocity.
4. Perform solution-adaptive mesh refinement on the computational grid based on the numerical evolution of the liquid volume fraction surrounding the liquid-gas interface.
5. Iterate until a converged solution is achieved based on the convergence criteria.

The configurations discussed herein are constructed with a hexagonal mesh having the following specifications:

- Quadrilateral map or submap meshing on all faces (Quadrilateral three-dimensional cells).
- Boundary-layer uniform-grids attached to the liquid jet inlet and outlet to promote cell orientation normal to the liquid jet trajectory.
- Mesh density concentrated near the liquid jet. Additional mesh nodes are placed near the liquid jet trajectory to provide greater solution resolution in the regions of high flow gradients and liquid-gas interface.

Note that the mesh shown in Fig. 3.3 represents the original mesh distribution. Each hexagonal cell around and within the liquid-gas interface was subdivided into eight hexagonal cells after the solution-adaptive mesh refinement. For full configuration within the column and bag breakup regimes, the original mesh had 393,750 cells that were refined to 883,326 cells. The mesh for full configuration within the shear breakup regime was made up of 695,058 cells.

3.4.2 Parallel Processing Setup

All computations can be carried out using either serial or parallel processing, but, parallel processing is recommended for the full configuration model. The ability to compute the breakup of three-dimensional transient liquid jets within a reasonable time is considered to be decades away, as documented by recent researchers (i.e., Aalburg, 2002). Adding the third dimension and two orders of magnitude resolution will increase the number of cells factor by 10^8 and the number of time steps by 10^4. In this study, these requirements can be overcome by running different cases concurrently on a 3-processor parallel Linux cluster (3 P4 2.5Ghz with 1GB DDR SDRAM) and five P4 desktops (Dell Dimension P4 HT 3.6Ghz with 4GB DDR2 SDRAM). The present parallel processing setup is outlined in Appendix C.

3.5 Boundary and Operating Conditions

Simulations of liquid jets in uniform crossflow were conducted at various crossflow Weber numbers for initial jet diameters of 0.5 and 2 mm. The liquid and gas properties and the test conditions considered during the present numerical investigation are summarized in Table 3.3.

3.5.1 Boundary Conditions

Boundary conditions specified for the present investigation are as follows:

- Velocity inlet boundary condition was used for the liquid jet inlet and the gaseous crossflow inlet. The specification of the gaseous crossflow velocity determines the crossflow Weber number, which in turn define entirely the breakup regime

mode (column, bag, and shear) for liquid jets with small Ohnesorge numbers (Oh < 0.1) (Aalburg et al., 2005).

- Pressure outlet boundary condition was used for the gaseous crossflow outlet and the liquid-gas (mixture) outlet to set the boundary conditions to atmospheric pressure conditions corresponding to the conditions of the experimental measurements used for validation.
- No-slip wall boundary condition was used for the top wall. The liquid jet exit was flush-mounted with a no-slip wall on both the measurements employed for validation and most of practical applications of liquid jets in crossflow.
- Interior boundary conditions were used for the trajectory of the liquid jet at no crossflow.

3.5.2 Operating Conditions

The flow in the computational domain was modeled as incompressible. The operating pressure condition in FLUENT was set to 101325 Pa, allowing all pressure calculations to be treated as gauge pressures. Inlet air is modeled in the simulations at various velocity magnitudes (depending on the crossflow Weber number) employing the magnitude and direction velocity specification method, allowing the flow direction to be specified accurately by using a trapezoidal-shaped computational domain. Inlet liquid is modeled in the simulations at various velocity magnitudes (depending on the breakup regime) employing the same method. The exit mixtures (air and ethyl alcohol) are exhausted at the atmospheric static (gauge) pressure, where all pressure boundary conditions are relative to the specified operating pressure. The effect of gravity on the liquid jet velocity is small (< 0.07%) and can be neglected.

3.6 Solution Convergence

The convergence criteria are based on continuity and x-, y- and z-velocity residuals. A popular approach for judging the convergence is to require the unscaled residuals to drop by three orders of magnitude in each time step. However, this particular approach is not appropriate in the following cases: (1) If a good initial guess is provided, (2) if the governing equation contains non-linear source terms, and (3) if the variable of interest is nearly zero everywhere. In the present study, integrated quantities were monitored in addition to examining residual levels in order to determine convergence. At the beginning of the simulation when the jet was placed in still air, the jet diameter was monitored at a fixed streamwise distance from the nozzle exit and the solution was judged to be convergent when the jet diameter agrees with the experimental data of jet diameter. Additionally the effect of the presence of surface tension at the liquid-gas interface was evaluated on a two-dimensional cylindrical element, as shown in Fig. 3.4(a). The pressure enclosed within a two-dimensional liquid column is balanced by the surface tension:

$$2\sigma / D = p \tag{3.11}$$

where D represents the diameter of a two-dimensional liquid column and p is the pressure. The pressure distribution of a two-dimensional cylindrical element of an ethyl alcohol jet of 0.5 mm diameter calculated with FLUENT is shown in Fig. 3.4(b). The computed average pressure difference across the interface was 94 Pa, which is within 5% of the theoretical value of 89 Pa and thus in reasonable agreement. The sharp rise of the

pressure across the liquid-gas interface suggests that numerical diffusion attributable to the multiphase modeling in FLUENT is reasonably small.

When the liquid jet was simulated then in uniform gaseous crossflow, in addition to the unscaled residuals, the liquid phase properties including jet cross-stream deformation, jet velocity, and column and surface wavelengths were monitored and compared with experimental measurements in order to judge convergence.

Table 3.1 Under-relaxation factors employed in the numerical investigation.

Under-Relaxation	
Parameters	Factors
Pressure	0.3
Density	1.0
Body Forces	1.0
Momentum	0.3
Volume Fraction	0.2

Table 3.2 The dimensions of the liquid jets in crossflow geometries employed for bag and shear breakup simulations.

Geometry Description	dj (mm)	a	b	c	d	e	f	g
Bag breakup	0.5	5dj	10dj	5dj	10dj	20dj	21.9dj	2dj
Shear breakup	2	5dj	4dj	5dj	10dj	20dj	21.9dj	dj

Table 3.3 The liquid and gas properties of the conditions considered during the present numerical investigation.

Liquid	Ethyl Alcohol
Density, kg/m^3	790
Liquid/gas density ratio, ρ_L/ρ_G	645
Liquid viscosity, kg/m.s x 10^{-4}	12
Liquid/gas viscosity ratio, μ_L/μ_G	67
Surface tension, N/m x 10^{-3}	22.3
Nozzle exit diameter, mm	0.5 and 2.0
Crossflow Weber number, We_G	3.5, 8, and 220
Crossflow Reynolds number, Re_G	388 – 6148
Liquid jet momentum ratio, q	120, 130, and 274
Liquid jet Ohnesorge number, Oh x 10^{-3}	< 12.8

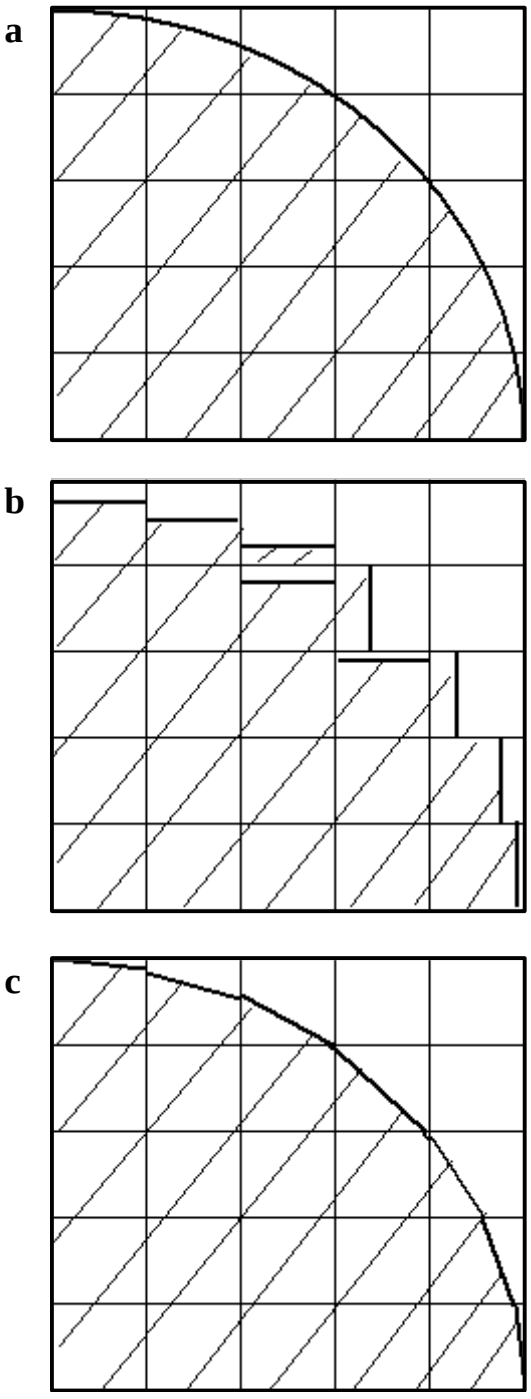

Figure 3.1 Interface scheme. (a) Actual Interface. (b) Interface Represented by Donor-Acceptor Scheme. (c) Interface Represented by Geometric Reconstruction (piecewise-linear) Scheme.

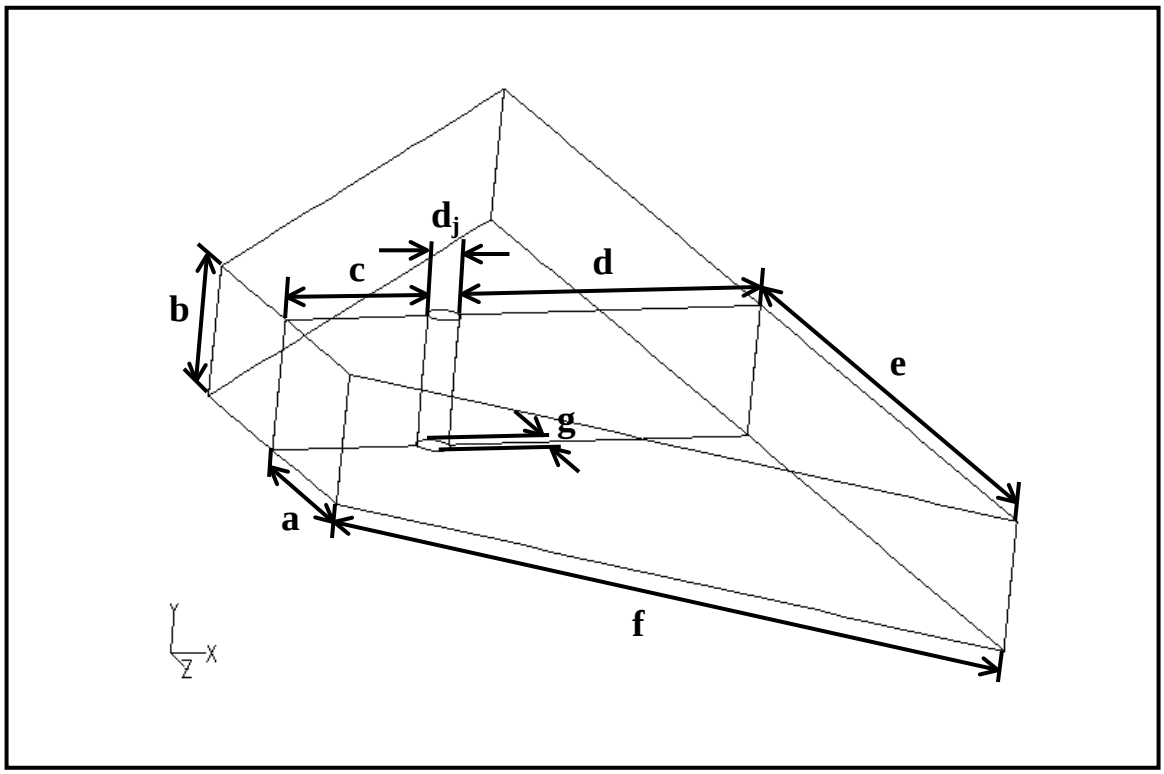

Figure 3.2 Geometry of the full configuration computational domain.

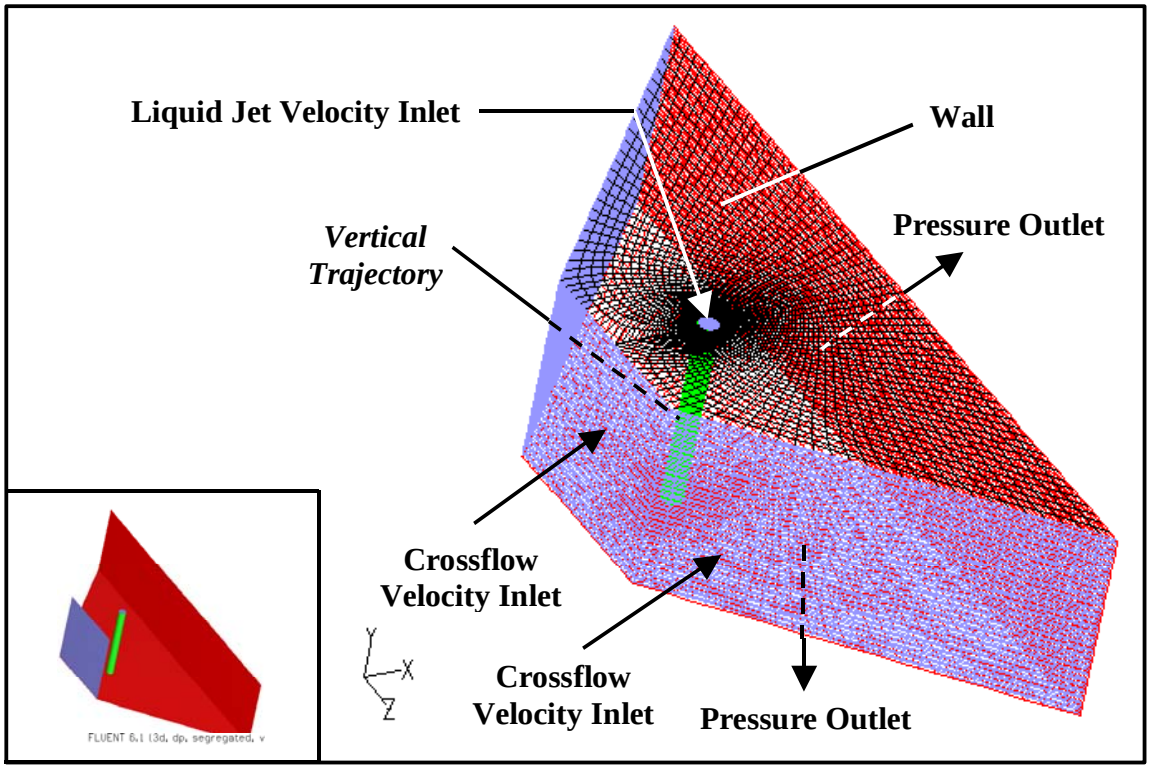

Figure 3.3 Computational grid of the full configuration computational domain.

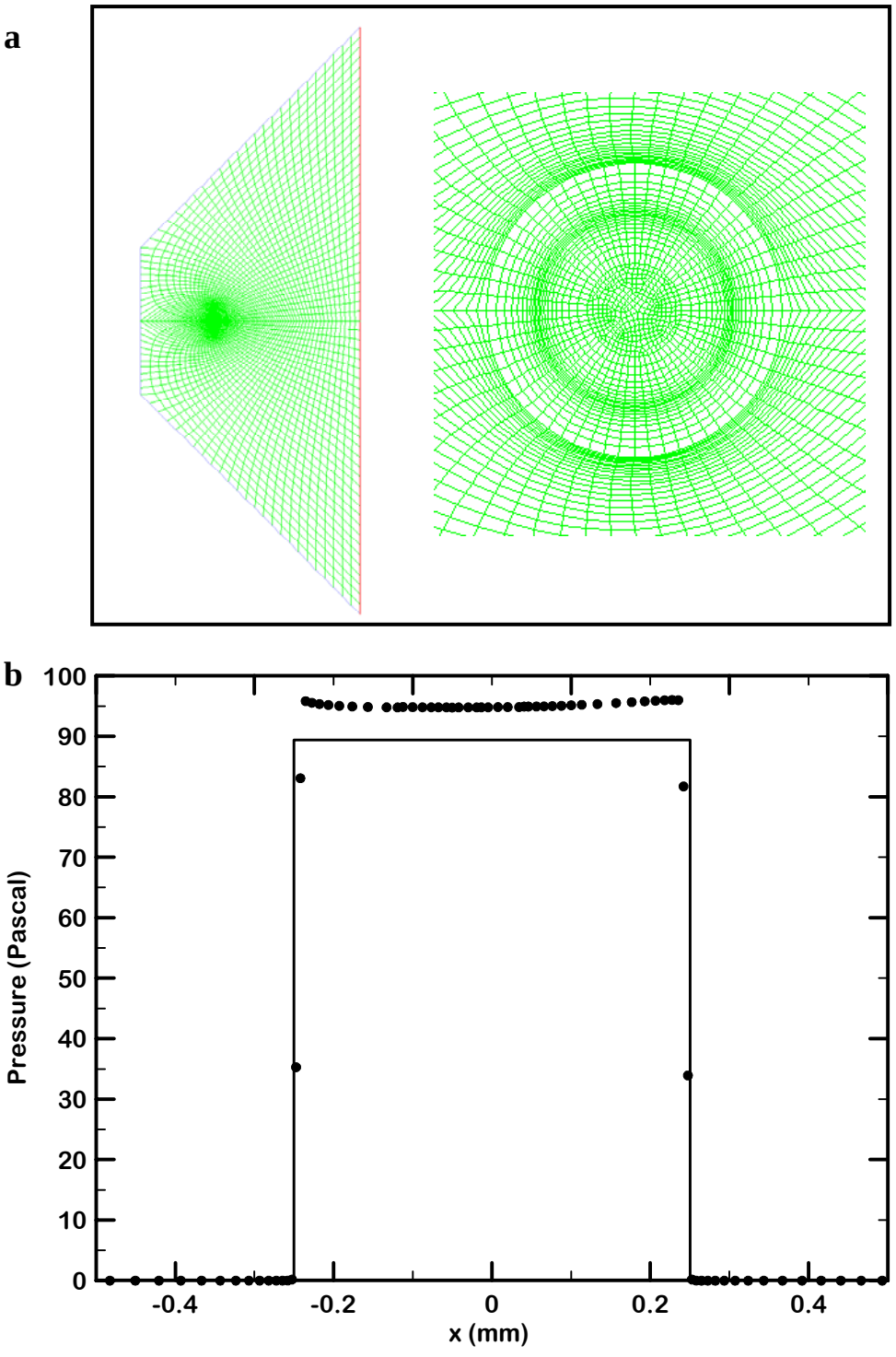

Figure 3.4 (a) Two-dimensional cylindrical jet element for surface tension test. (b) Pressure distribution of the two-dimensional cylindrical jet element (test liquid = ethyl alcohol).

CHAPTER IV

EXPERIMENTAL RESULTS

4.1 Overview

This chapter presents results and discussion related to the experimental investigation of the wave phenomena and droplets properties/transport dynamics of round nonturbulent liquid jets in uniform gaseous crossflow within the bag breakup regime. Pulsed photography is used to measure the column and downwind surface wavelengths, bag counts, node- and ring-droplet sizes after breakup, and the trajectories of the liquid droplets. Single- and double-pulsed shadowgraphy are used to measure the bag-droplet size after breakup, velocity of the jet surface, and the droplets velocities after breakup. High-speed imaging is used to visualize the waves' convection, bag and nodes dynamics, and droplets transport dynamics after the bag breaks up. All measurements presented herein have uncertainties of less than 10% (95% confidence), and are tabulated in Appendix B.

4.2 Flow Visualization

Pulsed photograph of a typical round nonturbulent liquid jet in quiescent air is shown in Fig. 4.1. The water jet presented herein has a jet diameter of 1 mm and a mean nozzle exit velocity of 27 m/s. The liquid jet exhibits a smooth surface with no initialization of atomization, even though the Reynolds number of the liquid jet is

relatively large (Re_L = 30,000). This behavior persisted over the observable length of the liquid jet and remained unchanged up to 75 jets diameter in the absence of crossflow, similar to past observations by Mazallon et al. (1999). With no perceptible deformation or variation of the cross-stream diameter, these results provide direct evidence that the primary breakup process of round nonturbulent liquid jet in crossflow is not due to the initial disturbances within the liquid jet caused by the liquid jet turbulence.

When viscous effects are small (Oh < 0.1), the breakup regime transitions are determined by the crossflow Weber number (Mazallon et al., 1999). For the aforementioned conditions, the liquid jet exhibits five breakup regimes: column breakup (We_G < 4), bag breakup (4 < We_G < 30), multimode breakup (30 < We_G < 110), shear breakup (110 < We_G) (Sallam et al., 2004), and catastrophic breakup. This chapter presents experimental studies related to the bag breakup of round nonturbulent liquid jets in uniform gaseous crossflow. Pulsed photograph of a typical round liquid jet in uniform gaseous crossflow within the bag breakup regime is shown in Fig. 4.2. The ethyl alcohol jet presented herein has a jet diameter of 1 mm, crossflow (left to right) Weber number of 10, and a liquid jet momentum ratio of 224. The image is taken at the plane of symmetry of the deflected liquid jet. The sketch of the breakup of a round nonturbulent liquid jet in uniform gaseous crossflow within the bag breakup regime is shown in Fig. 4.3. The breakup begins with the deformation of the liquid column from a circular cross-section into an ellipsoidal cross-section. This deformation is caused by the reduction of gas pressure along the sides of the liquid jet as the crossflow is being accelerated over the liquid column, as will be discussed in section 5.3.2. The increased drag force due to the now ellipsoidal cross-section enhances the tendency of the liquid column to deflect

downstream with respect to the gas motion. Thickened regions (nodes) appear along the liquid column characterized by the distance between nodes (column waves, λ_c). The nodes subsequently develop into ligament-like structures. Bag-like structures begin to appear as a result of the deformation of the central portion of the liquid column due to the high pressure produced by the stagnating gas on the upwind side of the flattened liquid column. With increasing streamwise distance along the liquid column, the bags grow progressively and eventually break up after approaching a maximum size. The remaining nodes connected by a pair of thin strings (resembling the ring associated to the bag breakup of drops as shown in Fig 1.4) deflect downstream due to the drag force of the crossflow. The remaining thin liquid strings eventually break up (Rayleigh-like breakup). The breakup process results in three distinctive groups of drops. (1) A poly-disperse array of large drops associated with the presence of the nodes (node-droplet, d_{Node}) and (2) ring-droplets due to the breakup of the thin liquid strings (ring-droplet, d_{Ring}), along with (3) a large number of much smaller drops (bag-droplet, d_{Bag}) associated with the breakup of the membrane of the bags.

4.3 Liquid Column Waves and Jet Surface Velocity

The column waves involve the deflection of the entire liquid column in the cross-stream direction. The column waves of typical round nonturbulent liquid jets in uniform gaseous crossflow within the bag breakup regime are shown in Fig. 4.4 for the following test conditions: (a) Water jet with nozzle exit diameter of 1 mm, crossflow (left to right) Weber number of 8, and a liquid jet momentum ratio of 614, (b) ethyl alcohol jet with nozzle exit diameter of 1 mm, crossflow (left to right) Weber number of 10, and a liquid jet momentum ratio of 224, (c) water jet with nozzle exit diameter of 1 mm, crossflow

(left to right) Weber number of 16, and a liquid jet momentum ratio of 302, and (d) ethyl alcohol jet with nozzle exit diameter of 1 mm, crossflow (left to right) Weber number of 20, and a liquid jet momentum ratio of 451. The images were taken at the plane of symmetry of the deflected liquid jet. The amplitude of the column wave grows with increasing distance in the streamwise direction of the liquid jet whereas the wavelength remains nearly constant. This suggests that the column waves convect along the liquid column, as also confirmed by the sequential snapshots obtained using high-speed imaging shown in section 4.5.

The column waves are attributed to Rayleigh-Taylor instability. When a dense fluid is supported by a lighter fluid, for inviscid fluids without surface tension, the growth rate of the disturbance was predicted by Rayleigh (1883) as:

$$\eta_{\text{Rayleigh}} = \sqrt{gkA} \tag{4.1}$$

where η is the growth rate of instabilities, g is the acceleration of gravity, $k = 2\pi/\lambda$ is the wave number, λ is the wavelength, $A = (\rho_2 - \rho_1)/(\rho_2 + \rho_1)$ is the Atwood number, and ρ_1 and ρ_2 are the densities of the lighter and heavier fluids, respectively.

In the absence of surface tension to stabilize the perturbation, Eqn. 4.1 shows that the growth rate will increase with the increase in the wave number. The effects of surface tension and uniform rotation on the growth rate of Rayleigh-Taylor instabilities for two-fluid and three-fluid systems were analytically investigated by El-Ansary et al. (2002). The growth rate of two-fluid systems accelerated by gravity can be computed via

$$\frac{\eta^2}{b} = g\left[\frac{\rho_2 - \rho_1}{\rho_2 + \rho_1} - \frac{k^2\sigma}{g(\rho_2 + \rho_1)}\right]$$

$$b^2 = \frac{k^2\eta^2}{4\Omega^2 + \eta^2} \tag{4.2}$$

where Ω is the angular velocity of the rotation. Neglecting the effect of rotation, Eqn. 4.2 can be rewritten as

$$\eta^2 = kg\frac{\rho_2 - \rho_1}{\rho_2 + \rho_1} - \frac{k^3\sigma}{\rho_2 + \rho_1} \tag{4.3}$$

When fluid layers were accelerated by air pressure, instead similar results were observed by Taylor (1950). To estimate the acceleration of the liquid jet due to the crossflow, one could approximate the drag force acting on the liquid jet to be equal to the drag force on a cylinder in a crossflow. The drag force on the liquid jet could then be approximated as:

$$F = C_D(\frac{1}{2}\rho_G|v|_G^2)(d_j L) = (\rho_L \frac{\pi}{4} d_j^2 L)a \tag{4.4}$$

where C_D is the drag coefficient, L is length of a cylindrical liquid column, and a is the acceleration of the liquid jet in the crossflow direction. Rearranging Eqn. 4.4, the acceleration of the crossflow can be approximated as

$$a = \frac{2C_D\rho_G|v|_G^2}{\pi\rho_L d_j} \tag{4.5}$$

Substitute Eqn. 4.5 into Eqn. 4.3 and setting g = a yield

$$\eta^2 = k\frac{2C_D\rho_G|v|_G^2}{\pi\rho_L d_j}\frac{\rho_L - \rho_G}{\rho_L + \rho_G} - \frac{k^3\sigma}{\rho_L + \rho_G} \tag{4.6}$$

For liquid jet in gaseous crossflow, $\rho_L >> \rho_G$. Therefore, Eqn. 4.6 can be written as

$$\eta = [k\frac{2C_D\rho_G|v|_G^2}{\pi\rho_L d_j} - \frac{k^3\sigma}{\rho_L}]^{1/2} \tag{4.7}$$

For a cylinder in crossflow, the drag coefficient depends on the crossflow Reynolds number (Re_G) given by (White, 1974)

$$C_{D,Cylinder} \approx 1 + 10\,Re_G^{-2/3}; \quad 1 < Re_G < 2x10^5 \tag{4.8}$$

For the range of crossflow Reynolds number ($793 < Re_G < 2456$) used in the present measurements, the drag coefficient can be approximated as one. The numerical solutions of the growth rate of Rayleigh-Taylor instabilities as a function of wave numbers are shown in Fig. 4.5 for the following test conditions: (a) Water as test liquid with nozzle exit diameter of 1 mm and crossflow Weber number of 8, and (b) ethyl alcohol as test liquid with nozzle exit diameter of 1 mm and crossflow Weber number of 28. The presence of surface tension results in damping the Rayleigh-Taylor instabilities at high wave number. To find the wave number corresponding to the maximum growth rate, one can differentiate Eqn 4.8 as follows:

$$\frac{d\eta}{dk} = \frac{(\frac{2C_D\rho_G|v|_G^2}{\pi\rho_L d_j} - \frac{3\sigma}{\rho_L}k^2)}{2(\frac{2C_D\rho_G|v|_G^2}{\pi\rho_L d_j}k - \frac{\sigma}{\rho_L}k^3)^{1/2}} \tag{4.9}$$

At maximum growth rate, $d\eta/dk = 0$. Eqn. 4.9 becomes

$$k^2 = \frac{2C_D}{3\pi}\frac{\rho_G|v|_G^2}{\sigma}\frac{1}{d_j} \tag{4.10}$$

Rearranging Eqn. 4.10 by substituting the wave number ($k = 2\pi/\lambda_c$) and the crossflow Weber number ($We_G = \rho_G d_j U_G/\sigma$) yields

$$\frac{\lambda_c}{d_j} = C_\lambda\sqrt{\frac{6\pi^3}{C_D}}We_G^{-0.5} \tag{4.11}$$

where C_λ is an empirical parameter of order of unity.

The wavelength, λ_c, of the column waves is defined herein as the distance between the nodes on the upwind side of the liquid jet, as shown in the inset of Fig. 4.6. The wavelengths of column waves for various test conditions, along with the measurements of Mazallon et al. (1999) are plotted as suggested by Eqn 4.11 in Fig. 4.6. The present measurements have maximum uncertainties of 9.9% (95% confidence). The computational results within the column and bag breakup regimes are also shown in Fig. 4.6, and are discussed later in section 5.6. The present measurements agree with the experimental results of Mazallon et al. (1999) within experimental uncertainties. Note that Mazallon et al. (1999) fitted a single correlation across the column, bag, and multimode breakup regimes. The data point in the multimode breakup regime (order of magnitude lower than the other data points) did post an acute effect to Mazallon et al. (1999) correlation, rendering it to be inaccurate in the bag breakup regime. The best-fit correlation of the wavelength of column waves measurements within the bag breakup regime is given by:

$$\frac{\lambda_c}{d_j} = 5.3 We_G^{-0.26} \tag{4.12}$$

The correlation coefficient of the fit is 0.62. The power of the crossflow Weber number in Eqn. 4.12 is not -0.5 as suggested by Eqn. 4.11, but the difference is not large in view of the approximations (i.e., assuming the force acting on the liquid jet is equal to the force acting on a cylinder in crossflow) used to find Eqn. 4.11 and experimental uncertainties resulted from the column waves irregularities. Present measurements are also correlated as suggested by Eqn. 4.11 in Fig. 4.6 yielding the following:

$$\frac{\lambda_c}{d_j} = 9.7 We_G^{-1/2} \tag{4.13}$$

The correlation coefficient of the fit is 0.56. For the range of present measurements, the average C_D equals 1.08. The empirical parameter, C_λ, can be computed via

$$C_\lambda \sqrt{\frac{6\pi^3}{C_D}} = 9.7 \tag{4.14}$$

resulting in a value of $C_\lambda = 0.7$, which is of order of unity. The reasonable value of the empirical coefficient and the fact that the wavelength of column waves was independent of the liquid jet momentum ratio as shown in the legend of Fig. 4.6 further support the present claim that the column waves within the bag breakup regime are caused by Rayleigh-Taylor instabilities.

The velocity of the liquid surface was measured by double-pulsed shadowgraphy, as shown in Fig. 4.7. The velocity of the liquid surface normalized by the nozzle exit

velocity approaches unity, independent of the streamwise distance traveled. This agrees with the assumption of negligible drag forces in the streamwise direction. The standard deviation of the measurements is 6%.

4.4 Liquid Surface Waves

A remarkable feature of liquid jets breakup in crossflow is the surface waves appearing along the downwind surface of the liquid column. These surface waves were not reported before in the literature. The downwind surface waves are shown in Fig. 4.8 for the following test conditions: (a) Water as test liquid with nozzle exit diameter of 1 mm, crossflow Weber number of 16, and a liquid jet momentum ratio of 614, (b) ethyl alcohol as test liquid with nozzle exit diameter of 1 mm, crossflow Weber number of 20, (c) water as test liquid with nozzle exit diameter of 1 mm, crossflow Weber number of 24, and a liquid jet momentum ratio of 1199, and a liquid jet momentum ratio of 903, and (d) ethyl alcohol as test liquid with nozzle exit diameter of 1 mm, crossflow Weber number of 28, and a liquid jet momentum ratio of 451. The camera was tilted 40 degrees in the downwind direction from the normal position to the crossflow, as shown in the inset of Fig. 4.8. The downwind surface waves originate near the sides of the downwind surface of the liquid column where the crossflow velocities are higher than any other region, suggesting that the behaviors are associated with aerodynamic stripping. The same phenomenon is also observed in the computed liquid jet within the bag breakup regime shown in section 5.3.2. For laminar flow past a circular cylinder, the maximum velocity (~1.6 U_G) and the flow separation occur at approximately 71.2^0 and 80.5^0 from the stagnation point in the upwind direction, respectively (White, 1974). When there is velocities difference across the interface between two fluids, the Kelvin-Helmholtz

instabilities can occur. Therefore, the downwind surface waves may be attributed to the shearing of liquid from the stagnation point in the upwind direction towards the point of separation, where the liquid surface is pulled from the sides of the liquid jet (near the point of separation) and is sheared towards the downwind direction.

The wavelength of the downwind surface waves (λ_s) is defined as the distance between troughs of the surface waves on the downwind side of the liquid jet, as shown in the inset of Fig. 4.9. The wavelengths of the downwind surface waves for various test conditions, along with the computational results are shown in Fig. 4.9. The downwind surface wavelength decreases as the crossflow Weber number increases within the bag breakup regime. The following shows the correlation of the downwind surface wavelengths measurements:

$$\lambda_s / d_j = 4.3(We)^{-0.33} \tag{4.15}$$

The correlation coefficient of the fit is 0.61.

4.5 Bag Formation

The sequential snapshots of the bag-like structures formed from the column waves for a typical round nonturbulent liquid jet in uniform gaseous crossflow are shown in Fig. 4.10. The water jet presented herein has a nozzle exit diameter of 1 mm, crossflow (left to right) Weber number of 8, and a liquid jet momentum ratio of 97. The region shown corresponds to the onset of the phenomena and the image was taken at the plane of symmetry of the deflected liquid jet. The column wave amplitude is observed to grow with increasing streamwise distance. The bag-like structure is formed as a result of

the deformation of the central portion of the liquid column due to the high pressure produced by the stagnating gas on the upwind side of the flattened liquid column.

A first bag is identified when the ratio of liquid jet cross-stream diameter to the nozzle exit diameter (d_s/d_j) between two adjacent nodes is greater than unity. The last bag along the liquid jet is associated with the end of the liquid core. The number of bags (N_B) formed along the liquid column can be predicted via dividing the length (L_s) of the liquid column from the onset of bag formation (y_{bf}) to the end of liquid core (y_b) by the column wavelength (λ_c):

$$N_B \sim \frac{L_s}{\lambda_c} \sim \frac{\sqrt{x_b^2 + (y_b - y_{bf})^2}}{\lambda_c}$$

$$N_B = C_b \frac{\sqrt{x_b^2 + (y_b - y_{bf})^2}}{\lambda_c} \tag{4.16}$$

where C_b is an empirical parameter of order of unity and x_b is the cross-stream distance from the center of the nozzle exit to the end of liquid core. The parameters employed herein are shown in Fig. 4.3. The number of bags for various test conditions is shown in Fig. 4.11. The best-fit correlation for the number of bags along the liquid jet is given by:

$$N_B = 0.82\{\frac{[x_b^2 + (y_b - y_{bf})^2]^{0.5}}{\lambda_c}\}^{1.1} \tag{4.17}$$

The correlation coefficient of the fit is 0.94. The coefficient and the power of the fit in Eqn. 4.17 are close to unity, as suggested by Eqn. 4.16. The difference is not large in view of the approximations used to find Eqn. 4.16.

4.6 Nodes Formation

Bag-structures with multiple-nodes layouts (typically 4, 5, …, 8 nodes) were observed in the bag breakup of round nonturbulent liquid jets in uniform gaseous crossflow. Four-node, five-node, and six-node layouts are shown in Figs. 4.12, 4.13, and 4.14, respectively. The water jet presented herein has a nozzle exit diameter of 1 mm, crossflow Weber number of 8, and a liquid jet momentum ratio of 65. The span-wise distance between the nodes increases in the streamwise direction. The images were taken at 77 degrees tilted in the upstream direction of the plane of symmetry of the deflected liquid jet. The bags typically start the breakup from the lower side of the bag structure as shown in Fig. 4.12 and Fig. 4.13. The nodes layout per bag affected the breakup mechanism as follows: For 4-node and 5-node bag breakup, the breakup of the bag-membrane typically starts from the lower surface and continue uninterrupted. For 6-node bag, however, the bag typically opens from the lower side in the downwind surface, stop momentarily on the strings of liquid connecting the two intermediate nodes, before completely breaks up as shown in Fig. 4.14.

The nodes layout occurrences are shown in Fig. 4.15. The present experimental results show that 49% of the bag-like structure exhibits 4-node layout, 28% displays a 5-node layout, and 20% shows a 6-node layout. Occasionally, 7-node layout and 8-node layout were observed, contributed to approximately 2% and 1% of total occurrences, respectively.

4.7 Breakup of the Bag-membrane

During the bag breakup, the bag-like structure grows progressively into a thin membrane while being convected in the streamwise direction. Eventually the thin

membrane breaks up after the "bag" reaches a maximum size. The breakup of the bag-membrane is shown in Fig. 4.16. A bag-membrane can opens from: (a) The bottom side in the downwind surface (42% occurrences), (b) the upper side in the downwind surface (10% occurrences), (c) the center in the downwind surface (15% occurrences), (d) the top and bottom sides in the downwind surface (27% occurrences), (e) the two sides in the upwind direction (4% occurrences), and (f) the top and bottom and the two sides in the upwind directions (2% occurrences). The water jet presented herein has a nozzle exit diameter of 1 mm, crossflow (left to right) Weber number of 8, and a liquid jet momentum ratio of 32. The bag-membrane typically opens from the bottom side in the downwind direction because the bottom side is progressively stretched by the increasing span-wise separation between the nodes in the streamwise direction. A bag seldom opens from the two sides in the upwind direction. In the breakup of the bag-membrane, the onset of breakup begins with the formation of ligaments. The bag-droplets subsequently formed at the tip of the ligaments due to Rayleigh breakup. The breakup of the membrane results in a large number of very small droplets (bag-droplet, d_{Bag}).

4.8 Ring Breakup

The ring breakup of a typical round nonturbulent liquid jet in uniform gaseous crossflow is shown in Fig. 4.17. The detachment of node-droplet of a typical round nonturbulent liquid jet in uniform gaseous crossflow is shown in Fig. 4.18. The water jet presented in both figures has a nozzle exit diameter of 1 mm, crossflow (left to right) Weber number of 8, and a liquid jet momentum ratio of 32. The ring breakup process is similar in nature to the ring breakup within the secondary breakup of droplets. The two strings of node drops connected by thinner liquid column breaks up (Rayleigh-like

breakup), resulting in a poly-disperse array of large drops associated with the presence of the nodes (node-droplet, d_{Node}) and the breakup of their connecting liquid columns (ring-droplet, d_{Ring}).

4.9 Breakup Outcomes

This section presents results and discussion related to the sizes of the liquid droplets, velocities of the liquid droplets, and trajectories of the liquid droplets produced by the breakup of the bag-like structures.

4.9.1 Droplets Sizes

The node- and ring-droplet produced by the ring breakup are shown in Fig. 4.19 for the following test conditions: (a) Water as test liquid with nozzle exit diameter of 0.5 mm, crossflow (left to right) Weber number of 4, and a liquid jet momentum ratio of 9, (b) ethyl alcohol as test liquid with nozzle exit diameter of 1 mm, crossflow (left to right) Weber number of 8, and a liquid jet momentum ratio of 88, (c) ethyl alcohol as test liquid with nozzle exit diameter of 1 mm, crossflow (left to right) Weber number of 10, and a liquid jet momentum ratio of 224, and (d) water as test liquid with nozzle exit diameter of 1 mm, crossflow (left to right) Weber number of 16, and a liquid jet momentum ratio of 302,. The formation of bag-droplet due to the breakup of the bag-membrane is shown in Fig. 4.20(a) to Fig. 4.20(c). The water jet presented herein has a jet diameter of 1 mm, crossflow (left to right) Weber number of 8, and a liquid jet momentum ratio of 32. The pulsed shadowgraph employed for measuring the SMD of the bag droplets are shown in Fig. 4.20(d) to Fig. 4.20(f) for the following test conditions: (d) Water as test liquids with nozzle exit diameter of 1 mm, crossflow (left to right) Weber number of 10, and a

liquid jet momentum ratio of 70, (e) water as test liquids with nozzle exit diameter of 1 mm, crossflow (left to right) Weber number of 20, and a liquid jet momentum ratio of 38, and (f) water as test liquids with nozzle exit diameter of 1 mm, crossflow (left to right) Weber number of 30, and a liquid jet momentum ratio of 38. The images in both figures were taken at the plane of symmetry of the deflected liquid jet. In these images, the smallest drops are associated with the breakup of the bag-membrane (bag-droplet, d_{Bag}); the largest drops are associated with the breakup of nodes (node-droplet, d_{Node}); and the medium size droplets are associated with the breakup of the thinner liquid columns connecting the node drops (ring-droplet, d_{Ring}).

The sizes of the liquid droplets due to node and ring breakup of round nonturbulent liquid jets in uniform gaseous crossflow are plotted in Fig. 4.21. The results shown in Fig. 4.21 also include the ring-droplet measurements of the secondary breakup of drops by Chou and Faeth (1998). The drop sizes are as follows:

$$SMD_{Node} / d_j = 11.4We^{-1.0} \tag{4.18}$$

$$SMD_{Ring} / d_j = 4.8We^{-1.0} \tag{4.19}$$

The correlation coefficients of the fits are 0.96 and 0.98, for the node- and the ring-droplets, respectively. The sizes of the node- and the ring-droplets depend on the crossflow Weber number. As the crossflow Weber number increases, the node- and ring-droplet become smaller. The ring-droplet size produced by the primary breakup of liquid jets and the secondary breakup of drops are similar confirming the analogy between the bag breakup of liquid jets in crossflow and the bag breakup of the drops subjected to shock wave disturbances.

The size of the liquid droplets due to the breakup of the bag-membrane of round nonturbulent liquid jets in uniform gaseous crossflow is plotted in Fig. 4.22. Also shown in Fig. 4.22 are the measurements of the Chou and Faeth (1998) for the secondary breakup of drops in the bag breakup regime. The correlation of the SMD of bag droplets is given by:

$$SMD_{Bag}/d_j \approx 0.14 \tag{4.20}$$

The standard deviation of the measurements is 15%. The size of the bag-droplet is independent of the crossflow Weber number. This confirms that the there is a minimum membrane thickness that must be attained before the onset of breakup of the bag-membrane. The sizes of the bag-droplets in the present study are larger than those in the case of the secondary breakup of drops within the bag breakup regime (Chou and Faeth, 1998). Unlike the secondary breakup of liquid drops, liquid jets in crossflow are anchored at the nozzle exit and the column waves are being convected continuously along the liquid column. As a result, the bag-like structure in the case of the liquid jet experiences various modes of disturbances that are not seen in the secondary breakup of liquid drops. Finally, the total volume of liquid droplets per bag structure is approximately equal to

$$A_{sc}\lambda_c \approx (\pi d_j^2/4)(5.3 d_j We_G^{-0.26}) \approx 4.2 d_j We_G^{-0.26} \tag{4.21}$$

4.9.2 Velocities of Liquid Droplets

Typical double-pulsed shadowgraphs for measuring the velocities of the liquid droplets are shown in Fig. 4.23 for the following test conditions: (a) Node-droplets,

water as test liquid with nozzle exit diameter of 1 mm, crossflow (left to right) Weber number of 16, and a liquid jet momentum ratio of 53, (b) Ring-droplets, water as test liquid with nozzle exit diameter of 1 mm, crossflow (left to right) Weber number of 24, and a liquid jet momentum ratio of 37, and (c) Bag-droplets, water as test liquid with nozzle exit diameter of 1 mm, crossflow (left to right) Weber number of 8, and a liquid jet momentum ratio of 90. The images were taken at the plane of symmetry of the deflected liquid jet. The streamwise and cross-stream velocities magnitudes were computed by measuring the cross-stream and streamwise distances traveled by the liquid droplets in a known time-step.

The streamwise and cross-stream velocities of the node-droplet as a function of node-droplet size are shown in Fig. 4.24. The velocities are nearly independent of drop sizes, or:

$$\frac{u_{Node}}{U_G} \approx 0.28$$

$$\frac{v_{Node}}{v_j} \approx 0.9 \qquad (4.22)$$

The standard deviations of the measurements are 8% and 14%, for cross-stream and streamwise velocities, respectively.

The streamwise and cross-stream velocities of the ring-droplet as a function of ring-droplet size are shown in Fig. 4.25. The velocities are nearly independent of drop sizes, or:

$$\frac{u_{Ring}}{U_G} \approx 0.27$$

$$\frac{v_{Ring}}{v_j} \approx 0.87 \tag{4.23}$$

The standard deviations of the measurements are 17% and 12%, cross-stream and streamwise velocities, respectively.

The streamwise and cross-stream velocities of the bag-droplet as a function of bag-droplet size after the breakup of the bag-membrane are shown in Fig. 4.26. The streamwise and cross-stream velocities of the bag-droplet are independent of the bag-droplet size. The following shows the correlation of the present measurements:

$$\frac{u_{Bag}}{U_G} \approx 0.34$$

$$\frac{v_{Bag}}{v_j} \approx 0.56 \tag{4.24}$$

The standard deviations of the measurements are 32% and 72%, cross-stream and streamwise velocities, respectively. The large standard deviation of the velocities measurements can be attributed to the mechanisms of the breakup of the bag-membrane. When a bag breaks up, the membrane can opens in several ways (section 4.7). Since the velocities of the bag-droplet were measured immediately after the breakup, the seemingly random opening of the bag-membrane would result in such large velocities variations.

Immediately after bag breakup, the node- and ring-droplet traveled with about the same velocities because the bag-like structure traveled as a whole before the breakup. When compared to the velocity of the node- and ring-droplet, the bag-droplet traveled with a higher cross-stream velocity but with a lower streamwise velocity. The

differences in the streamwise and cross-stream velocities can be attributed to the high pressure produced by the stagnating gas on the upwind side of the bag-like structure, propelling the bag-droplets in the cross-stream and negative streamwise directions (owing to the deflection of the liquid column) immediately after the breakup of the bag-membrane.

4.9.3 Trajectories of Liquid Droplets

The trajectories of node-droplet and bag-droplet for various test conditions are shown in Fig. 4.27. In Fig. 4.27, x is the cross-stream distance from the center of the liquid jet to the center of the liquid droplets, y_{Node} represents the streamwise distance from the nozzle exit to the center of the node-droplet, and y_{Bag} denotes the streamwise distance from the nozzle exit to the center of the bag-droplet. The following shows the correlation of the present measurements:

$$y_{Node}/(d_j q) = 1.64[x/(d_j q)]^{0.72} \tag{4.25}$$

$$y_{Bag}/(d_j q) = 0.82[x/(d_j q)]^{0.63} \tag{4.26}$$

The correlation coefficients of the fits are 0.98 and 0.89, for node- and bag-droplets, respectively. Based on the measurements, there are separate trajectories for the bag-droplets and the node-droplets. This could have practical applications for developing size sorting techniques. Note that both the bag- and node-droplet penetrated the crossflow further than a liquid jet within the bag breakup regime as measured by by Sallam et al. (2004). This is because the hemispherical-shaped bag-membrane has larger drag coefficient than the spherical-shaped node-droplet, resulting in the latter to show a steeper trajectory.

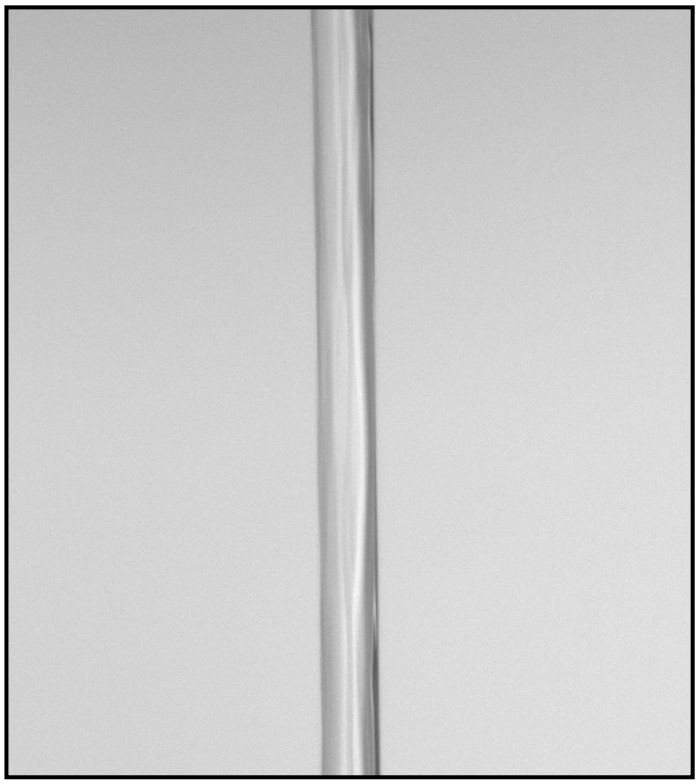

Figure 4.1 A round nonturbulent liquid jet in still air (test conditions: Water, $d_j = 1$ mm, $We_G = 0$, $Re_L = 30{,}000$, and $q = \infty$).

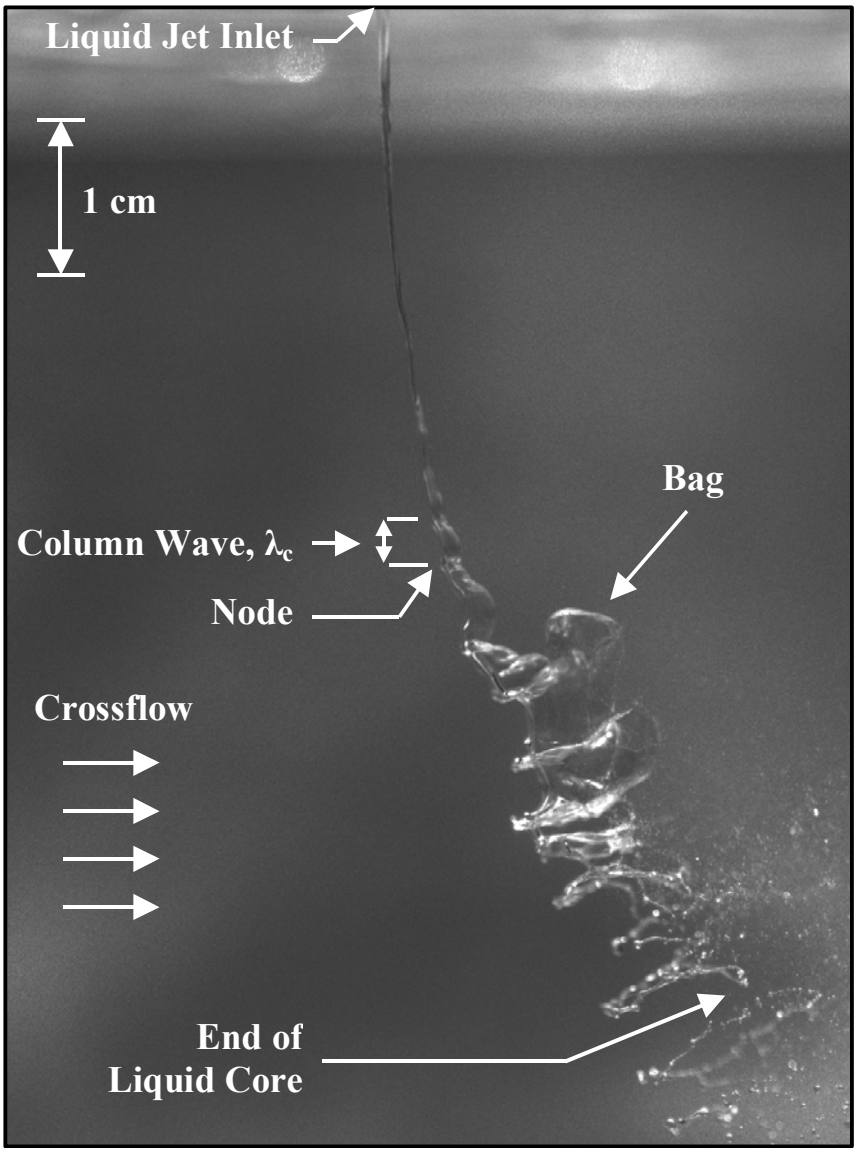

Figure 4.2 A round nonturbulent liquid jet in uniform gaseous crossflow within the bag breakup regime (test conditions: Ethyl Alcohol, d_j = 1 mm, We_G = 10, and q = 224).

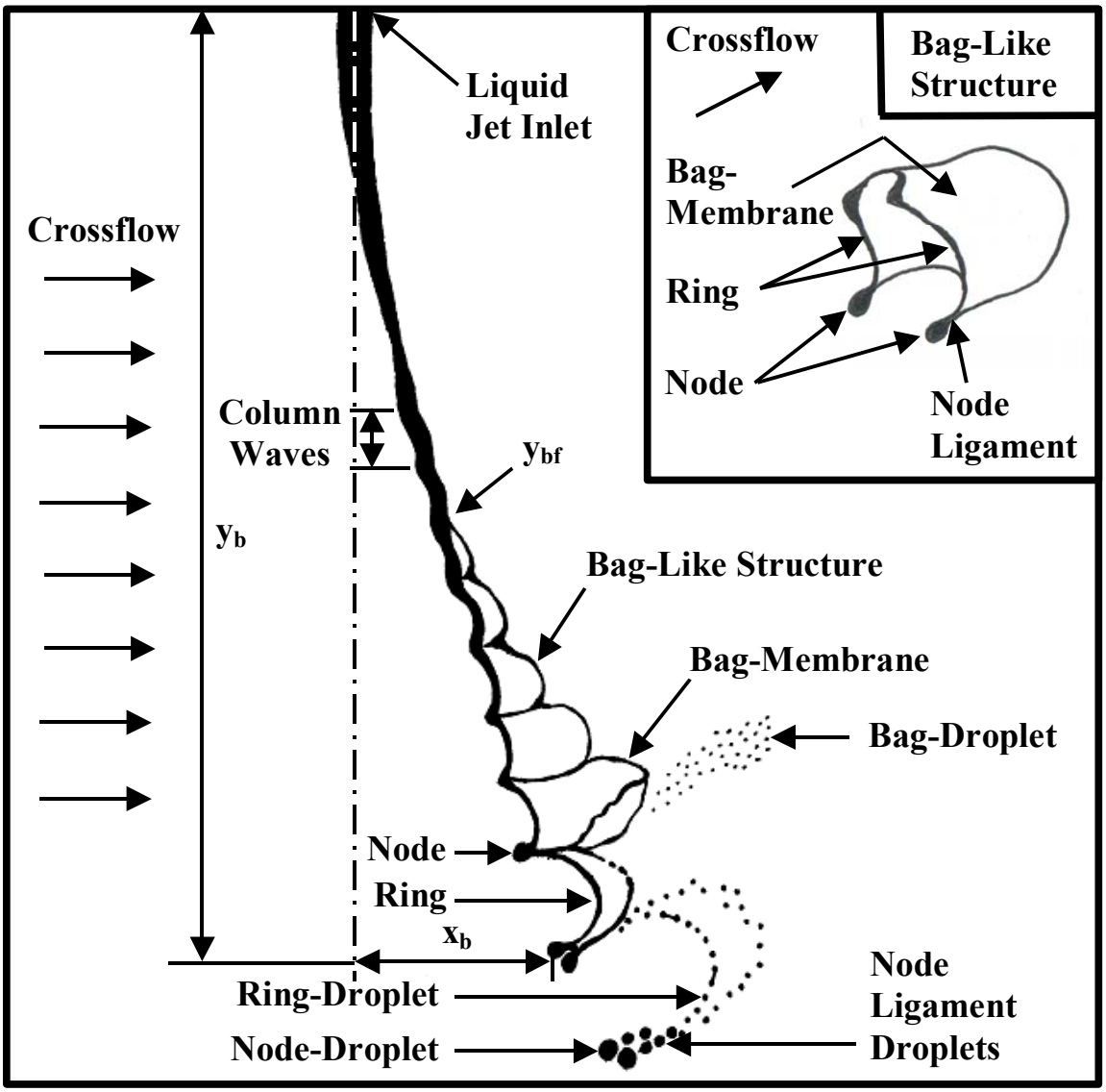

Figure 4.3 Sketch of a round nonturbulent liquid jet in uniform gaseous crossflow within the bag breakup regime.

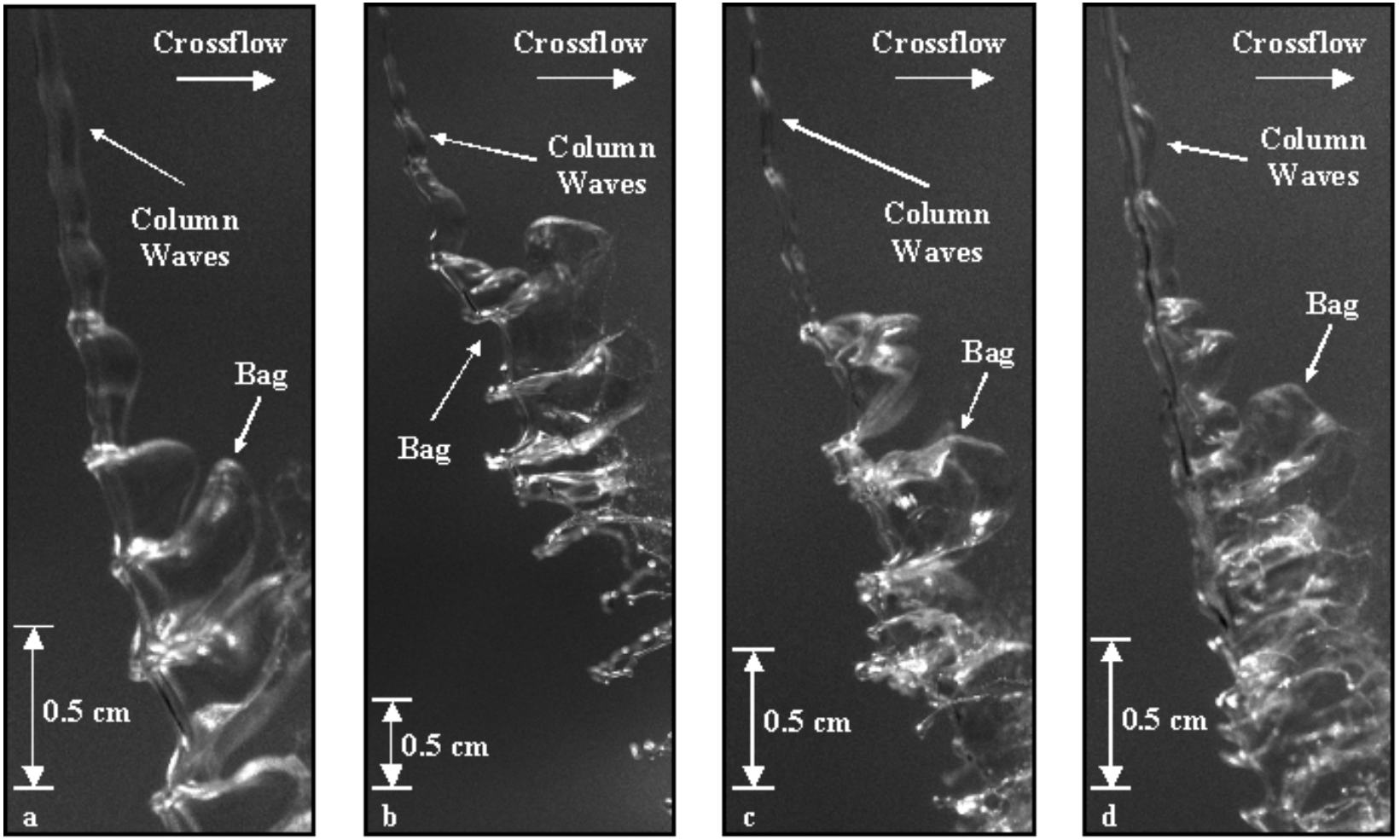

Figure 4.4 Column waves of round nonturbulent liquid jets in uniform gaseous crossflow within the bag breakup regime. Test conditions: (a) Water, d_j = 1 mm, We_G = 8, and q = 614, (b) Ethyl Alcohol, d_j = 1 mm, We_G = 10, and q = 224, (c) Water, d_j = 1 mm, We_G = 16, and q = 302, and (d) Ethyl Alcohol, d_j = 1 mm, We_G = 20, and q = 451.

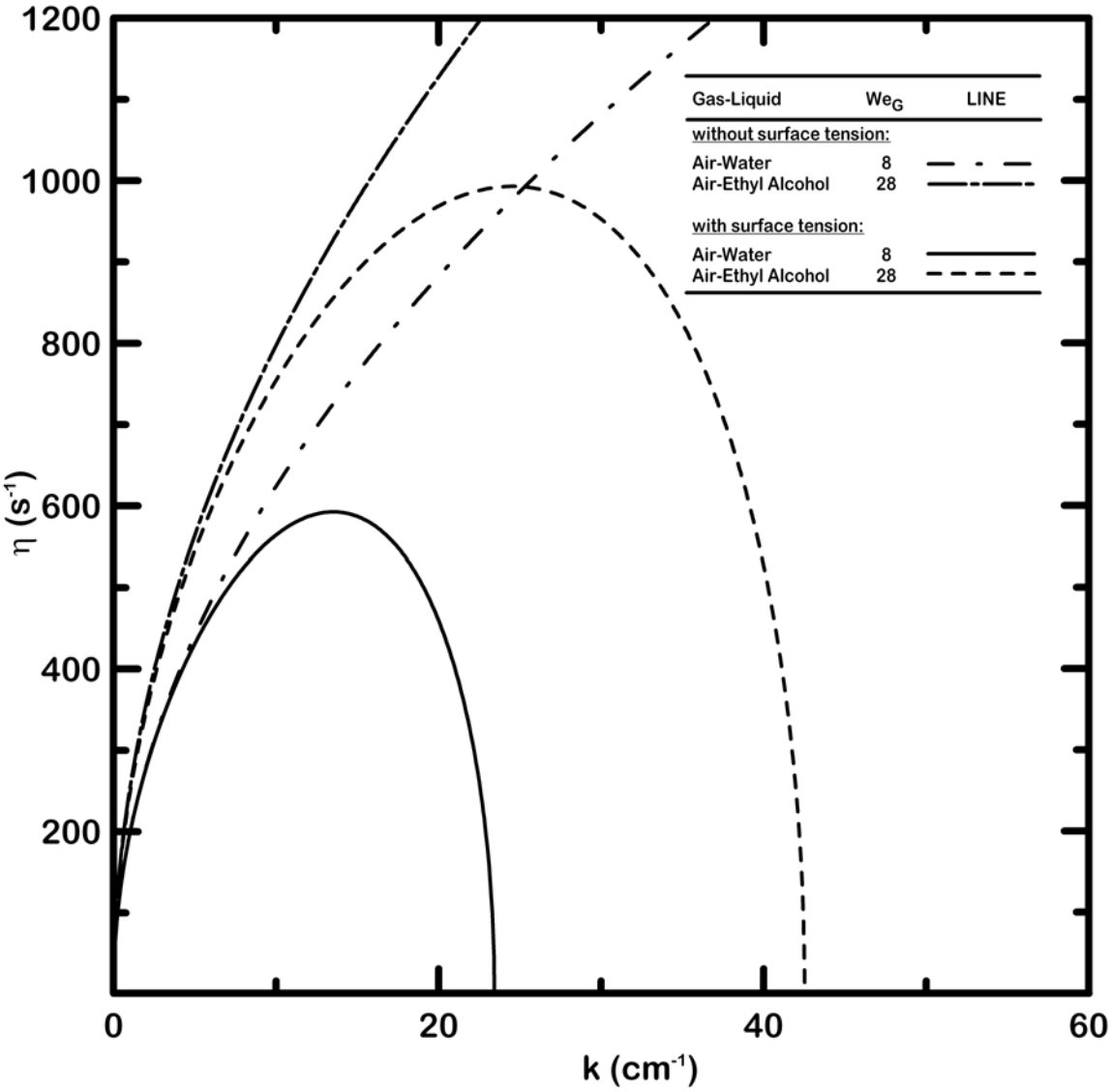

Figure 4.5 Numerical solutions of the growth rate (with and without surface tension) of Rayleigh-Taylor instabilities as a function of wave numbers. Test conditions: (a) Water, d_j = 1 mm, We_G = 8, and (b) Ethyl alcohol, d_j = 1 mm, We_G = 28.

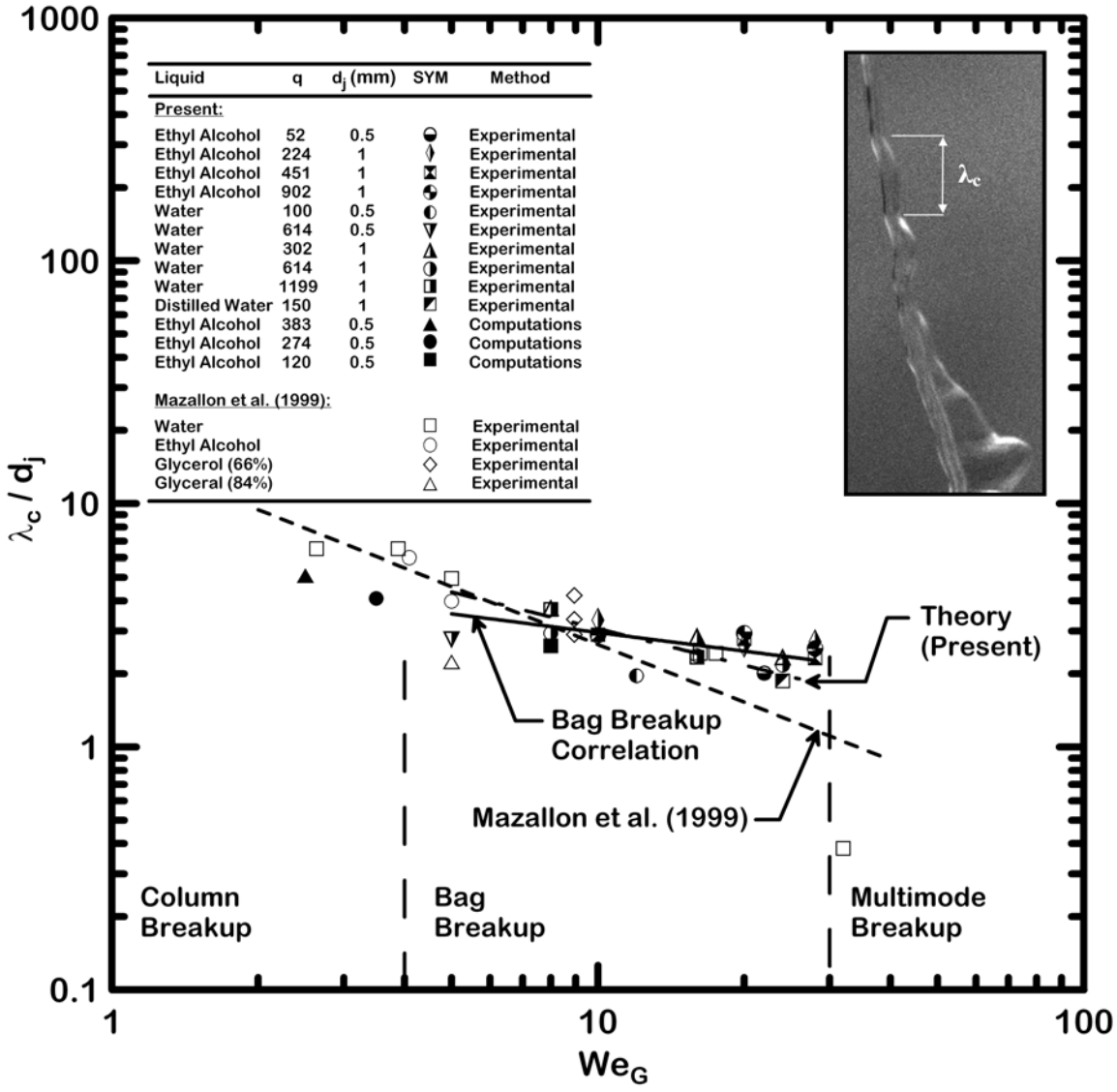

Figure 4.6 Wavelengths of column waves as a function of crossflow Weber number.

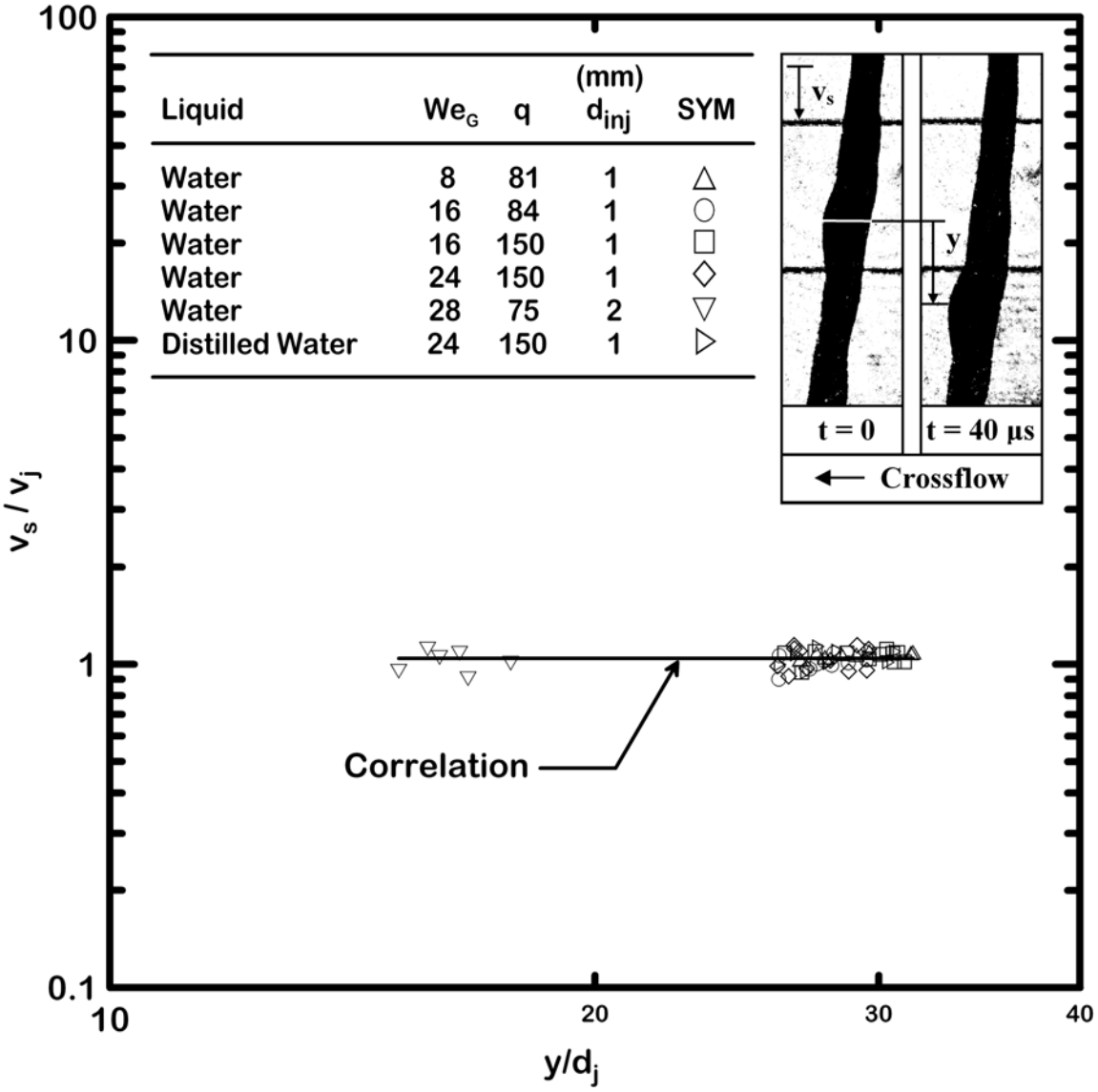

Figure 4.7 Velocity of liquid surface as a function of streamwise distance.

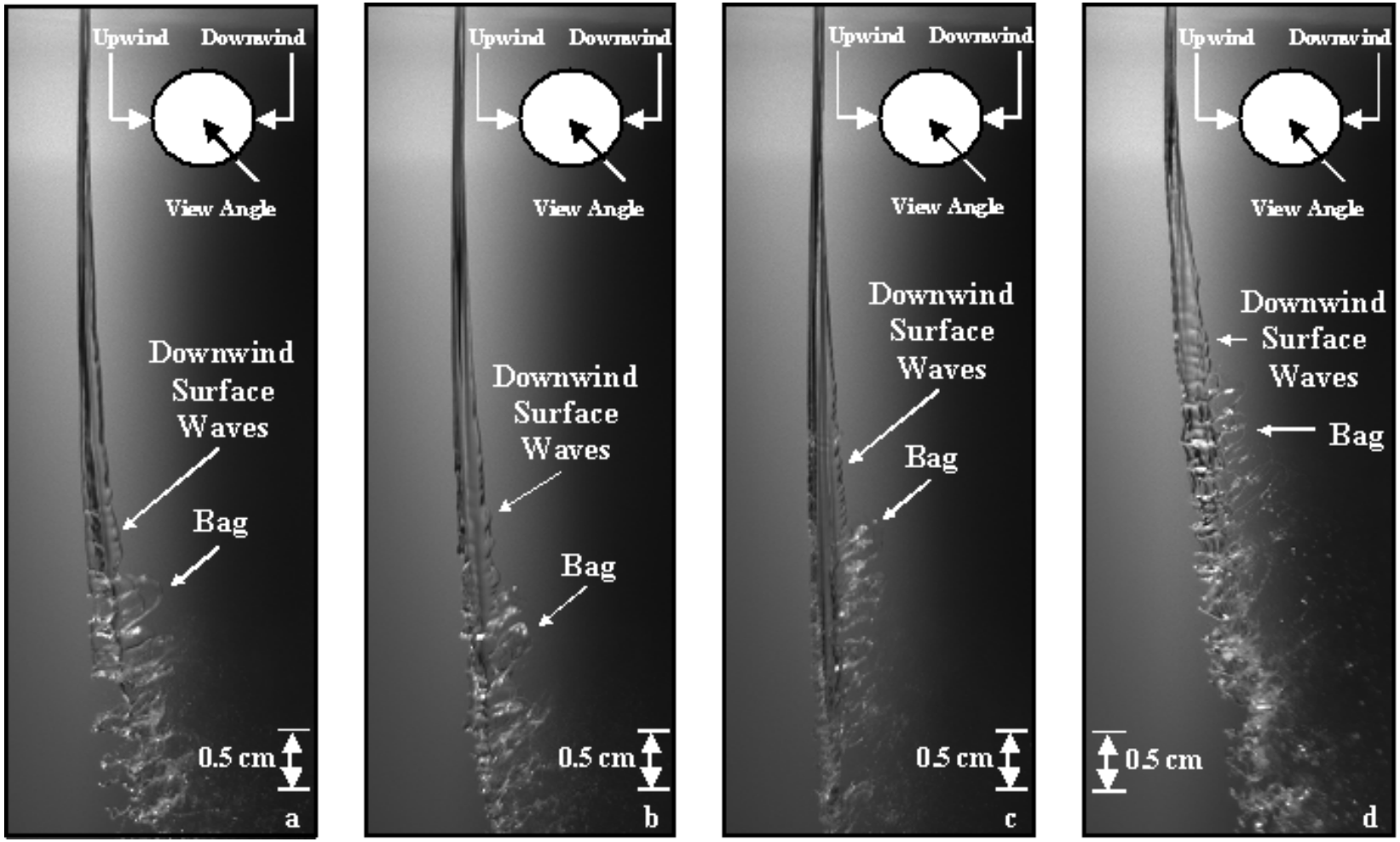

Figure 4.8 Downwind surface waves of round nonturbulent liquid jets in uniform gaseous crossflow within the bag breakup regime. Test conditions: (a) Water, d_j = 1 mm, We_G = 16, and q = 614, (b) Ethyl Alcohol, d_j = 1 mm, We_G = 20, and q = 903, (c) Water, d_j = 1 mm, We_G = 24, and q = 1199, and (d) Ethyl Alcohol, d_j = 1 mm, We_G = 28, and q = 451.

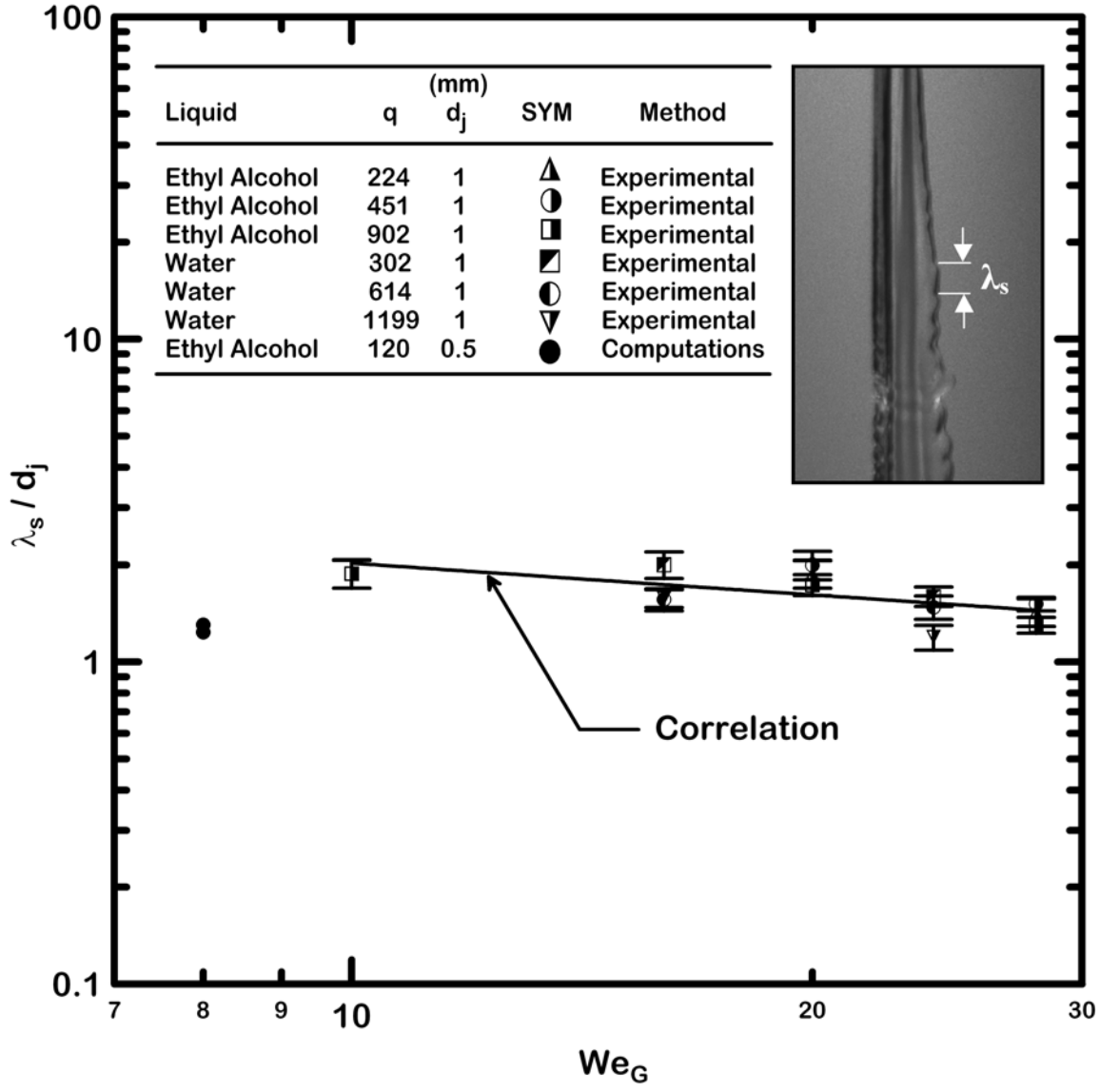

Figure 4.9 Wavelengths of downwind surface waves as a function of crossflow Weber number.

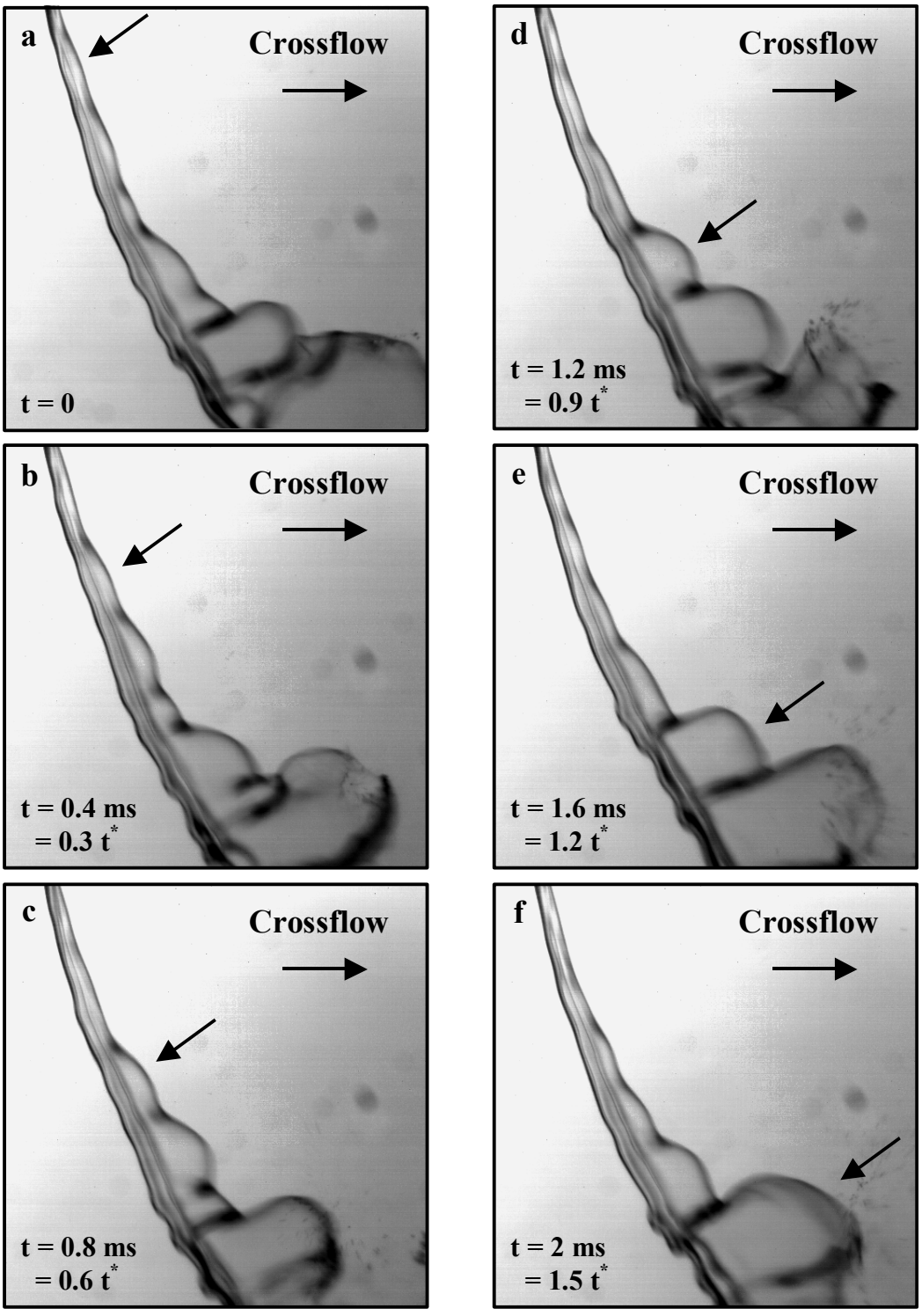

Figure 4.10 (a) – (f) Bag-like structures formed from the column waves within the bag breakup regime (test conditions: Water, d_j = 1 mm, We_G = 8, and q = 97).

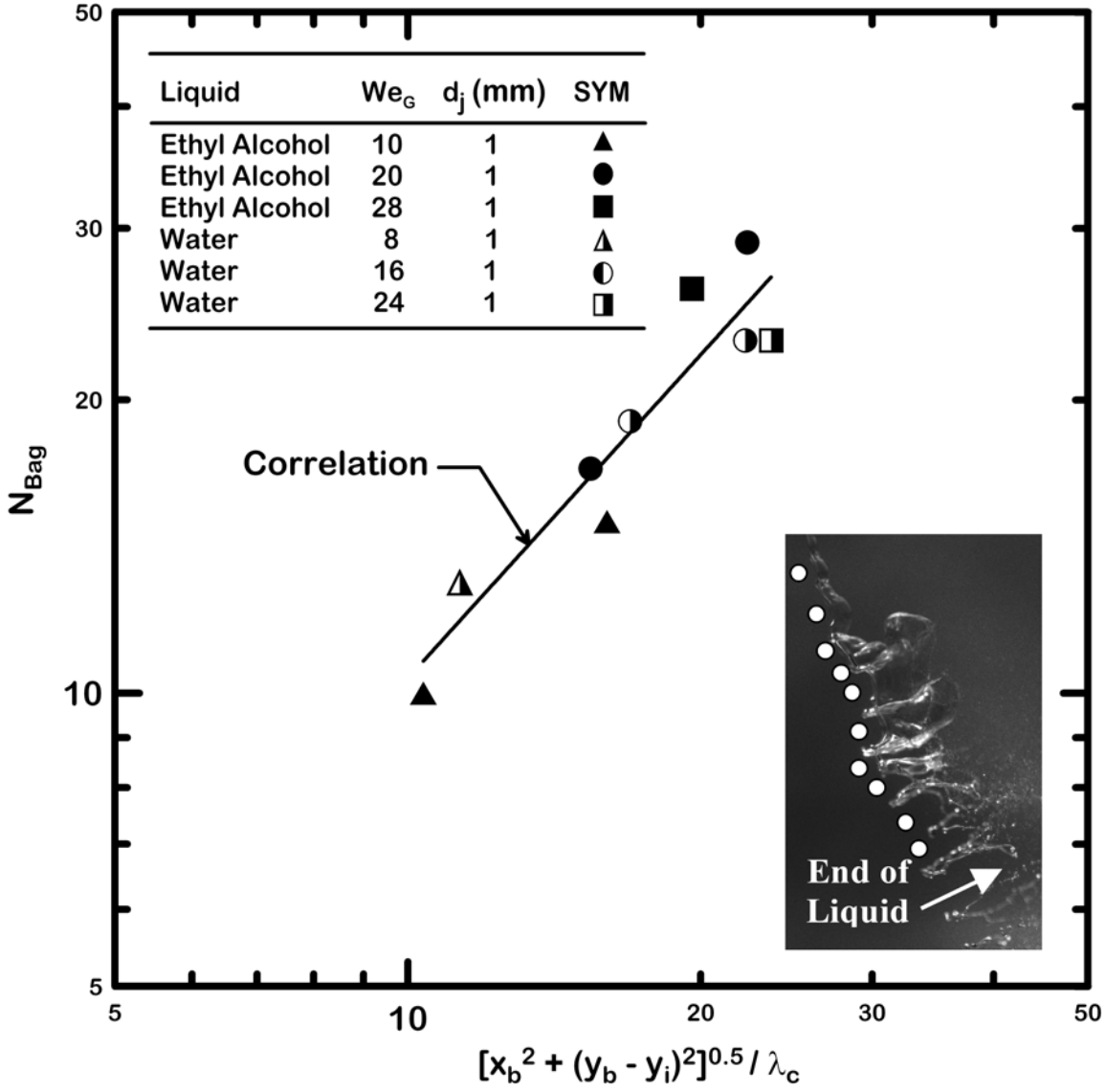

Figure 4.11 The number of bags formed along the liquid column of round nonturbulent liquid jets in uniform gaseous crossflow.

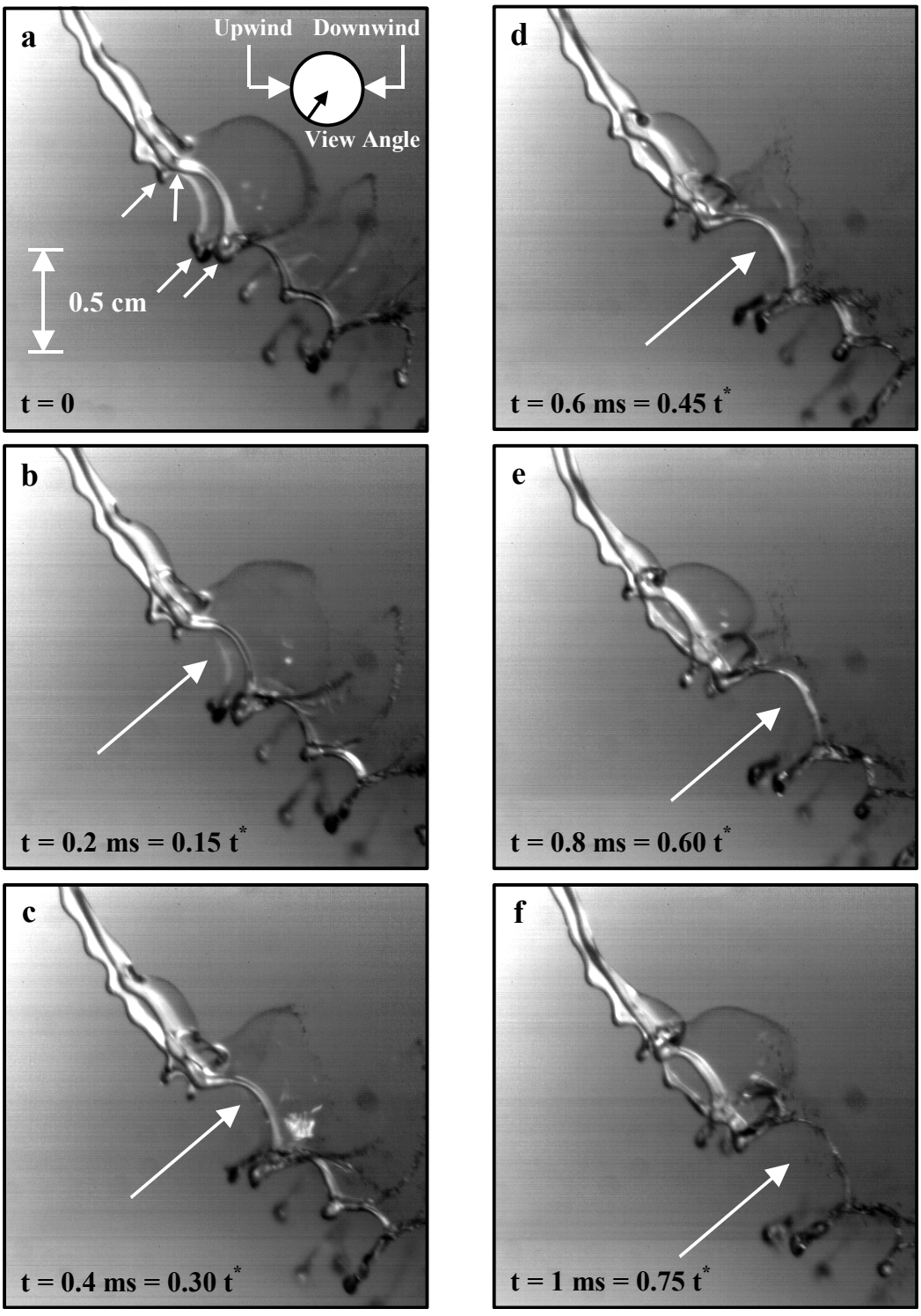

Figure 4.12 (a) – (f) Typical 4-node bag breakup of a round nonturbulent liquid jet in uniform gaseous crossflow (test conditions: Water, d_j = 1 mm, We_G = 8, and q = 65).

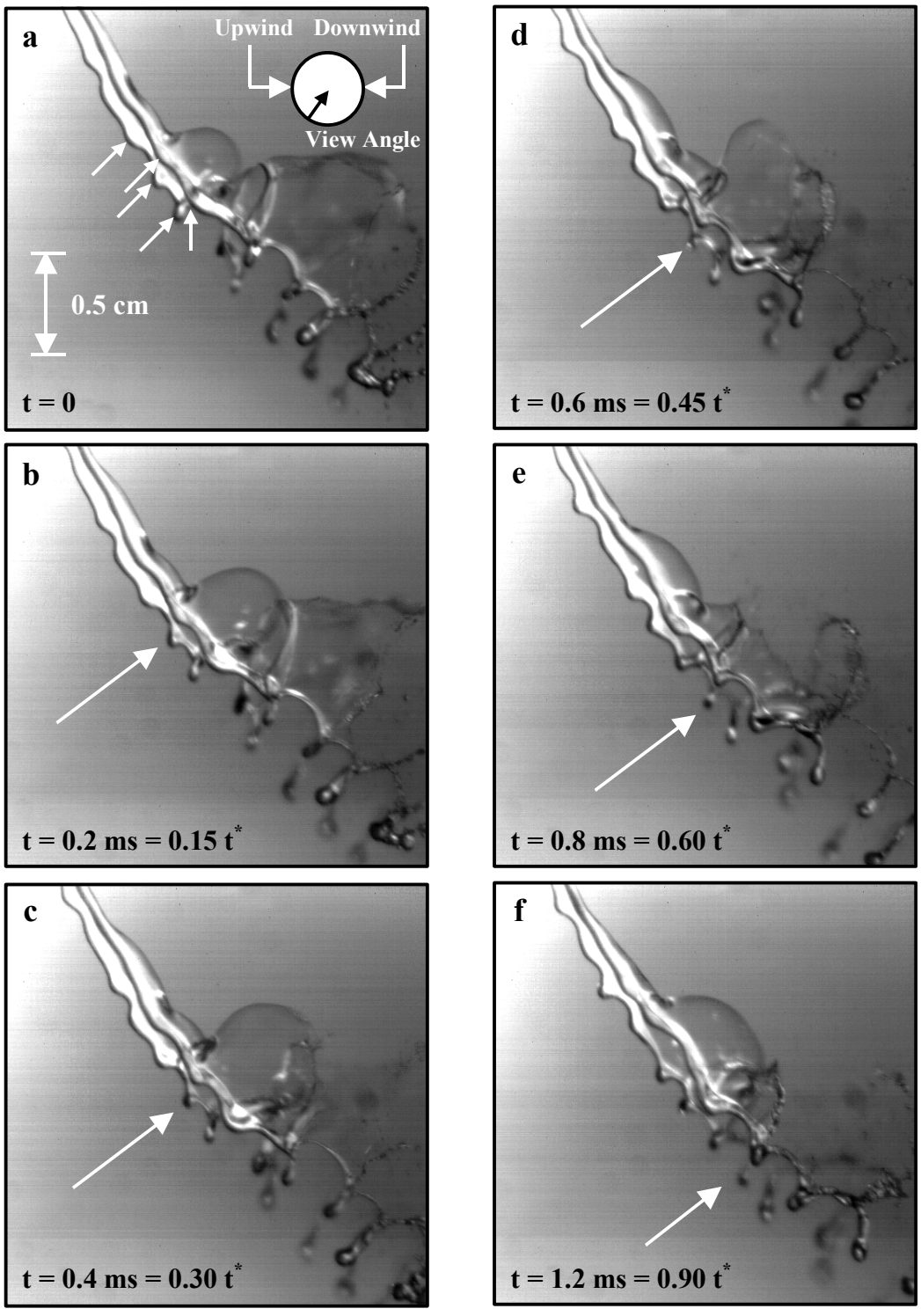

Figure 4.13 (a) – (f) Typical 5-node bag breakup of a round nonturbulent liquid jet in uniform gaseous crossflow (test conditions: Water, d_j = 1 mm, We_G = 8, and q = 65).

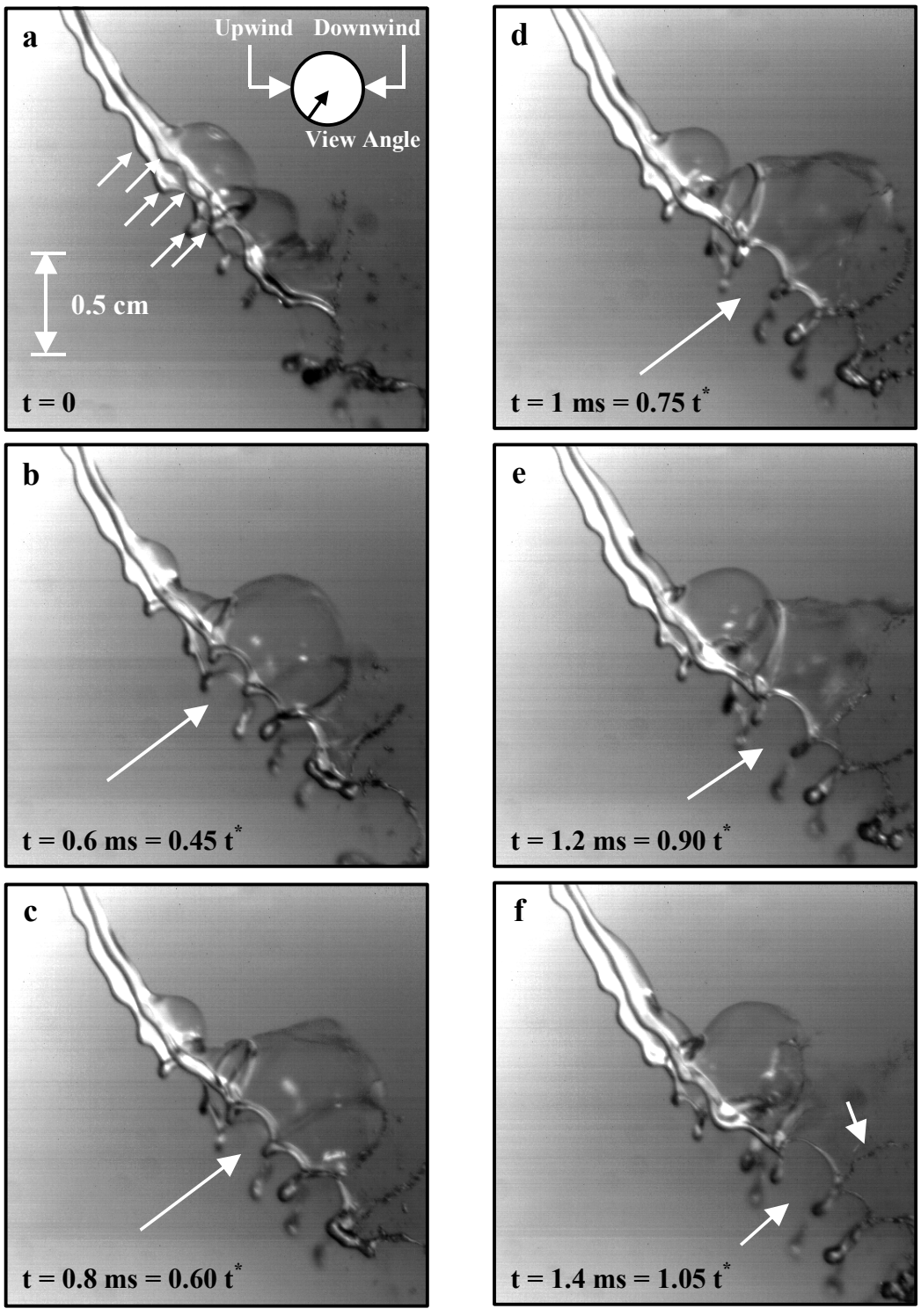

Figure 4.14 (a) – (f) Typical 6-node bag breakup of a round nonturbulent liquid jet in uniform gaseous crossflow (test conditions: Water, d_j = 1 mm, We_G = 8, and q = 65).

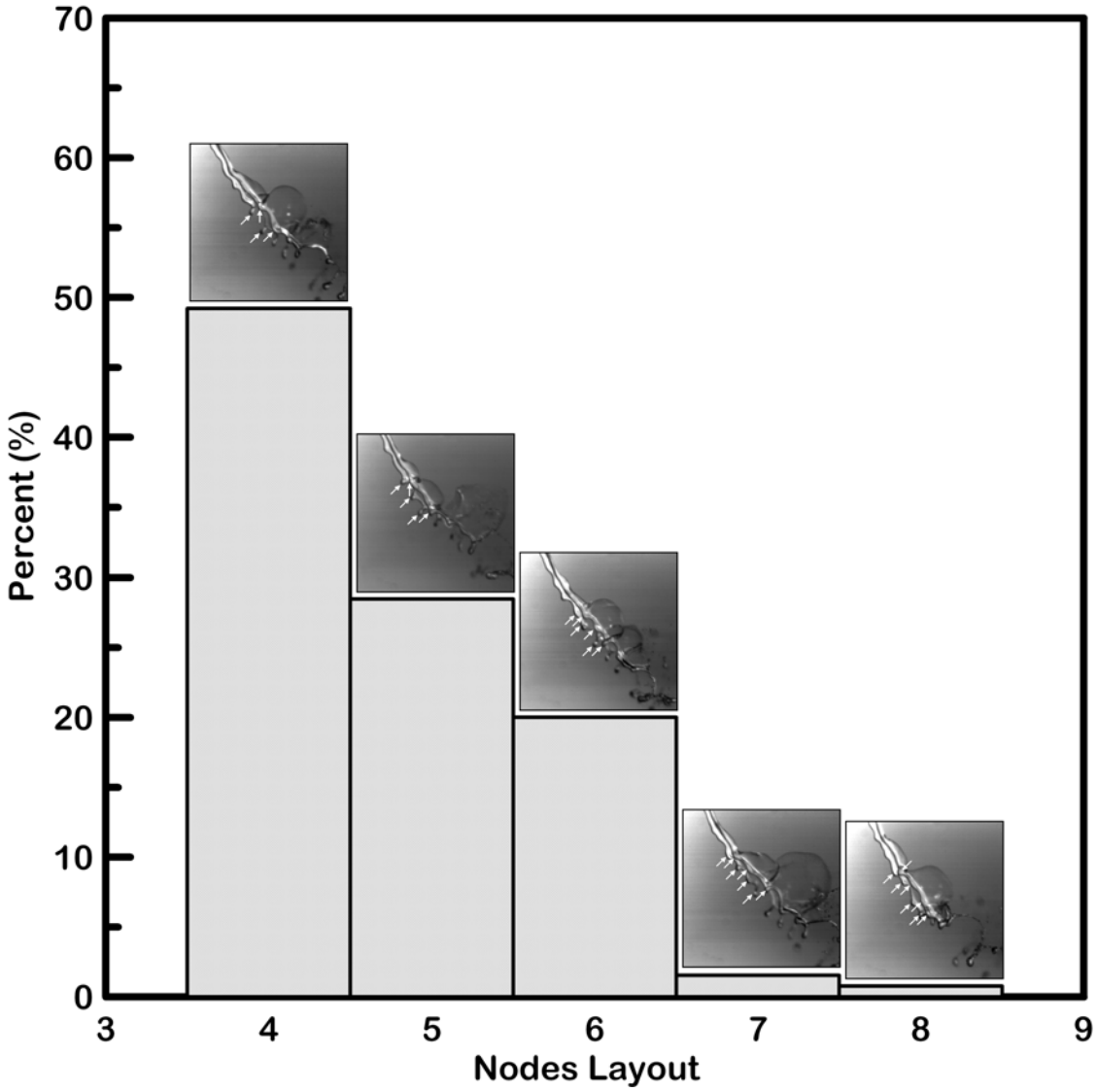

Figure 4.15 Nodes layout occurrences of round nonturbulent liquid jets in uniform gaseous crossflow (test conditions: Water, d_j = 1 mm, We_G = 8, and q = 65).

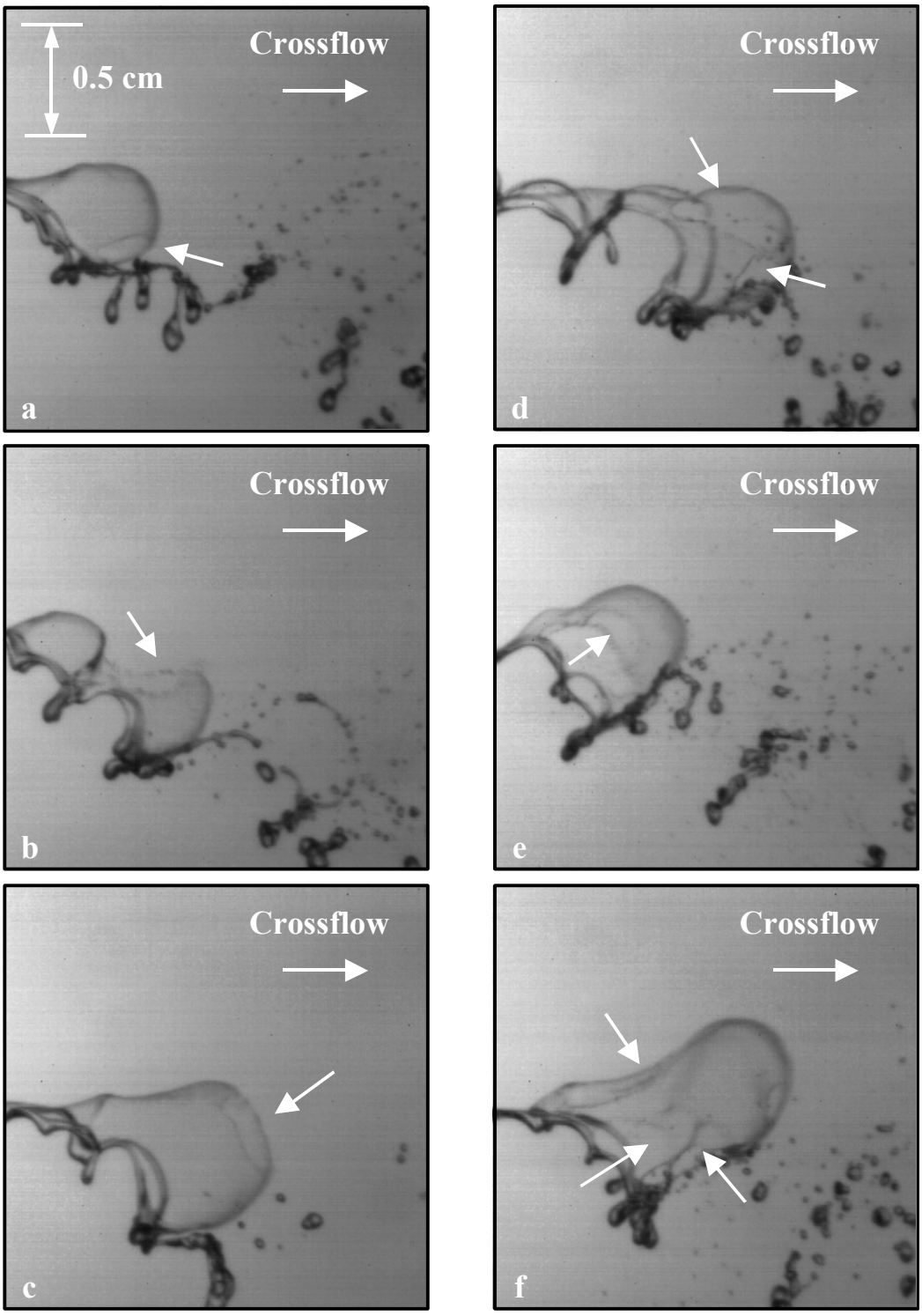

Figure 4.16 (a) – (f) The breakup of the bag-membrane of a round nonturbulent liquid jet in uniform gaseous crossflow (test conditions: Water, d_j = 1 mm, We_G = 8, and q = 32).

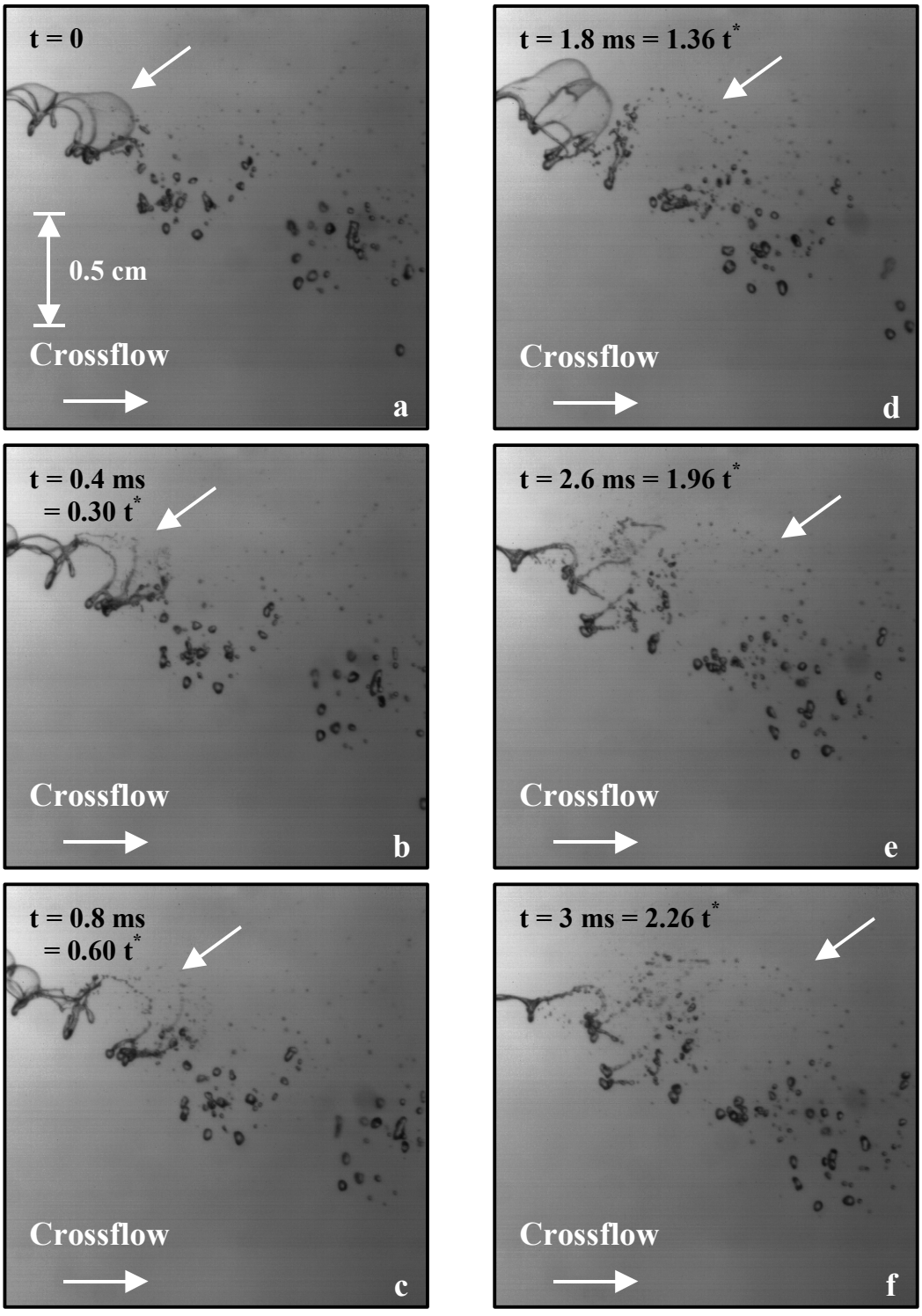

Figure 4.17 (a) – (f) Ring breakup of a round nonturbulent liquid jet in uniform gaseous crossflow (test conditions: Water, d_j = 1 mm, We_G = 8, and q = 32).

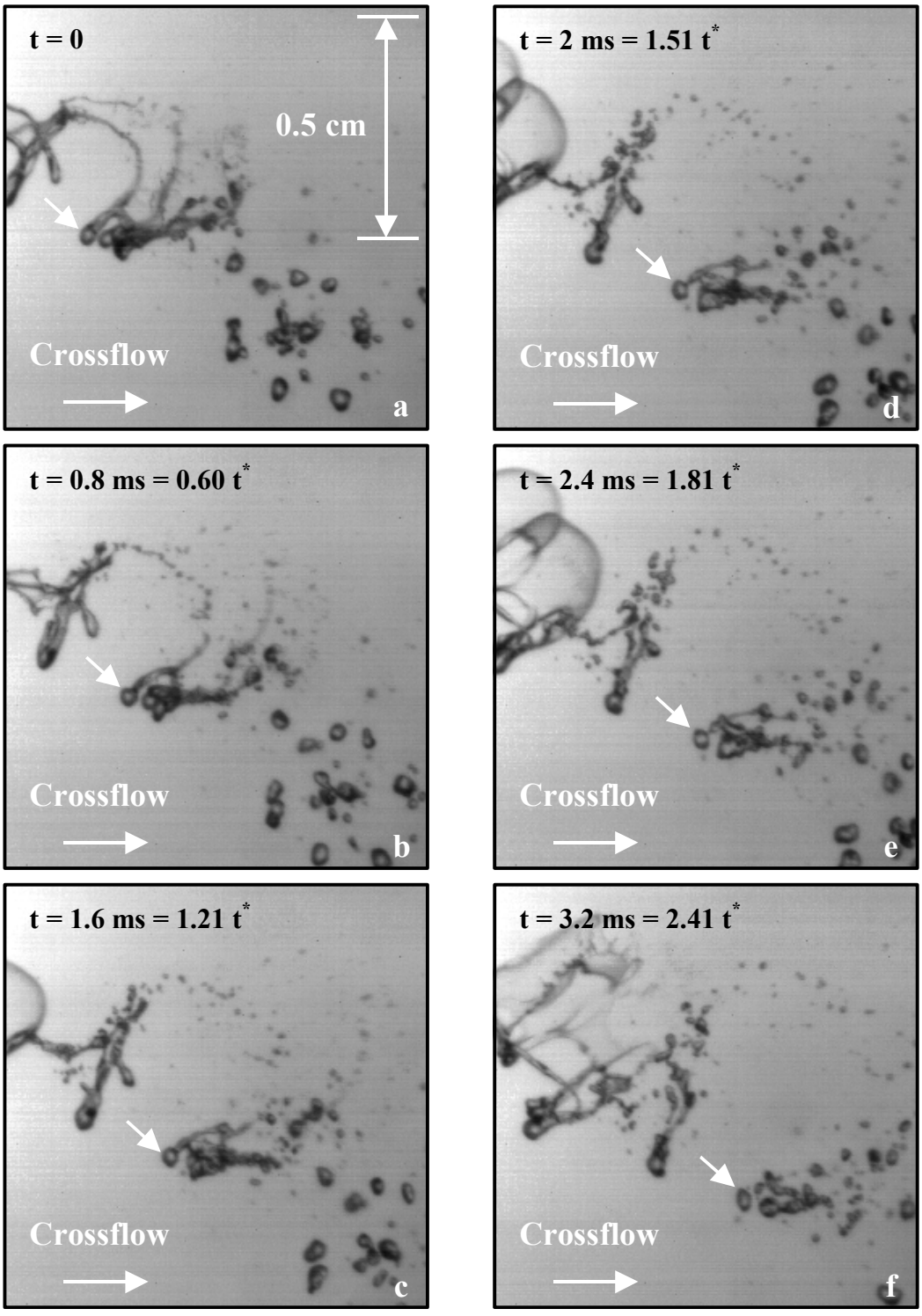

Figure 4.18 (a) – (f) The detachment of node-droplet of a round nonturbulent liquid jet in uniform gaseous crossflow (test conditions: Water, d_j = 1 mm, We_G = 8, and q = 32).

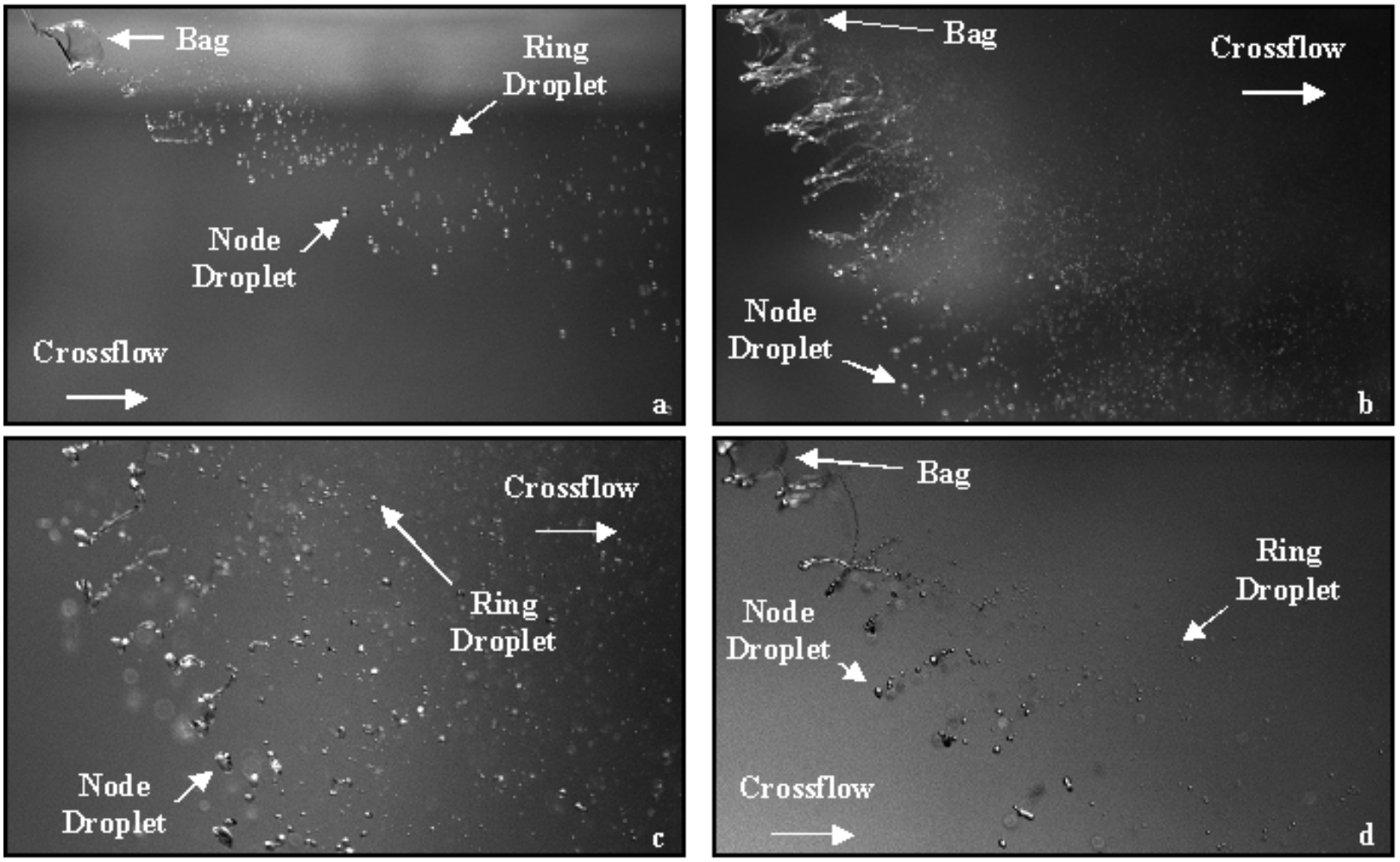

Figure 4.19 Node- and ring-droplet produced by the ring breakup of the bag-like structure. Test conditions: (a) Water, d_j = 0.5 mm, We = 4, and q = 9, (b) Ethyl Alcohol, d_j = 1 mm, We = 8, and q = 88, (c) Ethyl Alcohol, d_j = 1 mm, We = 10, and q = 224, and (d) Water, d_j = 1 mm, We = 16, and q = 302.

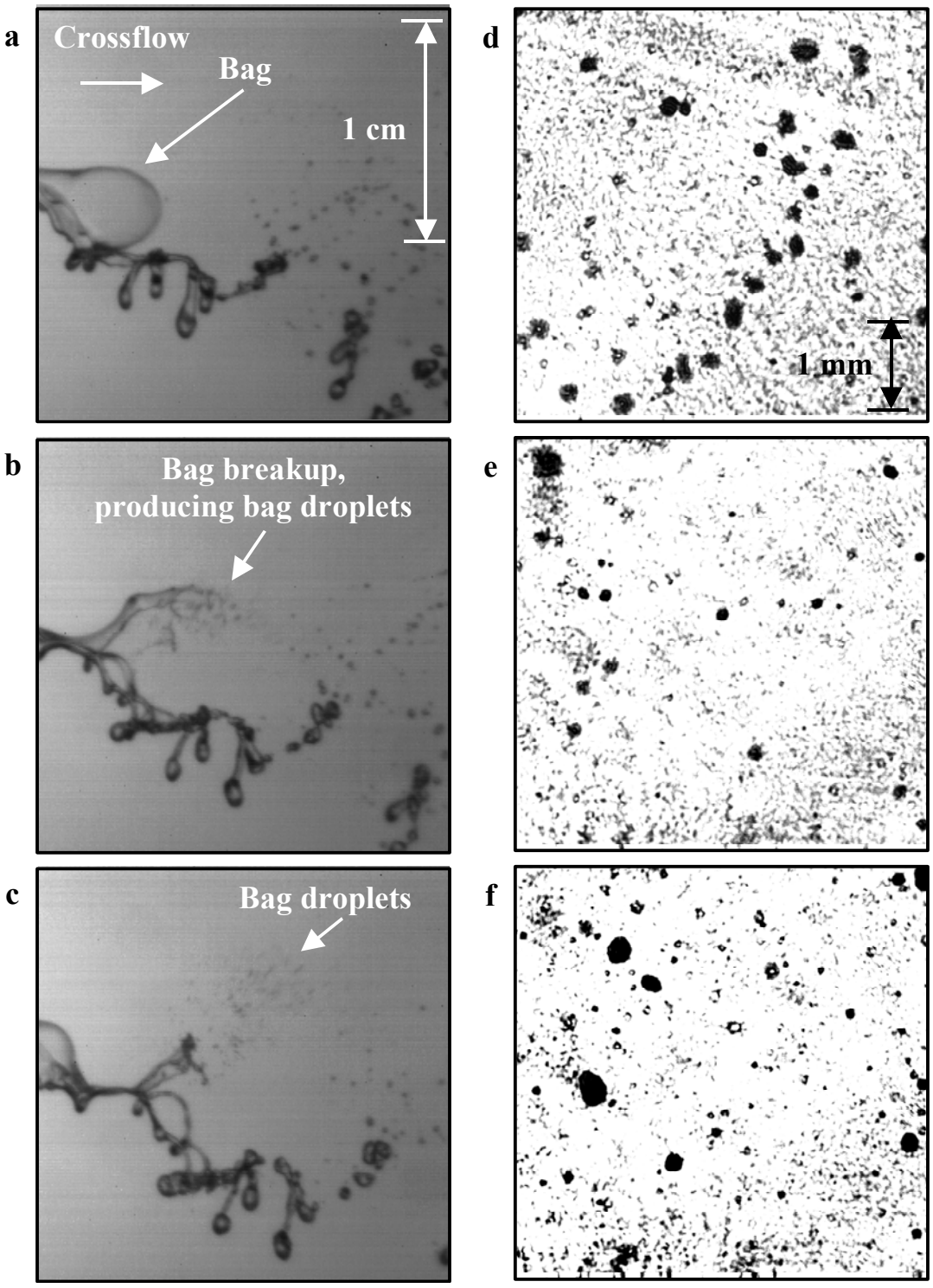

Figure 4.20 (a) – (c) Formation of the bag-droplet due to the breakup of the bag-membrane (test conditions: Water, d_j = 1 mm, We_G = 8, and q = 32). (d) – (f) Sample pulsed shadowgraph images employed for the SMD bag-droplet measurements (test conditions: (d) Water, d_j = 1 mm, We_G = 10, and q = 70, (e) Water, d_j = 1 mm, We_G = 20, and q = 38, and (f) Water, d_j = 1 mm, We_G = 30, and q = 38).

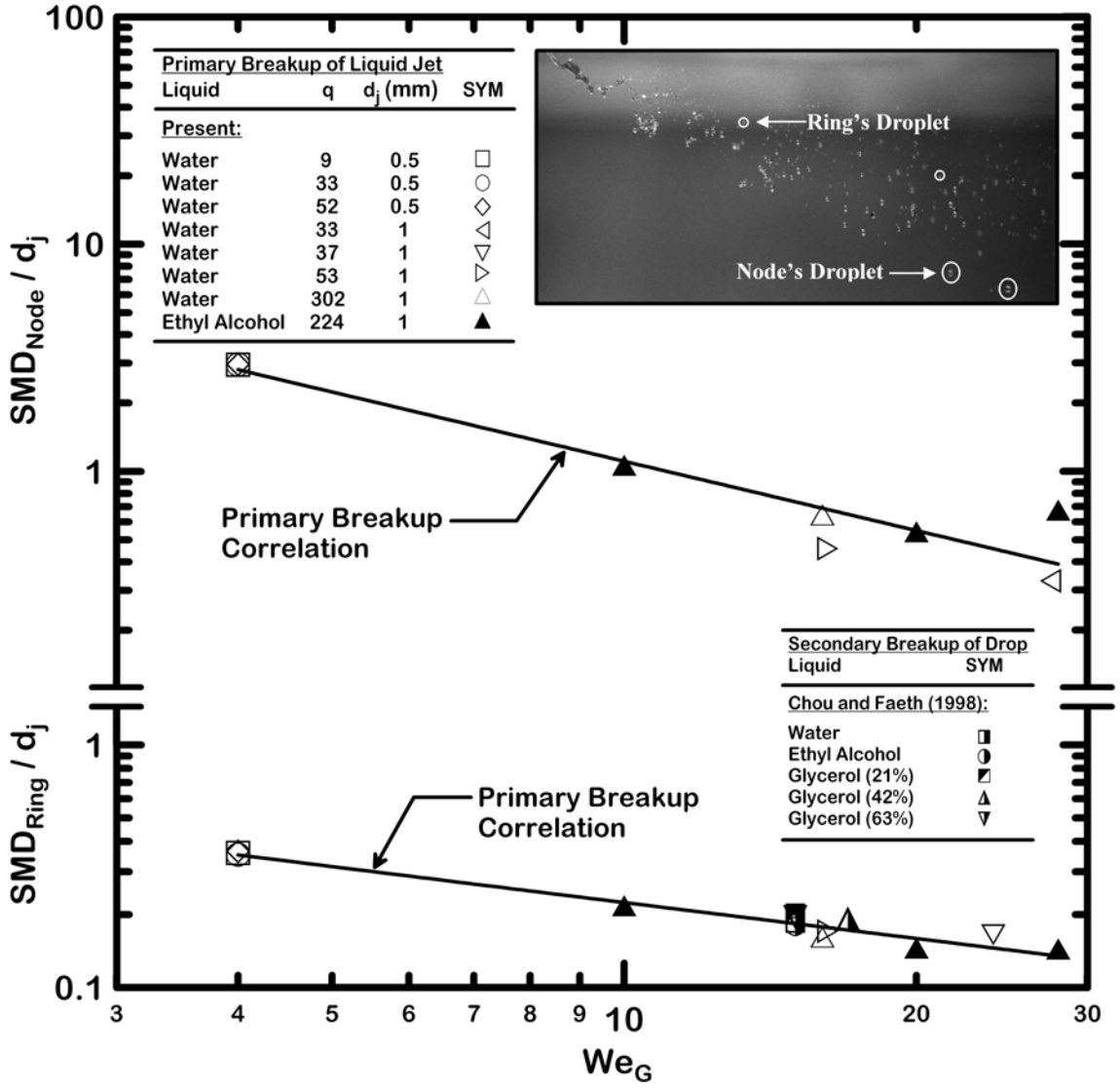

Figure 4.21 The sizes of liquid droplets due to node and ring breakup of round nonturbulent liquid jets in uniform gaseous crossflow.

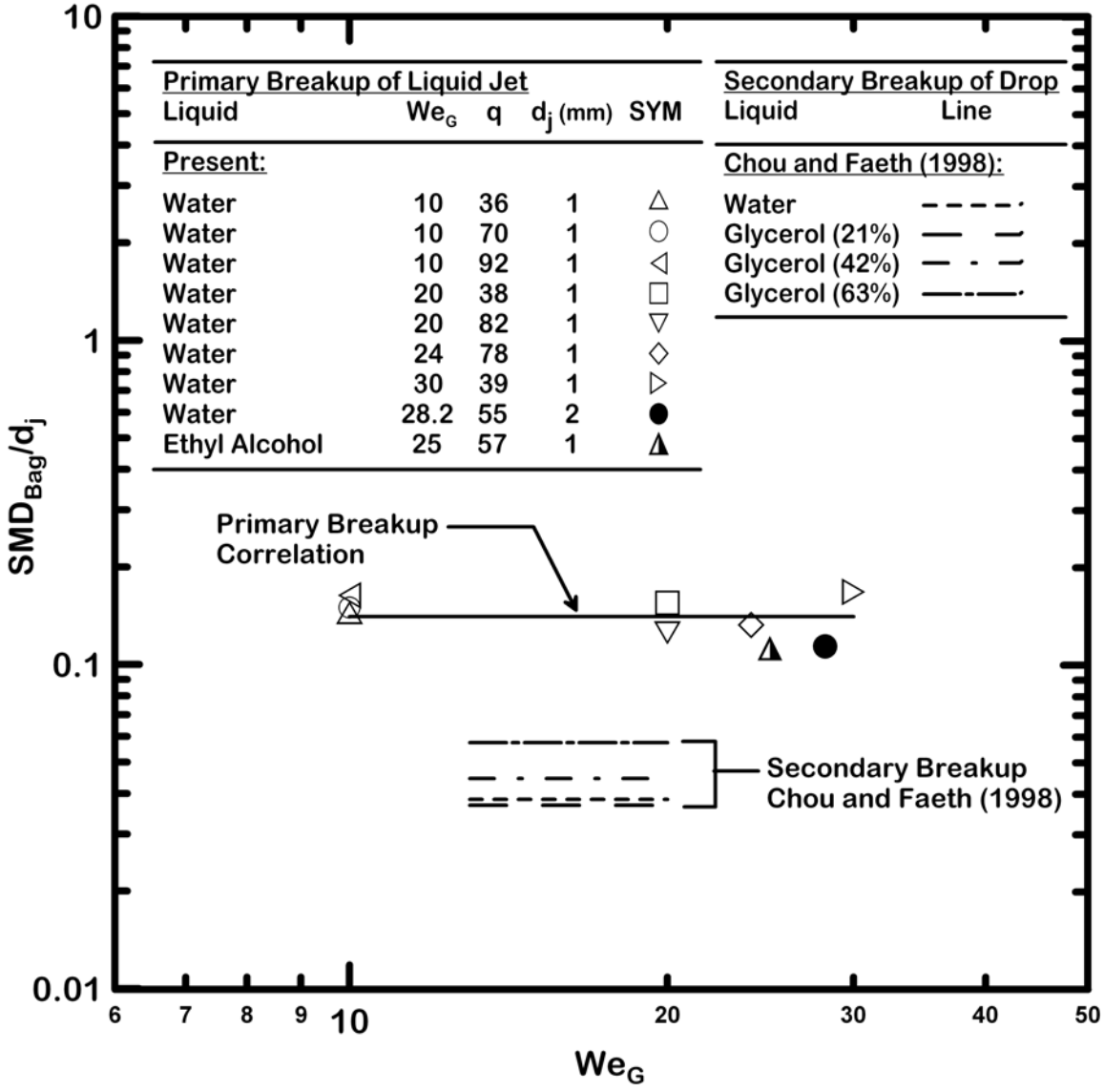

Figure 4.22 The size of liquid droplets due to the breakup of the bag-membrane of round nonturbulent liquid jets in uniform gaseous crossflow.

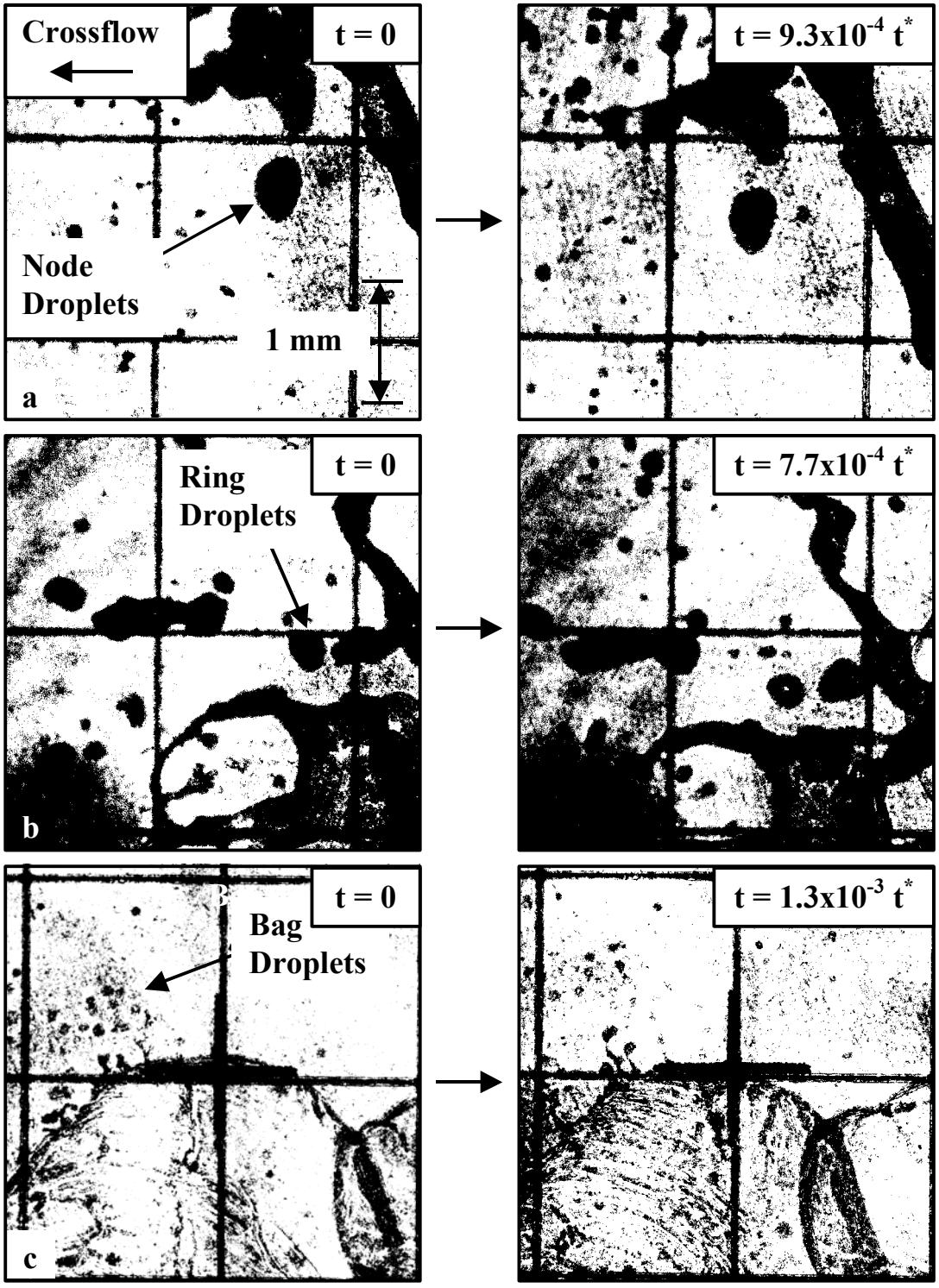

Figure 4.23 Typical double-pulsed shadowgraphs employed to measure the velocities of the liquid droplets: (a) Node-droplets, water, d_j = 1 mm, We_G = 16, and q = 53, (b) Ring-droplets, water, d_j = 1 mm, We_G = 24, and q = 37, and (c) Bag-droplets, water, d_j = 1 mm, We_G = 8, and q = 90. The grid shown is associated with the screen on which the images were projected and were used to make sure the images are aligned with the crossflow direction.

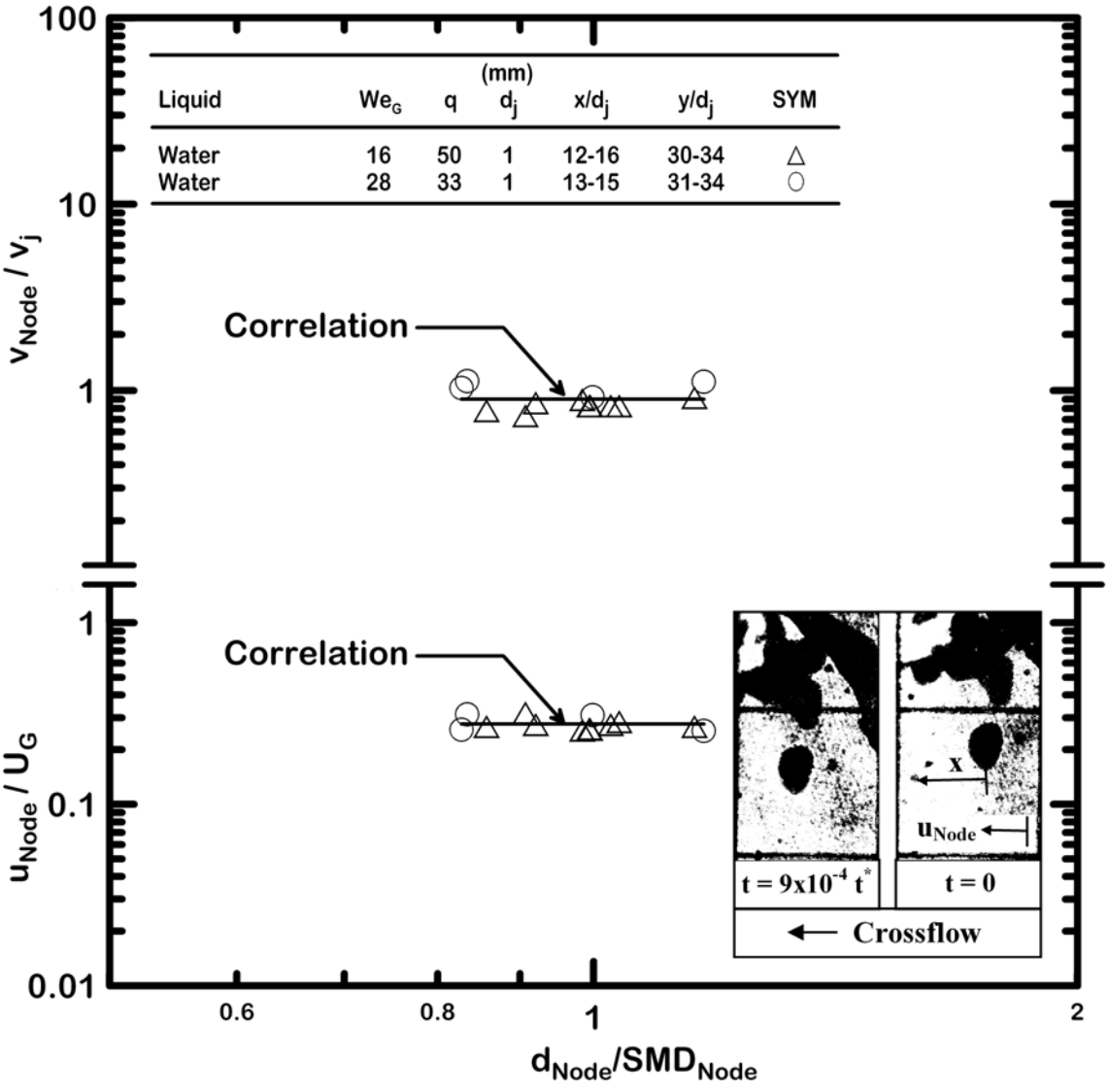

Figure 4.24 The streamwise and cross-stream velocities of the node-droplet as a function of node-droplet size.

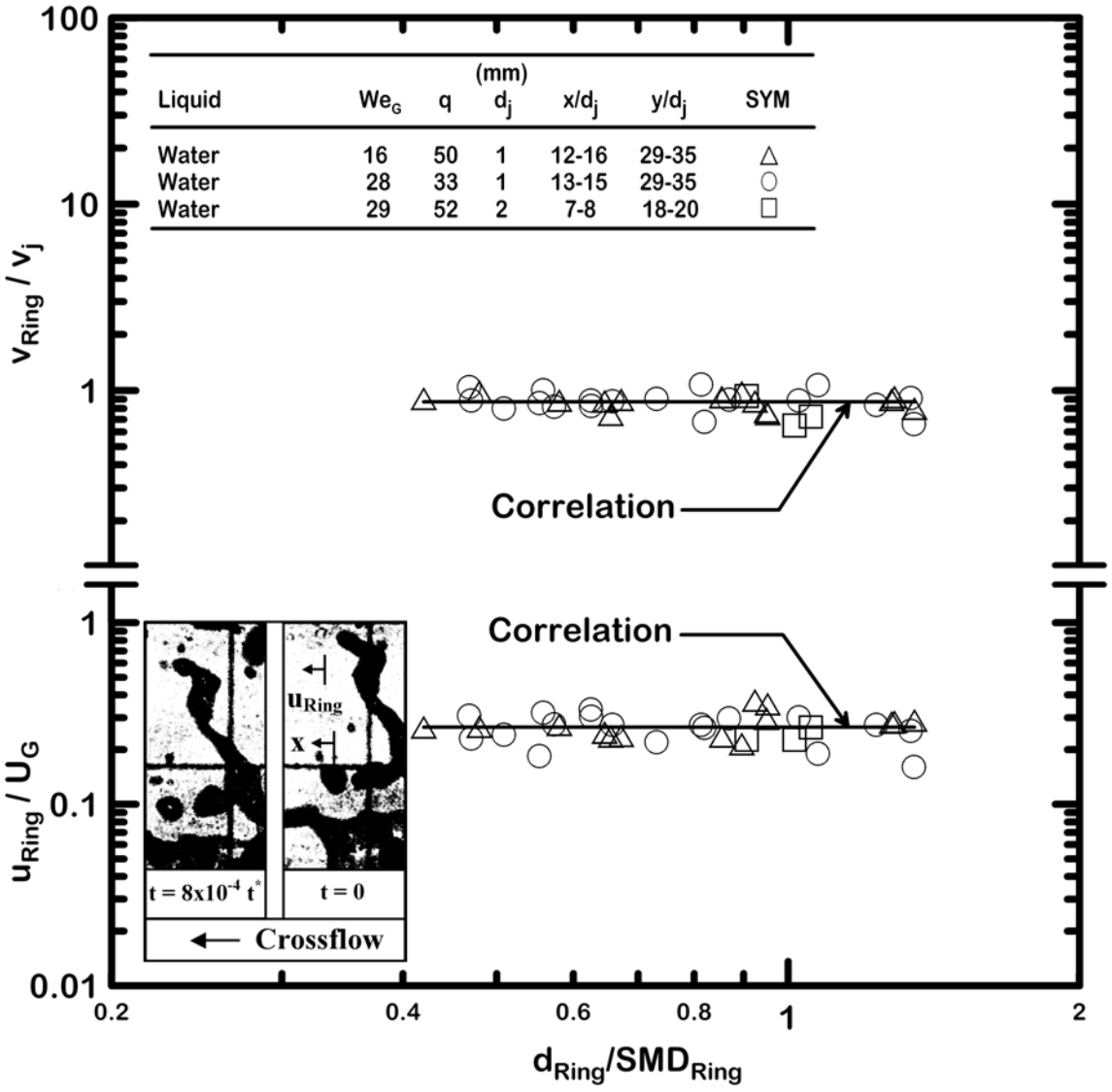

Figure 4.25 The streamwise and cross-stream velocities of the ring-droplet as a function of ring-droplet size.

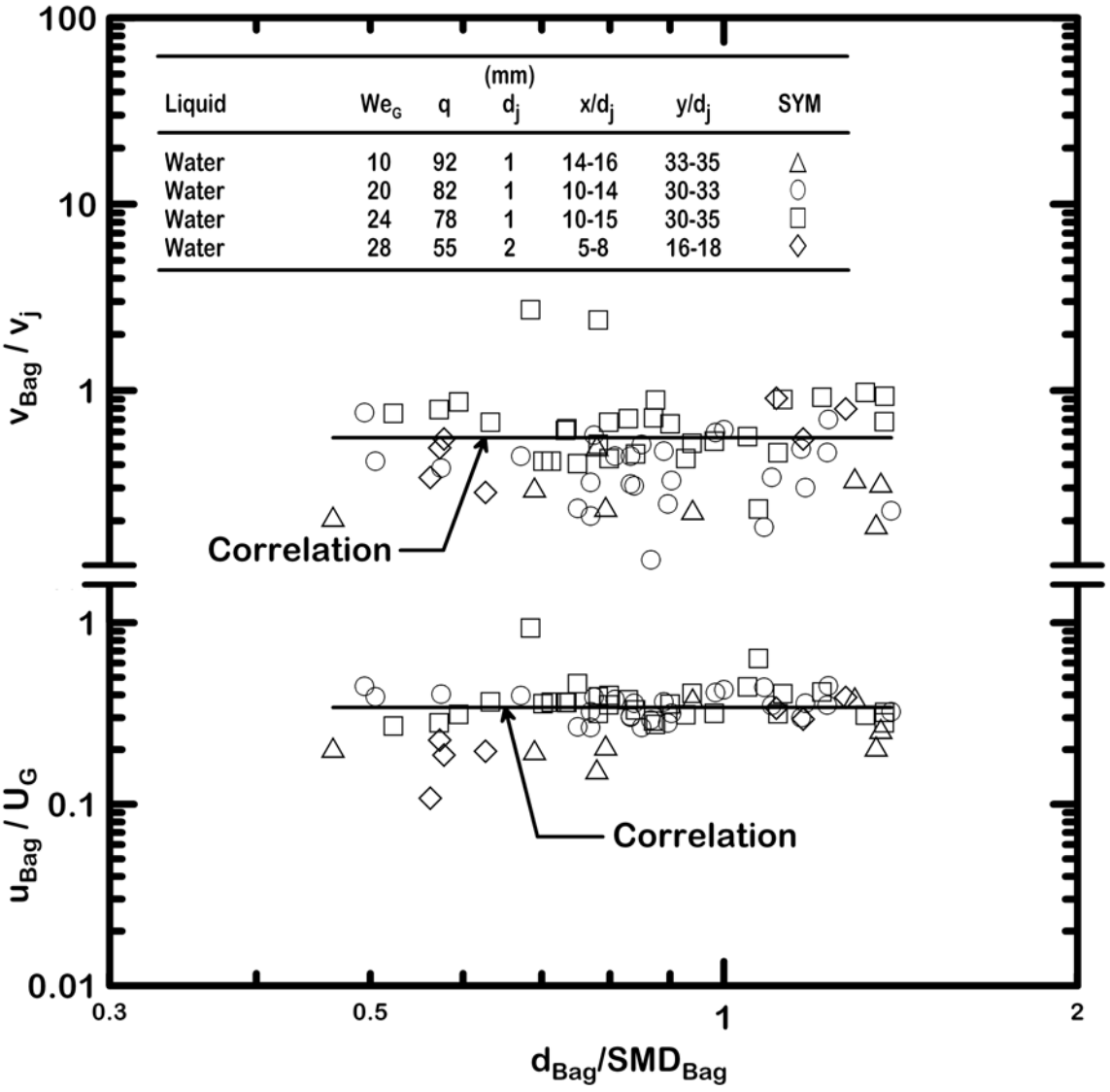

Figure 4.26 The streamwise and cross-stream velocities of the bag-droplet as a function of bag-droplet size.

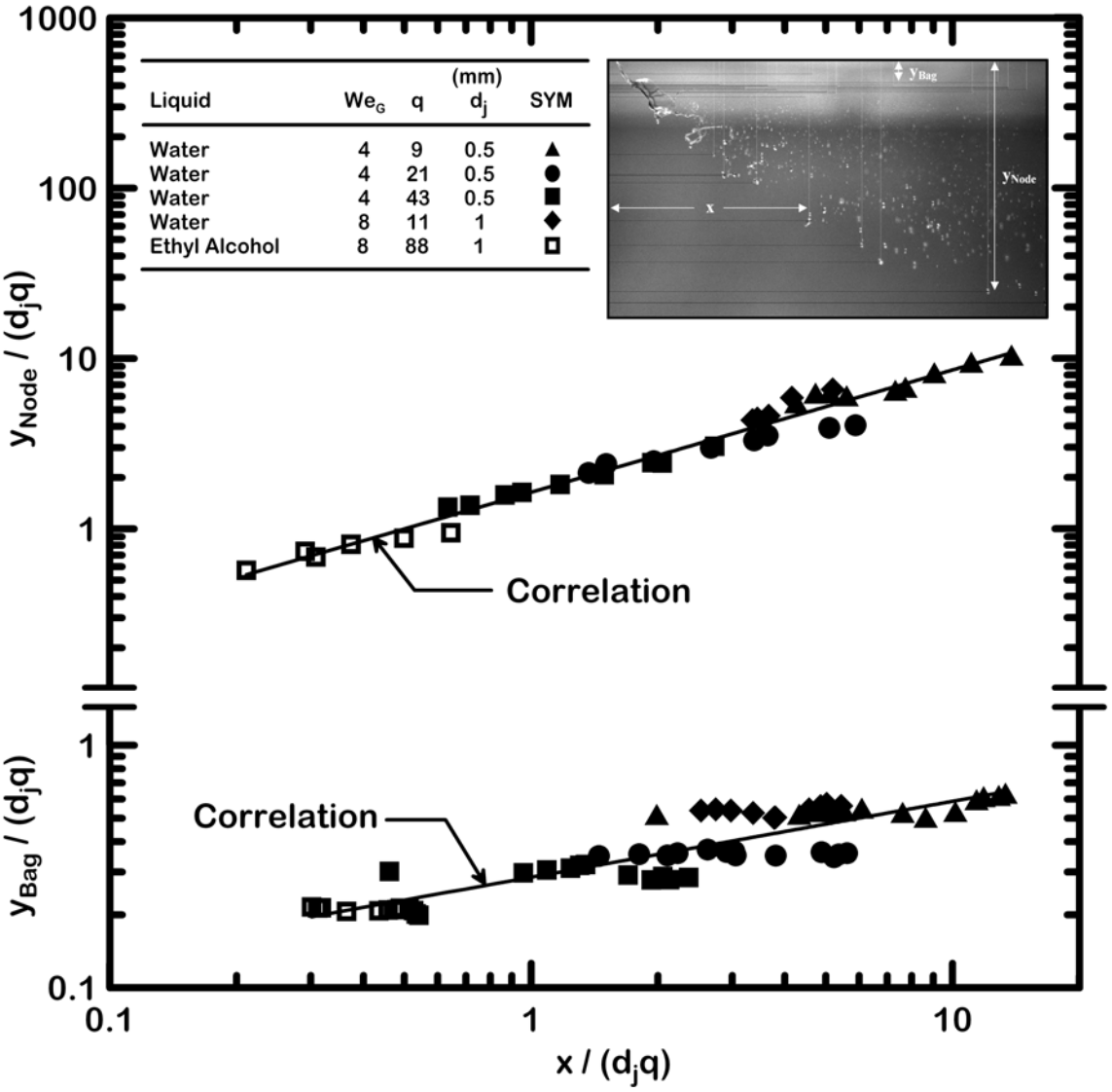

Figure 4.27 The trajectories of node-droplet and bag-droplet.

CHAPTER V

COMPUTATIONAL RESULTS

5.1 Overview

This chapter presents results and discussion related to the computational modeling of the deformation and onset of breakup conditions of round nonturbulent liquid jets in uniform gaseous crossflow within column, bag, and shear breakup regimes. The liquid jet cross-stream deformation, liquid jet span-wise deformation, liquid jet cross-sectional area, liquid jet velocities, wavelengths of column and surface waves, wake velocity defects behind the liquid jet, and wake width behind the liquid jet are calculated and discussed.

5.2 Computational Evaluation

The flow visualization of a typical round nonturbulent liquid jet in quiescent air is shown in Fig. 5.1. The ethyl alcohol jet computed herein has a jet diameter of 0.5 mm, a mean nozzle exit velocity of 7.6 m/s, and a jet Reynolds number (Re_L) of 2510. The velocity vectors are colored by the volume fraction (α) of multiphase mixture such that 1 represents 100% ethyl alcohol and 0% air and 0 denotes 0% ethyl alcohol and 100% air. The length of the velocity vector represents the velocity magnitude. The instantaneous change of colors from red inside the jet ($\alpha = 1$) to blue outside the jet ($\alpha = 0$) in the vicinity of the liquid-gas interface suggests that the numerical diffusion of the volume

fraction is negligible. This result is also confirmed with the surface tension test presented in section 3.6. In the absence of crossflow, the liquid column exhibits a smooth liquid surface with no initialization of atomization. This behavior is similar to the experimental observation of round supercavitating injector presented in section 4.2. The external flowfield shows that air is being entrained along the liquid-gas interface. A top hat velocity profile is observed in the internal flowfield within the liquid column. In the presence of crossflow, the nonturbulent liquid jet will experience different modes of breakup depending on the crossflow Weber number.

5.3 Flow Visualization

This section presents flow visualization within column breakup, bag breakup, and shear breakup regimes. The computations were carried out at small Ohnesorge numbers ($Oh < 0.1$).

5.3.1 Column Breakup Regime

The flow visualization of a typical liquid jet in uniform gaseous crossflow within the column breakup regime is shown in Fig. 5.2. The liquid jet presented in the column breakup regime has a nozzle exit diameter of 0.5 mm, crossflow Weber number of 3.5, crossflow Reynolds number of 388, liquid/gas density ratio of 645, and a liquid jet momentum ratio of 274. First, the liquid column deforms from a circular cross-section into an ellipsoidal cross-section normal to the direction of the crossflow. The lateral motion is eventually stabilized by the surface tension forces. Then, the increased drag forces due to the ellipsoidal cross-section enhance the tendency of the liquid column to

deflect downstream with respect to the gas motion. Disturbances are observed to convect along the liquid column, characterized by a wavelength, λ_c.

The temporal movement of the column waves along the liquid column of a typical liquid jet in uniform gaseous crossflow within the column breakup regime is shown in Fig. 5.3. The crossflow is from left to right, the left-most three-dimensional liquid jet is at $t = t_0$, and with an increment of $0.037t^*$ (i.e., $t = t_0+037t^*$, $t_0+0.074t^*$, …, $t_0+0.295t^*$), as the figures progress from left to right. The t^* is the aerodynamic characteristic time (Ranger and Nicholls, 1969). The liquid cross-stream and span-wise deformations are affected by the column waves that convect along the liquid column. This suggests that the surface properties are three-dimensional. In the presence of the varicose wave, the thickened region of the liquid column will have a lower pressure in comparison to the thinner region of the liquid column. This causes the liquid to move from the thinner region (higher pressure) to the thickened region (lower pressure), resulting in a Rayleigh-like breakup of the thin liquid column region.

A comparison of liquid jet cross-sections as a function of normalized streamwise ($y/(v_jt^*)$) for the two-dimensional (Aalburg et al., 2005) and the present three-dimensional computational model of a typical liquid jet in uniform gaseous crossflow within column breakup regime is shown in Fig. 5.4. The crossflow is from right to left, the right-most liquid cross-section is at $y/(v_jt^*) = 0.12$, and with an increment of 0.12 (i.e., $y/(v_jt^*) = 0.12, 0.24, \ldots, 0.60$), as the interfaces progress from right to left. The black circles represent the liquid jet at the nozzle exit. The color code for the liquid jet cross-sections is also shown in Fig. 5.4. The liquid cross-section computed by the two-dimensional model resembles that of the three-dimensional model. It can be observed that the cross-

section in the two-dimensional model translates in the cross-stream direction more than the three-dimensional model. This is because the cross-section of the two-dimensional model is allowed to move in the direction of the crossflow until it is traveling at the same velocity as the crossflow whereas the liquid jet in the three-dimensional model is anchored to the nozzle exit. Both models show that the liquid column deforms from a circular shape into an ellipsoidal cross-section as $y/(v_j t^*)$ increases, and that the cross-sections of the jet progressively begin to translate in the cross-stream direction as a result of the drag that is exerted by the gaseous crossflow.

In the two-dimensional model, the temporal time, t, is converted to streamwise distance (y) using y/v_j under the assumption that v_j is constant. In the absence of the third dimension, the two-dimensional slices of the jet cannot experience the streamwise interactions of the different cross-sections as a physical jet would typically do. Furthermore, the two-dimensional model could not account for the air entrainment along the upwind surface of the liquid column, particularly when the liquid column deformed into an ellipsoidal-shaped cross-section as shown in the external flowfield presented next. Therefore, computational model employing two-dimensional slices of jet is known to introduce simulation inaccuracies. Similar to a physical jet, one end of the three-dimensional liquid column is 'anchored' to the nozzle exit and the entire liquid column is free to deflect.

The internal flowfield of the liquid jet is a result of pressure and shear forces of the crossflow. The velocity vectors inside the jet cross-sections are shown in Fig. 5.5 for the same test conditions of Fig. 5.4. The crossflow is from right to left and the jet cross-sections are shown at various $y/(v_j t^*)$ which progress from the upper-left figure ($y/(v_j t^*)$ =

0.06) to the lower-left figure ($y/(v_j t^*) = 0.24$), and continue from the upper-right figure ($y/(v_j t^*) = 0.36$) to the lower-right figure ($y/(v_j t^*) = 0.54$). The green line represents the jet surface. The velocity vectors are computed relative to the motion of the center of the jet cross-section. The magnitudes are normalized by the characteristic liquid velocity due to Sallam et al. (2004) ($u_L = U_G/[1+(\mu_L\rho_L/\mu_G\rho_G)^{0.5}]$) and the color codes represent the velocity component in x-direction (direction of the crossflow) normalized by the characteristic liquid velocity. For clarity, only 1/6 of the total number of vectors is displayed. When the liquid cross-section is circular in shape (i.e., $y/(v_j t^*) = 0.12$), the normalized velocity magnitude in the xz-plane (within the cross-section) is largest along the liquid-gas interface stretching from the upwind stagnation point down to the two sides of the liquid jet. As $y/(v_j t^*)$ increases, the liquid is observed to flow from the upwind and downwind directions towards the two sides of the liquid jet. The internal flow is symmetric about the jet axis connecting the two stagnation points on the upwind and downwind surfaces of the cross-section. Counter-rotating vortex pair (Leong et al., 2000) is not observed within the liquid jet cross-section for a streamwise distance (y) of up to $0.5y_i$ (y_i is the location of the onset of breakup).

The *upwind* and *downwind* isometric views of the external flowfield of a round nonturbulent liquid jet in uniform gaseous crossflow within the column breakup regime (We_G=3.5) are shown in Fig. 5.6 and Fig. 5.7 using geometric pathline seeding feature of FLUENT. The conditions are identical to those shown in Figs. 5.4 and Fig. 5.5. The surface of the liquid jet is colored by the pressure coefficient (C_p) and the particle seeding is colored by the velocity magnitude ($|v|$) normalized by the crossflow velocity (U_G). Near the nozzle exit (i.e., $y/(v_j t^*) = 0.06$), the air being accelerated along the side of the

liquid column forms trailing vortices behind the liquid jet, which is similar to the flow around a solid cylinder. The presence of the trailing vortices can be visualized by observing the pathlines of the particle seeding being kept apart behind the liquid jet. The external flowfield shows that jet deformation is caused by accelerating gas along the side of the liquid column, resulting in the reduction of gas pressure along the sides. This causes the liquid within the cross-section to move in the span-wise direction towards the sides of the liquid column until it is eventually stabilized by the surface tension forces, as observed in the internal flowfield. As $y/(v_j t^*)$ increases, the stagnating gas on the upwind side progressively flattens the upwind surface of the liquid column. As a result, the liquid column deforms from a circular cross-section into an ellipsoidal cross-section. The increase in the liquid span-wise diameter (d_c) enhances the tendency of the air entrainment in the upwind direction of the liquid column, resulting in a three-dimensional flowfield that cannot be physically resolved by the two-dimensional model. Very near the nozzle exit (i.e., $y/(v_j t^*) = 0.03$), the pressure coefficient profile of the liquid column resembles the pressure coefficient profile of flow around a solid cylinder. For instance, the pressure coefficient is positive in the upwind direction of the liquid column, decreases towards zero, and becomes negative along the side of the liquid column. As $y/(v_j t^*)$ increases, the pressure coefficient progressively decreases along the sides of the liquid column. Near the stagnation values ($C_p \approx 1$), the stagnation point progressively spread out along the upwind surface of the liquid column. The low pressure along the sides of the jet further drops to increasingly smaller C_p values. The variation of pressure coefficient behind the liquid column is small.

In FLUENT, iso-vorticity surface can be created from the magnitude of the vorticity vector, which is defined as the curl of the velocity vector, $\xi = \nabla \times \vec{V}$. The vorticity magnitude is normalized by the strain rate ($\dot{\gamma} = (0.5\overline{\overline{D}} : \overline{\overline{D}})^{1/2}$), where ($\overline{\overline{D}} = \partial u_j / \partial x_i + \partial u_i / \partial x_j$). The non-dimensional iso-vorticity surfaces of the wake region of a round nonturbulent liquid jet in uniform gaseous crossflow within the column breakup regime are shown in Fig. 5.8. The iso-surfaces are colored by the vorticity magnitude normalized by the strain rate. The magnitude ranges from one to two so that the iso-vorticity surfaces of the wake behind the liquid column can be clearly visualized. For comparison purposes, the same scale will also be applied to both the bag and shear breakup regimes in the next two sections. The direction of the crossflow and the dimension of the liquid jet are shown in the upper left-figure and the liquid cross-sections are shown at various $y/(v_j t^*)$ which progress from the upper-left figure ($y/(v_j t^*) = 0.06$) to the lower-left figure ($y/(v_j t^*) = 0.24$), and continue from the upper-right figure ($y/(v_j t^*) = 0.36$) to the lower-right figure ($y/(v_j t^*) = 0.54$). Behind the liquid column, the wake consists of alternating pairs of vortices, similar to Karman vortex streets. Despite the crossflow velocity at the inlet being uniform, the flow behind the liquid jet is unsteady three-dimensional, typical of wake flows indicating the need for a three-dimensional model.

5.3.2 Bag Breakup Regime

The flow visualization of a typical liquid jet in uniform gaseous crossflow within the bag breakup regime is shown in Fig. 5.9. The liquid jet presented in the bag breakup regime has a nozzle exit diameter of 0.5 mm, crossflow Weber number of 8, crossflow

Reynolds number of 586, liquid/gas density ratio of 645, and a liquid jet momentum ratio of 120. The deformation of a liquid column in the bag breakup regime is visually similar to the deformation of a liquid column in the column breakup regime. The liquid jet first deforms from a circular cross-section into an ellipsoidal cross-section normal to the direction of the crossflow. The lateral motion is eventually stabilized by the surface tension forces. Then, the increased drag forces due to the ellipsoidal cross-section enhance the tendency of the liquid column to deflect downstream with respect to the gas motion. A remarkable feature of bag breakup is the appearance of both the column waves and the downwind surface waves along the liquid column, characterized by a wavelength, λ_c and λ_s, respectively.

The temporal movement of the column waves along the liquid column of full configuration and half configuration liquid jets in uniform gaseous crossflow within the bag breakup regime are shown in Fig. 5.10 and Fig. 5.11, respectively. The crossflow is from left to right, the left-most three-dimensional liquid jet is at $t = t_0$, and with an increment of $0.056t^*$, as the figures progress from left to right. The temporal movement of the column waves computed by the half configuration model resembles that of the full configuration model. Fig. 5.10 and Fig. 5.11 completed the flow visualization of liquid jet in crossflow within the bag breakup regime by providing the temporal movement of the jet surface that was not shown in Fig. 5.9. The column waves are due to the acceleration of the more-dense fluid (liquid jet) by the less-dense fluid (gaseous crossflow). The wavelengths of the column waves are attributed to the Rayleigh-Taylor instability. The temporal movement of surface waves along the downwind side of a typical liquid jet in uniform gaseous crossflow within the bag breakup regime is shown in

Fig. 5.12. The direction of the crossflow is out of the paper. These computational results of the development of downwind surface waves along the liquid column was confirmed by the experimental results reported in section 4.4. The downwind surface waves occur in the vicinity of the sides of the liquid column, suggesting that the behaviors are associated with aerodynamic stripping, as discussed in section 4.4. In the presence of the column waves and/or downwind surface waves, the liquid cross-stream and span-wise deformations are affected by the waves that convect along the liquid column. Thus, three-dimensional surface properties are expected within the bag breakup regime.

A comparison of liquid jet cross-sections as a function of normalized streamwise distance ($y/(v_j t^*)$) for the two-dimensional (Aalburg et al., 2005) and the present three-dimensional computational model is shown in Fig. 5.13 along with the present experimental measurements of the cross-stream deflection of the center of the jet within bag breakup regime. The crossflow is from right to left, the right-most liquid cross-section is at $y/(v_j t^*) = 0.18$, and with an increment of 0.18, as the interfaces progress from right to left. The black circles represent the liquid jet at the nozzle exit. The color code for the liquid jet cross-sections is shown in Fig. 5.13. At $y/(v_j t^*) = 0.18$, the liquid cross-section computed by the two-dimensional model is similar to the liquid cross-section computed by the three-dimensional model. At the next streamwise location, $y/(v_j t^*) = 0.36$, the cross-section computed by the two-dimensional model is observed to have translated more in the cross-stream direction than the three-dimensional model, owing to the fact that the two-dimensional slices of the jet cannot be anchored to the jet exit. Note that the cross-section predicted by the two-dimensional model at $y/(v_j t^*) = 0.36$ resembles the cross-section predicted by the three-dimensional model at $y/(v_j t^*) = 0.54$. The cross-

stream translation of the jet center computed by both the two-dimensional and the three-dimensional model agrees well with experiment visualization shown in Fig. 5.13(c). In general, the liquid column deformed from a circular cross-section into a triangular cross-section before turning into an ellipsoidal cross-section, and as $y/(v_j t^*)$ progresses, the jet translates in the cross-stream direction. According to the experimental observation in chapter four, beyond the onset of breakup, bag-like structures is expected to appear as a result of the deformation of the central portion of the liquid column caused by the high pressure produced by the stagnating gas flow on the upwind side of the flattened liquid column. The onset of breakup occurs when the liquid jet has attained a cross-stream diameter of about one half the initial jet diameter, as observed in the experiments by Mazallon et al. (1999) and Sallam et al. (2004) and the present computational predictions (Fig. 5.28).

Cross-sections of the liquid jet along with velocity vectors of the liquid phase relative to the motion of the jet center and normalized by the average liquid velocity (u_L) are shown in Fig. 5.14 for various normalized streamwise distances ($y/(v_j t^*)$) at conditions identical to those illustrated in Fig. 5.13. The crossflow is from right to left, the normalized streamwise location $y/(v_j t^*)$ progresses from 0.09 to 0.82. The green line represents the liquid/gas interface. The velocity vectors are colored according to the magnitude of the velocity component in x-direction normalized by the characteristic liquid velocity, and the lengths of the vectors represent the magnitude of the velocity in the xz-plane normalized by the characteristic liquid velocity. For clarity, only 1/4 of the total number of vectors is displayed. Similar to the column breakup regime, when the liquid cross-section is circular in shape (i.e., $y/(v_j t^*) = 0.18$), the normalized xz-velocity

within the cross-section is largest near the liquid-gas interface between the upwind surface and the two sides of the liquid jet. As $y/(v_j t^*)$ increases, an internal flow forms the two stagnation points towards the two sides of the liquid jet. This is due to the lower pressure along the sides of the jet which pulls the liquid away from both the upwind and downwind surfaces. Near the onset of breakup (i.e., $y/(v_j t^*) = 0.73$ and 0.82), a counter-rotating vortex pair is observed near the two sides of the liquid cross-section.

Upwind and the *downwind* isometric views of the external flowfield are shown in Fig. 5.15 and Fig. 5.16, respectively for the same test conditions as those in Figs. 5.13 and 5.14. The surface of the liquid jet is colored by the pressure coefficient (C_p) and the particle pathlines are colored by the velocity magnitude ($|v|$) normalized by the crossflow velocity (U_G). Near the nozzle exit (i.e., $y/(v_j t^*) = 0.09$), the air accelerates along the sides of the liquid column. The acceleration of the external flowfield along the sides of the liquid column is evident by increased velocity magnitudes and reduced pressure coefficients along the sides of the liquid jet. The resulting reduction of gas pressure along the sides of the jet causes the liquid within the cross-sections of the jet to move in the span-wise direction towards the two sides until it is eventually stabilized by progressively increasing surface tension forces. As $y/(v_j t^*)$ increases, the stagnating gas on the upwind side of the cross-section progressively flattens the upwind surface of the liquid column. The increase in the liquid span-wise diameter (d_c) enhances the tendency of the air entrainment in the upwind direction of the liquid column. Very near the nozzle exit (i.e., $y/(v_j t^*) = 0.03$), the pressure coefficient profile of the liquid jet resembles the pressure coefficient profile of a flow around a cylinder. Similar to column breakup, as $y/(v_j t^*)$ increases, the pressure coefficient progressively decreases along the sides of the

liquid column. Near the stagnation values ($C_p \approx 1$), the stagnation point progressively spread out along the upwind surface of the liquid column. The low pressure along the sides of the jet further drops to increasingly smaller C_p values. The variation of pressure coefficient along the downwind surface of the liquid column is small due to the formation of trailing vortices which is evident by the pathlines of the particle seeding behind the jet.

The non-dimensional iso-vorticity surfaces of the wake region of a round nonturbulent liquid jet in uniform gaseous crossflow within the bag breakup regime are shown in Fig. 5.17. The iso-surfaces are colored by the vorticity magnitude normalized by the strain rate. The direction of the crossflow and the dimension of the liquid jet are shown in the upper left-figure and the liquid cross-sections are shown at various $y/(v_j t^*)$ which progress from the upper-left figure ($y/(v_j t^*) = 0.09$) to the lower-left figure ($y/(v_j t^*) = 0.37$), and continue from the upper-right figure ($y/(v_j t^*) = 0.55$) to the lower-right figure ($y/(v_j t^*) = 0.82$). Similar to the liquid jet within column breakup regime, the wake consists of alternating pairs of vortices, similar to Karman vortex streets. The non-uniform flowfield behind the liquid jet dictates the path of the liquid droplets traveled after the breakup. As such, the non-dimensional iso-vorticity surfaces presented herein, in conjunction with the wake velocity defects shown in section 5.8, can provide the conditions required for modeling the dispersed phase flow.

5.3.3 Shear Breakup Regime

The flow visualization of a typical liquid jet in uniform gaseous crossflow within the shear breakup regime is shown in Fig. 5.18. The liquid jet presented in the shear breakup regime has a nozzle exit diameter of 2 mm, crossflow Weber number of 220, crossflow Reynolds number of 6148, liquid/gas density ratio of 645, and a liquid jet

momentum ration of 130. Unlike the column and bag breakup regimes, the liquid jet maintained a round jet configuration. The top view of Fig. 5.18 shows that there is no visible deflection of the liquid jet in the direction of the crossflow. Prior to the onset of breakup, the upwind surface of the liquid column was flattened.

The liquid jet cross-sections as a function of normalized streamwise distance ($y/(v_j t^*)$) for the two-dimensional (Aalburg et al., 2005) and the present three-dimensional computational model within the shear breakup regime are shown in Fig. 5.19. The crossflow is from right to left, the right-most liquid cross-section is at $y/(v_j t^*) = 0.04$, and with an increment of 0.044, as the figures progress from right to left. The black circles represent the liquid jet at the nozzle exit and the color codes represent the liquid jet cross-sections at different normalized streamwise distance $y/(v_j t^*)$. For all available times, the liquid cross-sections of the two-dimensional and the three-dimensional models are almost identical. At $y/(v_j t^*) = 0.22$, the upwind surface of the liquid column begins to flatten and surface waves start to appear in both the two-dimensional and three-dimensional models at almost the same location. Near the nozzle exit (i.e., $y/(v_j t^*) = 0.04$), the jet cross-section was circular. As $y/(v_j t^*)$ progresses, the crossflow flattens the upwind surface of the liquid column (i.e., $y/(v_j t^*) = 0.31$ and 0.35). Unlike the column and bag breakup regimes, however, the liquid column does not deform into an ellipsoidal cross-section. When comparing the liquid cross-section within the bag and shear breakup regimes at the same normalized streamwise distance ($y/(v_j t^*)$), the cross-section of the liquid column within the bag breakup regime is more aerodynamically shaped (i.e., does not contain sharp corner) than the corresponding cross-section in the shear breakup regime. For shear breakup, the upwind surface of the liquid column was flattened, resulting in a liquid

column that is similar to a blunt body. Therefore, the separation of the gaseous crossflow occurs at the relatively sharp corners along the upwind surface of the liquid jet, resulting in only limited deformation of the liquid column and no apparent deflection in the cross-stream direction. Beyond $y/(v_j t^*) = 0.35$, shear breakup is expected to occur. At the onset of breakup, the liquid cross-stream diameter is about the same as the initial jet diameter, as was observed in the experiments by Sallam et al. (2004) and the present computational investigation (Fig. 5.28).

Cross-sections of a liquid jet along with velocity vectors of the liquid phase relative to the motion of the jet center and normalized by the characteristic liquid velocity (u_L) are shown in Fig. 5.20 for various normalized streamwise distance ($y/(v_j t^*)$) at conditions identical to those illustrated in Fig. 5.19. The crossflow is from right to left, the normalized streamwise location $y/(v_j t^*)$ progresses from 0.04 to 0.33. The green line represents the liquid/gas interface. The velocity vectors are colored according to the magnitude of the velocity component in x-direction normalized by the characteristic liquid velocity, and the lengths of the vectors represent the magnitude of the velocity in the xz-plane normalized by the characteristic liquid velocity. For clarity, only 1/2 of the total number of vectors is displayed. When the liquid cross-section is circular (i.e., $y/(v_j t^*) = 0.18$), the normalized xz-velocity within the cross-section is largest near the liquid-gas interface between the upwind surface and the two sides of the liquid jet. As $y/(v_j t^*)$ increases (i.e., $y/(v_j t^*) = 0.26$), the flattened upwind surface pushes the liquid towards the two sides of the liquid jet. Up to the onset of breakup (i.e., $y/(v_j t^*) = 0.33$), no counter-rotating vortex pair was present within the liquid cross-section.

Upwind and the *downwind* isometric views of the external flowfield are shown in Fig. 5.21 and Fig. 5.22, respectively at conditions identical to those shown in Figs. 5.19 and Fig. 5.20. The surface of the liquid jet is colored by the pressure coefficient (C_p) and the particle pathlines are colored by the velocity magnitude ($|v|$) normalized by the crossflow velocity (U_G). Near the nozzle exit (i.e., $y/(v_j t^*) = 0.07$), the pathlines of the particle seeding signified the presence of trailing vortices. Close to the nozzle exit, the crossflow velocity at the side of the jet accelerates to velocities lower than those observed in bag breakup. As such, the reduction of gas pressure along the side of the liquid column is lower than those observed in bag breakup, resulting in only limited deformation of the liquid jet prior to the onset of breakup. As $y/(v_j t^*)$ increases, the stagnating gas on the upwind side of the cross-section flattened the upwind surface of the liquid column. The flattened upwind surface enhances the tendency of the air entrainment in the upwind direction of the liquid column. However, the flattened upwind surface resulted in no apparent deflection of the liquid column. Very near the nozzle exit (i.e., $y/(v_j t^*) = 0.02$), the pressure coefficient profile of the liquid jet resembles the pressure coefficient profile of flow around a solid cylinder. When the upwind surface along the liquid column was flattened by the crossflow, the stagnation point progressively spread out along the upwind surface of the liquid column. The flattening of the upwind liquid column shifted the region of negative pressure coefficient from the sides of the liquid jet towards the upwind direction. Away from the flattened upwind surfaces towards the downwind direction of the liquid column, the variation of pressure coefficient behind the liquid column is small and the liquid jet had a nearly constant pressure coefficient close to zero. This ties in with the observation that the separation is

occurring at the relatively sharp corners along the upwind surface of the liquid jet prior to the onset of breakup.

The non-dimensional iso-vorticity surfaces of the wake region are shown in Fig. 5.23. The iso-surfaces are colored by the vorticity magnitude normalized by the strain rate. The direction of the crossflow is shown in the upper left-figure. The liquid cross-sections are shown at various $y/(v_j t^*)$ which progress from the upper-left figure ($y/(v_j t^*) = 0.04$) to the lower-left figure ($y/(v_j t^*) = 0.18$), and continue from the upper-right figure ($y/(v_j t^*) = 0.26$) to the lower-right figure ($y/(v_j t^*) = 0.33$). Unlike the column and bag breakup, the wake consists of non-alternating pairs of vortices. This phenomenon may be related to the separation of the crossflow at the relatively sharp corners along the upwind surface of the liquid jet.

5.4 Liquid Jet Deformation

5.4.1 Liquid Cross-stream Deformation

The liquid cross-stream deformation (d_s/d_j) as a function of normalized streamwise distance ($y/(v_j t^*)$) at different temporal time (t) of round nonturbulent liquid jets in uniform gaseous crossflow within the column ($We_G = 3.5$), bag ($We_G = 8$), and shear ($We_G = 220$) breakup regimes is shown in Fig. 5.24. The experimental and the two-dimensional computational results of Aalburg et al. (2005) are also included in the Fig. 5.24. In the two-dimensional model, the temporal time, t, is converted to y/v_j under the assumption that v_j is constant. Since the time scale is converted to the spatial scale in order to compute the third dimension, the two-dimensional model cannot be used to study the temporal solution of a liquid jet cross-section at a fixed y location. In the three-

dimensional model, the third dimension provides the distance y from the nozzle exit, allowing the liquid jet cross-section at a fixed y location to be studied at different temporal time (i.e., $t = t_0$, $t = t_0 + 0.3t^*$,…, etc.). In column breakup, the present results agree with the experimental measurements and the two-dimensional computations of Aalburg et al. (2005) within experimental and computational uncertainties. The present results show that the liquid cross-stream deformation fluctuates with the temporal time (t). This may be attributed to the waves' traveling along the liquid column, particular when the liquid cross-section turns ellipsoidal. The half configuration model was also attempted and the simulated results agree with the full configuration computations. In the bag breakup regime, the fluctuation of the liquid cross-stream deformation with the temporal time (t) is small. In the shear breakup regime, the cross-stream deformation does not exhibit any considerable amount of fluctuation with the temporal time (t). The present full configuration results can be correlated with a 3rd order polynomial, as given below:

$$\text{Column: } d_s/d_j = 1 - 0.53\, y/(v_j t) - 0.005\, [y/(v_j t)]^2 - 0.53\, [y/(v_j t)]^3 \quad (5.1)$$

$$\text{Bag: } d_s/d_j = 1 - 0.41\, y/(v_j t) - 0.41\, [y/(v_j t)]^2 + 0.28\, [y/(v_j t)]^3 \quad (5.2)$$

$$\text{Shear: } d_s/d_j = 1 + 0.025\, y/(v_j t) - 1.42\, [y/(v_j t)]^2 + 1.35\, [y/(v_j t)]^3 \quad (5.3)$$

Taking the 2nd derivatives of Eqn. 5.1-5.3, a point of inflection is observed at $y/(v_j t^*) = 0.49$, $y/(v_j t^*) = 0.35$, for bag and shear breakup, respectively. The inflection point signifies that the jet is attempting to oscillate back to a circular configuration under the influence of the surface tension forces.

5.4.2 Liquid Span-wise Deformation

The liquid span-wise deformation (d_c/d_j) as a function of normalized streamwise distance ($y/(v_j t^*)$) at different temporal time (t) of round nonturbulent liquid jet in uniform gaseous crossflow within the column ($We_G = 3.5$), bag ($We_G = 8$), and shear ($We_G = 220$) breakup regimes is shown in Fig. 5.25. In column and bag breakup, a point of inflection is visually presence, showing that the surface tension is attempting to oscillate the liquid span-wise diameter back to a round jet configuration. At the maximum $y/(v_j t^*)$ observed in the present study, the liquid column is approaching the maximum span-wise deformation. The fluctuation of the liquid span-wise deformation with the temporal time (t) is small. The present full configuration results can be correlated with a 3rd order polynomial, as given below:

$$\text{Column: } d_c/d_j = 1 - 0.23\, y/(v_j t) + 3\,[y/(v_j t)]^2 - 3\,[y/(v_j t)]^3 \quad (5.4)$$

$$\text{Bag: } d_c/d_j = 1 - 0.43\, y/(v_j t) + 3.47\,[y/(v_j t)]^2 - 2.34\,[y/(v_j t)]^3 \quad (5.5)$$

$$\text{Shear: } d_c/d_j = 1 - 0.005\, y/(v_j t) - 0.44\,[y/(v_j t)]^2 + 3.45\,[y/(v_j t)]^3 \quad (5.6)$$

Taking the 2nd derivatives of Eqn. 5.4-5.6, a point of inflection is observed at $y/(v_j t^*) = 0.33$, $y/(v_j t^*) = 0.49$, $y/(v_j t^*) = 0.04$, for column, bag, and shear breakup, respectively. A positive point of inflection with $y/(v_j t^*)$ being positive exists in all breakup regimes, signifies that the surface tension is attempting to oscillate the liquid span-wise cross-section back to a circular configuration.

5.4.3 Liquid Cross-sectional Area

The liquid cross-sectional area normalized by the nozzle exit area as a function of normalized streamwise distance ($y/(v_j t^*)$) at different temporal time (t) of round

nonturbulent liquid jets in uniform gaseous crossflow within the column ($We_G = 3.5$), bag ($We_G = 8$), and shear ($We_G = 220$) breakup regimes is shown in Fig. 5.26. In FLUENT, the cross-sectional area is computed by summing the areas of the facets (either triangular or quadrilateral) that define the surface. In column breakup, the liquid cross-sectional area fluctuates with the temporal time (t). The fluctuation may be attributed to the disturbances traveling along the liquid column, particular when the liquid cross-section turns ellipsoidal. The half configuration model for column breakup was also simulated and the liquid cross-sectional area normalized by nozzle exit area had a maximum deviation of 8.4% from unity. In the bag breakup regime, the fluctuation of the liquid cross-sectional area with temporal time (t) is small. The half configuration for bag breakup was also simulated and the liquid cross-sectional area normalized by nozzle exit area had a maximum deviation of 31.1% from unity. In the shear breakup regime, the liquid cross-sectional area does not exhibit any considerable amount of fluctuation with the temporal time (t). In all breakup regimes, the liquid cross-sectional area normalized by the nozzle exit area approaches unity ($A_{sc}/A_j \approx 1$), independent of $y/(v_j t^*)$.

5.5 Liquid Jet Velocities

The normalized mass-weighted average velocity of the liquid cross-section ($v_{s(mass\text{-}avg)}/v_j$) as a function of streamwise distance (y/d_j) at different temporal time (t) of round nonturbulent liquid jets in uniform gaseous crossflow within the column ($We_G = 3.5$), bag ($We_G = 8$), and shear ($We_G = 220$) breakup regimes is shown in Fig. 5.27. In FLUENT, the mass-weighted average of a quantity is computed by dividing the summation of the product of the selected field variable (i.e., $\sum_{i=1}^{n} v_i \rho_i \left| \overrightarrow{v_i} \cdot \overrightarrow{A_i} \right|$) and the

absolute value of the dot product of the facet area and momentum vectors by the summation of the absolute value of the dot product of the facet area and momentum vectors (i.e., $\sum_{i=1}^{n} \rho_i \left| \overrightarrow{v_i} \cdot \overrightarrow{A_i} \right|$). In all breakup regimes, the mass-weighted average velocity of the liquid cross-section normalized by the liquid jet velocity approaches unity ($v_{s(mass\text{-}avg)}/v_j \approx 1$), independent of the streamwise distance traveled. This agrees with the experimental measurements performed within the bag breakup regime in section 4.3, where the velocity of the liquid surface normalized by nozzle exit velocity approaches unity ($v_s/v_j \approx 1.0$), independent of the streamwise distance traveled. In column and bag breakup, the half configuration model was also simulated and had a maximum deviation of 4.7% from unity.

5.6 Column and Surface Waves

The wavelengths of column waves are plotted as a function of crossflow Weber number in Fig. 4.6, respectively. The computational results of the column breakup regime were obtained from the full configuration model and the computational results of the bag breakup regime were obtained from the half configuration model to reduce computational time. The computed wavelengths agree with the present experimental results and Mazallon et al. (1999) measurements within experimental and computational uncertainties. The wavelengths of downwind surface waves are plotted as a function of crossflow Weber number within the bag breakup regime in Fig. 4.9. The computed results were obtained from the full configuration model and were comparable to those measured in the experiments.

5.7 Onset of Primary breakup

An important aspect of the primary breakup of round nonturbulent liquid jets in gaseous crossflow is the deformation of the liquid column at the onset of breakup. The deformation at the onset of primary breakup as a function of crossflow Weber number is shown in Fig. 5.28. The computational results within the bag and shear breakup regimes were simulated for a time duration of $2t^*$ and $2.5t^*$, respectively. Measurements shown on the plot include experimental results from Mazallon et al. (1999) and Sallam et al. (2004) for liquid jet in crossflow, along with the experimental correlation of Hsiang and Faeth (1992) for the secondary breakup of drops subjected to shock wave disturbances. In shear breakup, the upwind surface of the liquid column is flattened slightly and there is no significant deformation of the liquid column, as discussed in connection with Figs. 5.24 and 5.25. In bag and shear breakup, the computed results of $d_j/d_i \approx 2.0$ at $We_G = 8$ and $d_j/d_i \approx 1.1$ at $We_G = 220$, are in excellent agreement with the experimental measurements, $d_j/d_i \approx 2$ at $We_G = 8$ and $d_j/d_i \approx 1$ at $We_G = 220$ (Sallam et al., 2004) and therefore further confirm the accuracy of the present computational model.

To determine the conditions required for the onset of breakup for round nonturbulent liquid jets in uniform gaseous crossflow within the shear breakup regime, Sallam et al. (2004) observed that the appearance of drops was always preceded by the appearance of ligaments protruding downstream from the region near the sides of the liquid jet toward the wake behind the jet. It was argued that the liquid motion required to form a ligament originated from the viscous shear layer beginning at the upstream stagnation point of the crossflow before separating from the liquid jet on the downstream side of the crossflow (Sallam et al., 2004). The size of these ligaments can be obtained

by equating the surface energy of a drop to the kinetic energy of an equivalent volume within this viscous sublayer as follows:

$$\frac{1}{2}\rho_L[\frac{4}{3}\pi(\frac{d_L}{2})^3]u_L^2 = C_L\sigma 4\pi(\frac{d_L}{2})^2 \tag{5.7}$$

Or simply

$$u_L^2 = \frac{12C_L\sigma}{\rho_L d_L} \tag{5.8}$$

where d_L is the diameter of ligament at onset and C_L is an empirical constant on the order of unity. Equation 5.8 describes the minimum characteristic liquid velocity required to initiate the onset of breakup. Within a finite diameter liquid jet, the shear layer along the periphery of the jet from which the ligaments form can not grow indefinitely; therefore, the ligament diameter at onset are as follows (Sallam et al., 2004):

$$\frac{d_L}{d_j} = 0.07(\frac{\mu_L/\mu_G}{We_G})^{1/2}; \quad \frac{\mu_L/\mu_G}{We_G} < 2 \tag{5.9}$$

and

$$\frac{d_L}{d_j} = 0.095; \quad \frac{\mu_L/\mu_G}{We_G} > 2 \tag{5.10}$$

Substituting Eqn. 5.9 into Eqn. 5.8 and setting u_L equal to $u_{L,threshold}$ (where $u_{L,threshold}$ is the threshold of the liquid velocity required to produce droplets) yields

$$u_{L,threshold}^2 = \frac{171C_L\sigma}{\rho_L d_j(\frac{\mu_L/\mu_G}{We_G})^{1/2}}; \quad \frac{\mu_L/\mu_G}{We_G} < 2 \tag{5.11}$$

Substituting Eqn. 5.10 into Eqn. 5.8 yields

$$u_{L,threshold}^2 = \frac{126 C_L \sigma}{\rho_L d_j}; \qquad \frac{\mu_L/\mu_G}{We_G} > 2 \tag{5.12}$$

For the present test conditions, the ratio $(\mu_L/\mu_G)/We_G$ is equal to 8.4 and 0.3 for bag and shear breakup, respectively. For a C_L of unity, $u_{L,threshold}^2$ becomes 7.1 and 4.4 m^2/s^2, for the bag and shear breakup, respectively. From the present solutions computational results, the maximum liquid velocities ($u_{L,max}$) within the cross-section prior to the onset of breakup were 3.19 m/s ($u_{L,max}^2$ = 10.2 m^2/s^2) and 4.24 m/s ($u_{L,max}^2$ = 18.0 m^2/s^2), for bag and shear breakup, respectively. Note that the maximum velocity lies near the liquid-gas interface along the sides of the liquid jet, as observed from the internal flowfields in Figs. 5.14 and Fig. 5.20, bag and shear breakup, respectively. For a ligament formed by a hemispherically distorted liquid surface, if one assumed that the velocity profile within the ligament took a parabolic form and the average liquid velocity is approximately half its maximum value, then the present computational results yield an average liquid velocity ($u_{L,avg}^2$) of 5.1 m^2/s^2 and 9.0 m^2/s^2, for bag and shear breakup, respectively. Hence, for liquid jet within the bag breakup regime, the average liquid velocity ($u_{L,avg}^2$ ~ 5.1 m^2/s^2) is lower than the threshold of the liquid velocity ($u_{L,threshold}^2$ = 7.1 m^2/s^2), hence, no ligaments could be formed. However, for liquid jet within the shear breakup regime, the average liquid velocity ($u_{L,avg}^2$ ~ 9.0 m^2/s^2) is higher than the threshold of the liquid velocity ($u_{L,threshold}^2$ = 4.4 m^2/s^2), hence, the ligaments have enough energy to form along the jet surface.

5.8 Jet Wake

The wake velocity defect, U_G - u, and wake width; $z_{1/2}$, of the flow behind the liquid jet is computed to provide the properties of the dispersed phase flow. A sketch of the wake region of round nonturbulent liquid jets in uniform gaseous crossflow is shown in Fig. 5.29.

The normalized wake velocity defect $[(U_G-u)/(U_G-u_c)]$ in the inner wake region; $z < z_{1/2}$, as a function of normalized span-wise distance $(z/z_{1/2})$ for bag and shear breakup are shown in Fig. 5.30. The computational results are plotted for different streamwise (y) and cross-stream (x) distances. The velocity defect is described by the following correlation:

$$[(U_G - u)/(U_G - u_c)] = 1 - 0.01(z/z_{1/2}) + 0.46(z/z_{1/2})^2 + 0.015(z/z_{1/2})^3 - 3.93(z/z_{1/2})^4 - 0.007(z/z_{1/2})^5 + 2.5(z/z_{1/2})^6; \quad -1 < z/z_{1/2} < 1 \qquad (5.13)$$

For the range $0 < z/z_{1/2} < 1$, the correlation is given by:

$$[(U_G - u)/(U_G - u_c)] = 1 + 0.34(z/z_{1/2}) - 4.8(z/z_{1/2})^2 + 23.5(z/z_{1/2})^3 - 49.7(z/z_{1/2})^4 + 40.7(z/z_{1/2})^5 - 11.1(z/z_{1/2})^6; \quad 0 < z/z_{1/2} < 1 \qquad (5.14)$$

The difference between Eqns. (5.13) and (5.14) are probably due to asymmetry in the vortex shedding behind the liquid jet. The similarity solution in the inner wake region was valid for the range of the streamwise ($0.8 < y/d_j < 9.5$) and the cross-stream ($2 < x/d_j < 9$) distances considered in this study. To obtain a similarity solution for $z > z_{1/2}$, a different scaling is required.

For the farfield behind a solid cylinder, the power law of the growth of the width

of a wake (White, 1974) is:

$$z_{1/2} \alpha x^{1/2} \tag{5.15}$$

The wake half width normalized by the span-wise diameter of the jet as a function of the cross-stream distance normalized by the span-wise diameter of the jet for bag and shear breakup is shown in Fig. 5.31. The following shows the correlation of the present results

$$z_{1/2}/d_c = 1.14(x/d_c)^{0.41} \tag{5.16}$$

The correlation coefficient of the fits is 0.95. The wake half width normalized by the jet span-wise diameter is independent of the streamwise distance ($0.8 < y/d_j < 9.5$). The power coefficient of 0.41 of the present correlation along with a empirical factor of almost unity (1.14) is surprisingly close to the power law for the growth a of wake behind a solid cylinder considering that the deformation of the liquid jet as well as the internal circulation of the liquid all have potential effects on the flow field around the liquid jet. This result is another indication confirming the accuracy of the present computations.

The centerline velocity (u_c) of the wake region as a function of the cross-stream distance normalized by the span-wise diameter of the jet for bag and shear breakup is shown in Fig. 5.32. The following shows the correlation of the present results

$$(U_G - u_c)/U_G = 1.06; \quad 2 < x/d_j < 9, 0.8 < y/d_j < 9.5 \tag{5.17}$$

The standard deviation of the computed results is 5%. The centerline velocity of the wake region is independent of the cross-stream distance normalized by the span-wise diameter of the jet.

The normalized velocity defect in the outer wake region; $z > z_{1/2}$, as a function of normalized span-wise distance for bag and shear breakup is shown in Fig. 5.33 for different streamwise (y) and cross-stream (x) distances. The following shows the correlation of the present results for $0 < (z - z_{1/2})/(z_o - z_{1/2}) < 0.045$

$$[(U_G - u) / (U_G - u_{max})] = 47[(z - z_{1/2})/(z_o - z_{1/2})] - 521[(z - z_{1/2})/(z_o - z_{1/2})]^2 \quad (5.18)$$

A similarity solution for $(z - z_{1/2})/(z_o - z_{1/2}) > 0.045$ remains unknown.

The width of the outer wake region normalized by the nozzle exit diameter as a function of cross-stream distance normalized by the nozzle exit diameter for bag and shear breakup is shown in Fig. 5.34. The following shows the correlation of the present results

$$z_o/d_j = 9.5(x/d_j)^{0.3} \quad (5.19)$$

The correlation coefficient of the fits is 0.99. The width of the outer wake region normalized by the nozzle exit diameter is independent of the streamwise distance for $0.8 < y/d_j < 9.5$.

The sum of the maximum velocity (u_{max}) and the centerline velocity (u_c) of the wake region normalized by the crossflow velocity as a function of the cross-stream distance normalized by the nozzle exit diameter for bag and shear breakup is shown in Fig. 5.35. The following shows the correlation of the present results

$$(u_{max} + u_c)/U_G = 1.03; \quad 2 < x/d_j < 9, \; 0.8 < y/d_j < 9.5 \quad (5.20)$$

The standard deviation of the computed results is 5%.

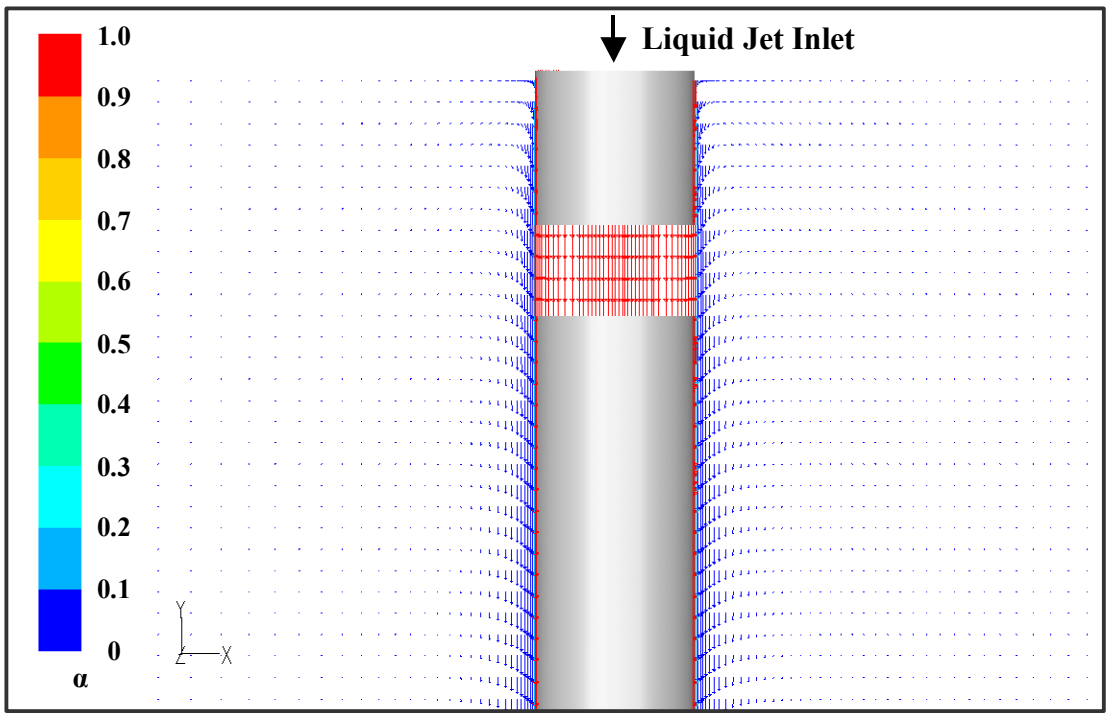

Figure 5.1 Flow visualization of a round nonturbulent liquid jet in quiescent air.

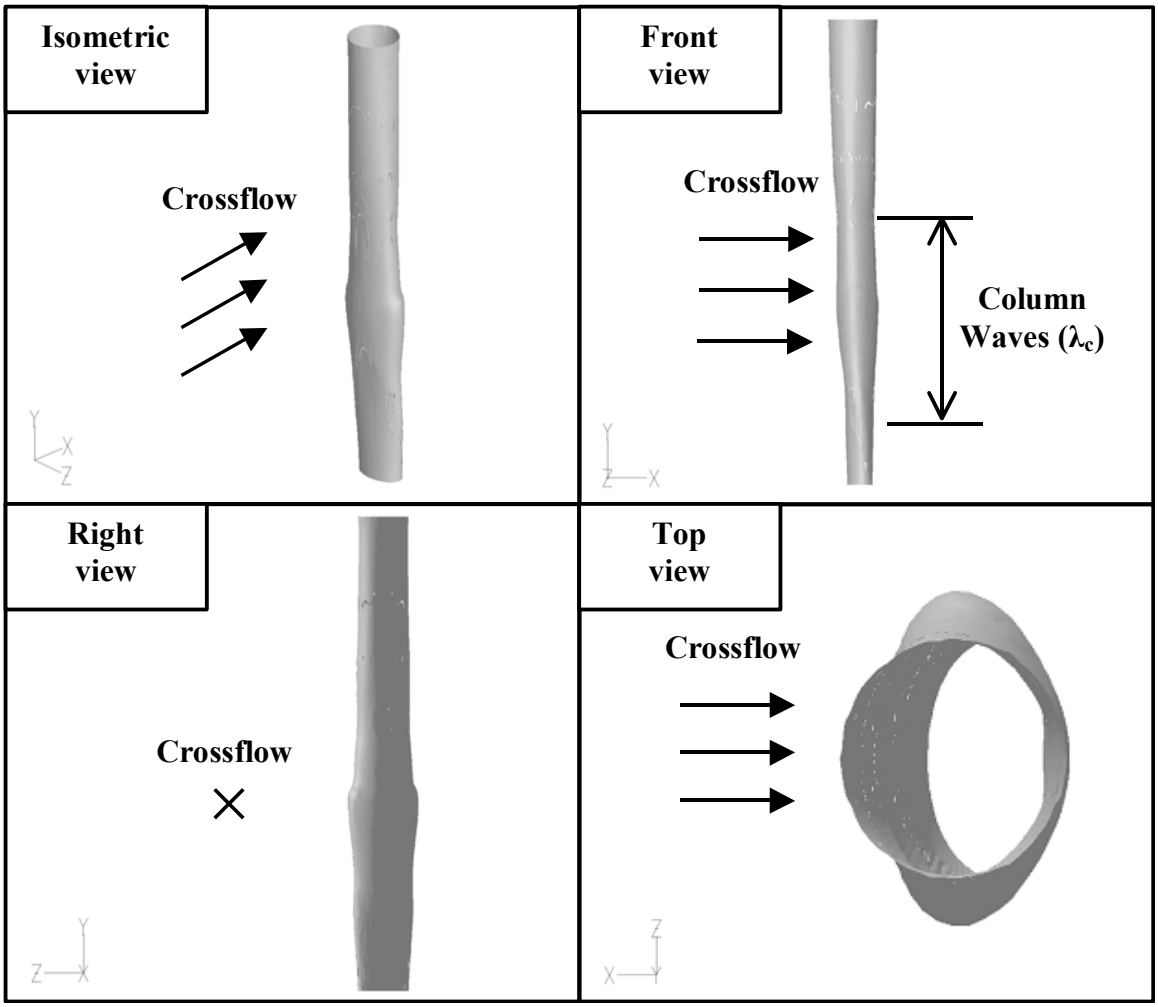

Figure 5.2 Flow visualization of a round nonturbulent liquid jet in uniform gaseous crossflow within column breakup regime ($We_G = 3.5$).

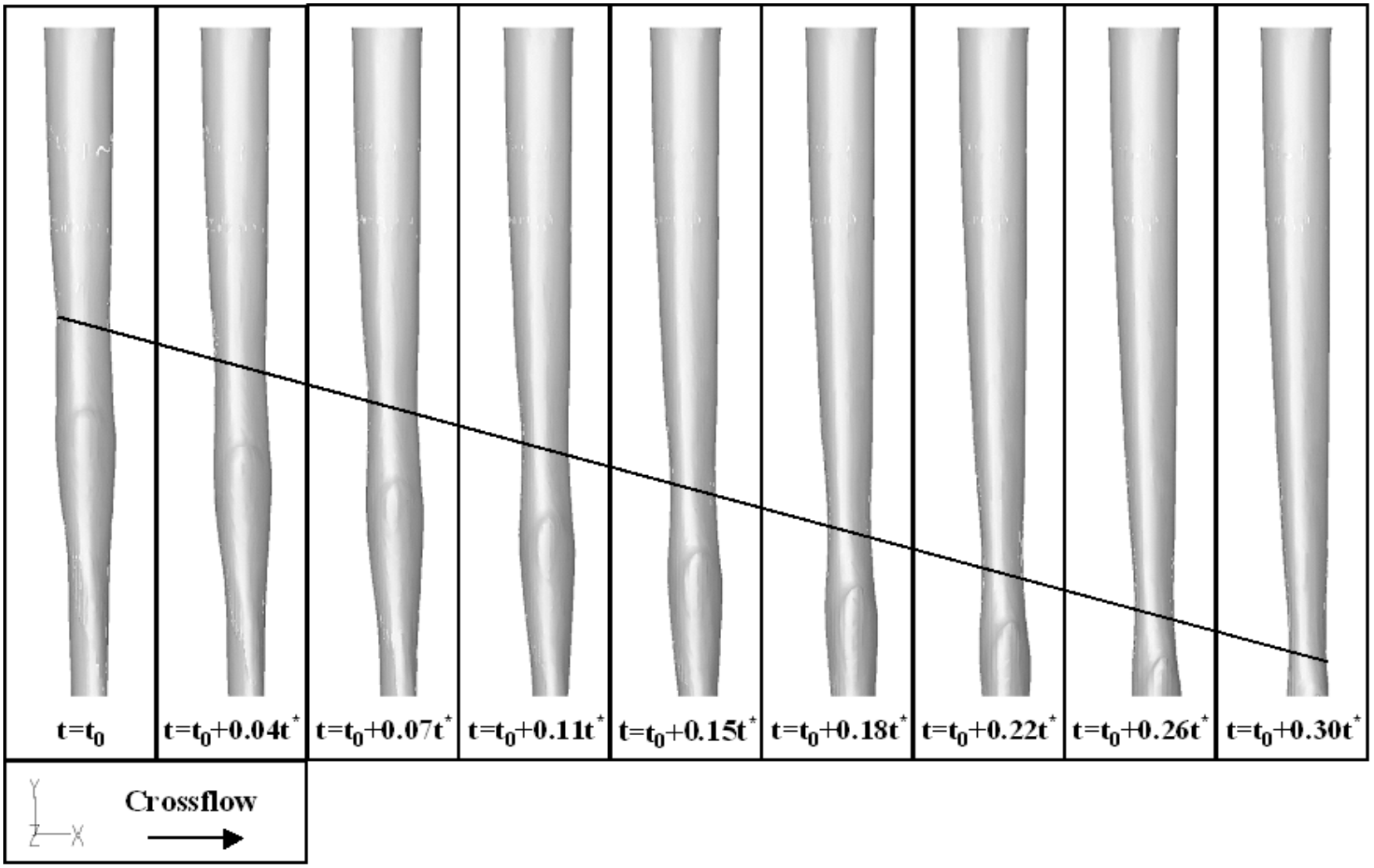

Figure 5.3 Temporal movement of column waves along the liquid column of a round nonturbulent liquid jet in uniform gaseous crossflow within column breakup regime (We_G = 3.5).

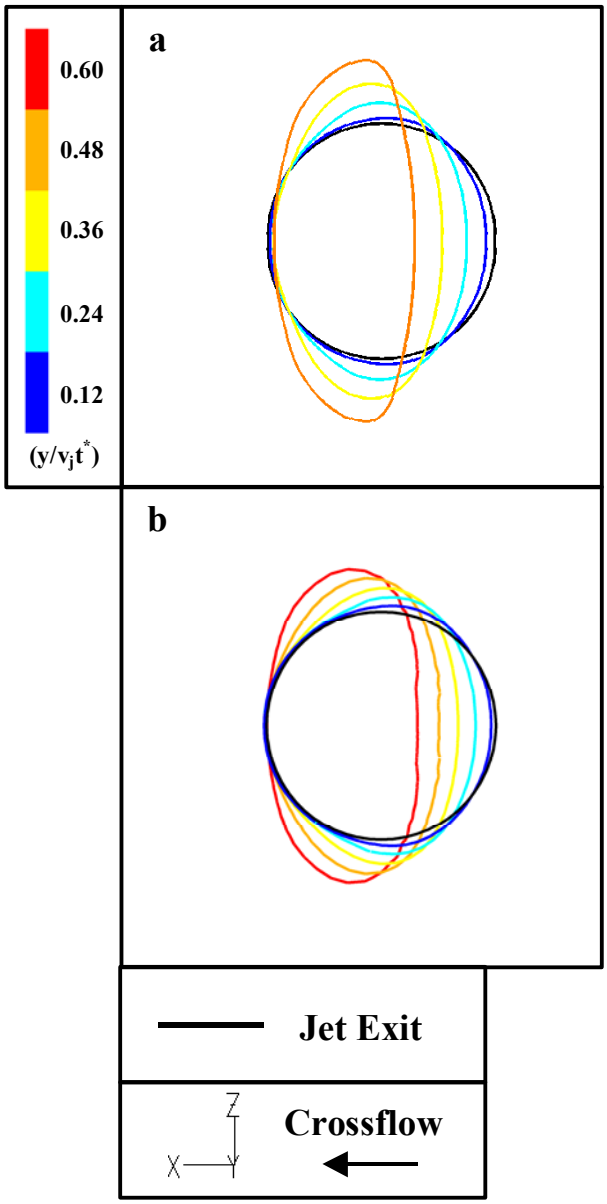

Figure 5.4 Visualization of liquid jet cross-sections as a function of normalized streamwise distance ($y/(v_j t^*)$) of a round nonturbulent liquid jet in uniform gaseous crossflow within column breakup regime (We_G = 3.5). (a) Two-dimensional computational model (Aalburg et al., 2005). (b) Present three-dimensional computational model.

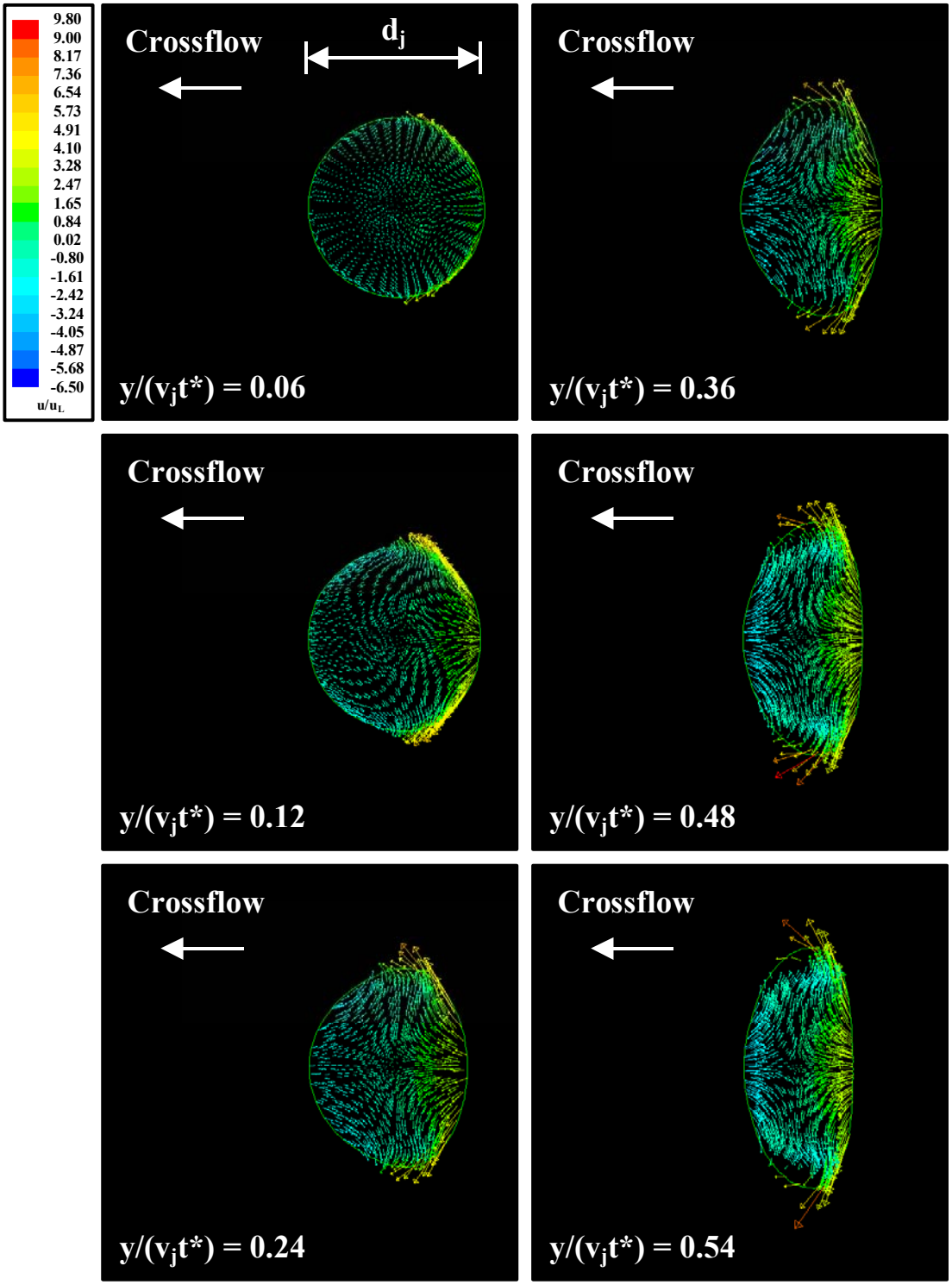

Figure 5.5 Internal flowfield of a round nonturbulent liquid jet in uniform gaseous crossflow within column breakup regime (We_G = 3.5). Green line = liquid/gas interface. Length of vector represents xz-velocity normalized by u_L. For clarity, only 1/6 of the total numbers of vectors are displayed.

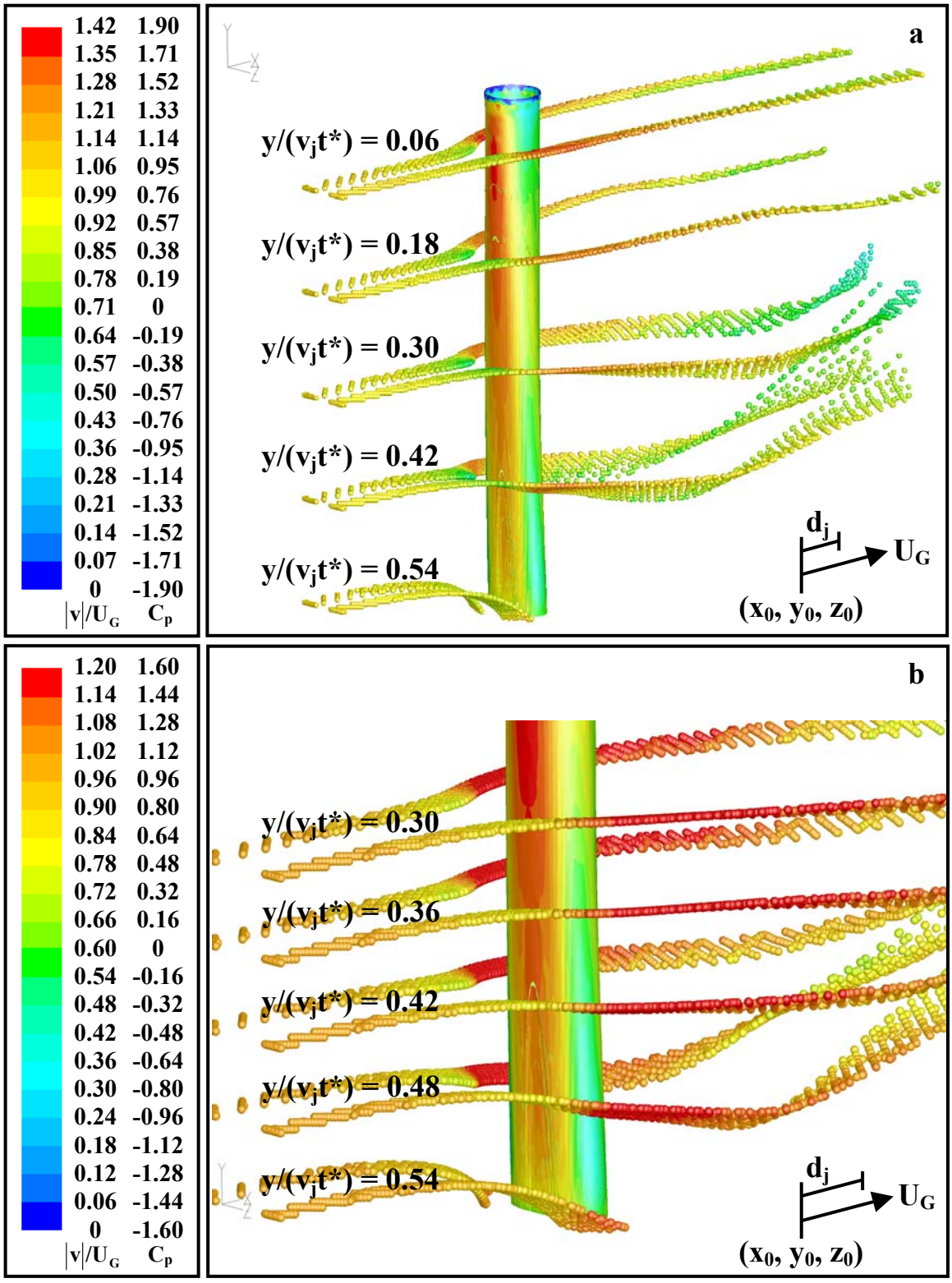

Figure 5.6 *Upwind* isometric view of the external flowfield of a round nonturbulent liquid jet in uniform gaseous crossflow within column breakup regime (We_G = 3.5). Liquid jet surface is colored by C_p. Particle seeding is colored by $|v|/U_G$.

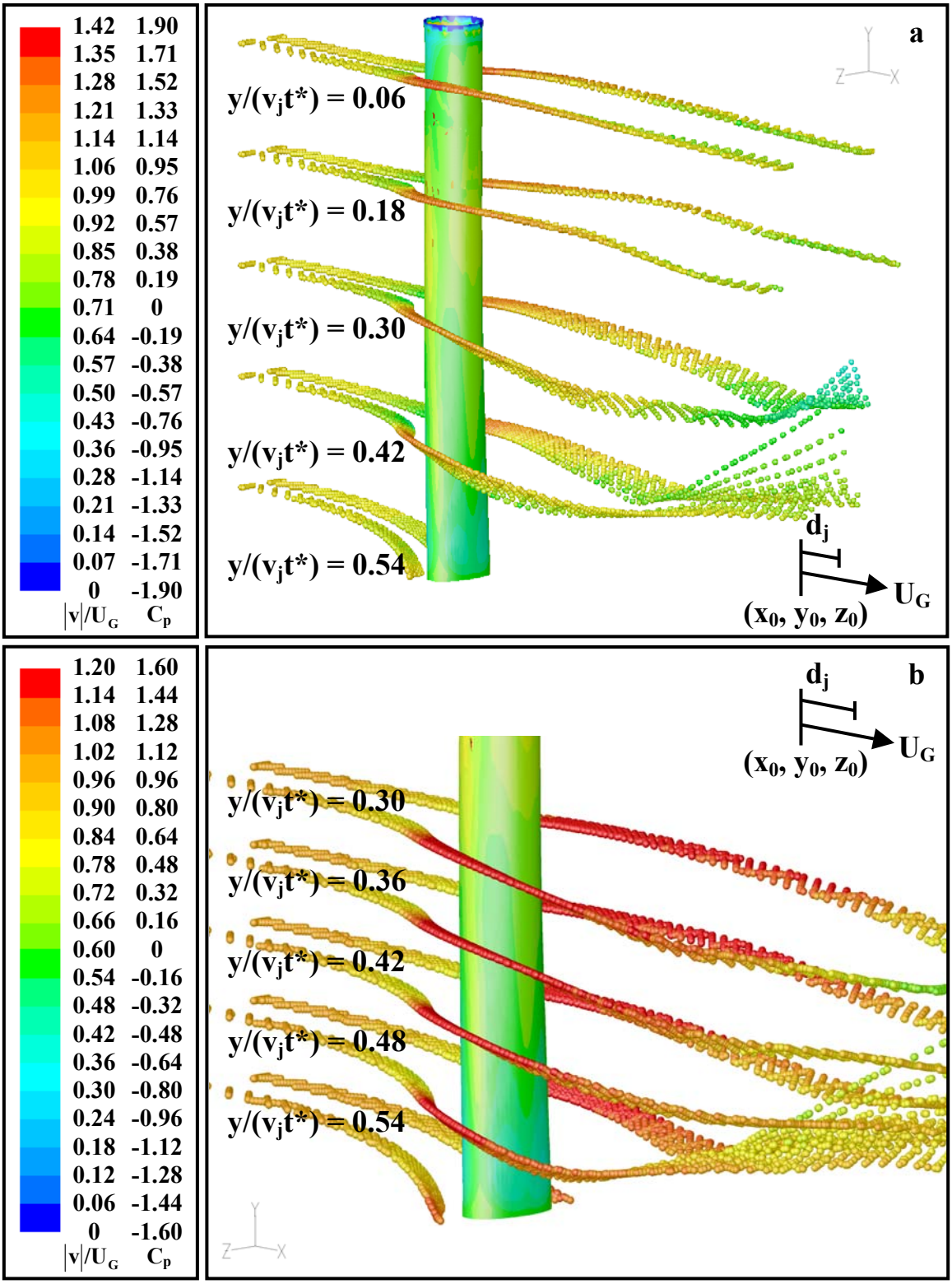

Figure 5.7 *Downwind* isometric view of the external flowfield of a round nonturbulent liquid jet in uniform gaseous crossflow within column breakup regime (We_G = 3.5). Liquid jet surface is colored by C_p. Particle seeding is colored by $|v|/U_G$.

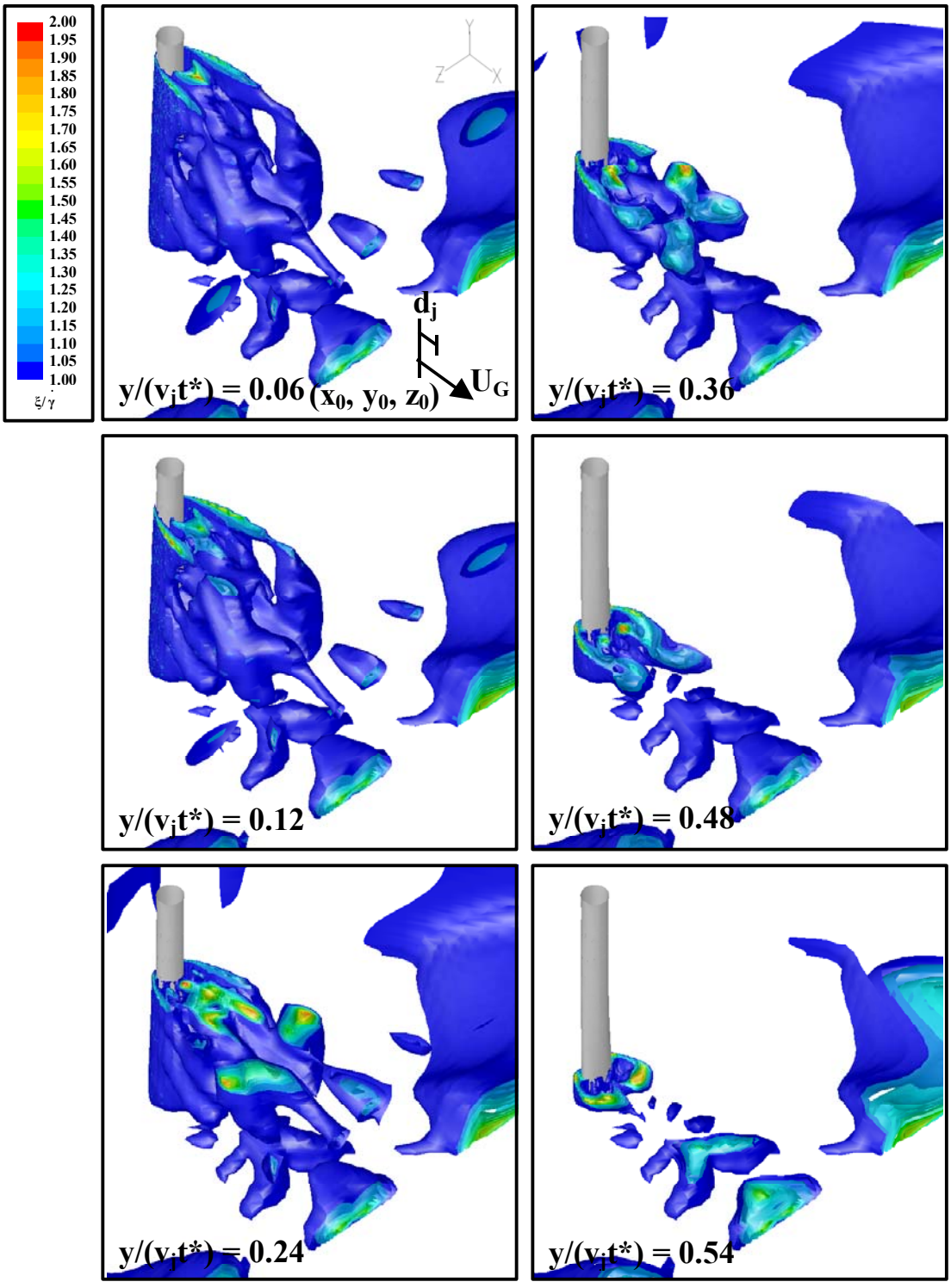

Figure 5.8 Non-dimensional iso-vorticity surfaces of the wake region of a round nonturbulent liquid jet in uniform gaseous crossflow within column breakup regime (We_G = 3.5). Iso-vorticity surface is colored by $\xi/\dot{\gamma}$.

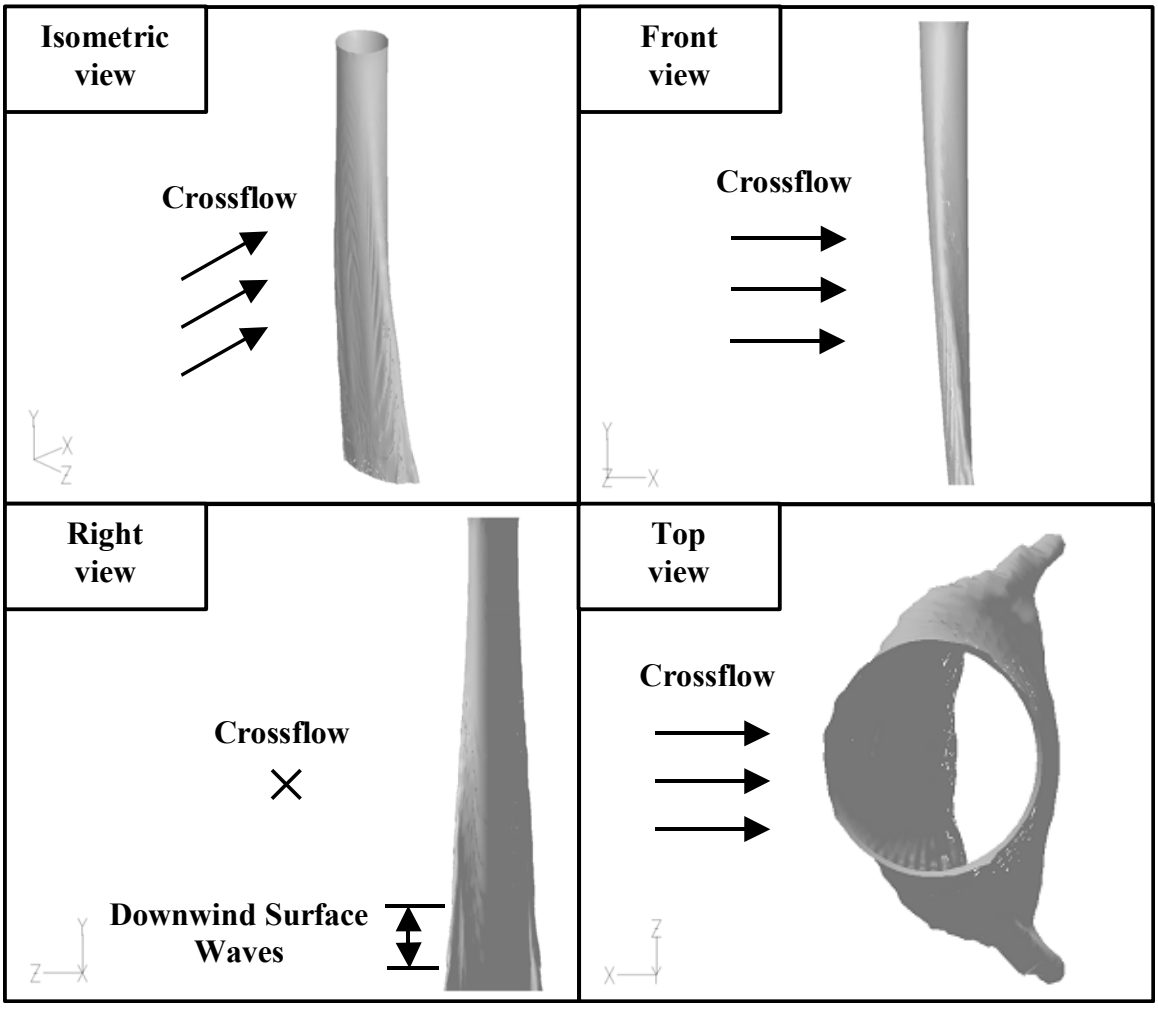

Figure 5.9 Flow visualization of a round nonturbulent liquid jet in uniform gaseous crossflow within bag breakup regime ($We_G = 8$).

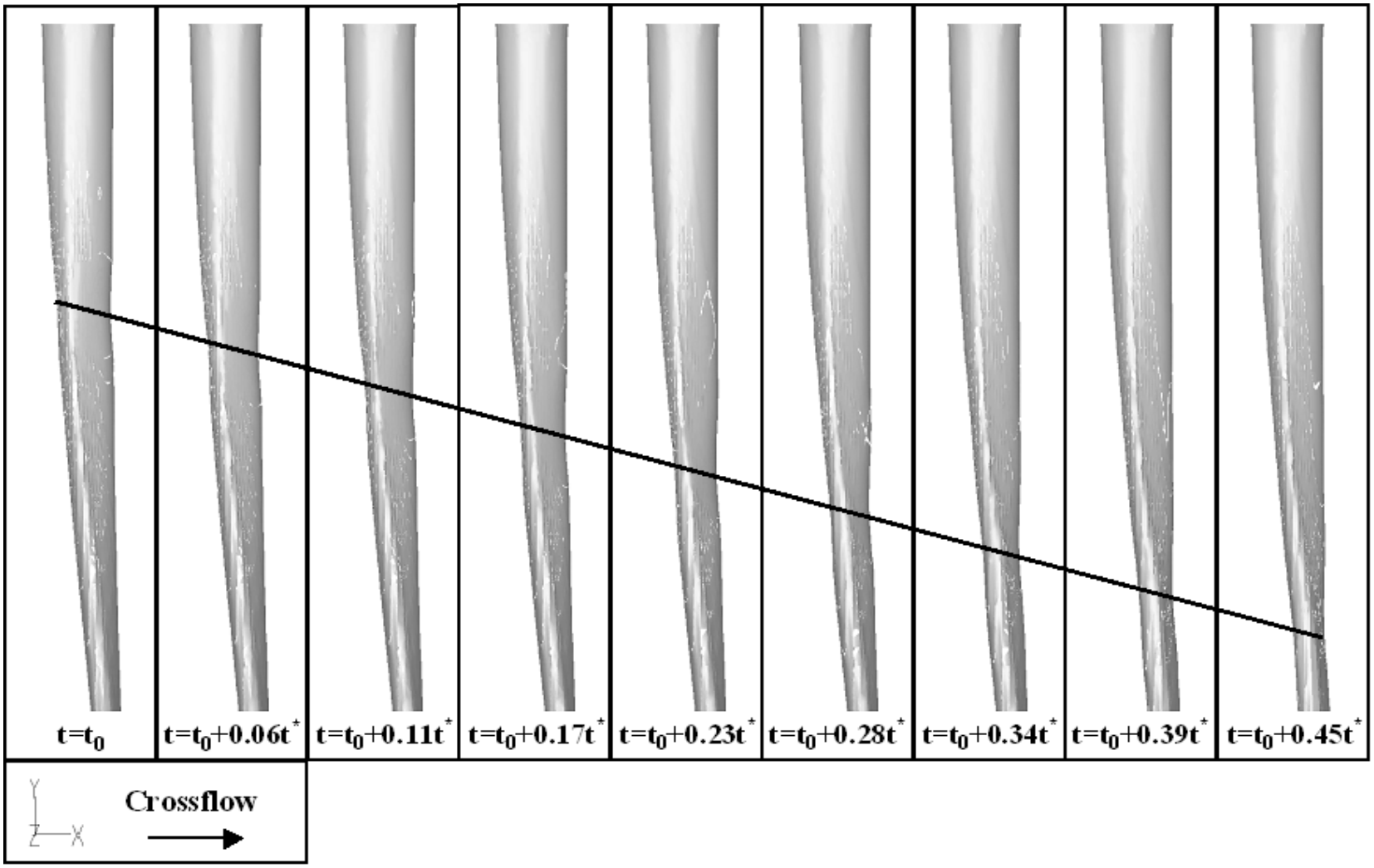

Figure 5.10 Temporal movement of column waves along the liquid column of a round nonturbulent liquid jet in uniform gaseous crossflow within bag breakup regime (full configuration, $We_G = 8$).

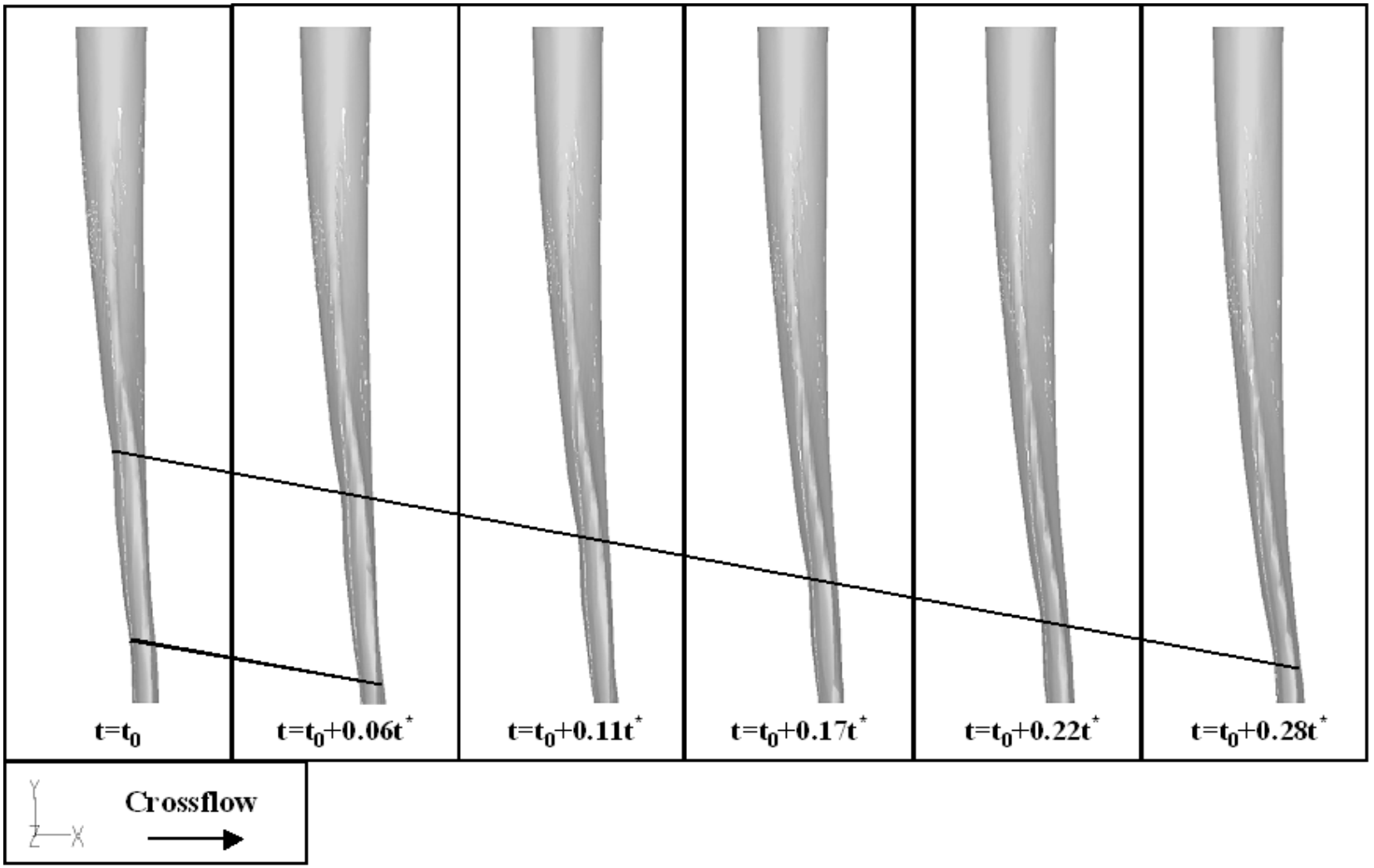

Figure 5.11 Temporal movement of column waves along the liquid column of a round nonturbulent liquid jet in uniform gaseous crossflow within bag breakup regime (half configuration, $We_G = 8$).

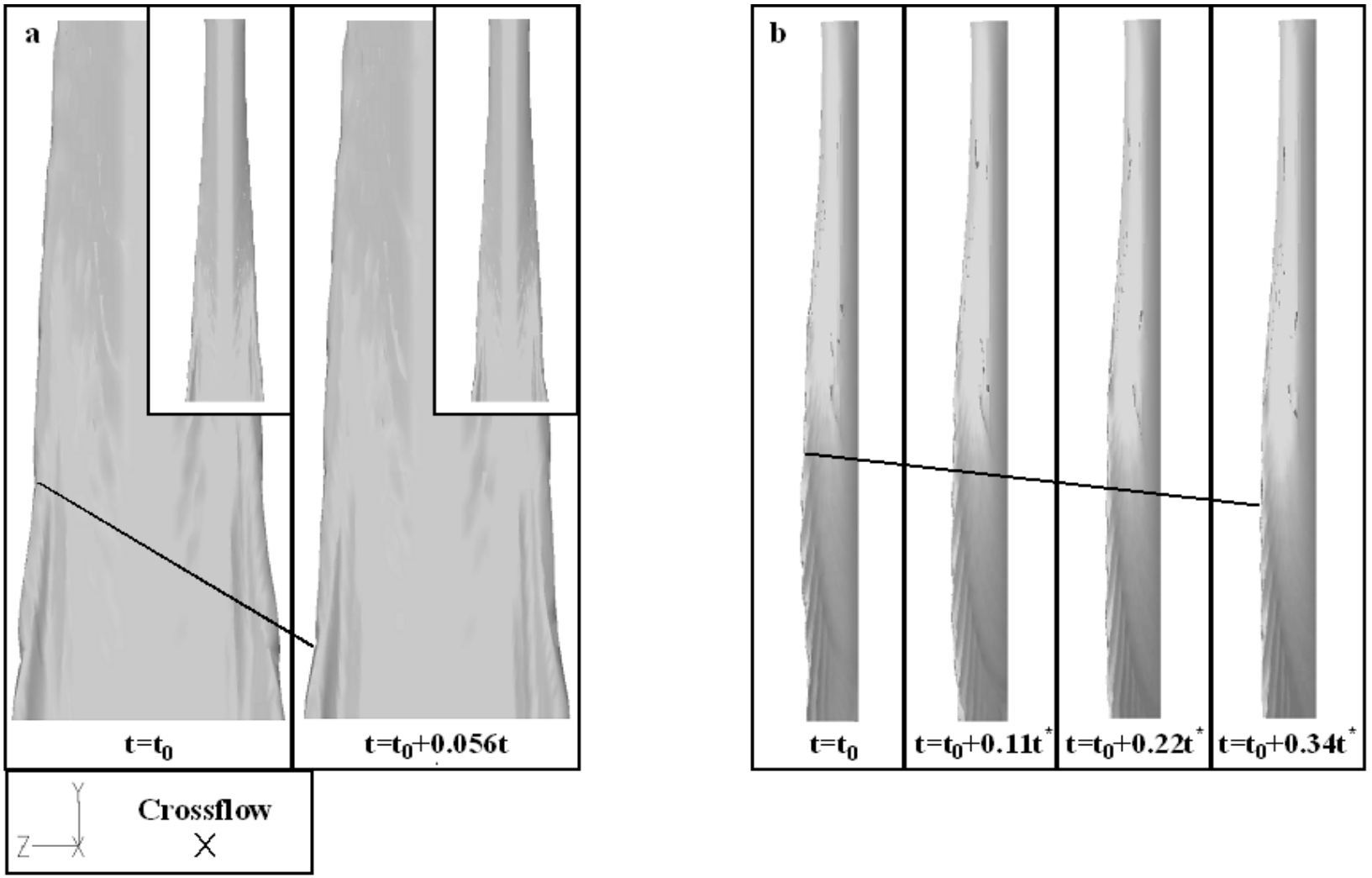

Figure 5.12 Temporal movement of downwind surface waves of a round nonturbulent liquid jet in uniform gaseous crossflow within bag breakup regime ($We_G = 8$). (a) Full configuration, and (b) half configuration.

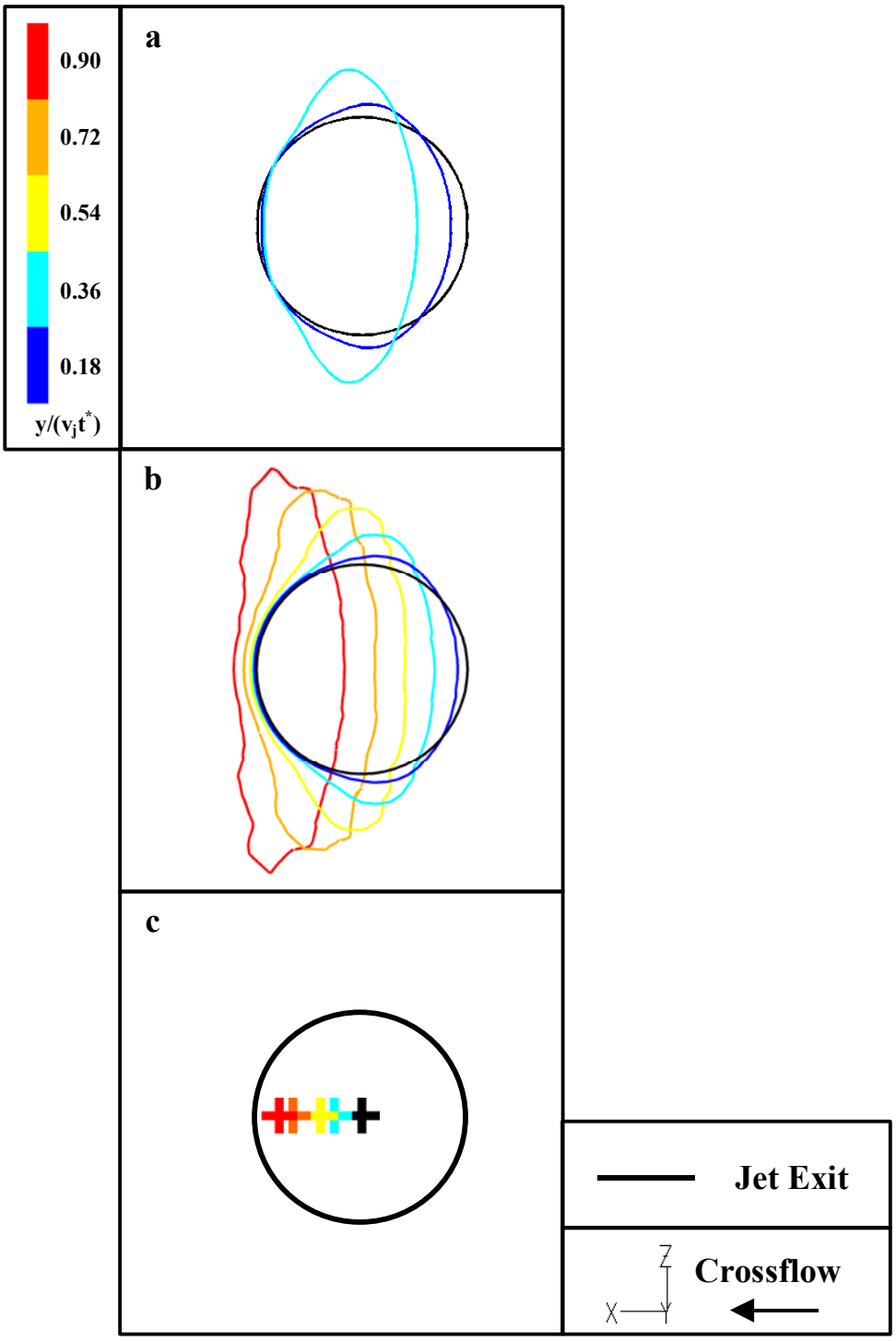

Figure 5.13 Visualization of liquid jet cross-sections as a function of normalized streamwise distance ($y/(v_j t^*)$) of round nonturbulent liquid jets in uniform gaseous crossflow within bag breakup regime ($We_G = 8$). (a) Two-dimensional computational model (Aalburg et al., 2005). (b) Present three-dimensional computational model. (c) Present experiments.

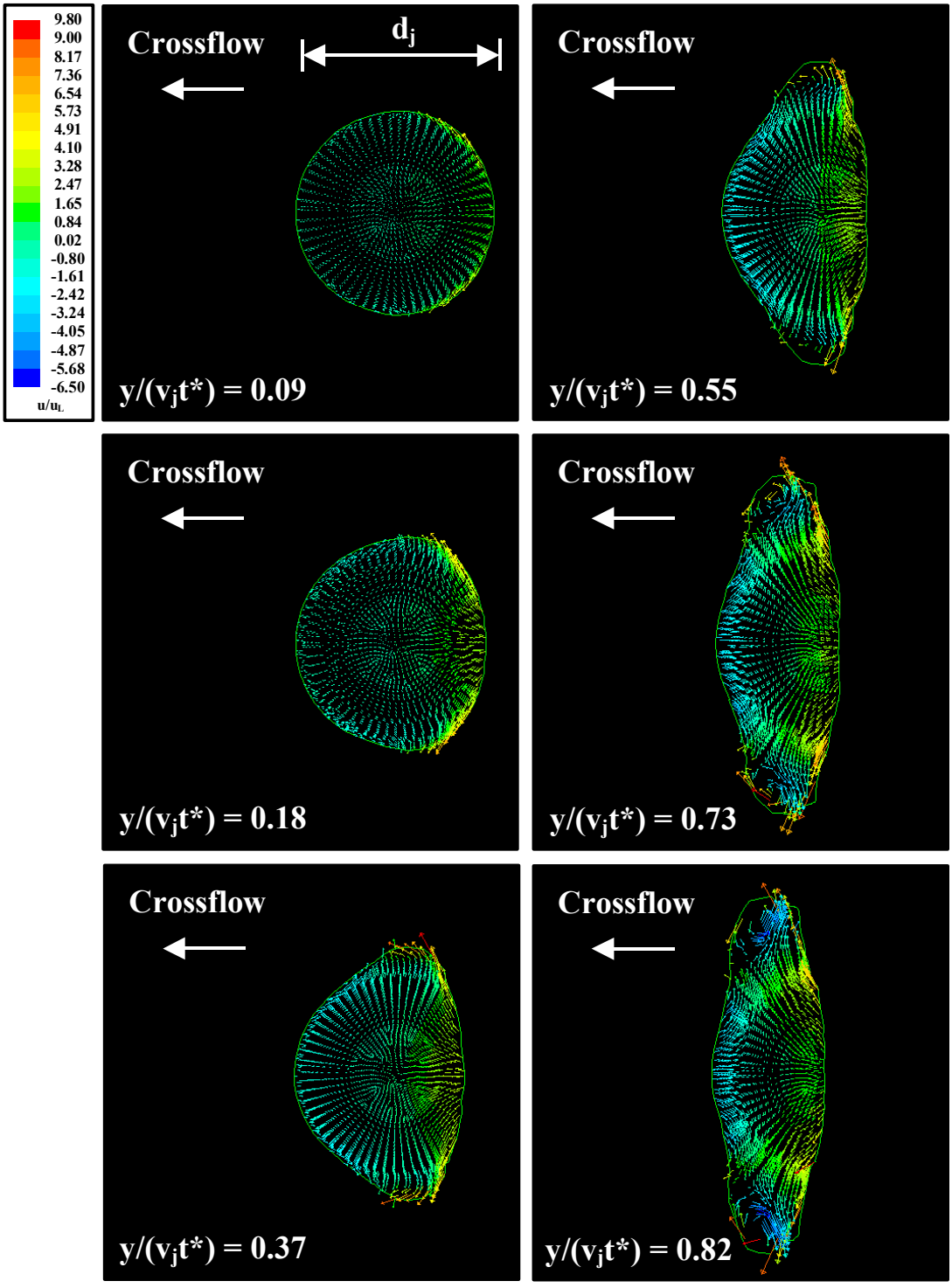

Figure 5.14 Internal flowfield of a round nonturbulent liquid jet in uniform gaseous crossflow within bag breakup regime (We_G = 8). Green line = liquid/gas interface. Length of vector represents xz-velocity normalized by u_L. For clarity, only 1/4 of the total numbers of vectors are displayed.

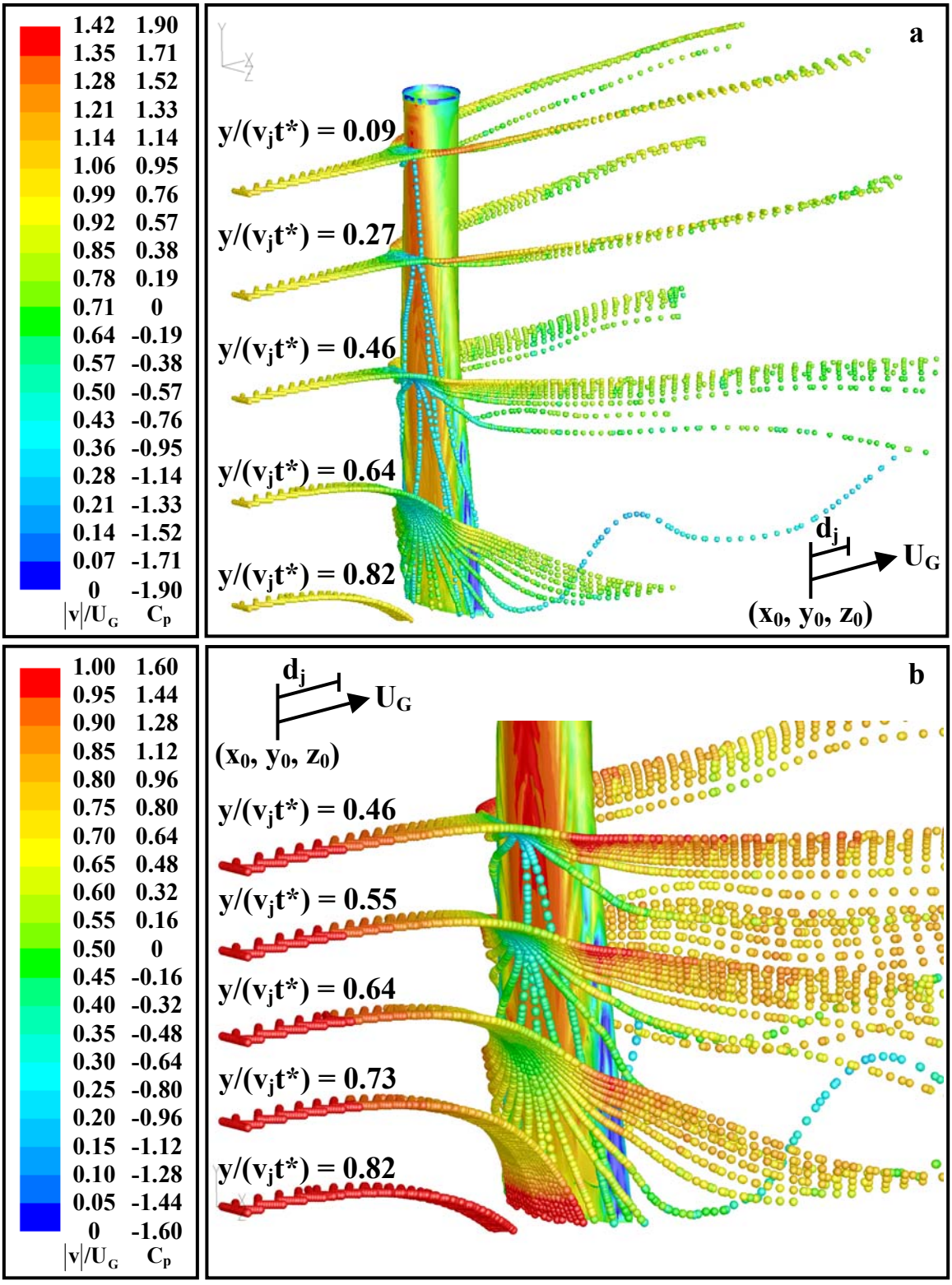

Figure 5.15 *Upwind* isometric view of the external flowfield of a round nonturbulent liquid jet in uniform gaseous crossflow within bag breakup regime (We_G = 8). Liquid jet surface is colored by C_p. Particle seeding is colored by $|v|/U_G$.

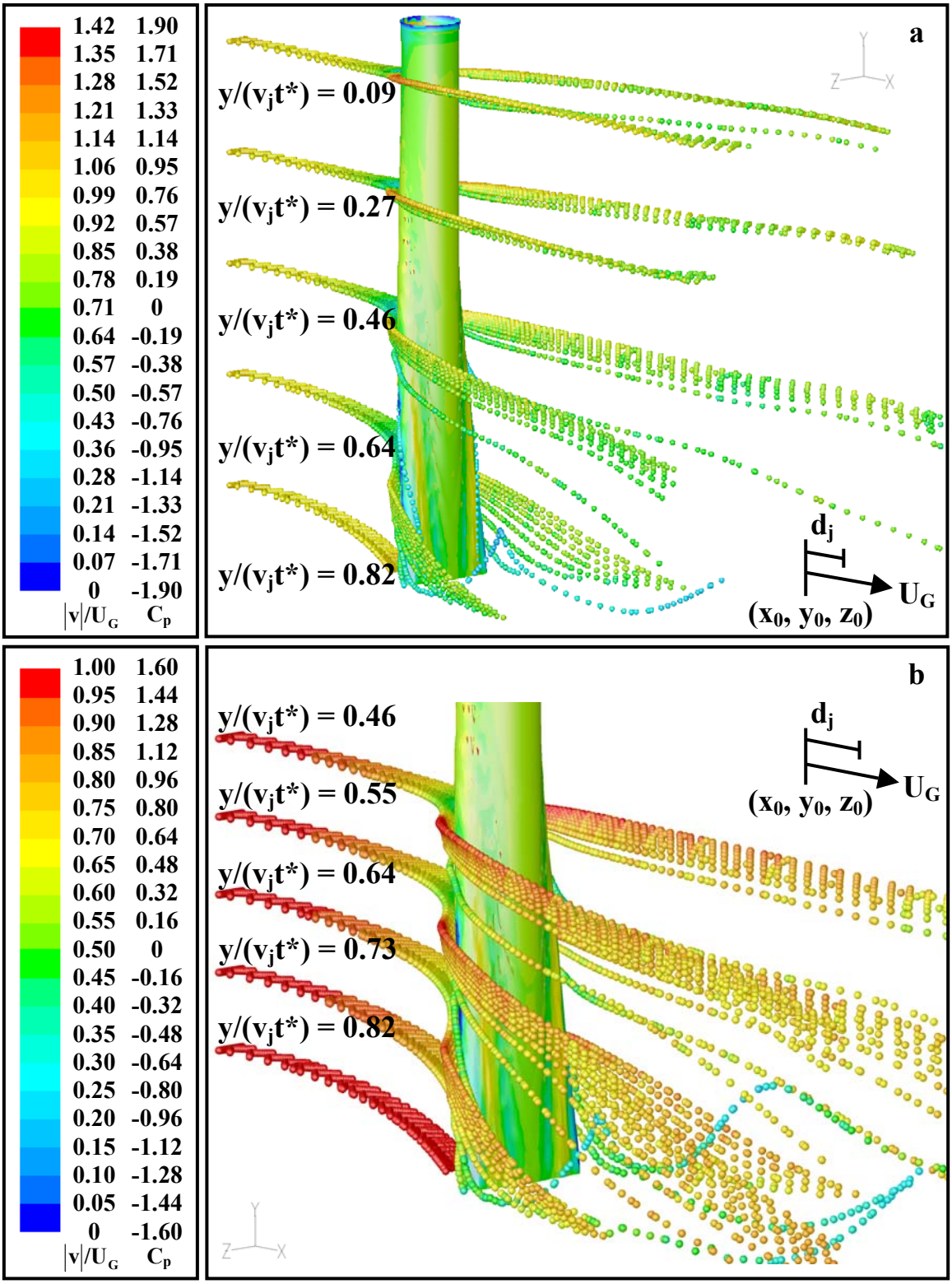

Figure 5.16 *Downwind* isometric view of the external flowfield of a round nonturbulent liquid jet in uniform gaseous crossflow within bag breakup regime (We_G = 8). Liquid jet surface is colored by C_p. Particle seeding is colored by $|v|/U_G$.

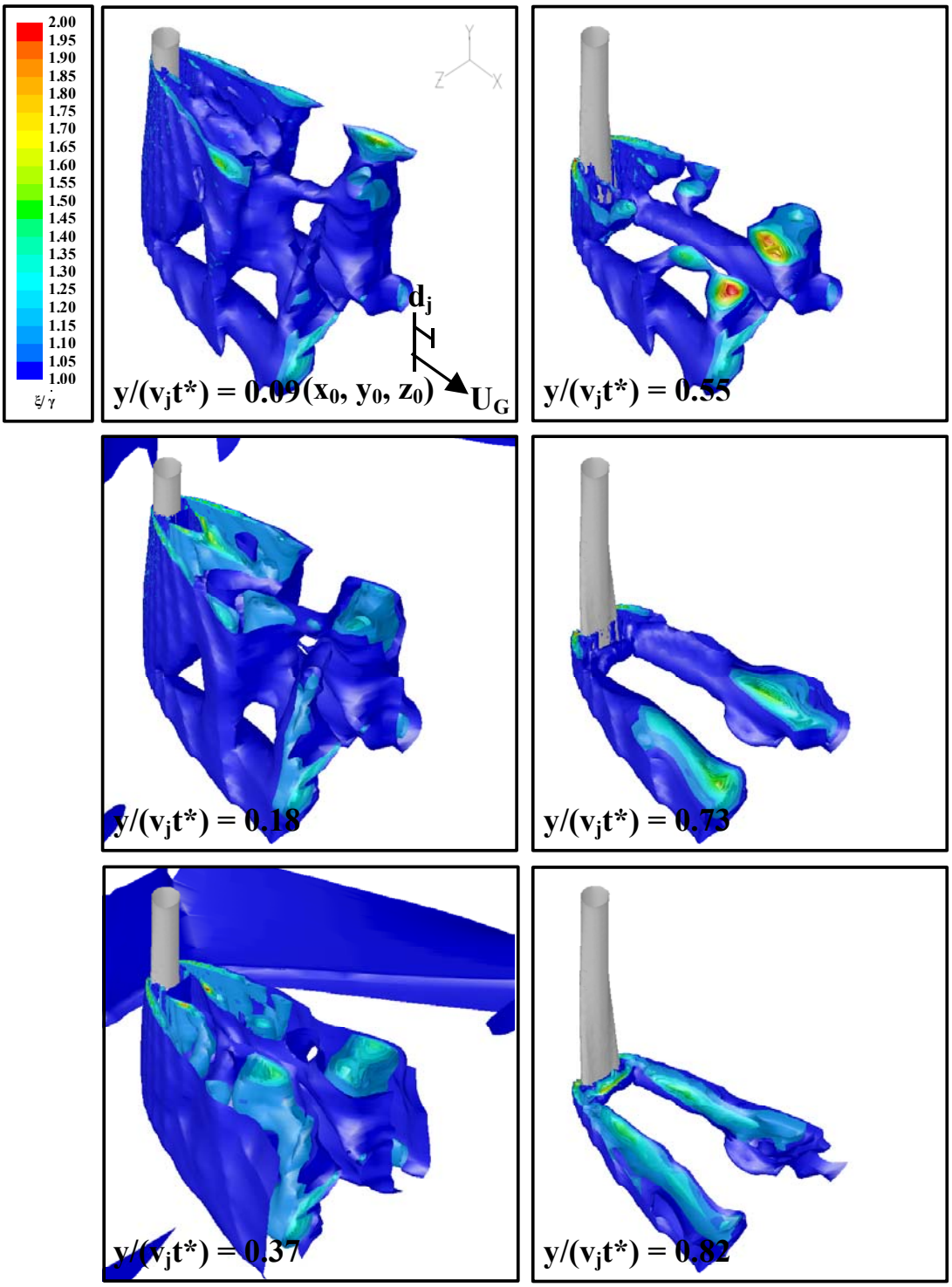

Figure 5.17 Non-dimensional iso-vorticity surfaces of the wake region of a round nonturbulent liquid jet in uniform gaseous crossflow within bag breakup regime (We_G = 8). Iso-vorticity surface is colored by $\xi/\dot{\gamma}$.

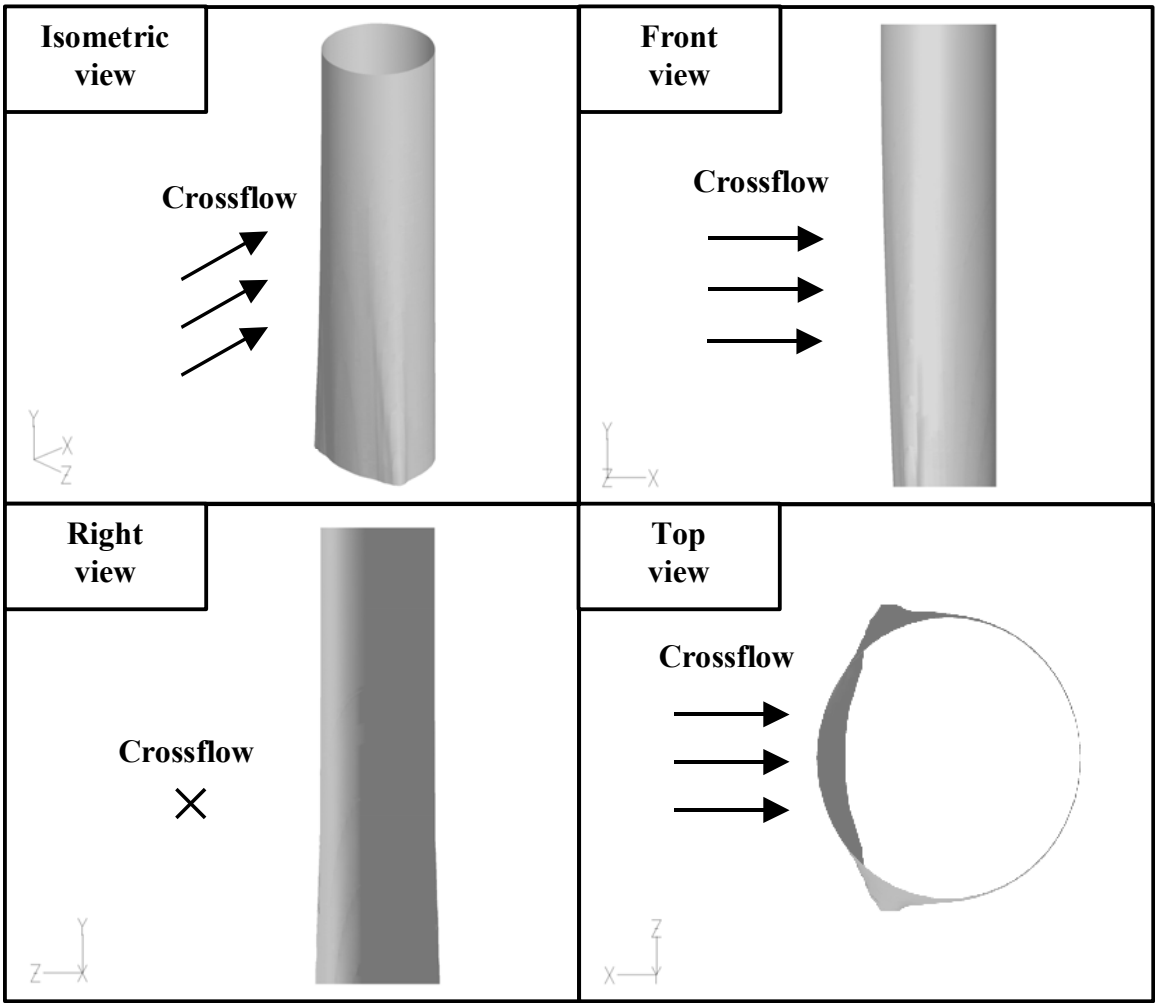

Figure 5.18 Flow visualization of a round nonturbulent liquid jet in uniform gaseous crossflow within shear breakup regime ($We_G = 220$).

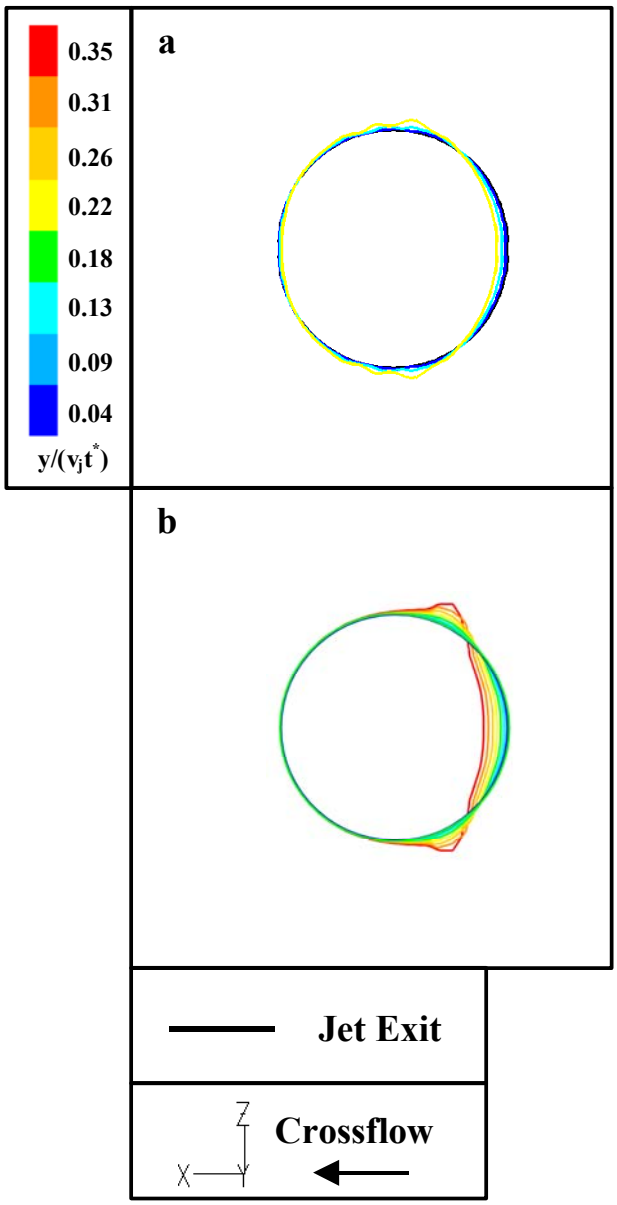

Figure 5.19 Visualization of liquid jet cross-sections as a function of normalized streamwise distance ($y/(v_j t^*)$) of a round nonturbulent liquid jets in uniform gaseous crossflow within shear breakup regime (We_G = 220). (a) Two-dimensional computational model (Aalburg et al., 2005). (b) Present three-dimensional computational model.

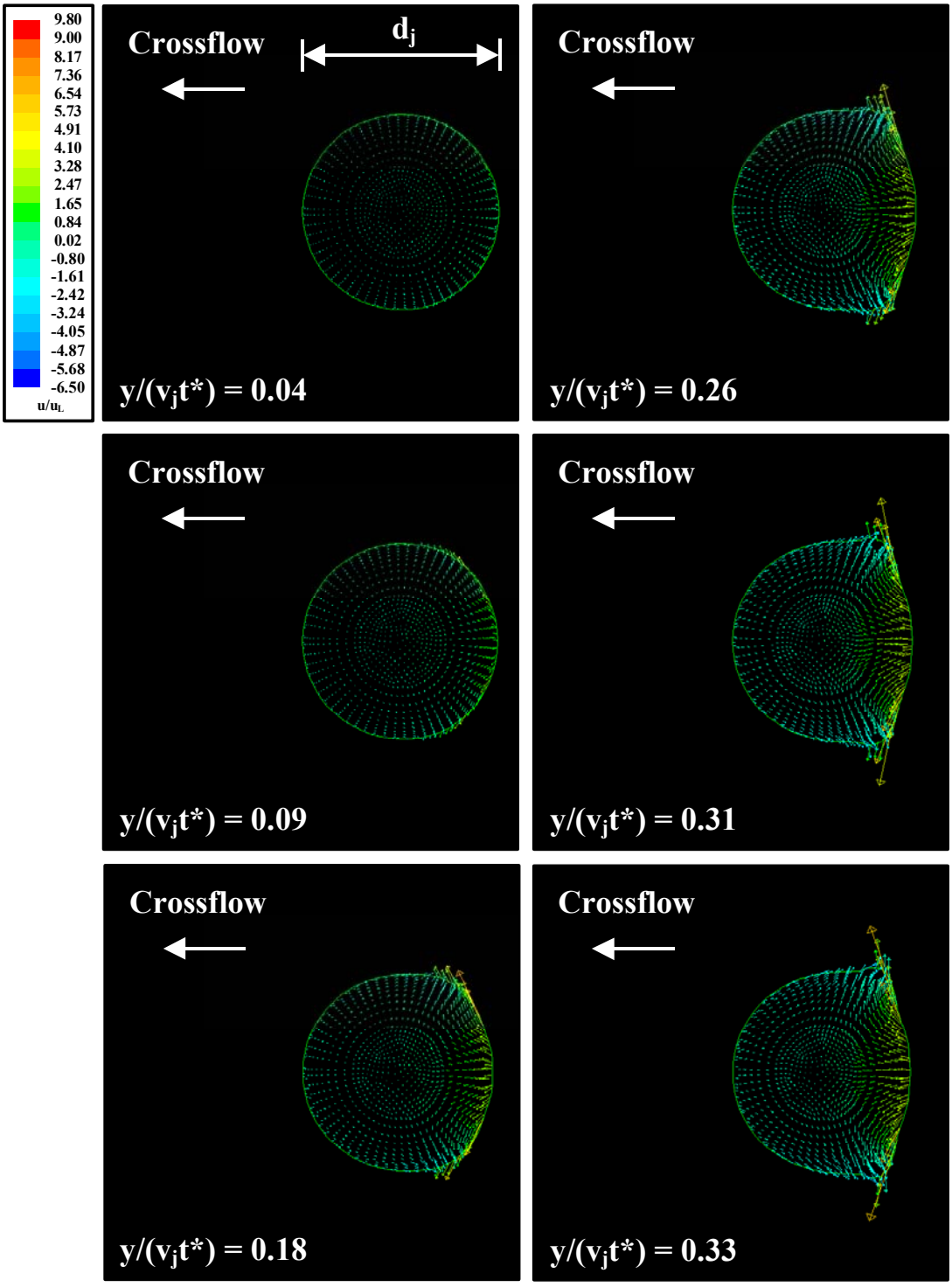

Figure 5.20 Internal flowfield of a round nonturbulent liquid jet in uniform gaseous crossflow within shear breakup regime (We_G = 220). Green line = liquid/gas interface. Length of vector represents xz-velocity normalized by u_L. For clarity, only 1/2 of the total numbers of vectors are displayed.

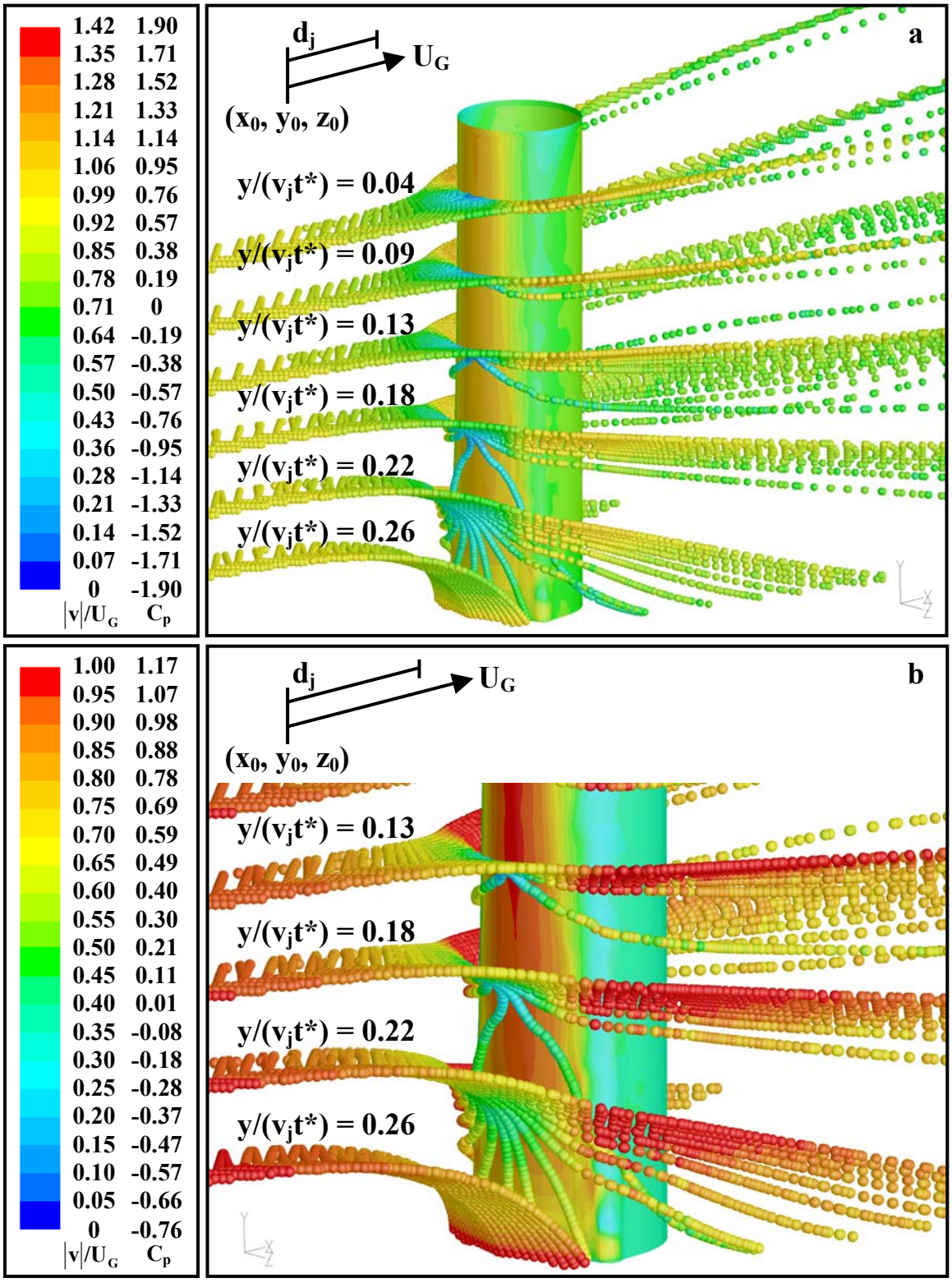

Figure 5.21 *Upwind* isometric view of the external flowfield of a round nonturbulent liquid jet in uniform gaseous crossflow within shear breakup regime (We_G = 220). Liquid jet surface is colored by C_p. Particle seeding is colored by $|v|/U_G$.

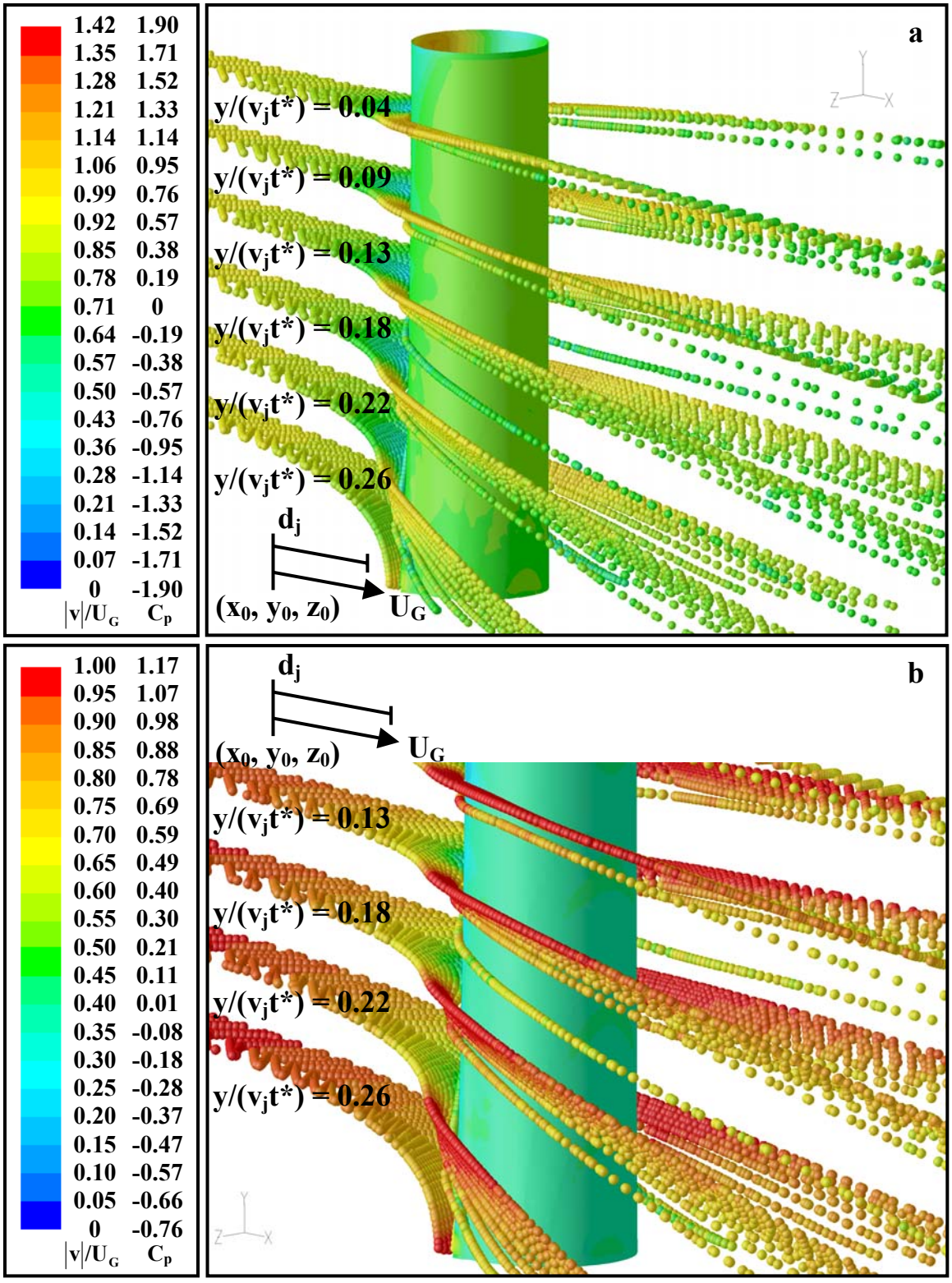

Figure 5.22 *Downwind* isometric view of the external flowfield of a round nonturbulent liquid jet in uniform gaseous crossflow within shear breakup regime (We_G = 220). Liquid jet surface is colored by C_p. Particle seeding is colored by $|v|/U_G$.

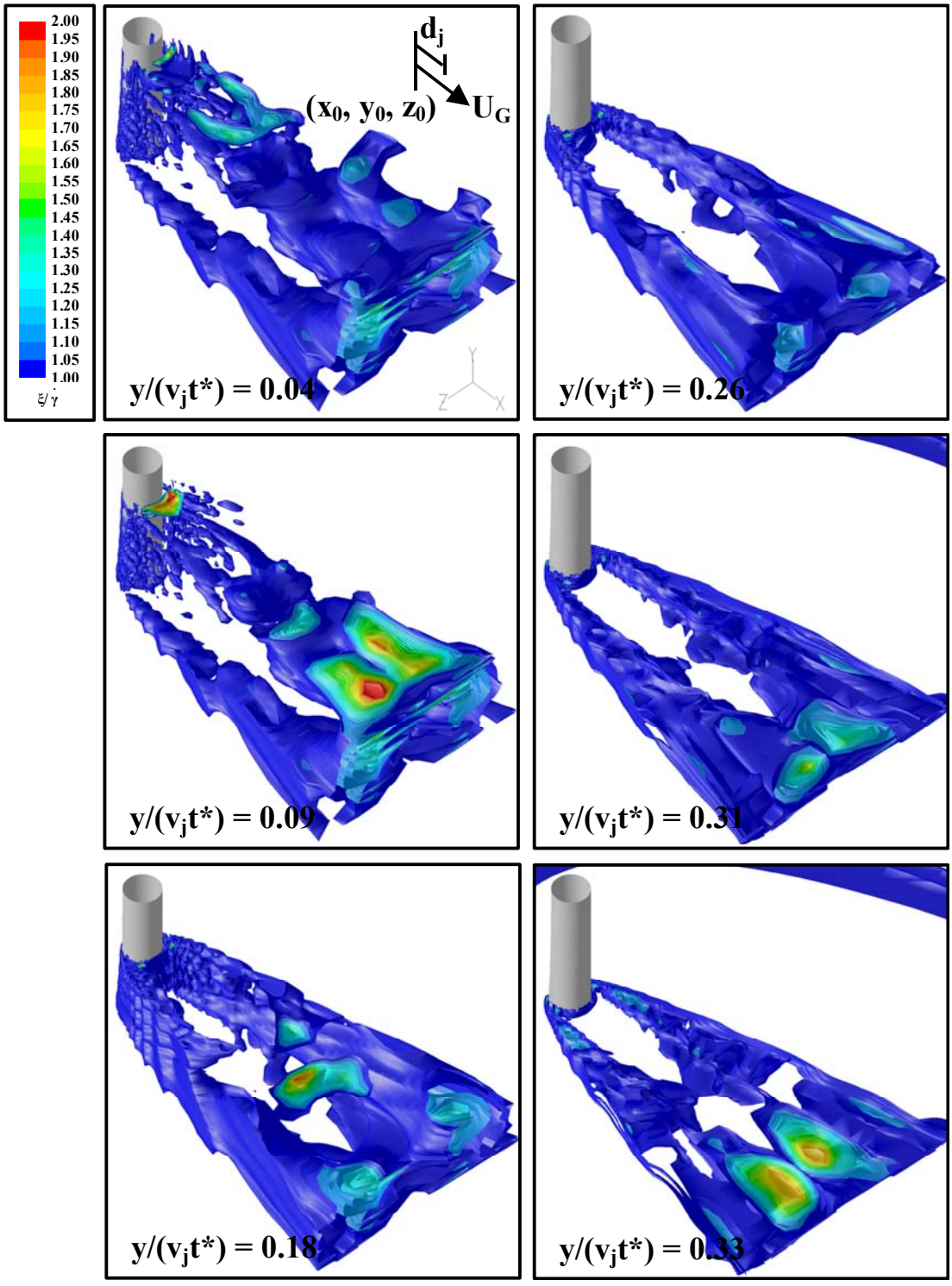

Figure 5.23 Non-dimensional iso-vorticity surfaces of the wake region of a round nonturbulent liquid jet in uniform gaseous crossflow within shear breakup regime ($We_G = 220$). Iso-vorticity surface is colored by $\xi/\dot{\gamma}$.

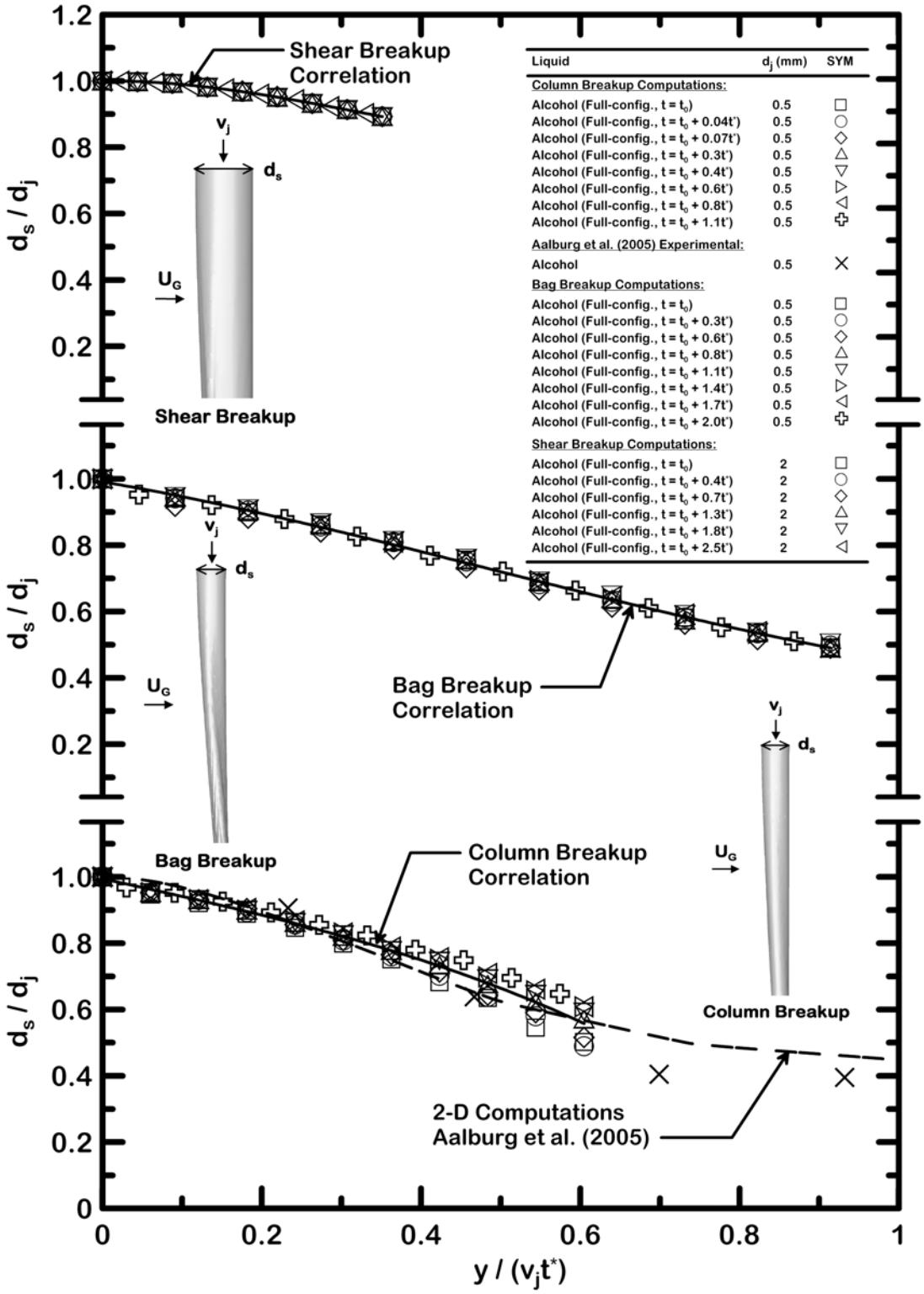

Figure 5.24 Normalized liquid cross-stream deformation as a function of normalized streamwise distance ($y/(v_j t^*)$) at different temporal time (t) of round nonturbulent liquid jets in uniform gaseous crossflow within column ($We_G = 3.5$), bag ($We_G = 8$), and shear ($We_G = 220$) breakup regime.

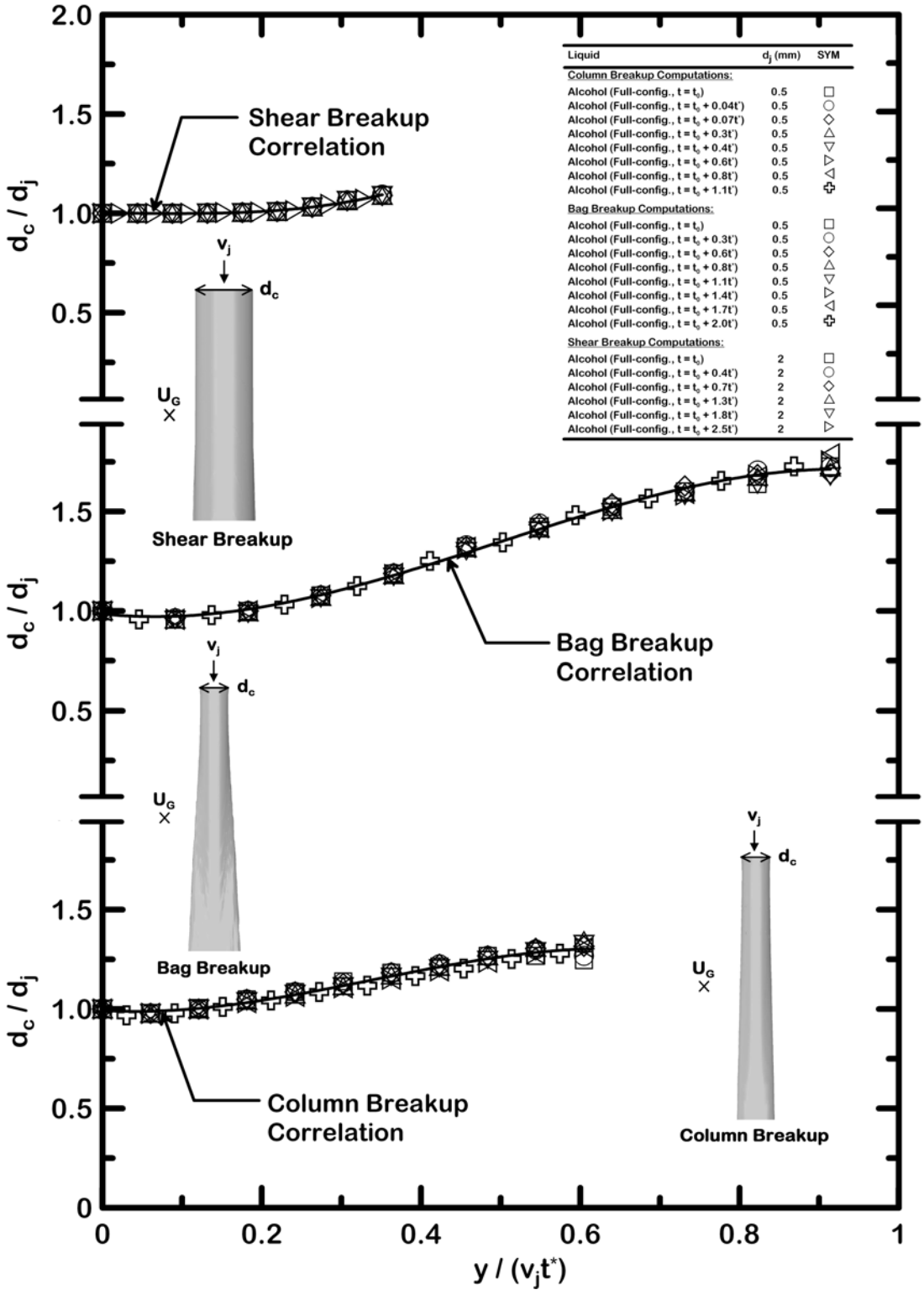

Figure 5.25 Normalized liquid span-wise deformation as a function of normalized streamwise distance ($y/(v_j t^*)$) at different temporal time (t) of round nonturbulent liquid jets in uniform gaseous crossflow within column (We_G = 3.5), bag (We_G = 8), and shear (We_G = 220) breakup regime.

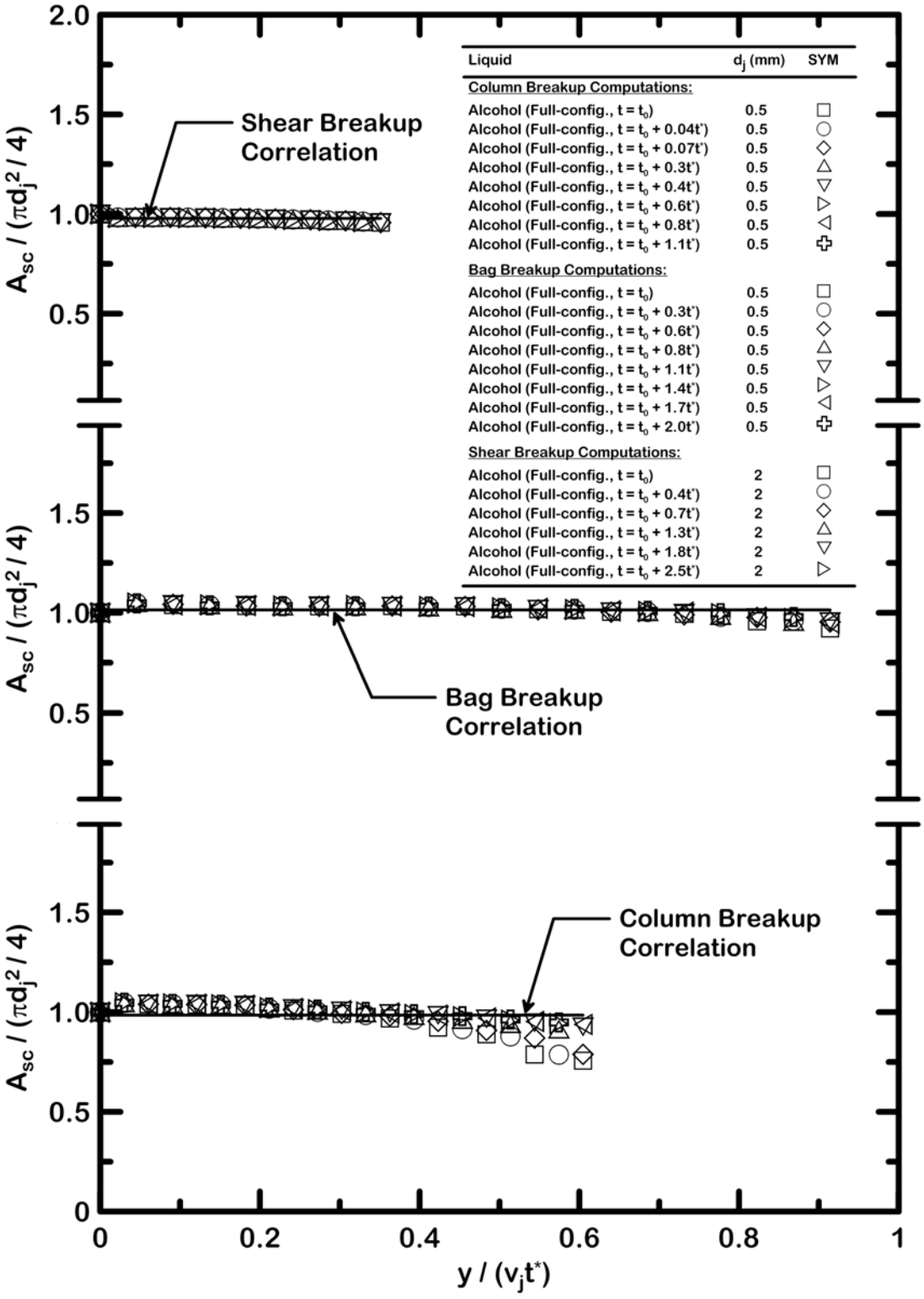

Figure 5.26 Normalized liquid cross-sectional area as a function of normalized streamwise distance ($y/(v_j t^*)$) at different temporal time (t) of round nonturbulent liquid jets in uniform gaseous crossflow within column (We_G = 3.5), bag (We_G = 8), and shear (We_G = 220) breakup regime.

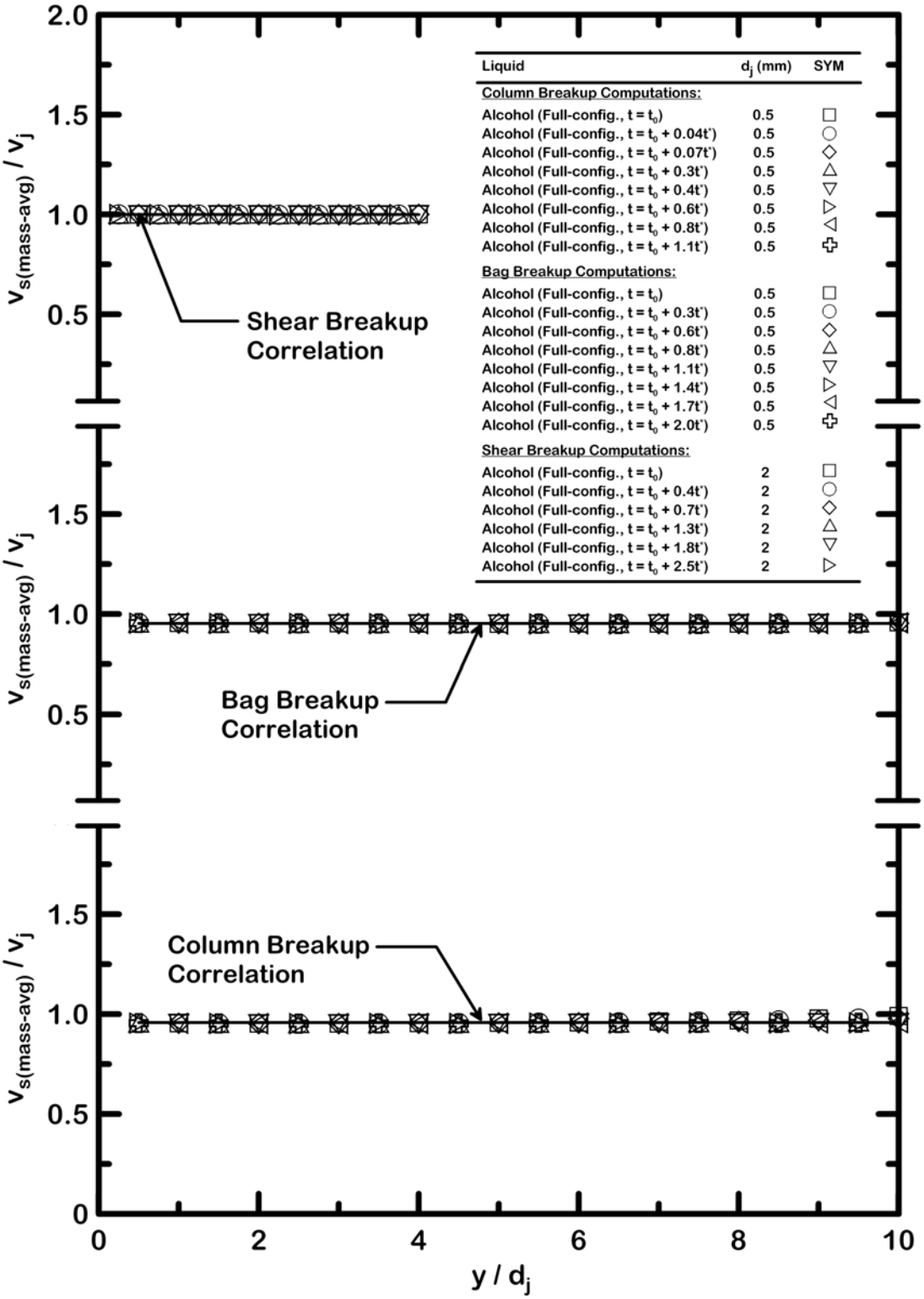

Figure 5.27 Normalized mass-weighted average velocity of the liquid cross-section as a function of streamwise distance at different temporal time (t) of round nonturbulent liquid jets in uniform gaseous crossflow within column (We_G = 3.5), bag (We_G = 8), and shear (We_G = 220) breakup regime.

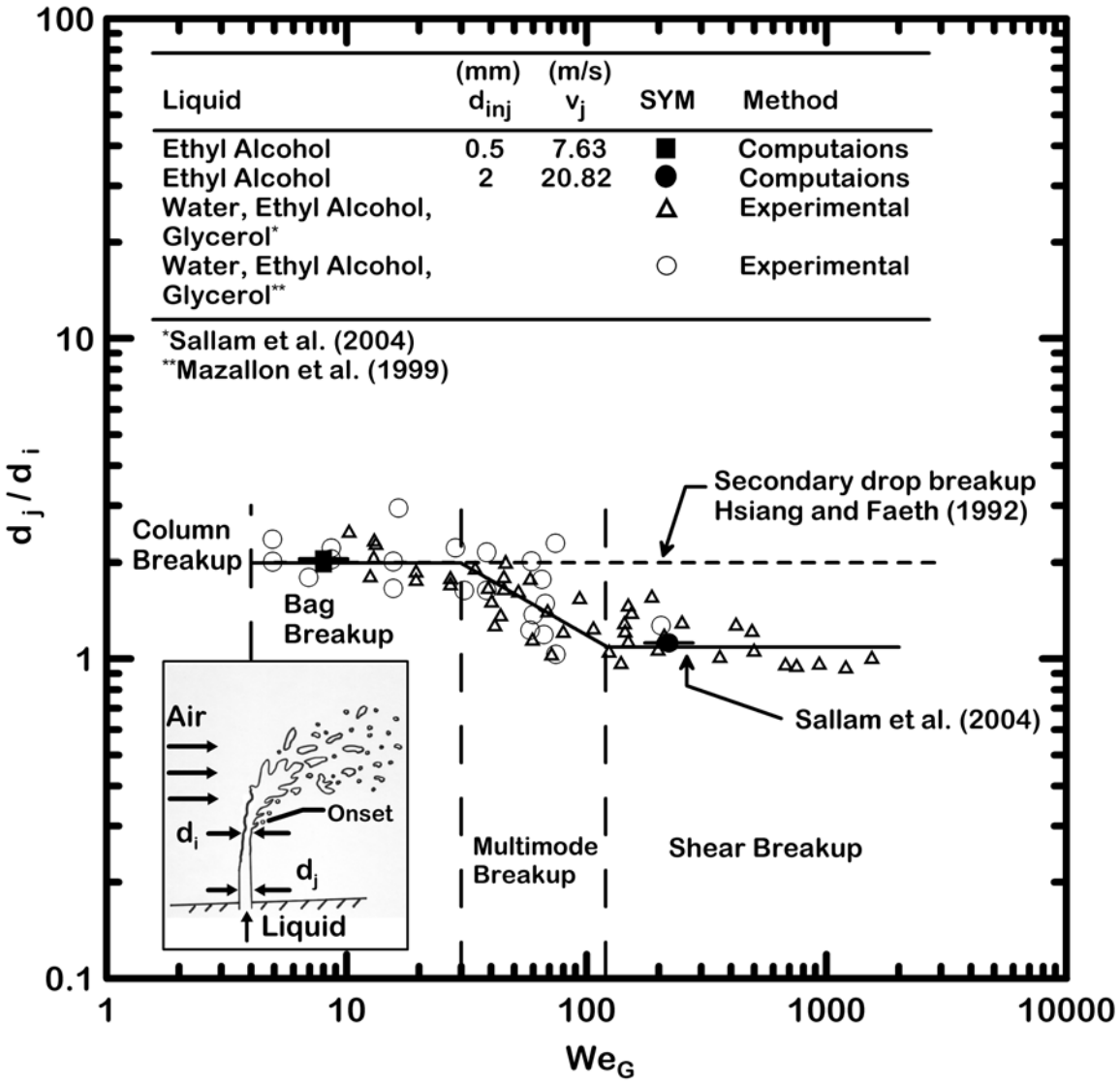

Figure 5.28 Deformations at the onset of primary breakup as a function of crossflow Weber number.

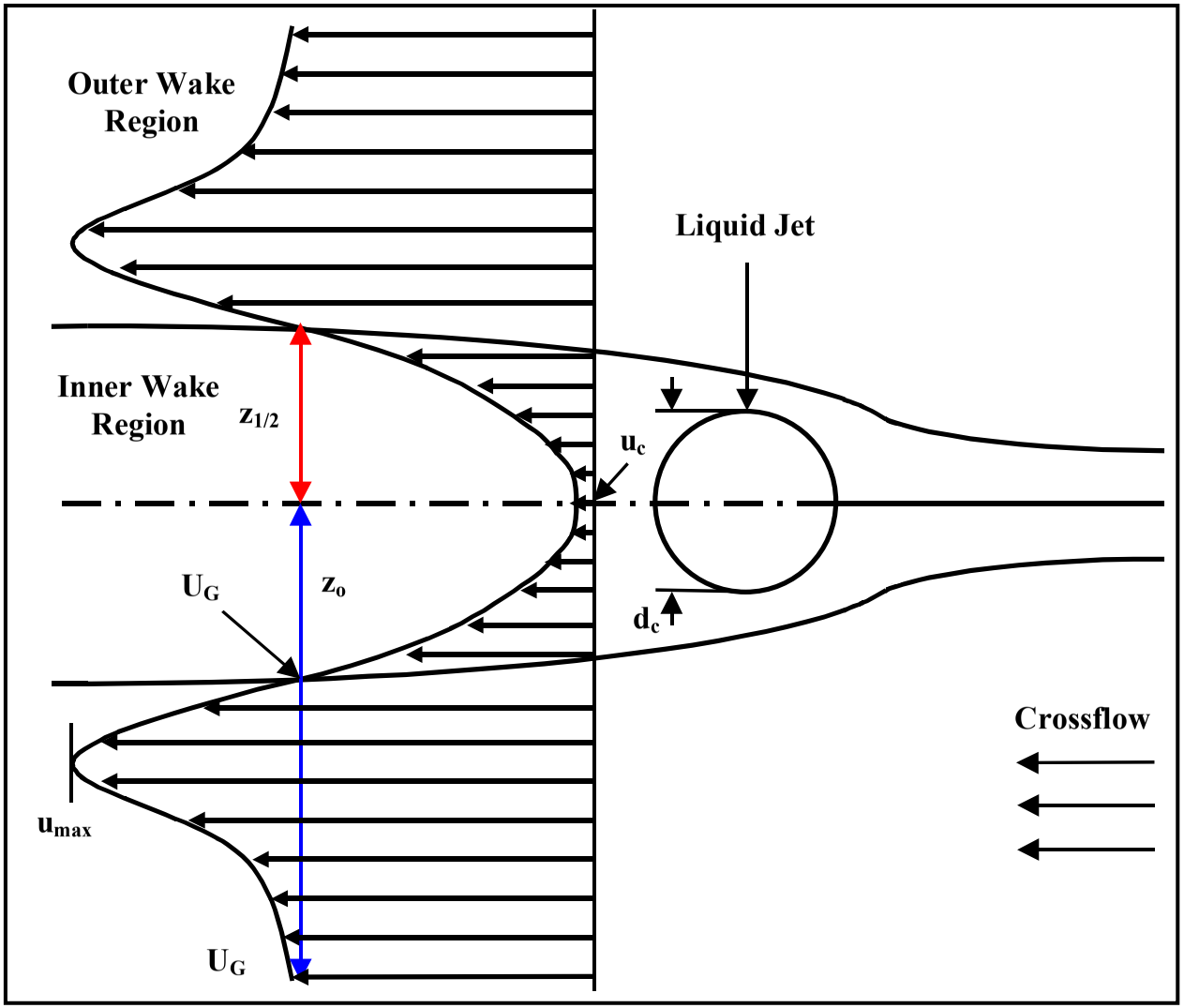

Figure 5.29 Sketch of the wake region of round nonturbulent liquid jets in uniform gaseous crossflow.

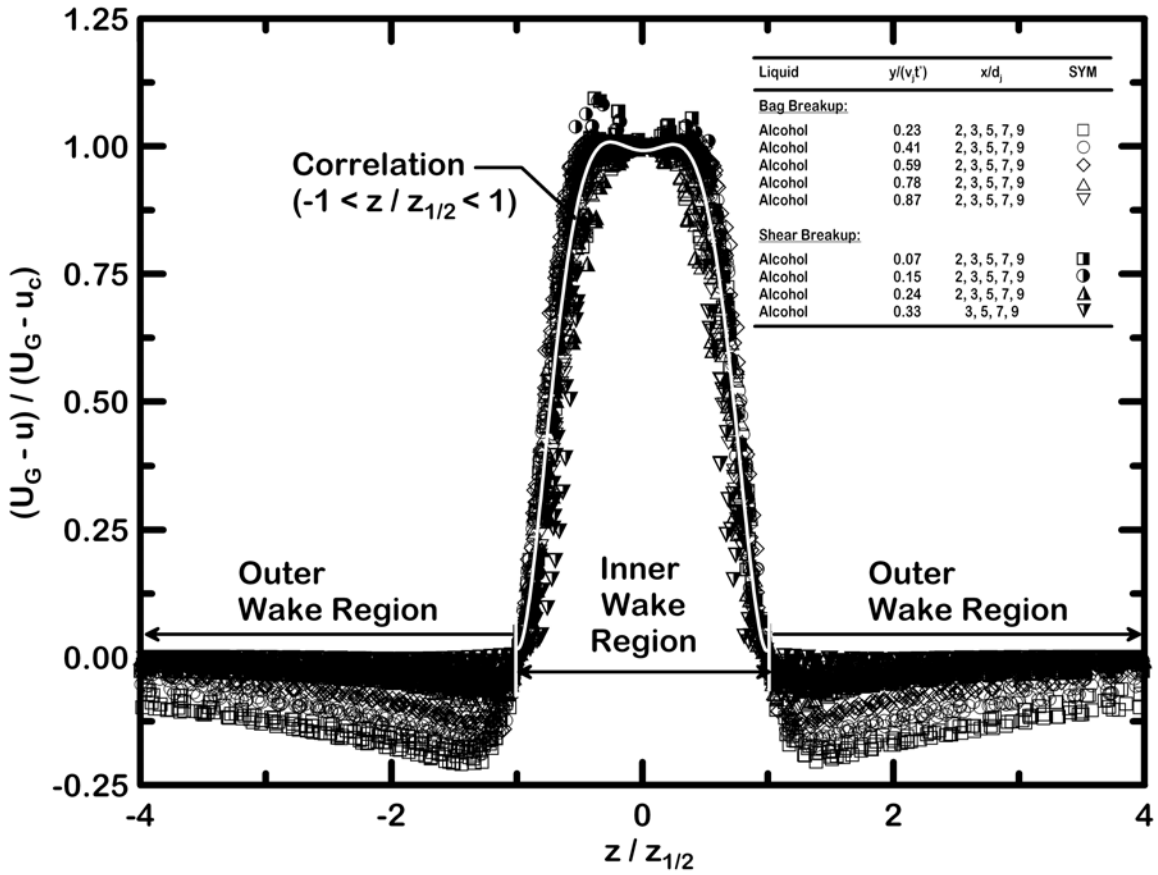

Figure 5.30 Normalized inner wake velocity defect ($z < z_{1/2}$) as a function of normalized span-wise distance for bag and shear breakup.

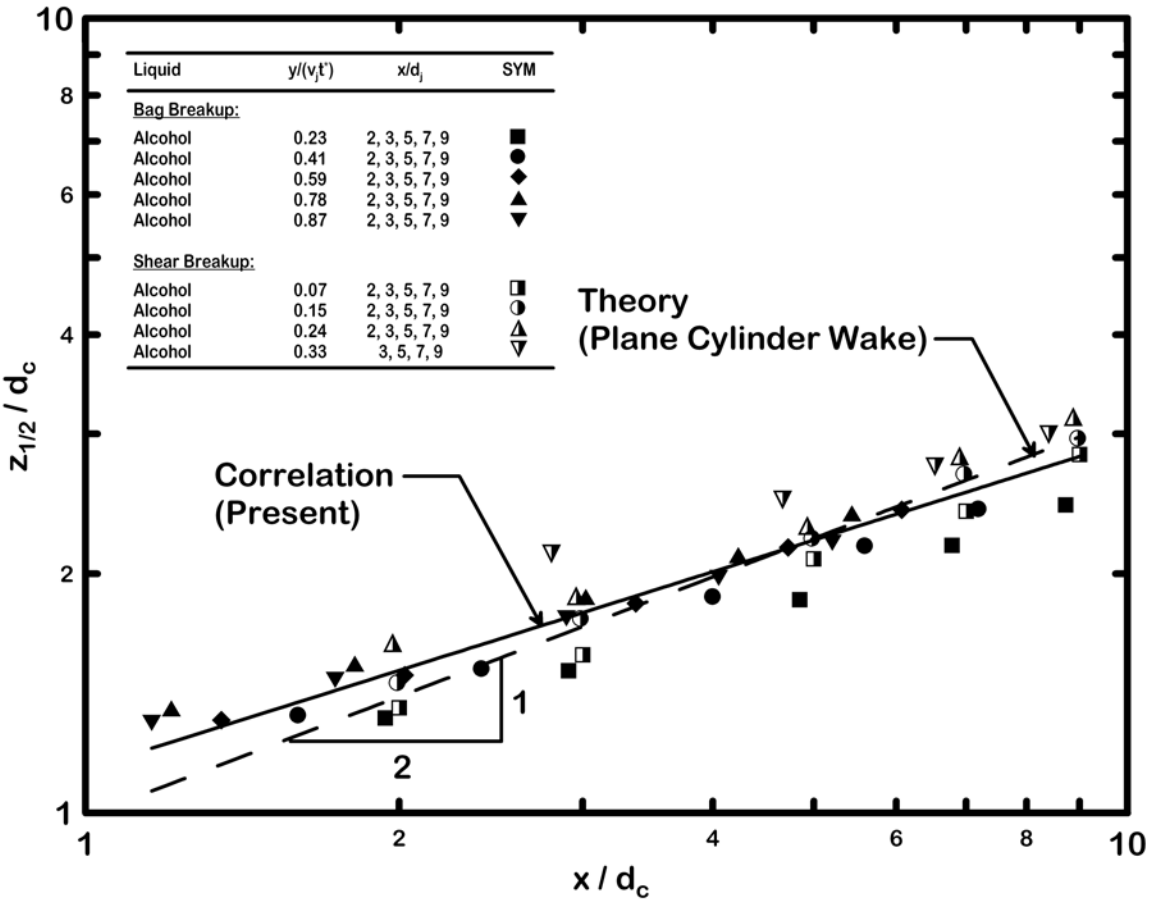

Figure 5.31 Wake half width normalized by the jet span-wise diameter as a function of cross-stream distance normalized by the jet span-wise diameter for bag and shear breakup.

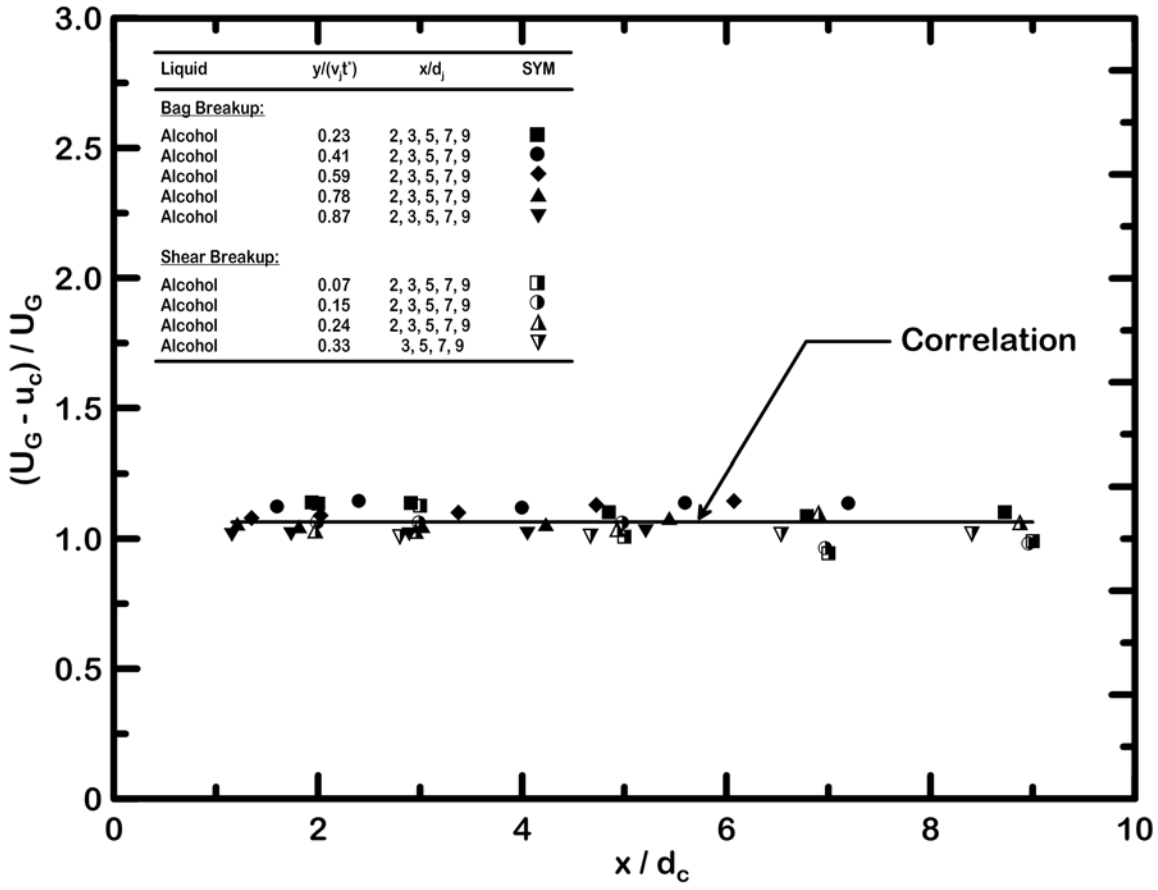

Figure 5.32 Centerline velocity of the wake region as a function of cross-stream distance normalized by the jet span-wise diameter for bag and shear breakup.

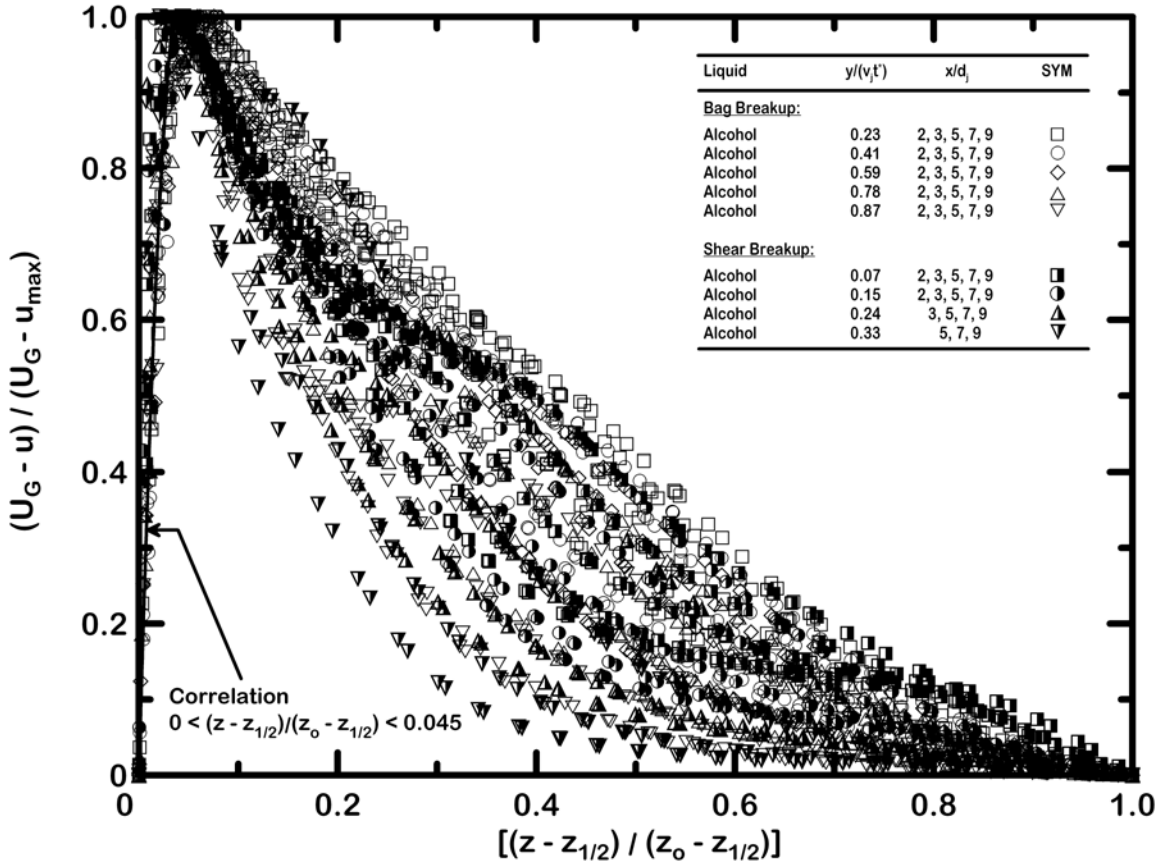

Figure 5.33 Normalized outer wake velocity defect ($z > z_{1/2}$) as a function of normalized span-wise distance for bag and shear breakup.

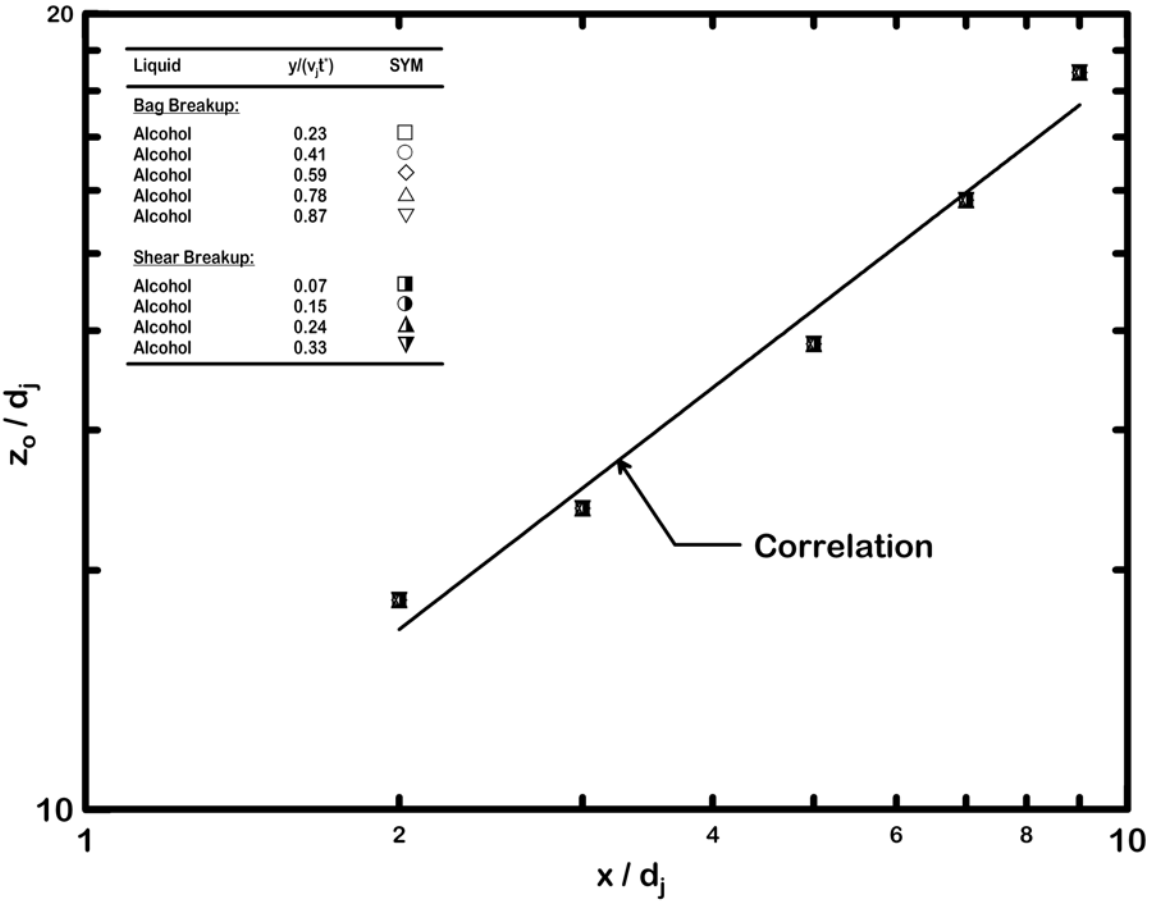

Figure 5.34 Width of the outer wake region normalized by the nozzle exit diameter as a function of the cross-stream distance normalized by the nozzle exit diameter for bag and shear breakup.

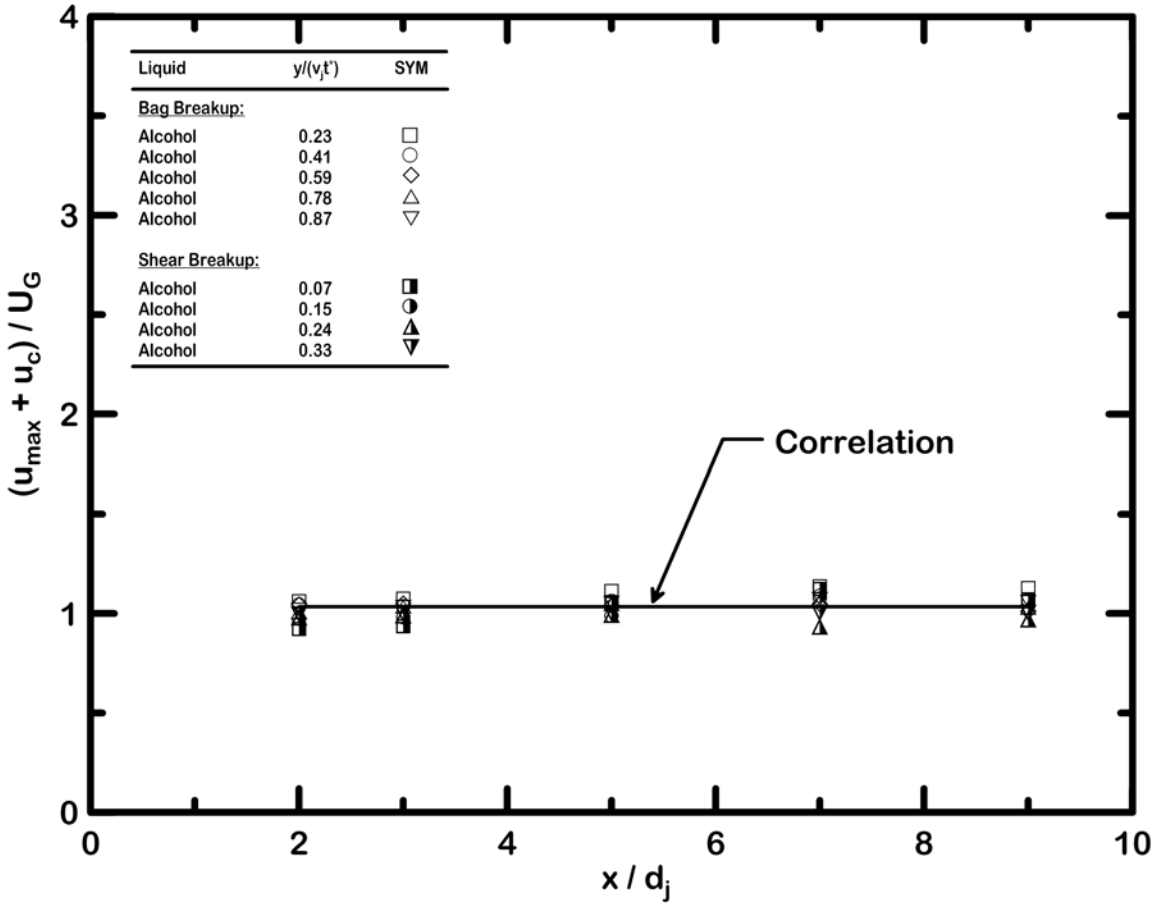

Figure 5.35 The sum of maximum velocity and centerline velocity of the wake region normalized by the crossflow velocity as a function of cross-stream distance normalized by the nozzle exit diameter for bag and shear breakup.

CHAPTER VI

SUMMARY AND CONCLUSIONS

6.1 Summary

The experimental study of this research presented pulsed photography, single- and double-pulsed shadowgraphy, and high-speed imaging measurements of the wave phenomena and the droplets properties/transport dynamics of round nonturbulent liquid jets in uniform gaseous crossflow within the bag breakup regime. Observations related to the formation and the breakup of the bag-like structures were documented and discussed. Test conditions included pressure-fed supercavitating nozzles of 0.5 mm, 1 mm, and 2 mm using water (tap and distilled) and ethyl alcohol as the test liquids for various crossflow Weber numbers (4 to 29) and liquid jet momentum ratio (9 to 1199) and small Oh number (< 0.1).

A three-dimensional time-accurate computational study of the deformation and surface properties of round nonturbulent liquid jets in uniform gaseous crossflow within the column, bag, and shear breakup regime has been carried out using the Volume of Fluid (VOF) model. The surface tension test and computed surface properties including jet diameter in still air, jet cross-stream deformation, jet velocity, and column and surface wavelengths employed for validation tests agree with theoretical results and experimental measurements within experimental and computational uncertainties. Observations

related to the entire flow field of the external (gaseous) and the internal (liquid) phases and the impact on the different breakup regimes were discussed.

6.2 Conclusions

The major conclusions of the present experimental study are as follows:

1. The breakup of nonturbulent liquid jets in crossflow is not due to initial disturbances within the jet but rather due to the aerodynamic effects of the crossflow.
2. In bag breakup, the column waves are attributed to Rayleigh-Taylor instability, which, in the presence of surface tension, will tend to have maximum growth rate at a unique range of wave numbers.
3. The velocity of the liquid surface normalized by the nozzle exit velocity approaches unity, independent of the streamwise distance of the liquid jet.
4. The column waves convect along the liquid column with increasing amplitude.
5. The bag-like structure is formed as a result of the deformation of the central portion of the liquid column due to high pressure produced by the stagnating gas on the upwind side of the flattened liquid column.
6. The downwind surface waves occur in the vicinity of the sides of the downwind surface of the liquid column. The downwind surface wavelength decreases as the crossflow Weber number increases.
7. The number of bags formed along the liquid column depends on the length of liquid column from the onset of bag formation to the end of liquid core normalized by the column wavelength.

8. Bag-structures with multiple-nodes layouts (typically 4, 5, …, 8 nodes) were observed. The 4- to 6-node layouts are the one most typically observed. The nodes layout per bag affected the breakup mechanism of the bags. The span-wise distance between the nodes increases in the streamwise direction of the liquid jet.
9. During the bag breakup, the bag-like structure grows progressively in the streamwise direction and eventually breaks up after reaching a maximum size. The bag-membrane typically opens from the bottom side in the downwind direction because the bottom side is progressively stretched by the increasing span-wise separation between the nodes. The onset of breakup begins with the formation of ligaments. The bag-droplets subsequently formed at the tip of the ligaments due to Rayleigh breakup. The breakup of the membrane results in a large number of very small droplets (bag-droplet, d_{Bag}).
10. During the ring breakup, the two strings of node drops connected by thinner liquid column breaks up (Rayleigh breakup), resulting in a poly-disperse array of large drops associated with the presence of the nodes (d_{Node}) and the breakup of their connecting liquid columns (d_{Ring}).
11. The sizes of the droplets produced are related to the breakup of the bag-like structure. The smallest drops are associated with the breakup of the membrane of the bags; the largest drops are associated with the breakup of nodes; and the medium size droplets are associated with the breakup of the thinner liquid columns connecting the node drops. The total volume of liquid droplets per bag structure is approximately equal to $4.2 d_j We_G^{-0.26}$.

12. The Sauter Mean Diameter (SMD) of the node- and ring-droplet are inversely proportional to the crossflow Weber number (We_G). The SMD of the bag-droplet is constant, independent of We_G.
13. The streamwise and cross-stream velocities of the node-, ring-, and bag-droplet are independent of their sizes. Immediately after bag breakup, the node- and ring-droplet traveled with approximately the same streamwise and cross-stream velocities. The bag-droplet traveled with a higher cross-stream velocity but a lower streamwise velocity than the node- and the ring-droplets due to the high pressure produced by the stagnating gas on the upwind side of the bag-like structure, propelling the bag-droplets after the breakup of the bag-membrane in the cross-stream and negative streamwise directions (owing to the deflection of the liquid column).
14. The different upper and lower trajectories for bag- and node-droplet suggested that separation of bag- and node-droplet for spraying and atomization applications are possible.

The major conclusions of the present computational study are as follows:

1. In column and bag breakup, the liquid column deforms from a circular cross-section into an ellipsoidal cross-section. The lateral motion is eventually stabilized by the surface tension forces. The increased drag forces due to the ellipsoidal cross-section enhance the tendency of the liquid column to deflect downstream with respect to the gas motion.
2. In column and bag breakup, jet deformation is caused by accelerating gas along the side of the liquid column, resulting in the reduction of gas pressure along the

sides. This forces the liquid within the cross-section to move in the span-wise direction toward the two sides of the liquid column until the jet cross-section is eventually stabilized by the surface tension forces.

3. In shear breakup, the liquid column maintained a circular configuration. Prior to the onset of breakup, the upwind surface of the liquid column was flattened. As such, the flow around the liquid column resembled the flow around a blunt body. Separation occurred near the sides of the upwind surface of the jet, terminating the deformation of the liquid column before the onset of breakup.
4. In column breakup, varicose column waves are observed to convect along the liquid column, characterized by a wavelength separation, λ_c. In bag breakup, both sinuous column waves and downwind surface waves are observed to convect along the liquid column, characterized by a wavelength separation, λ_c and λ_s, respectively. Therefore, the surface properties of liquid jets in gaseous crossflow are three-dimensional.
5. In the present three-dimensional model the jet is anchored to the nozzle exit. This is not possible with the two-dimensional model of Aalburg et al. (2005) and thus the present model predicts the trajectory of the liquid jet more accurately.
6. Vortex shedding is observed behind the liquid jet for all breakup regimes. In column and bag breakup, the wake consists of alternating pairs of vortices similar to Karman vortex streets. In shear breakup, however, the wake consists of non-alternating pairs.

7. In bag breakup, the flowfield inside the liquid jet prior to the onset of primary breakup consists of a counter-rotating vortex pair. This was not observed in column and shear breakup.
8. In all breakup regimes, the temporal liquid cross-sectional area normalized by the nozzle exit area (A_{sc}/A_j) and the temporal mass-weighted average velocity of the liquid cross-section ($v_{s(mass\text{-}avg)}/v_j$) are of unity. This suggests little or no drag forces in the streamwise direction.
9. The wake region of the liquid jet for both bag and shear breakup regimes and for a downstream distance of 10 span-wise jet diameters, can be described as follows:
    i. The normalized wake velocity defect as a function of normalized span-wise distance is independent of the streamwise and cross-stream directions.
    ii. The inner wake width normalized by the jet span-wise diameter agrees with the theoretical predictions for a wake behind a cylinder. The centerline velocity of the wake region is independent of the cross-stream distance normalized by the jet span-wise diameter.
    iii. The width of the outer wake region normalized by the nozzle exit diameter is independent of the streamwise distance.
    iv. The sum of the maximum velocity and the centerline velocity of the wake region normalized by the crossflow velocity is independent of the cross-stream distance normalized by the nozzle exit diameter.

6.3 Recommendations for future Studies

Based on the present experimental and computational results for the deformation, wave phenomena, and breakup outcomes of round nonturbulent liquid jets in uniform gaseous crossflow, the following recommendations are made concerning future study of these processes:

1. The present experimental study of round nonturbulent liquid jets in uniform gaseous crossflow within the bag breakup regime was carried out at small Ohnesorge number (< 0.1). As many practical applications, e.g., diesel engines, are subjected to high viscous effects, addressing the measurements at high Ohnesorge number (> 0.1) is suggested.
2. Although the breakup mechanisms of the liquid jets within the bag breakup regime are identified experimentally in this study, the parameters that control the physical mechanism of membrane breakup is not completely understood. The location of the onset of breakup of the bag-membrane, the thickness of the membrane prior to breakup, and the variations in the velocities of bag-droplet clearly merit more attention.
3. As many practical atomizers are often subjected to some level of ambient velocity fluctuations, addressing the turbulent effect of the crossflow is suggested.
4. A time-accurate three-dimensional computational model that extends beyond the onset of breakup is needed to study the breakup mechanisms of liquid jets in crossflow that are difficult to address experimentally.
5. The crossflow Weber number for the breakup regime transitions from shear breakup to catastrophic breakup of liquid jets in crossflow is not known. The

experimental study can be performed in a shock tube with instrumentation setup similar to the present study. The study may also be approached computationally using a model that is more time efficient than the one used in the present study.

BIBLIOGRAPHY

Aalburg, C., van Leer, B., Faeth, G. M., and Sallam, K. A., 2005, "Properties of Nonturbulent Round Liquid Jets in Uniform Gaseous Crossflows," *Atomization and Sprays*, vol.15, no.3, pp. 271-294.

Aalburg, C., van Leer, B., and Faeth, G. M., 2003, "Deformation and Drag Properties of Round Drops Subjected to Shock Wave Disturbances," *AIAA J.*, vol. 4, no. 2, pp. 2371-2378.

Aalburg, C., 2002, "Deformation and Breakup of Round Drops and Nonturbulent Liquid Jets in Uniform Crossflow," *PhD Dissertation*, University of Michigan, Aerospace engineering and Scientific Computing, Ann Arbor, MI.

Brackbill, J. U., Kothe, D. B., Zemach, C., 1992, "A Continuum Method for Modeling Surface Tension," *J. Comput. Phys.*, 100:335-354.

Chorin, A. J., 1968, "Numerical Solution of the Navier-Stokes Equations," *Math. Comp.*, vol. 22, no. 104, pp. 745-762.

Chryssakis, C. A. and Assanis, D. N., 2005, "A Secondary Atomization Model for Liquid Droplet Deformation and Breakup under High Weber Number Conditions," *ILASS Americas, 18th Annual Conference on Liquid Atomization and Spray Systems*, Irvine, CA, May 2005.

Crow, E. L., Davis, F. A., and Maxfield, M. W., 1955, Statistics Manual, Dover Press.

Dai, Z. and Faeth, G. M., 2001, "Temporal Properties of Secondary Breakup in the Multimode Breakup Regime," *Int. J. Multiphase Flow*, vol. 27, pp. 217-236.

El-Ansary, N. F., Hoshoudy, G. A., Abd-Elrady, A. S., and Ayyad, H. A., 2002, "Effects of Surface Tension and Rotation on the Rayleigh-Taylor Instability," *Phys. Chem. Chem. Phys.*, vol. 4, 1464-1470.

Faeth, G. M., 1997, "Spray Combustion Phenomena," In: *Twenty Sixth Symposium (International) on Combustion*, The Combustion Institute, Pittsburgh, Pennsylvania, U. S. A., pp. 1593-1612.

Faeth, G. M., Hsiang, L.-P., Wu, P.-K, 1995, "Structure and Breakup Properties of Sprays," *Int. J. Multiphase Flow*, vol. 21, Suppl., pp. 99-127.

Fluent User Services Center, Modeling Turbulence, March 2005, http://www.fluentusers.com/fluent/doc/ori/html/ug/node408.htm.

Fluent User Services Center, Parallel Processing, November 2004, http://www.fluentusers.com/fluent/doc/ori/html/ug/node1115.htm.

Fluent User Services Center, Choosing the Pressure-Velocity Coupling Method, September 2004, http://www.fluentusers.com/fluent/doc/ori/html/ug/node912.htm.

Fluent User Services Center, Choosing the Discretization Scheme, September 2004, http://www.fluentusers.com/fluent/doc/ori/html/ug/node906.htm.

Fluent User Services Center, General Multiphase Model, July 2004, http://www.fluentusers.com/fluent/doc/ori/html/ug/node772.htm.

Geary, E. L. and Margettes, M. J., 1969, "Penetration of a High Velocity Gas Stream by a Water Jet," *Journal of Spacecraft*, Vol. 6, No. 1, pp. 79-81.

Godunov, S. K., Zabrodin, A. V., and Prokopov, G. P., 1961, "A computational Scheme for Two-Dimensional Non-Stationary Problems of Gas Dynamics and Calculation of the Flow from a Shock Wave Approaching a Steady State," *USSR Computational Mathematics and Math Physics*.

Harten, A., 1983, "High Resolution Schemes for Hyperbolic Conservation Laws," *J. Comp. Phys.*, vol. 49, no. 12, p.357.

Heister, S. D., Nguyen, T. T., and Karagozian, A. R., 1989, "Modeling of Liquid Jets Injected Transversely into a Supersonic Crossflow," *AIAA J.*, vol. 27, no. 12, pp.1727-1734.

Hinze, J. O., 1955, "Fundamentals of the Hydrodynamic Mechanism of Splitting in Dispersion Processes," *AICHE Journal*, vol. 1, pp. 289-295.

Hirt, C. W. and Nichols, B. D., 1981, "Volume of Fluid (VOF) Method for the Dynamics of Free Boundaries," *J. Comput. Phys.*, 39:201-225.

Hsiang, L.-P. and Faeth, G. M., 1992, "Near-Limit Drop Formation and Secondary Breakup," *Int. J. Multiphase Flow*, vol. 18, no. 5, pp. 635-652.

Hwang, S. S., Liu, Z., and Reitz, R. D., 1996, "Breakup mechanisms and drag coefficients of High-speed vaporizing Liquid Drops," *Atomization and Sprays*, vol. 6, pp. 353-376.

Inamura, T., 2000, “Trajectory of a Liquid Jet Traversing Subsonic Airstreams,” *J. Prop. Power*, vol. 16, no. 1, pp.155-157.

Kitamura, Y. and Takahashi, T., 1976, “Stability of a Liquid Jet in Air Flow Normal to the Jet Axis,” *J. Chem. Japan*, vol. 9, no.4, pp.282-286.

Kuzman, R., 1976, Handbook of Thermodynamic Tables and Charts, Hemisphere: Washington.

Leong, M. Y., McDonell, V. G., and Samuelsen, G. S., 2000, “Mixing of an Airblast-Atomized Fuel Spray Injected Into a Crossflow of Air,” NASA/CR-2000-210467, UCI-ARTR-00-05.

Less, D. M. and Schetz, J. A., 1986, “Transient Behavior of Liquid Jets Injected Normal to a High-Velocity Gas Stream,” *AIAA J.*, Vol. 24, No. 12, pp. 1979-1985.

Li, H., 1990, “Transverse Liquid Fuel Jet Breakup, Burning, and Ignition,” DOE/ER/13910-T3, FG03-88ER13910.

Mazallon, J., Dai, Z., and Faeth, G. M., 1999, “Primary Breakup of Nonturbulent Round Liquid Jets in Gas Crossflows,” *Atomization and Sprays*, vol. 9, no. 3, pp. 291-311.

Moffat, R. J., 1985 “Using Uncertainty Analysis in the Planning of an Experiment,” *J. Fluid E*ng., vol. 107, 173-178.

Nguyen, T. T. and Karagozian, A. R., 1992, “Liquid Fuel Jet in Subsonic Crossflow,” *J. Prop. Power*, vol. 8, no. 1, pp. 21-29.

NOAA Satellite and Information Service, Local Climatological Data, November 2005, http://www7.ncdc.noaa.gov/IPS/index.jsp.

Ranger, A. A. and Nicholls, J. A., 1969, “The Aerodynamic Shattering of Liquid Drops,” *AIAA J.*, vol. 7, no. 2, pp. 285-290.

Responsive Engineering, Water Jet Cutting, October 2005, http://www.responsive-engineering.com/streamline/waterjet-cutting.htm.

Sallam, K. A., Aalburg, C., and Faeth, G. M., 2004, “Breakup of Round Nonturbulent Liquid Jets in Gaseous Crossflows,” *AIAA J.*, vol. 42, no. 12, pp. 2529-2540.

Schetz, J. A., Kush, E. A., and Joshi, P. B., 1980, “Wave Phenomena in Liquid Jet Breakup in a Supersonic Crossflow,” *AIAA J.*, vol. 15, no. 2, pp. 774-778.

Schetz, J. A. and Padhye, A., 1977, “Penetration and Breakup of Liquids in Subsonic Airstreams,” *AIAA J.*, vol. 15, no. 10, pp. 1385-1390.

Sussman, M., Smereka, P., and Osher, S., 1994, “A Level Set Approach for Computing Solutions to Incompressible Two-Phase Flow,” *J. Comp. Phys.*, vol. 114, no. 1, pp. 146-159.

Vich, G., 1997, “Destabilisation d’un Jet Liquide par un Ecoulement Gazeux Perpendiculaire,” Ph.D. Dissertation, University of Rouen, Rouen.

White, F. M., 1974, Viscous Fluid Flow, Mc-Graw-Hill, Inc.

Wilcox, D. C., 1998, “Turbulence Modeling for CFD,” DCW Industries, Inc., La Canada, California.

Wu, P.-K., Kirkendall, K. A., Fuller, R. F., and Nejad, A. S., 1997, “Breakup Processes of Liquid Jets in Subsonic Crossflows,” *J. Prop. Power*, vol. 13, no. 1, pp. 64-73.

Yi, Y. and Reitz, R. D., 2004, “Modeling the Primary Breakup of High-Speed Jets,” *Atomization and Sprays*, vol. 14, pp. 53-80.

Yi, Y. and Reitz, R. D., 2002, “A One-Dimensional Breakup Model for Low-Speed Jets,” *Atomization and Sprays*, vol. 12, pp. 667-685.

Youngs, D. L., 1982, “Time-Dependent Multi-Material Flow with Large Fluid Distortion,” *Numerical Methods for Fluid Dynamics*. Acedemic Press.

APPENDIX A

EXPERIMENTAL UNCERTAINTY ANALYSIS

A.1 Uncertainties of the Measured Quantities

In this study, the uncertainties of the measured quantities are assessed based on the analysis of Crow et al. (1955). By assuming that the measured quantities are normally distributed variable, t, the uncertainties can be computed using the following equation:

$$U_t = \frac{s(t_{\alpha/2,\ n-1})}{\sqrt{n}} \tag{A.1}$$

where s is the standard deviation, $t_{\alpha/2,\ n-1}$ denotes the t deviate for f = n-1 degrees of freedom, the probability of exceeding which is P(t) = α/2, and n represents the total number of measurements. The overall uncertainties of the measured quantities reported in this study are taken at a 95% confidence level.

A.2 Uncertainties of the Derived Quantities

To assess how errors propagate through the derived quantities (i.e., SMD_{Bag}) that were obtained from the measured quantities (i.e., d_{Bag}), the uncertainties of the derived quantities are evaluated based on the analysis of Moffat (1985). In this analysis, variables r are considered that are functions of n other independent variables, X_i, as follows:

$$r = f(X_1, X_2, \ldots, X_i) \tag{A.2}$$

where each X_i has its own uncertainty value U_{X_i}. The uncertainty of the result r is then given by the following expression:

$$\frac{U_r}{r} = \left[\sum_{i=1}^{n} \left(\frac{\partial \ln r}{\partial X_i} U_{X_i} \right)^2 \right]^{1/2} \tag{A.3}$$

which depends on the individual uncertainty of each measured variable, U_{X_i}. All the uncertainties reported in the present study are taken at a 95% confidence level.

A.3 Uncertainty Analysis

This section discussed the corresponding uncertainties of the measured and derived quantities tabulated in Appendix B. All measurements performed had experimental uncertainties of less than 10% (95% confidence).

A.3.1 Column and Downwind Surface Wavelengths Uncertainties

The uncertainties of the column and downwind surface wavelengths are accessed based on Eqn. A.1. Repeated measurements of a single test condition were taken, resulting in an uncertainty of less than 10% (95% confidence). The maximum uncertainties were computed as 9.94% and 9.98%, column and downwind surface wavelengths, respectively. The uncertainties for each test conditions are tabulated in Table B.1 and Table B.3, respectively.

A.3.2 Droplets Sizes and Sauter Mean Diameter Uncertainties

The diameter of a droplet is obtained in pixel dimension and converted to laboratory dimensions using a length/pixel conversion factor, R_c. The diameter of a node-, ring-, and bag-droplet are given by the following equation:

$$d_{Droplets,i} = dx_{pixel,i}\, R_c \tag{A.4}$$

where $dx_{pixel,i}$ is the diameter of drop i in pixel dimensions. Repeated measurements of the size of a single node-, ring-, or bag-droplet indicated that the diameter could be sized to ±1 pixel on each boundary, resulting in an uncertainty of ±2 pixels in the diameter measurement. Thus,

$$(U_{d_{Droplets}})_m = 2R_c \tag{A.5}$$

where the subscript m denotes the physical measurement of the drop diameter. Accounting for the uncertainty of R_c, the overall uncertainty of $U_{d_{Droplets,i}}$ then becomes:

$$U_{d_{Droplets,i}} = \{[\partial d_{Droplets,i} / \partial R_c \quad U_{R_c}]^2 + [(U_{d_{Droplets}})_m]^2\}^{1/2} \tag{A.6}$$

where the subscript i refers to the specific drop being considered. The uncertainty given by Eqn. A.6 was calculated to obtain an uncertainty representative of the droplet size measurements.

The Sauter Mean Diameter (SMD) of a droplet size distribution is defined as

$$SMD \equiv \sum_{i=1}^{N} d_{Droplets,i}^{\ 3} \Big/ \sum_{i=1}^{N} d_{Droplets,i}^{\ 2} \tag{A.7}$$

Applying Eqn. A.3 to the overall uncertainty of SMD becomes:

$$U_{SMD}/SMD = \{[\partial(\ln\ SMD)/\partial d_{Droplets}\ \ U_{d_{Droplets}}]^2 + [(U_{SMD}/SMD)_{sample}]^2\}^{1/2} \quad (A.8)$$

where $(U_{SMD}/SMD)_{sample}$ is the uncertainty resulting from the finite sample size. From Eqn. A.7,

$$\partial(\ln\ SMD)/\partial d_{Droplets} = \{3/SMD - 2\sum_{i=1}^{N} d_{Droplets,i} / \sum_{i=1}^{N} d^2_{Droplets,i}\} \quad (A.9)$$

Eqn. A.9 was evaluated for node-, ring-, and bag-droplet and the corresponding maximum uncertainties are shown in Table B.6 to B.8 in Appendix B.

A.3.3 Jet Surface and Droplets Velocities Uncertainties

The x-velocity of any single droplet is

$$u = dx_{Droplets} / dt \quad (A.10)$$

where $dx_{Droplet}$ is the cross-stream distance between the two images of a single droplet. The Nd:YAG lasers have an uncertainty of pulse spacing of 7 ns, which can be neglected. Thus, the uncertainty of the velocity measurements can be evaluated in similar fashion as the droplet diameter uncertainty (i.e., ±2 pixels), and is calculated using the following equation:

$$(U_{u_{Droplets}}/u_{Droplets})_m = (2R_c)/(u_{Droplets}dt) \quad (A.11)$$

The same analysis can be applied to the y-velocity of any single droplet and the liquid surface velocity. Eqn. A.11 was evaluated for liquid surface velocity and node-, ring-, and bag-droplet velocities, the corresponding maximum uncertainties are shown in Table B.2 and Table B.9 to Table B.11, respectively.

A.3.4 Jet Surface and Droplets Trajectories Uncertainties

The droplet positions in the cross-stream (x) and streamwise (y) directions were measured from the center of the nozzle exit to the center of the droplet to plot the droplet trajectory. The uncertainty of the droplet trajectory can be evaluated in similar fashion as the droplet diameter uncertainty (i.e., ±2 pixels). The maximum uncertainties for the droplets positions are shown in Table B.9 to B.13. The same analysis can be applied to the streamwise distance of the jet, the maximum uncertainty is shown in Table B.2.

APPENDIX B

EXPERIMENTAL DATA

Table B.1 Wavelengths of column waves.

Liquid	d_j (mm)	We_G	q	$(\lambda_c/d_j)_{avg}$
Ethyl Alcohol	1	10	224	3.331±0.313
			451	2.900±0.283
			902	2.887±0.279
		20	224	2.628±0.256
			451	2.793±0.266
			902	2.941±0.209
		28	224	2.712±0.265
			451	2.320±0.230
			902	2.543±0.251
	0.5	22	52	2.013±0.200
Water (Tap)	1	8	302	3.745±0.362
			614	2.936±0.292
			1199	3.687±0.341
		16	302	2.866±0.284
			614	2.380±0.234
			1199	2.345±0.233
		24	302	2.355±0.234
			614	2.171±0.214
	0.5	5	614	2.765±0.185
		12	100	1.964±0.189
Water (Distilled)	1	24	150	1.875±0.171

Table B.2 Jet surface velocity.

Liquid	d_j (mm)	We_G	q	y/d_j (U_{max} = 0.1%)	v_s/v_j (U_{max} = 0.2%)
Water (Tap)	1	8	81	27.45	1.08
				27.79	1.05
				29.06	1.07
				26.81	1.03
				28.44	1.08
				31.41	1.08
				29.60	1.10
				31.51	1.09
		16	84	27.20	0.97
				28.05	0.99
				27.46	1.00
				26.01	0.90
				28.72	1.01
				29.49	1.03
				28.14	1.08
				26.03	1.06
				27.76	1.02
			150	30.67	1.02
				30.03	1.07
				30.83	1.09
				30.61	1.08
				29.60	1.04
				27.40	1.09
				30.34	1.11
				26.88	0.94
				31.13	1.02
				28.67	1.08
				26.23	1.08
		24	150	29.57	1.11
				26.59	1.12
				29.09	1.15
				28.00	1.03
				26.38	0.92
				27.06	0.97
				29.50	0.96
				26.79	1.10
				25.96	0.99
				28.74	0.95
				26.59	1.15

Table B.2 Jet surface velocity (con't).

Liquid	d_j (mm)	We_G	q	y/d_j (U_{max} = 0.1%)	v_s/v_j (U_{max} = 0.2%)
Water (Tap)	2	28	75	16.68	0.90
				15.11	0.95
				17.73	1.01
				15.75	1.11
				16.48	1.08
				16.02	1.05
Water (Distilled)	1	24	150	30.72	1.09
				30.43	1.02
				27.96	1.01
				26.06	1.00
				29.64	1.10
				26.67	1.07
				28.29	1.10
				27.06	0.95
				27.52	1.14
				27.92	1.02

Table B.3 Wavelengths of downwind surface waves.

Liquid	d_j (mm)	We_G	q	$(\lambda_s/d_j)_{avg}$
Ethyl Alcohol	1	10	902	1.880±0.185
		20	224	1.877±0.184
			451	1.995±0.198
			902	1.734±0.130
		28	224	1.429±0.141
			451	1.513±0.072
			902	1.301±0.073
Water (Tap)	1	16	302	2.001±0.185
			614	1.562±0.122
			1199	1.574±0.100
		24	302	1.597±0.111
			614	1.478±0.123
			1199	1.192±0.104

Table B.4 Bag counts.

Liquid	d_j (mm)	We_G	q	N_{Bag}	$\{[x_b^2 + (y_b - y_{bf})^2]^{0.5}/\lambda_c\}$
Ethyl Alcohol	1	10	224	10	10
			451	15	16
		20	224	17	15
			451	29	22
		28	224	26	20
Water (Tap)	1	8	302	13	11
		16	302	19	17
			614	23	22
		24	302	23	24

Table B.5 Nodes layout occurrences of the bag structure.

Liquid	d_j (mm)	We_G	q	Nodes Layout	Occurrences (%)
Water (Tap)	1	8	65	4	49.2
				5	28.5
				6	20.0
				7	1.5
				8	0.8

Table B.6 Sauter Mean Diameter of the node-droplet.

Liquid	**d_j (mm)**	**We_G**	**q**	**SMD_{Node}/d_j (U_{max} = 12.7%)**
Ethyl Alcohol	1	10	224	1.07±9.7%
		20	224	0.54±8.4%
		28	224	0.68±8.2%
Water (Tap)	0.5	4	9	2.95±5.2%
			33	2.95±5.4%
			52	2.96±6.1%
	1	16	302	0.64±6.8%
		16.2	53	0.46±2.2%
		27.5	33	0.33±12.7%

Table B.7 Sauter Mean Diameter of the ring-droplet.

Liquid	**d_j (mm)**	**We_G**	**q**	**SMD_{Ring}/d_j (U_{max} = 21.6%)**
Ethyl Alcohol	1	10	224	0.47±21.6%
		20	224	0.21±19.2%
		28	224	0.21±20.3%
Water (Tap)	0.5	4	9	1.29±10.1%
			33	1.25±10.3%
			52	1.33±9.9%
	1	16	302	0.26±15.6%
		16.2	53	0.29±3.1%
		24	37	0.27±7.8%

Table B.8 Sauter Mean Diameter of the bag-droplet.

Liquid	**d_j (mm)**	**We_G**	**q**	**SMD_{Bag}/d_j (U_{max} = 12.3%)**
Ethyl Alcohol	1	25	57	0.11±5.7%
Water (Tap)	1	10	36	0.14±4.4%
			70	0.15±4.3%
			92	0.16±8.4%
		20	38	0.15±4.3%
			82	0.13±5.9%
		24	78	0.13±5.8%
		30	39	0.17±5.0%
	2	28.2	55	0.11±12.3%

Table B.9 Velocities of node-droplet.

Liquid	d_j (mm)	We_G	q	x/d_j (U_{max} = 0.1%)	u_{Node}/U_G (U_{max} = 0.1%)	y/d_j (U_{max} = 0.03%)	v_{Node}/v_j (U_{max} = 0.4%)	d_{Node}/SMD_{Node} (U_{max} = 12.9%)
Water (Tap)	1	16.2	50	15.16	0.27	31.01	0.78	0.86±4.6%
				15.49	0.28	30.61	0.83	1.04±4.5%
				12.27	0.27	31.45	0.92	1.16±4.4%
				15.63	0.28	33.39	0.86	0.92±4.5%
				15.22	0.32	31.13	0.73	0.91±4.5%
				14.18	0.28	32.07	0.83	1.02±4.5%
				11.96	0.26	30.62	0.89	0.98±4.5%
				13.95	0.26	33.04	0.83	0.99±4.5%
				11.80	0.26	29.63	0.83	1.00±4.5%
		27.5	33	13.76	0.31	33.28	1.13	0.83±12.9%
				12.67	0.26	32.64	1.03	0.83±12.9%
				14.32	0.31	30.77	0.92	1.00±12.8%
				13.05	0.25	33.41	1.12	1.17±12.8%

Table B.10 Velocities of ring-droplet.

Liquid	d_j (mm)	We_G	q	x/d_j (U_{max} = 0.1%)	u_{Ring}/U_G (U_{max} = 0.2%)	y/d_j (U_{max} = 0.1%)	v_{Ring}/v_j (U_{max} = 0.8%)	d_{Ring}/SMD_{Ring} (U_{max} = 9.1%)
Water (Tap)	1	16.2	53	13.57	0.37	29.39	0.88	0.92±3.8%
				15.20	0.21	34.78	0.98	0.90±3.9%
				15.71	0.24	34.87	0.89	0.67±4.4%
				14.08	0.27	31.68	0.90	0.42±5.8%
				14.35	0.28	31.44	0.89	0.58±4.7%
				11.97	0.28	31.07	0.92	1.29±3.5%
				15.31	0.30	32.12	0.77	0.95±3.8%
				14.26	0.27	31.45	0.99	0.48±5.3%
				14.22	0.25	31.10	0.88	0.65±4.4%
				12.76	0.29	30.20	0.80	1.35±3.5%
				14.46	0.36	30.61	0.75	0.95±3.8%
				15.15	0.24	30.09	0.74	0.66±4.4%
				15.74	0.24	33.26	0.92	0.85±3.9%
	1	24	37	13.08	0.18	30.40	0.86	0.55±8.7%
				13.52	0.25	30.70	0.91	1.34±7.9%
				14.60	0.16	31.43	0.66	1.35±7.9%
				14.76	0.30	30.26	0.89	0.87±8.2%
				15.41	0.27	34.55	1.08	0.81±8.2%
				13.71	0.19	31.14	1.07	1.07±8.0%
				14.49	0.22	30.45	0.90	0.73±8.3%
				14.79	0.27	29.99	0.84	1.23±8.0%
				15.33	0.30	30.16	0.88	1.03±8.1%
				14.39	0.30	29.79	0.83	0.63±8.5%
				14.65	0.24	30.20	0.80	0.51±8.9%
				14.85	0.26	29.36	0.68	0.82±8.2%
				12.53	0.32	30.41	1.00	0.56±8.7%
				15.08	0.33	29.61	0.88	0.63±8.5%
				14.45	0.28	31.97	0.82	0.57±8.7%
				14.27	0.23	31.66	0.88	0.47±9.0%
				14.33	0.31	31.20	1.04	0.47±9.1%
				14.23	0.27	29.65	0.87	0.66±8.4%
	2	29	52	8.10	0.23	17.58	0.65	1.02±8.2%
				8.01	0.27	19.77	0.73	1.06±8.1%
				7.31	0.23	19.56	0.94	0.91±8.6%

Table B.11 Velocities of bag-droplet.

Liquid	d_j (mm)	We_G	q	x/d_j (U_{max} = 0.1%)	u_{Bag}/U_G (U_{max} = 0.3%)	y/d_j (U_{max} = 0.1%)	v_{Bag}/v_j (U_{max} = 1.8%)	d_{Bag}/SMD_{Bag} (U_{max} = 11.5%)
Water (Tap)	1	10	92	15.85	0.21	33.74	0.21	0.46±11.5%
				15.66	0.21	34.87	0.19	1.35±8.8%
				13.50	0.16	35.01	0.50	0.78±9.6%
				13.97	0.20	34.56	0.30	0.69±9.9%
				14.44	0.21	32.99	0.24	0.79±9.6%
				14.34	0.26	34.99	0.32	1.36±8.8%
				15.31	0.39	34.92	0.34	1.29±8.9%
				15.48	0.38	33.98	0.23	0.94±9.2%
		20	82	11.06	0.40	30.80	0.45	0.67±9.2%
				11.15	0.39	30.67	0.42	0.51±11.1%
				11.41	0.40	30.58	0.38	0.57±10.1%
				12.51	0.45	33.10	0.70	1.23±7.0%
				13.06	0.45	33.44	0.76	0.49±11.2%
				12.55	0.41	31.24	0.60	0.98±7.6%
				12.84	0.43	31.45	0.62	1.00±7.6%
				12.92	0.36	31.87	0.31	0.84±8.2%
				12.27	0.27	31.53	0.23	0.75±8.6%
				12.60	0.28	31.48	0.25	0.90±7.9%
				12.93	0.29	30.62	0.12	0.87±8.0%
				11.13	0.37	29.96	0.47	0.89±7.9%
				11.42	0.38	29.68	0.45	0.81±8.3%
				12.94	0.39	33.14	0.58	0.78±8.5%
				11.27	0.27	30.16	0.32	0.77±8.5%
				12.79	0.32	30.32	0.23	1.39±6.8%
				12.66	0.32	29.84	0.21	0.77±8.5%
				11.37	0.27	31.17	0.51	0.85±8.1%
				13.74	0.30	31.95	0.49	1.16±7.2%
				13.55	0.35	31.64	0.47	1.22±7.0%
				14.22	0.44	30.88	0.19	1.08±6.7%
				10.31	0.30	30.19	0.45	0.83±8.2%
				10.66	0.31	29.64	0.32	0.83±8.2%
				10.99	0.32	29.87	0.33	0.90±7.9%
				13.94	0.35	31.95	0.34	1.10±7.3%
				13.95	0.36	31.65	0.30	1.17±7.1%

Table B.11 Bag-droplet velocities (con't).

Liquid	d_j (mm)	We_G	q	x/d_j (U_{max} = 0.1%)	u_{Bag}/U_G (U_{max} = 0.3%)	y/d_j (U_{max} = 0.1%)	v_{Bag}/v_j (U_{max} = 1.8%)	d_{Bag}/SMD_{Bag} (U_{max} = 15.1%)
Water (Tap)	1	24	78	12.21	0.36	29.66	0.42	0.70±8.6%
				12.38	0.36	29.71	0.42	0.71±8.5%
				13.03	0.94	29.61	2.72	0.68±8.7%
				13.79	0.32	30.61	2.40	0.78±8.2%
				10.26	0.28	34.62	0.89	0.87±7.7%
				10.76	0.31	34.67	0.87	0.59±9.5%
				12.17	0.41	32.77	0.89	1.12±7.0%
				12.37	0.42	32.98	0.92	1.21±6.9%
				12.65	0.64	33.55	0.23	1.07±7.2%
				12.97	0.36	33.26	0.61	0.73±8.4%
				13.04	0.32	32.76	0.53	0.98±7.4%
				12.43	0.37	31.79	0.68	0.63±9.2%
				12.56	0.36	31.72	0.66	0.90±7.6%
				12.89	0.38	31.83	0.71	0.83±7.9%
				14.86	0.29	34.73	0.71	0.87±7.7%
				15.10	0.28	34.45	0.68	1.37±6.7%
				12.41	0.41	30.69	0.52	0.94±7.5%
				12.76	0.40	29.74	0.43	0.80±8.1%
				12.71	0.31	34.00	0.98	1.32±6.7%
				12.60	0.32	33.72	0.93	1.37±6.7%
				11.12	0.28	33.37	0.79	0.57±9.7%
				10.98	0.27	33.22	0.75	0.52±10.3%
				14.09	0.46	30.29	0.41	0.75±8.3%
				13.97	0.44	31.26	0.57	1.05±7.2%
				14.22	0.31	33.96	0.43	0.93±7.5%
				14.62	0.35	33.57	0.68	0.80±8.1%
				12.44	0.36	31.27	0.62	0.74±8.4%
				13.46	0.39	30.80	0.52	0.78±8.2%
				13.66	0.32	30.69	0.46	1.11±7.1%
				14.00	0.33	30.27	0.46	0.84±7.9%
	2	28.2	55	6.05	0.20	16.32	0.28	0.63±14.6%
				6.13	0.23	16.40	0.49	0.57±15.0%
				6.08	0.19	15.75	0.55	0.58±15.0%
				4.63	0.11	15.49	0.34	0.56±15.1%
				7.81	0.34	17.68	0.91	1.11±13.1%
				8.32	0.39	17.30	0.80	1.27±12.9%
				7.97	0.29	16.51	0.55	1.17±13.0%

Table B.12 Trajectories of node-droplet [$(U_{x_{Node}})_{max} = 0.8\%$, $(U_{y_{Node}})_{max} = 0.8\%$].

Liquid	d_j (mm)	We_G	q	$x_{Node}/(d_j q)$	$y_{Node}/(d_j q)$
Ethyl Alcohol	1	8	88	0.21	0.57
				0.31	0.68
				0.29	0.74
				0.37	0.81
				0.50	0.88
				0.64	0.95
Water (Tap)	0.5	4	9	4.26	5.51
				4.73	6.27
				5.12	6.30
				5.61	6.04
				7.32	6.52
				7.72	6.78
				9.05	8.25
				11.08	9.51
				13.80	10.46
			21	1.37	2.13
				1.51	2.40
				1.95	2.50
				2.67	2.99
				3.38	3.31
				3.64	3.53
				5.10	3.91
				5.89	4.06
			43	0.63	1.35
				0.72	1.37
				0.87	1.58
				0.95	1.64
				1.17	1.82
				1.49	2.07
				1.94	2.45
				2.05	2.44
				2.72	3.05
	1	8	11	3.35	4.35
				3.44	4.44
				3.66	4.61
				4.15	5.89
				5.19	6.59

Table B.13 Trajectories of bag-droplet [$(U_{x_{Bag}})_{max} = 1\%$, $(U_{y_{Bag}})_{max} = 4\%$].

Liquid	d_j (mm)	We_G	q	$x_{Bag}/(d_j q)$	$y_{Bag}/(d_j q)$
Ethyl Alcohol	1	8	88	0.30	0.46
				0.31	0.46
				0.32	0.46
				0.36	0.43
				0.44	0.43
				0.46	0.44
				0.48	0.44
				0.49	0.45
				0.51	0.45
				0.53	0.43
				0.53	0.41
				0.54	0.40
Water (Tap)	0.5	4	9	1.99	2.68
				4.32	2.70
				4.74	2.86
				4.88	2.84
				5.23	2.83
				5.53	2.88
				6.09	3.03
				7.61	2.80
				8.64	2.55
				10.15	2.85
				11.40	3.55
				11.85	3.77
				12.88	3.85
				13.35	4.03
			21	1.45	1.22
				1.80	1.26
				2.11	1.23
				2.23	1.29
				2.62	1.38
				2.91	1.32
				3.03	1.33
				3.06	1.24
				3.81	1.23
				4.89	1.31
				5.23	1.19

Table B.13 Trajectories of bag-droplet (con't).

Liquid	d_j (mm)	We_G	q	$x_{Bag}/(d_j q)$	$y_{Bag}/(d_j q)$
Water (Tap)	0.5	4	21	5.37	1.26
				5.62	1.28
			43	0.46	0.91
				0.96	0.89
				1.09	0.94
				1.24	0.97
				1.30	1.02
				1.35	1.04
				1.70	0.85
				1.93	0.77
				2.05	0.83
				2.13	0.78
				2.36	0.81
	1	8	11	2.53	2.89
				2.74	2.96
				2.98	2.89
				3.36	2.77
				3.77	2.52
				3.80	2.54
				4.57	2.96
				4.87	3.14
				5.03	3.28
				5.44	3.15

Table B.14 Water density and viscosity variations.

Date	Pressure[a] (kPa)	Temperature[b] (^{o}C)	Density[*] (kg/m^{3})	Viscosity[†] (kg/m.s x 10^{-4})
1-Jul-05	96.70	25.56	996.33	8.84
2-Jul-05	96.57	26.11	996.17	8.74
3-Jul-05	96.26	28.89	995.33	8.22
4-Jul-05	96.91	23.89	996.83	9.19
5-Jul-05	97.08	25.56	996.33	8.84
6-Jul-05	96.94	25.56	996.33	8.84
7-Jul-05	96.91	25.56	996.33	8.84
8-Jul-05	96.98	25.56	996.33	8.84
9-Jul-05	96.91	26.11	996.17	8.74
10-Jul-05	96.74	26.11	996.17	8.74
11-Jul-05	96.74	26.67	996.00	8.63
12-Jul-05	97.08	28.33	995.50	8.33
13-Jul-05	96.94	27.78	995.67	8.43
14-Jul-05	96.70	26.11	996.17	8.74
15-Jul-05	96.77	28.33	995.50	8.33
16-Jul-05	96.87	26.67	996.00	8.63
17-Jul-05	96.70	27.78	995.67	8.43
18-Jul-05	96.84	28.33	995.50	8.33
19-Jul-05	96.87	28.89	995.33	8.22
20-Jul-05	96.98	29.44	995.17	8.12
21-Jul-05	97.14	29.44	995.17	8.12
22-Jul-05	97.18	30.00	995.00	8.02
23-Jul-05	97.11	30.56	994.83	7.93
24-Jul-05	96.94	28.89	995.33	8.22
25-Jul-05	96.64	30.56	994.83	7.93
26-Jul-05	96.64	26.67	996.00	8.63
27-Jul-05	97.28	23.33	997.00	9.31
28-Jul-05	97.35	23.33	997.00	9.31
29-Jul-05	97.42	23.89	996.83	9.19
30-Jul-05	97.38	26.67	996.00	8.63
31-Jul-05	97.25	26.67	996.00	8.63
1-Aug-05	97.11	27.22	995.83	8.53
2-Aug-05	96.94	28.89	995.33	8.22
3-Aug-05	96.84	28.89	995.33	8.22
4-Aug-05	97.11	28.89	995.33	8.22
5-Aug-05	97.42	27.78	995.67	8.43
6-Aug-05	97.21	27.22	995.83	8.53
7-Aug-05	97.04	27.78	995.67	8.43
8-Aug-05	96.98	27.22	995.83	8.53
9-Aug-05	96.94	27.22	995.83	8.53
10-Aug-05	96.94	27.22	995.83	8.53

[a, b] Obtained from NOAA Satellite and Information Service.
[*, †] Obtained from Handbook of Thermodynamics Tables and Charts (Kuzman, 1976).

Table B.14 Water density and viscosity variations (con't)

Date	Pressure[a] (kPa)	Temperature[b] (^{o}C)	Density[*] (kg/m^{3})	Viscosity[†] (kg/m.s x 10^{-4})
11-Aug-05	96.77	27.22	995.83	8.53
12-Aug-05	96.64	30.00	995.00	8.02
13-Aug-05	96.60	27.22	995.83	8.53
14-Aug-05	96.81	23.89	996.83	9.19
15-Aug-05	97.18	23.89	996.83	9.19
16-Aug-05	97.21	23.89	996.83	9.19
17-Aug-05	96.67	28.33	995.50	8.33
18-Aug-05	96.43	30.56	994.83	7.93
19-Aug-05	96.67	30.00	995.00	8.02
20-Aug-05	97.08	28.89	995.33	8.22
21-Aug-05	97.21	26.67	996.00	8.63
22-Aug-05	96.81	26.67	996.00	8.63
23-Aug-05	96.60	26.11	996.17	8.74
24-Aug-05	96.64	28.89	995.33	8.22
25-Aug-05	96.87	28.33	995.50	8.33
26-Aug-05	96.64	29.44	995.17	8.12
27-Aug-05	96.53	25.56	996.33	8.84
28-Aug-05	96.50	26.11	996.17	8.74
29-Aug-05	96.37	25.56	996.33	8.84
30-Aug-05	96.37	26.11	996.17	8.74
31-Aug-05	96.67	25.56	996.33	8.84
1-Sep-05	97.04	26.67	996.00	8.63
2-Sep-05	97.28	26.67	996.00	8.63
3-Sep-05	97.42	26.11	996.17	8.74
4-Sep-05	97.35	25.56	996.33	8.84
5-Sep-05	97.35	24.44	996.67	9.06
6-Sep-05	97.38	24.44	996.67	9.06
7-Sep-05	97.48	26.11	996.17	8.74
8-Sep-05	97.28	25.56	996.33	8.84
9-Sep-05	96.98	25.00	996.50	8.94
10-Sep-05	96.87	25.56	996.33	8.84
11-Sep-05	97.04	24.44	996.67	9.06
12-Sep-05	96.84	26.67	996.00	8.63
13-Sep-05	96.47	29.44	995.17	8.12
14-Sep-05	96.60	23.33	997.00	9.31
Average			995.93	8.60
Uncertainty (%)			0.01	1.0

[a, b] Obtained from NOAA Satellite and Information Service.
[*, †] Obtained from Handbook of Thermodynamics Tables and Charts (Kuzman, 1976).

Table B.15 Ethyl alcohol density and viscosity variations.

Date	Pressure[a] (kPa)	Temperature[b] (^{o}C)	Density[*] (kg/m^{3})	Viscosity[†] (kg/m.s x 10^{-4})
1-Jul-05	96.70	25.56	784.56	10.84
2-Jul-05	96.57	26.11	784.11	10.72
3-Jul-05	96.26	28.89	781.89	10.14
4-Jul-05	96.91	23.89	785.89	11.19
5-Jul-05	97.08	25.56	784.56	10.84
6-Jul-05	96.94	25.56	784.56	10.84
7-Jul-05	96.91	25.56	784.56	10.84
8-Jul-05	96.98	25.56	784.56	10.84
9-Jul-05	96.91	26.11	784.11	10.72
10-Jul-05	96.74	26.11	784.11	10.72
11-Jul-05	96.74	26.67	783.67	10.61
12-Jul-05	97.08	28.33	782.33	10.26
13-Jul-05	96.94	27.78	782.78	10.37
14-Jul-05	96.70	26.11	784.11	10.72
15-Jul-05	96.77	28.33	782.33	10.26
16-Jul-05	96.87	26.67	783.67	10.61
17-Jul-05	96.70	27.78	782.78	10.37
18-Jul-05	96.84	28.33	782.33	10.26
19-Jul-05	96.87	28.89	781.89	10.14
20-Jul-05	96.98	29.44	781.44	10.03
21-Jul-05	97.14	29.44	781.44	10.03
22-Jul-05	97.18	30.00	781.00	9.91
23-Jul-05	97.11	30.56	780.50	9.82
24-Jul-05	96.94	28.89	781.89	10.14
25-Jul-05	96.64	30.56	780.50	9.82
26-Jul-05	96.64	26.67	783.67	10.61
27-Jul-05	97.28	23.33	786.33	11.30
28-Jul-05	97.35	23.33	786.33	11.30
29-Jul-05	97.42	23.89	785.89	11.19
30-Jul-05	97.38	26.67	783.67	10.61
31-Jul-05	97.25	26.67	783.67	10.61
1-Aug-05	97.11	27.22	783.22	10.49
2-Aug-05	96.94	28.89	781.89	10.14
3-Aug-05	96.84	28.89	781.89	10.14
4-Aug-05	97.11	28.89	781.89	10.14
5-Aug-05	97.42	27.78	782.78	10.37
6-Aug-05	97.21	27.22	783.22	10.49
7-Aug-05	97.04	27.78	782.78	10.37
8-Aug-05	96.98	27.22	783.22	10.49
9-Aug-05	96.94	27.22	783.22	10.49
10-Aug-05	96.94	27.22	783.22	10.49

[a, b] Obtained from NOAA Satellite and Information Service.
[*, †] Obtained from Handbook of Thermodynamics Tables and Charts (Kuzman, 1976).

Table B.15 Ethyl alcohol density and viscosity variations (con't).

Date	Pressure[a] (kPa)	Temperature[b] (^{o}C)	Density[*] (kg/m^{3})	Viscosity[†] (kg/m.s x 10^{-4})
11-Aug-05	96.77	27.22	783.22	10.49
12-Aug-05	96.64	30.00	781.00	9.91
13-Aug-05	96.60	27.22	783.22	10.49
14-Aug-05	96.81	23.89	785.89	11.19
15-Aug-05	97.18	23.89	785.89	11.19
16-Aug-05	97.21	23.89	785.89	11.19
17-Aug-05	96.67	28.33	782.33	10.26
18-Aug-05	96.43	30.56	780.50	9.82
19-Aug-05	96.67	30.00	781.00	9.91
20-Aug-05	97.08	28.89	781.89	10.14
21-Aug-05	97.21	26.67	783.67	10.61
22-Aug-05	96.81	26.67	783.67	10.61
23-Aug-05	96.60	26.11	784.11	10.72
24-Aug-05	96.64	28.89	781.89	10.14
25-Aug-05	96.87	28.33	782.33	10.26
26-Aug-05	96.64	29.44	781.44	10.03
27-Aug-05	96.53	25.56	784.56	10.84
28-Aug-05	96.50	26.11	784.11	10.72
29-Aug-05	96.37	25.56	784.56	10.84
30-Aug-05	96.37	26.11	784.11	10.72
31-Aug-05	96.67	25.56	784.56	10.84
1-Sep-05	97.04	26.67	783.67	10.61
2-Sep-05	97.28	26.67	783.67	10.61
3-Sep-05	97.42	26.11	784.11	10.72
4-Sep-05	97.35	25.56	784.56	10.84
5-Sep-05	97.35	24.44	785.44	11.07
6-Sep-05	97.38	24.44	785.44	11.07
7-Sep-05	97.48	26.11	784.11	10.72
8-Sep-05	97.28	25.56	784.56	10.84
9-Sep-05	96.98	25.00	785.00	10.96
10-Sep-05	96.87	25.56	784.56	10.84
11-Sep-05	97.04	24.44	785.44	11.07
12-Sep-05	96.84	26.67	783.67	10.61
13-Sep-05	96.47	29.44	781.44	10.03
14-Sep-05	96.60	23.33	786.33	11.30
Average			783.48	10.56
Uncertainty (%)			0.0004	0.009

[a, b] Obtained from NOAA Satellite and Information Service.
[*, †] Obtained from Handbook of Thermodynamics Tables and Charts (Kuzman, 1976).

Table B.16 Surface tension measurements.

Attempt	$\sigma_{tap\ water}$ (N/m x 10^{-3}) (Stillwater)	$\sigma_{tap\ water}$ (N/m x 10^{-3}) (Tulsa)	$\sigma_{distilled\ water}$ (N/m x 10^{-3})
1	72.20	72.20	72.20
2	72.40	73.42	72.10
3	72.71	73.62	72.10
4	74.13	72.20	75.75
5	75.75	73.62	75.75
Mean	73.44±1.86	73.01±0.92	73.58±2.46

APPENDIX C

PARALLEL PROCESSING SETUP

Parallel processing in FLUENT involves communication between FLUENT, a host processor, and a set of computer-node processors. In parallel processing, FLUENT divides the grid and associated computations into multiple partitions, assigning one or more partitions to a different computer node. The number of partitions must be an integral multiple of the number of computer nodes available (i.e., 4 partitions for 1, 2, and 4 computer nodes). The computer-node processes can then be executed on a massively-parallel computer system (i.e., a 3-processor parallel Linux cluster). Since parallel processing efficiency decreases as the ratio of communication time to computation time increases, parallel processing works most effectively with high-density meshes requiring an exceedingly large number of computations. The host processor interprets commands from FLUENT's graphics-related interface - cortex, distributing those commands to the other nodes via a single designated compute node, known as "Node-Ø" and a socket communicator. Node-Ø distributes the host command to other parallel nodes; where each parallel node simultaneously executes the same program on its own data set, or partitioned grid region. Each node is "virtually" connected to all other nodes, and relies on Node-Ø to send and receive data arrays, synchronize numerical operations, perform global operations (i.e., data summations over all cells), and maintain machine connectivity (Fluent User Services Center, 2004).

To employ the parallel solver in FLUENT, the computational grid first needs to be subdivided (partitioned) into cell groups that can be analyzed by separated processors. It is recommended to perform the partition after setup of all other solver parameters due to model dependencies (i.e., grid adaption on non-conformal interfaces and sliding-mesh encapsulation). The basic procedures for manual partitioning of a simulation in FLUENT are:

- Select Principal Axes bisection method, and number of grid partitions based on the number of computer nodes available. The Principal Axes specification bisects the computational domain in a coordinate frame aligned with the principal axes of the grid.
- Allow partitions to cross zone boundaries by enabling the Across Zones check button.
- Select Encapsulate Grid Interfaces to allow cells surrounding all non-conformal grid interfaces (i.e., sliding-mesh interface) to reside in a single partition at all times during calculations. In addition, check Encapsulate for Adaption to allow additional layers cell encapsulation such that cell transfer is not necessary during parallel adaption.
- Activate Merge and Smooth iterative optimization schemes and set the number of iterations to 0, allowing the optimization scheme to be applied until completion without a limit on the number of iterations. Smooth optimization attempts to minimize the number of interfaces between partitions by swapping cells between partitions. Merge optimization attempts to eliminate orphan clusters that can

degrade multigrid performance and increase parallel communication costs from each partition.

- Turn on Pre-Test option to improve Principal Axes bisection by testing all coordinate directions and choose the direction yielding the fewest partition interfaces.
- Examine partition statistics and look for small values of interface ratio variation and global interface ratio while maintaining a balanced load across the partitions. For example, the following sample output has interface ratio variation of 1.3% - 3.1% and global interface ratio of 2.07% (i.e., 0.018 + 0.031 + 0.013 = 0.0207).

```
3 Partitions:
P   Cells I-Cells Cell Ratio  Faces I-Faces Face Ratio Neighbors
0  111341    5001      0.045 344385    6272      0.018         1
1  111429    7762      0.070 343096   10743      0.031         2
2  111256    2275      0.025 345369    4471      0.013         1
```

The basic procedures of implementing a parallel simulation in FLUENT are:

- Start parallel solver and spawn additional computer nodes.
- Read in previously partitioned case (and data) file.
- Start solution calculations.

The time-accurate analyses are conducted using a time step equals to 0.2 μs with 35 sub-iterations per time step to meet the proposed solution convergence (refer to section 3.6) and to maintain solution stability. In some cases, the number of sub-iterations was increased to uphold the aforementioned criteria. For full configuration within the bag breakup regime, the simulation requires 17 seconds to perform a single iteration on a P4 desktop (Dell Dimension P4 HT 3.6Ghz with 4GB DDR2 SDRAM ≈ 3-partitioned parallel solver). For full configuration within the shear breakup regime, the

simulation requires 26 seconds to perform a single iteration on a 3-partitioned parallel solver (3 P4 2.5Ghz with 1GB DDR SDRAM). The simulation for shear breakup regime requires approximately 7 months for the crossflow Weber number to reach 220, and an additional computational time of approximately 2 months to establish a converged solution. To speed up simulation convergence, the converged solution of the column breakup regime was interpolated into the computational grid of the bag breakup regime to serve as the initial conditions. Different configurations (i.e., full configuration and half configuration) of different grids (i.e., bag breakup and shear breakup regimes) were setup to run concurrently on the 3-processor parallel Linux cluster and five P4 desktops, allowing the simulations to be completed within the research timeframe.

VITA

Chee-Loon Ng

Candidate for the Degree of

Doctor of Philosophy

Thesis: DEFORMATION, WAVE PHENOMENA, AND BREAKUP OUTCOMES OF ROUND NONTURBULENT LIQUID JETS IN UNIFORM GASEOUS CROSSFLOW.

Major Field: Mechanical Engineering

Biographical:

Personal Data: Born in Malaysia, May 10 1974, the son of Sin-Hua Ng and Swee-Leng Ong.

Education: Received Bachelor of Science degree and Master of Science degree in Mechanical Engineering from Oklahoma State University, Stillwater, Oklahoma in July 1998 and December 1999, respectively. Completed the requirements for Doctor of Philosophy degree in Mechanical Engineering from Oklahoma State University, Stillwater, Oklahoma in July 2006.

Experience: Employed by Oklahoma State University, Department of Mechanical and Aerospace Engineering as a graduate research assistant, 1998 to 1999. Employed by STATS ChipPAC, Ltd., Singapore as a ball attach process and encapsulation process engineer, 2001. Employed by Oklahoma State University, Department of Mechanical and Aerospace Engineering as a graduate research assistant, 2003 to 2006.

Professional Memberships: Golden Key National Honor Society, Tau Beta Pi – National Engineering Honor Society, Pi Tau Sigma – Mechanical Engineering National Honor Society, The America Society of Mechanical Engineering, American Institute of Aeronautics and Astronautics, American Physical Society.

Name: Chee-Loon Ng Date of Degree: July, 2006

Institution: Oklahoma State University Location: Stillwater, Oklahoma

Title of Study: DEFORMATION, WAVE PHENOMENA, AND BREAKUP OUTCOMES OF ROUND NONTURBULENT LIQUID JETS IN UNIFORM GASEOUS CROSSFLOW.

Pages in Study: 202 Candidate for the Degree of Doctor of Philosophy

Major Field: Mechanical Engineering

Scope and Method of Study: An experimental and computational research is performed to study the deformation and breakup of round nonturbulent liquid jets in uniform gaseous crossflow. Pulsed photography and shadowgraphy in conjunction with high-speed imaging were used to study the wave phenomena and the droplets properties/transport dynamics of a nonturbulent liquid jet injected into a uniform crossflow within the bag breakup regime. The computational study extended the previous two-dimensional study by adding the third dimension, allowing the wave properties to be modeled. The computational simulation employed the Volume of Fluid (VOF) formulation of FLUENT, and was run on a 3-processors parallel Linux cluster and P4 desktops. The validated, time-accurate, CFD simulation analyzes the surface properties of the liquid jets within the column, bag, and shear breakup regimes by considering the effects of surface tension, liquid viscosity, and crossflow Weber number at large liquid/gas density ratios (>500) and small Ohnesorge numbers (< 0.1).

Findings and Conclusions: Present experimental results show that the column waves along the liquid jet are attributed to Rayleigh-Taylor instabilities and the nodes layout per bag affected the breakup mechanisms of the bags. Three distinctive sizes of droplets were produced in the bag breakup regime. The size of bag-droplets normalized by the nozzle exit diameter was constant. The different trajectories for bag- and node-droplets suggested that separation of bag- and node-droplets is possible. The computational results included jet deformations, jet cross-sectional area, jet velocity, wake velocity defect, wake width, and wavelengths of column and surface waves. Present computational results yielded a similarity solution for the inner wake region. In bag breakup, the lower pressure along the sides of the jet pulled the liquid away from both the upwind and downwind surfaces of the liquid cross-section. In shear breakup, the flattened upwind surface pushed the liquid towards the two sides of the jet. In bag breakup, the flow field inside the liquid jet consisted of a counter-rotating vortex pair that was not observed in column and shear breakup. Finally, Phenomenological analyses were effective to understand the conditions for breakup regime transitions.

ADVISOR'S APPROVAL: Khaled A. Sallam